STABILITY OF SELF BALANCING TRANSPORTERS

A Thesis
Presented to
The Academic Faculty

by

Arnoldo Castro

In Partial Fulfillment
of the Requirements for the Degree
Doctor of Philosophy in the
Woodruff School of Mechanical Engineering

Georgia Institute of Technology
December 2019

STABILITY OF SELF BALANCING TRANSPORTERS

Approved by:

Professor William Singhose, Advisor
Woodruff School of Mechanical Engineering
Georgia Institute of Technology

Professor Michael Leamy
Woodruff School of Mechanical Engineering
Georgia Institute of Technology

Professor Thomas Kurfess
Woodruff School of Mechanical Engineering
Georgia Institute of Technology

Professor David G. Taylor
Woodruff School of Mechanical Engineering
Georgia Institute of Technology

Professor Khalid Sorensen
Woodruff School of Mechanical Engineering
Georgia Institute of Technology

Date Approved: 6 November 2019

ACKNOWLEDGEMENTS

I would like to thank the many people who have helped one way or another in making it possible for me to complete this goal in my life:

My advisor, Dr. William Singhose, for providing his guidance along all these years, for sharing his profound knowledge and his unique vision of this project, and for being a very patient and motivating advisor.

My committee members, Dr. Thomas Kurfess, Dr. David Taylor, Dr. Khalid Sorensen, and Dr. Michael Leamy, for their patience, support, and valuable feedback. I would like to give special thanks to Dr. Michael Leamy who provided valuable support at a difficult moment.

My labmates, who provided a stimulating intellectual environment, unique insights, help and advise over the years. I would like to give special thanks to C.J. Adams, James Potter, Ali Alsaibie, and Xiashu Liu for their help in carrying out experiments and their contributions to my projects.

My friends Doris, Samar, Paul, Mauricio, Victor, Caitlin, Diego, Jackie, Marie, and Laura, among many others, who gave me emotional support, encouragement, a soccer team to play with, and social activites.

The Fulbright Program for making it possible to attend Georgia Tech, the University of Costa Rica and the Government of Costa Rica, for their financial support.

Finally, my parents and my brothers for all the sacrifices they made for providing me with a good education and the opportunities to follow my dreams. My sister for being my best friend and her concerns for my well-being. My uncles for being there when I needed the most. All of them for their unconditional support, love, and for making me the person I am today.

SUMMARY

A class of personal transporters based on two-wheeled inverted-pendulum machines has emerged as alternative transportation system for urban and indoor environments. However, these machines are inherently unstable. Typical use conditions can lead to very unstable and dangerous conditions. Furthermore, the control system does not attempt to stabilize the system laterally, which creates a fast-acting tip-over that is extremely challenging for the user to anticipate and mitigate.

In this work, a vehicle and user model are developed to investigate the potential operating conditions that can cause failure during normal use. This model aims to provide a more thorough description of the wheel-ground interaction, as well as the oscillatory and unstable dynamic behavior of two-wheeled inverted-pendulum transporters..

The models also serves as a test platform for evaluating traction-control methods that have not typically. These new traction-control methods can potentially ameliorate the dangers associated with wheel slipping and lateral instability.

TABLE OF CONTENTS

LIST OF TABLES

LIST OF FIGURES

CHAPTER I

INTRODUCTION

The past two decades have seen the commercialization of personal transporters in various configurations of a two-wheeled inverted pendulum. Both Segway-type machines [50, 62] and "hoverboards" [21, 40, 63] have made significant impacts in our society. Although such machines offer high maneuverability and a small footprint, complex dynamics and non-ideal conditions make them prone to unexpected behavior that can pose significant dangers.

A two-wheeled inverted pendulum is composed of a base platform with a wheel mounted on each side, as shown in Figure 1. The wheels are driven forward and backward in order to move the base and toward a balancing state. When the base or a part of the base (hoverboards) tilts in one direction, the controller accelerates the wheels in the same direction in order to restore the upright position. To turn the base about a vertical axis, the wheels are rotated at different speeds. In contrast to acceleration or breaking motions, turning maneuvers must be commanded in a more complex way than simply leaning forward or backward. For example, the second-generation Segway requires handlebar tilting. Furthermore, there is no balancing control or actuation forces in the roll direction. A limited amount of roll stability is designed into the machines via the wheel separating distance.

One of the most recognized versions of two-wheeled inverted pendulums is the Segway personal transporter. Figure 2 shows the Segway i167. A newer version of this device is the Segway i2, shown in Figure 3. The main difference between these two devices is the way turns are commanded. When using the Segway i167 the operator twists the left hand grip to input the desired turn direction. Meanwhile, on

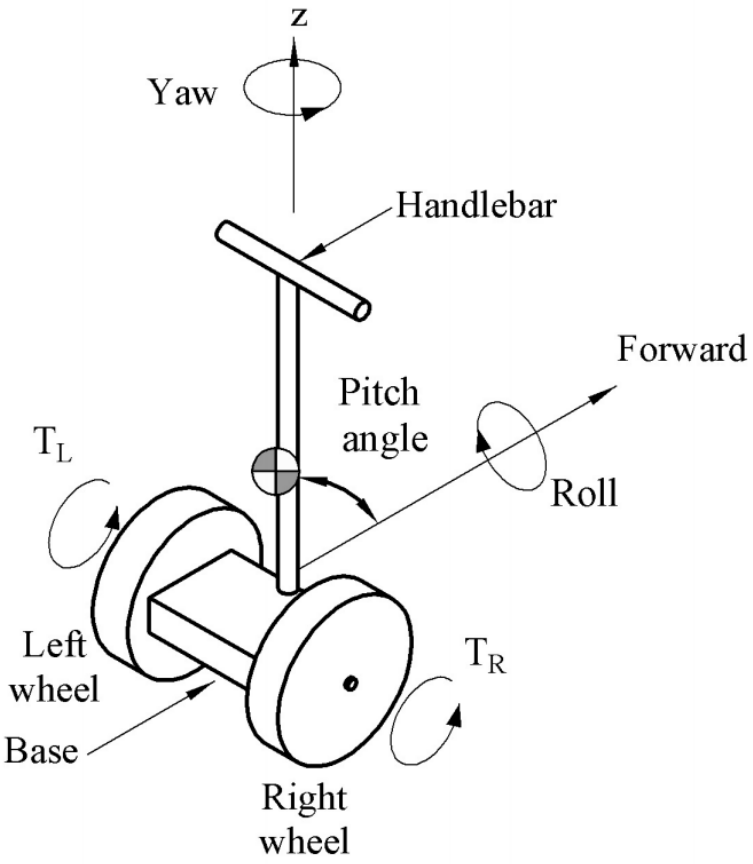

Figure 1: Two-wheeled inverted pendulum

the Segway i2, the handlebar assembly is tilted towards the direction of the turn, as illustrated in Figure 3 . In order to tilt the handlebar comfortably, the operator must lean in the direction of the turn. This affects the dynamics of the transporter-person system in the roll direction.

Because such systems have to change their wheel speeds to avoid falling over, or risk racing off in an unstable manner, there must be large and consistent traction forces between the wheels and the ground. Limited ground traction can prevent the device from balancing itself and the rider.

Unequal traction can be caused by one of the wheels slipping or getting stuck in the ground or lodged against an obstacle. Such scenarios can cause unintended rotational motions that cause the vehicle and/or rider to tip over. A significant contribution of

Figure 2: Segway i167

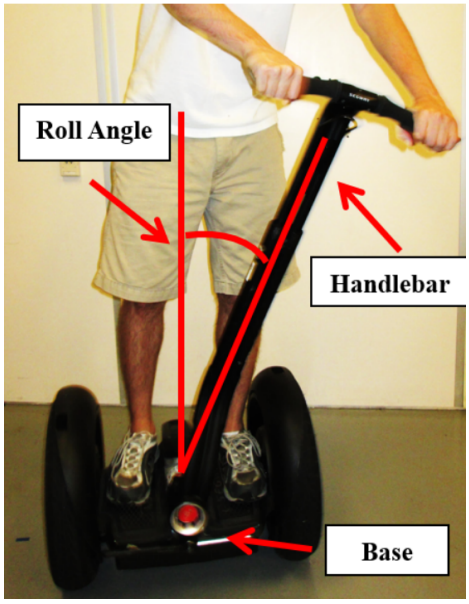

Figure 3: Segway i2

this thesis is an analysis showing how such loss of traction in one wheel can lead to tipping over.

Roll instability can happen for a variety of reasons. For example, it can result

from an aggressive turning maneuver commanded by the operator. Another scenario where such can event take place is when one wheel encounters an obstacle that induces a large roll-inducing disturbance force. Similarly, roll instability can occur as a result of traveling through uneven ground or as a result of an unexpected turning motion induced by one wheel slipping on the ground.

Another version of a two-wheeled inverted pendulum transporter, the Segway MiniPro uses a smaller handlebar-like assembly that is meant to be operated with the knees. This device is shown in Figure 4.

Figure 4: Segway MiniPro

More recently, a new class of commercially-available devices called hoverboards have been released to the marketplace. These machines do not have any type of handlebar and the platform in which the user stands is deformable. The left and right sides of the platform can rotate relative to one another. This rotation is used to drive the wheel motors. Figure 5 shows a schematic of this device from a patent [12].

Self balancing transporters must use a feedback controller to balance. Two of the main developers of the Segway, Morrell and Fields, described the control system of a Segway as a PD controller. [41]

The control system on the Segway commercial product is certainly more complex

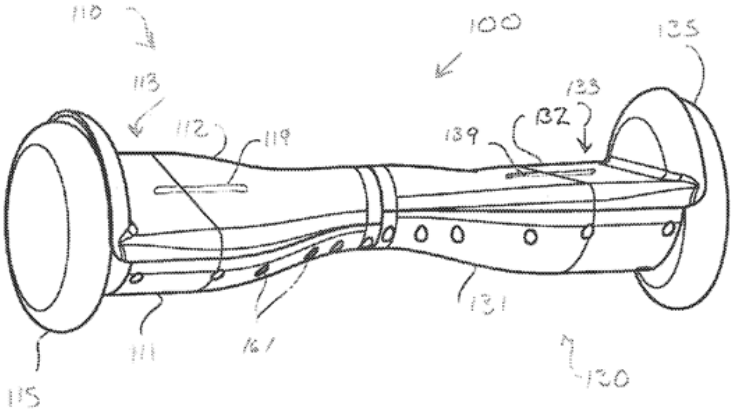

Figure 5: Hoverboard schematic from patent US8,738,278

than that disclosed by Morrel and Fields but the PD controller they described gives a sufficient representation of the control characteristics. The feedback control law presented in their paper is:

$$T_l = K_p\left(\theta_p - \theta_{des}\right) + K_d\dot{\theta}_p - T_\beta \tag{1}$$

$$T_r = K_p\left(\theta_p - \theta_{des}\right) + K_d\dot{\theta}_p + T_\beta \tag{2}$$

$$T_\beta = K_{ff}\dot{\beta}_{des} + K_{\beta p}\left(\dot{\beta} - \dot{\beta}_{des}\right) + K_{\beta i}\int_0^t \left(\dot{\beta} - \dot{\beta}_{des}\right) dt \tag{3}$$

where K_p is the proportional gain, and K_d is the derivative gain of the pitch controller. The feedforward, proportional, and integral gains of the turning controller are: K_{ff}, $K_{\beta p}$, and $K_{\beta i}$. The turning command is represented by T_β. The desired and measured pitch angles are: θ_{des} and θ_p. The desired and measured yaw rates are: $\dot{\beta}_{des}$ and $\dot{\beta}$.

Some commercial self balancing transporters also incorporate traction control [42]. Segway personal transporters, for example, measure the wheel acceleration. If it surpasses a specified maximum value, then this is interpreted as wheel slip. In such cases, the torque applied from the motors to the wheels is reduced, or set to zero. This allows the wheel to free wheel and, hopefully, regain traction. The controller

computes an inverse inertia by dividing the acceleration by the applied torque. When the inverse inertia is greater than a preset minimum value, the torque is gradually increased again in an attempt to regain pitch balance.

Simple analyses can predict the conditions under which these types of vehicles can become unstable. In order to maintain proper balance, there must be sufficient traction forces between the wheels and the ground. The traction force required for pitch stability can be affected by the posture of the vehicle and the inclination of the ground.

When the required traction force is greater than what the surface can provide, wheel slipping will occur. Two obvious ways in which the available traction can be reduced is by reducing the normal force or by reducing the coefficient of friction. The reduction in the normal force when turning can also cause one wheel to slip.

Figure 6 shows the required friction coefficient to keep a simple pendulum body in static equilibrium while the vehicle is at rest or when the wheel is rotating at constant speed. Note that as the body leans forward, the required traction between the wheel and ground increases. If not enough traction is available, then the wheel slips and accelerates. If the wheel cannot spin any faster and the torque is not enough to keep the body upright, then it will fall forward. The results come from a foundational model that will be described in Chapter 2.

The research in this dissertation develops and studies dynamic models that capture the fundamental behavior of self-balancing transporters. In particular, attention is placed on the tire-ground dynamics and body movements to understand the conditions that can generate instabilities during common maneuvers. These models are used to analyze the effectiveness of existing and new control methods designed to counteract these effects.

Previous work on wheeled inverted pendulum transporters has been primarily

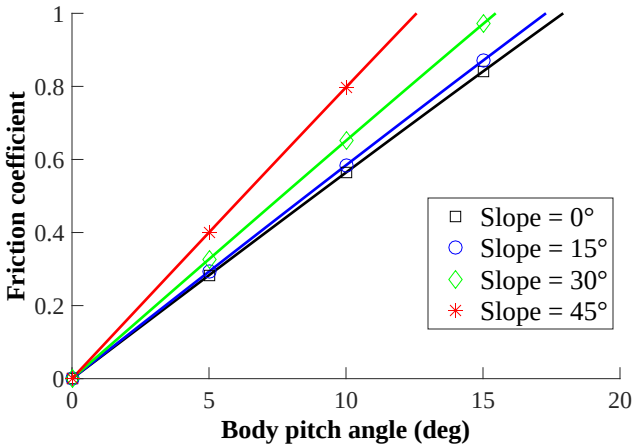

Figure 6: Requiered traction coefficient to maintain body balance

directed toward pitch stabilizing methods [5, 17, 18, 36, 38, 45, 53, 57, 64]. For example, Pathak *et al.* developed a method of nonlinear model predictive control that is suitable for controlling two-wheeled inverted pendulums [45]. Adding to the complexity of controller design, the physical parameters of riders are time-varying. For example, riders may shift their posture or center of mass at any moment. Sinha and Joseph developed a control technique for dynamic systems with periodically varying parameters, and demonstrated the technique on a triple inverted pendulum [53]. Kim *et al.* [34] developed a controller to offset centrifugal rolling forces during turning motions. More complex techniques have been explored to address the robustness problem [3, 46].

A few studies have explored the stabilization and performance of self-balancing transporters in non-ideal conditions. Kausar et al. designed a controller to improve the stability of a two-wheeled inverted pendulum traveling on an uneven surface [30, 31]. A bump on the road was simulated as a continuous height function. This study assumed no slipping and no contact loss between the wheel and the ground. Using the integrated squared error of the pitch angle as a performance measure a gain scheduling technique was shown to be more effective in stabilizing the pitch angle.

In Harber *et al.* [19] experiments were performed on a Segway i2 transporter to

analyze the response of the device riding over bumps of various sizes. It was found that the transporter can bounce vertically, pitch forward, or turn unexpectedly. Zheng *et al.* developed a sliding mode controller that can stabilize a simulation of a self balancing robot on uneven terrains [65].

The problem of lateral or roll stability has been overlooked by most of the research done of these types of transporters. Kim et. al. developed a self-stabilizing transporter with an on-board mechanism that moves the center of gravity laterally in order to compensate for the centrifugal force that is generated when doing a turn [34]. In another study, Todoru *et. al.* analyzed the influence of system parameters in the roll stability of two wheeled inverted pendulums and found the maximum road inclination for different speeds and the maximum allowable speed for a given surface lateral traction coefficient [59].

The effect that wheel slip has on the dynamics of self-balancing transporters has been studied by few researchers. Jones *et al.* added a reaction wheel to improve the pitch stability of the vehicle when traveling on lower friction surfaces [23]. Their controller did not work on high friction surfaces because of unmodeled tire dynamics that were not taking into account when designing the controller. The same group attempted to limit wheel slip by means of this reaction wheel controller and found that doing so also degrades the pitch stability [11].

Sorensen *et al.* studied the traction dynamics to understand the system behavior during wheel slip [54]. They implemented a Coulomb friction model and relaxed the no slip condition of the wheel. They found the maximum angular acceleration of the wheel without slipping as $\alpha_s \geq \frac{\mu g}{r}$ and the minimum torque at the onset of slip is $\mu(\frac{Jg}{r} + rM_t g)$. They also found the angular acceleration after the onset of slip and simulated several responses to leaning effort for different coloumb friction models.

Kim and Sorensen also compared the brush tire and Coulomb friction models effectiveness in simulating the slip onset and general wheeled inverted pendulum

motion [33]. During a single wheel simulation, the onset of slip occurs later in coloumb model than in the brush tire model. If the static coefficient of the Coloumb model is set equal to the peak coefficient of the brush model, both models show similar behavior.

In this research, descriptions of wheel-ground interaction are included in the dynamic models of two-wheeled self-balancing transporters. Simple dynamic descriptions of the human rider are also included. Experiments have been performed to obtain realistic parameters to describe these motions. Further details have been added to the dynamics of the tires and the ground to account for irregular surfaces, and collisions between a wheel and an object. Finally, existing and new traction and balancing control methods are tested for their efficacy in making this class of vehicles more robust to non-ideal situations.

1.1 Contributions

1.1.1 Dynamic models of self-balancing transporters

This thesis presents the dynamic equations of motion for two types of self-balancing transporters. The first type is called a two-wheeled inverted pendulum of which the most popular product is the Segway. The second type is popularly known as a hoverboard. The model of a Segway is then used to study the effect of adverse conditions during operation. Experiments were performed to capture the dynamic behavior of the hoverboard. Using the data gathered from these experiments, the model parameters were calibrated to approximate the model response to that of a commercial hoverboard. Experiments were also done to measure the human motion associated with operating these vehicles. Specifically, the lean angle of the person during turning motions was measured for both the Segway and the hoverboard.

1.1.2 Evaluation of stability during dangerous maneuvers or detrimental conditions

The dynamic models are used to study the effects of adverse operating conditions such as wheel slipping, sharp turns, or uneven terrain.

To study the effect of wheel slipping a wheel-ground traction model based on the Magic Formula [44] was introduced into the dynamic equations of motion. Then, the conditions where one or two wheels encountered a low-friction surface were simulated. The effects of the length of the low-friction surface patch, the leaning angle of the operator, and the maximum coefficient of friction were studied. In addition, the effect of changes in different parameters of the wheel-ground traction model were also analyzed with simulations.

The lateral stability of the vehicle was also tested via simulations. Turns at different speeds and turning radius were simulated and the dynamic behavior of the vehicle was examined to characterize the danger of these situations. Particularly, a very sharp turn can make a vehicle tip-over within fractions of a second and this was confirmed by simulation results. In addition, the effect of the human motions on the wheel-ground forces was studied by examining these forces in terms of the human inertial and kinematical variables.

The effect of irregular ground surfaces was thoroughly studied. The effect of inclined ground on the wheel-ground traction was studied using basic dynamic analysis. From this analysis the physical limitations of a vehicle to climb a slope were determined. A generalized description of an irregular surface was introduced in term of the radius of curvature of the ground. Two types of surfaces where defined: bumps and holes. Any other surface can be described as a combination of these two. Analytical expressions were found for the speed limits at which a vehicle can travel over these surfaces. Finally, the self-balancing transporter was simulated going over constant and variable slope surfaces at different initial speeds, pitch angles, and slope angles

to examine the effect on the ability of the transporter to balance.

1.1.3 Safe operating ranges and control methods to extend operability

Three traction control methods are presented. One traction control method is based on limiting the angular acceleration of the wheels. An excessive wheel angular acceleration might indicate that the wheel-ground traction is significantly reduced and the wheel speeds up increase rapidly as there is little resistance to the torque input from the motors. The angular acceleration limit can be set as a constant value or it can be continuously adjusted to match the expected angular acceleration of the wheel according to the measured yaw rate and acceleration of the vehicle. Another traction control method is based on comparing the measured yaw rate of the vehicle or the yaw rate input from the vehicle handlebar with the difference in the angular speed of both wheels. Taking into account the direction in which the torques are being applied to the wheels, it can be determined which wheel is slipping and in which direction.

The contributions provided in this thesis advance the state of knowledge ragarding inverted pendulum transporters. A rich description of their dangerous properties is provided. Finally, some of the dangers of wheel slip have been mitigated via new traction-control methods.

1.2 Thesis outline

Chapter 2 presents the dynamic equations of motion of a self-balancing two-wheeled inverted pendulum and of a hoverboard. Vehicle parameters that approximate the response of the model to that of a commercial hoverboard are presented. Experiments showing the human motions during turning maneuvers for both Segways and hoverboards are introduced.

Chapter 3 presents an extended dynamic model of a two-wheeled inverted pendulum transporter that includes a wheel-ground traction representation. Simulations

showing the effects of having one or two wheels slipping on the ground during acceleration or braking maneuvers are shown. The effects of the ground-friction coefficient, the leaning angle of the operator, and the length of the low-friction patch are studied. The effects of the variation of the parameters of the wheel-ground traction model are shown.

Chapter 4 examines the roll stability of such vehicles. First, the equations that represent the normal forces between the wheels and the ground are introduced. From the equations, operational limits for a two-wheeled vehicle are found. Then, the equations are extended to include the effects of the operator leaning in different directions. Dynamic simulations are used to determine how sharp turning motions can affect the pitch stability of the vehicle and how quickly a tip-over condition can occur.

Chapter 5 examines the effects of non-flat surfaces on vehicle stability. The effect of a constant slope on the wheel-ground traction is studied to determine the operational limits of the vehicle. Then, a generalized description of an uneven surface is introduced to study the effects of traveling over a non-constant slope. Finally, dynamic simulations are used to study the effects on vehicle stability different surface characteristics and operational parameters.

Chapter 6 introduces three control methods to limit the wheel slip. A first control method based on a wheel acceleration constant limit is studied and simulated to evaluate its effectiveness. A second method, based on the first one, is developed by making this acceleration limit adjustable. Finally, a third method based on the yaw rate comparison between the one measured by a gyroscope and the one calculated based on wheel angular speeds is introduced.

Lastly, Chapter 7 summarizes the contributions of this thesis and provides suggestions for future work.

CHAPTER II

FOUNDATIONAL DYNAMIC MODELS

This section describes foundational models of the two most popular self-balancing transporters: Segways and Hoverboards. The models capture the most important parameters of each device. Note that the models are intended for use in investigating unexpected and possibly dangerous machine motions. Therefore, the riders are modeled as passive inertias. The models are structured such that straightforward physical testing can be used to appropriately select the modeling parameter values.

2.1 Two-wheeled inverted pendulum transporter

Figure 7 shows a schematic diagram of a two-wheeled Segway-type inverted-pendulum human transporter constrained to travel on flat ground. The lumped combination of the base, handlebar, and person forms the inverted pendulum. The rider is modeled as rigidly standing on the base with no permissible motion relative to the base and handlebars. Novice operators or operators experiencing a rapid or unexpected turn may not lean into the turn, so the effect of the person leaning during turns should not be modeled for such cases..

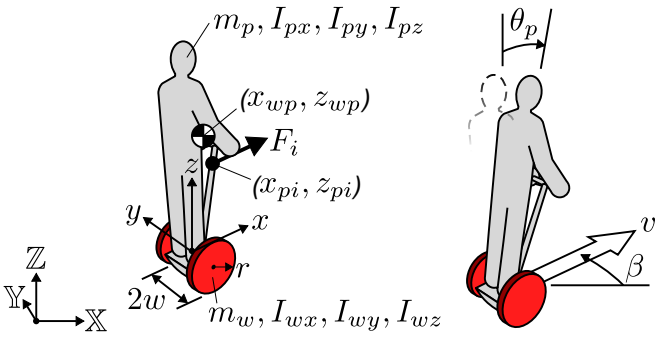

Figure 7: Schematic representation of a two-wheeled Segway-type inverted pendulum transporter.

Attached to the base of the pendulum are two motors that drive each of the wheels by supplying torques T_r and T_l to the right and left wheels, respectively. It is assumed that the wheels roll with perfect ground traction. The wheel radii are r and distance between them is $2w$. The origin of the body-fixed reference frame is set at the midpoint between the two wheels. The mass center of the inverted pendulum is located at x_{wp} and z_{wp}. In order to utilize experimental tests, an excitation force F_i is applied to the handlebar in the x-direction at the location of x_{pi} and z_{pi}.

The pendulum mass is m_p, its rotational inertias are I_{px}, I_{py}, and I_{pz}, and it is symmetrical about the x-z plane. The wheels are treated as uniform disks with mass m_w, rotational inertias I_{wx}, I_{wy}, and I_{wz}; furthermore, I_{wx} and I_{wz} are equal. The pendulum pitch angle is given by θ_p. The transporter's yaw angle around the $\mathbb{Z}$-axis is given by β. The vehicle speed is indicated by v. The equations of motion for the pitch (θ), yaw (β), and vehicle forward speed (v), were obtained using a commercial multi-body dynamics software package [28]. These equations are:

$$\begin{bmatrix} I_{py} + m_p(x_{wp}^2 + z_{wp}^2) & 0 & m_p(z_{wp}\cos\theta_p - x_{wp}\sin\theta_p) \\ m_p(z_{wp}\cos\theta_p - x_{wp}\sin\theta_p) & 0 & (m_p + 2m_w + 2I_y/r^2) \\ 0 & \begin{matrix} I_{pz} + 2I_{xz} + 2m_w w^2 \\ +2I_y w^2/r^2 + (I_{px} - I_{pz})\sin^2\theta_p \\ +m_p(x_{wp}\cos\theta_p + z_{wp}\sin\theta_p)^2 \end{matrix} & 0 \end{bmatrix} \begin{bmatrix} \ddot{\theta}_p \\ \ddot{\beta} \\ \dot{v} \end{bmatrix}$$

$$= \begin{bmatrix} [(I_{pz} - I_{px}) \sin\theta_p \cos\theta_p \\ +m_p(x_{wp} \cos\theta_p + z_{wp} \sin\theta_p) \\ (x_{wp} \sin\theta_p - z_{wp} \cos\theta_p)]\dot{\beta}^2 \\ \\ m_p(x_{wp} \cos\theta_p + z_{wp} \sin\theta_p)(\dot{\beta}^2 - \dot{\theta}_p^2) \\ \\ [2(I_{px} - I_{pz}) \sin\theta_p \cos\theta_p \\ -m_p(x_{wp} \cos\theta_p + z_{wp} \sin\theta_p) \\ (2x_{wp} \sin\theta_p - 2z_{wp} \cos\theta_p)]\dot{\beta}\dot{\theta}_p \\ +m_p(x_{wp} \cos\theta_p + z_{wp} \sin\theta_p)\dot{\beta}v \end{bmatrix} + \begin{bmatrix} T_l + T_r + F_i(x_{pi} \sin\theta_p - z_{pi} \cos\theta_p) \\ -m_p g(x_{wp} \cos\theta_p \\ +z_{wp} \sin\theta_p) \\ \\ -F_i - (T_l + T_r)/r \\ \\ y_{pi}F_i + w(T_l - T_r)/r \end{bmatrix} \tag{4}$$

While small angle approximations of these equations may save computing effort, extreme failure conditions involve angles beyond the linear regime for which the use of this full nonlinear model is necessary. Note that experimental testing has been conducted in order to select appropriate parameter values [8]. These are shown in Table 1.

2.2 Hoverboard Vehicle model

Figure 8 shows a diagram of a hoverboard and rider. The model consists of two base platforms. A person operates the vehicle while standing with one foot on each of the platforms. Attached to each base are motors that are used to drive each of the wheels. It is assumed that the wheels roll without slipping. The distance between the wheels is $2b$, while their radii are r. All of the following points discussed are referenced to the midpoint between the centers of the two wheels. The center of mass of the person is located by the coordinates x_p and z_p. The center of mass of each of the platforms is at x_{bi}, y_{bi}, and z_{bi}, where $i = l, r$ for the left and right side, respectively. The

Table 1: Segway controller gains and system parameters

Parameter	Value
K_p	373.44 N·m/rad
K_d	7.821 N·m·s/rad
K_{ff}	78.06 N·m·s/rad
$K_{\beta p}$	242.7 N·m·s/rad
$K_{\beta i}$	23.22 N·m/rad
x_{wp}	-0.0182 m
z_{wp}	0.868 m
I_{px}	45.11 kg· m^2
I_{py}	49.68 kg· m^2
I_{pz}	4.39 kg· m^2
I_{wx}	0.06925 kg· m^2
I_{wy}	0.068 kg· m^2
I_{wz}	0.06925 kg· m^2
m_p	122.9 kg
m_w	4.5 kg
w	0.268 m
r	0.2415 m

inverted-pendulum-person has a mass of m_p and inertias of I_{px}, I_{py}, and I_{pz}. The wheels have a mass of m_w and inertias of $I_{wx} = I_{wz}$, and I_{wy}. The pendulum is symmetrical about the xz plane. The pitch angle of the pendulum is indicated by θ_i where $i = p, bl, br$ for the person, the left base, and the right base, respectively. The yaw angle around the z axis is indicated by β. The speed of the vehicle is indicated by v. These coordinates are indicated in Fig. 9. A commercial multi-body dynamics software package [28] was used to obtain the equations of motion.

As a first step, the dynamic equations of the system were obtained while excluding the person. It was assumed that the center of mass of each side of the vehicle is located directly on top of the axis of rotation when the pitch angle, θ_i is zero and at the center of each of the base platforms. This means that $x_{bi} = 0$, $y_{bi} = \pm 0.5b$, and z_{bi} for $i = l, r$. The dynamic equations of motion of the vehicle under these assumptions are:

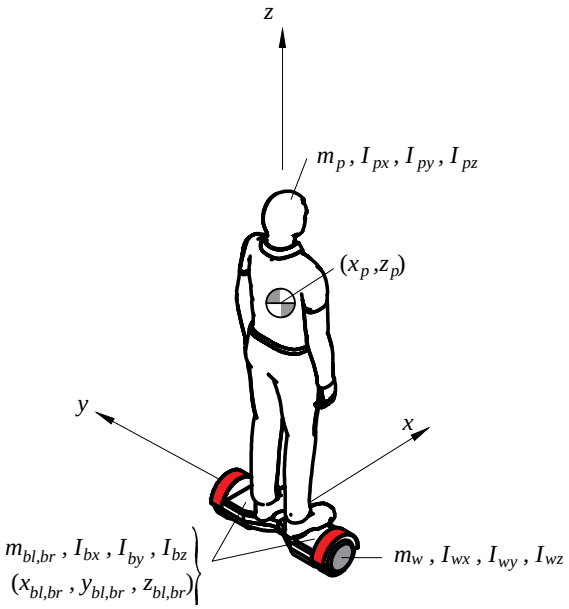

Figure 8: Dynamic Model of a Hoverboard.

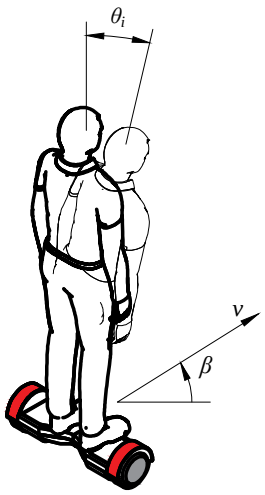

Figure 9: Coordinates of the Dynamic Model of a Hoverboard.

$$T_l + (I_{bz} - I_{bx} - m_b z_b^2)\sin\theta_{bl}\cos\theta_{bl}\dot{\beta}^2 + m_b z_b \cos\theta_{bl}\dot{v} + (I_{by} + m_b z_b^2)\ddot{\theta}_{bl} \\ -m_b z_b g \sin\theta_{bl} - 0.5 m_b b z_b \cos\theta_{bl}\ddot{\beta} = 0 \tag{5}$$

$$T_r + (I_{bz} - I_{bx} - m_b z_b^2)\sin\theta_{br}\cos\theta_{br}\dot{\beta}^2 + m_b z_b \cos\theta_{br}\dot{v} + (I_{by} + m_b z_b^2)\ddot{\theta}_{br} \\ +0.5 m_b b z_b \cos\theta_{br}\ddot{\beta} - m_b z_b g \sin\theta_{br} = 0 \tag{6}$$

$$
\begin{aligned}
m_b z_b \cos\theta_{bl}\ddot{\theta}_{bl} + m_b z_b \cos\theta_{br}\ddot{\theta}_{br} + 2(m_b + m_w + I_{wy}/r^2)\dot{v} - (T_l + T_r)/r \\
-m_b z_b(\sin\theta_{bl}(\dot{\beta}^2 + \dot{\theta}_{bl}^2) + \sin\theta_{br}(\dot{\beta}^2 + \dot{\theta}_{br}^2)) = 0
\end{aligned}
\tag{7}
$$

$$
\begin{aligned}
b(T_l - T_r)/r + 2(I_{bx} - I_{bz})\sin\theta_{bl}\cos\theta_{bl}\dot{\beta}\dot{\theta}_{bl} + 2(I_{bx} - I_{bz})\sin\theta_{br}\cos\theta_{br}\dot{\beta}\dot{\theta}_{br} \\
+0.5 m_b z_b \sin\theta_{bl}(2\dot{\beta}v + b\dot{\theta}_{bl}^2 + 4 z_b \cos\theta_{bl}\dot{\beta}\dot{\theta}_{bl}) \\
+0.5 m_b b z_b \cos\theta_{br}\ddot{\theta}_{br} + 0.5(4I_{bz} + 4I_{wxz} + 4m_w b^2 + 4I_{wy}b^2/r^2 \\
+2(I_{bx} - I_{bz})\sin\theta_{bl}^2 + m_b(b^2 + 2z_b^2\sin\theta_{bl}^2) - 2(I_{bz} - I_{bx} - m_b z_b^2) \\
\sin\theta_{br}^2)\ddot{\beta} - 0.5 m_b z_b \sin\theta_{br}(b\dot{\theta}_{br}^2 - 2\dot{\beta}v - 4 z_b \cos\theta_{br}\dot{\beta}\dot{\theta}_{br}) \\
-0.5 m_b b z_b \cos\theta_{bl}\ddot{\theta}_{bl} = 0
\end{aligned}
\tag{8}
$$

2.3 Two wheeled single axis dual inverted pendulum vehicle with passenger

To obtain the equation of motions of the system when a person is riding a hoverboard device, a passive human rider is assumed. That means, the rider rests on top of the hoverboard but does not exert any active torque on it, only weight forces are applied. It is assumed that the person is a rigid body that is able to rotate around the same axis of rotation of the wheels and the platform. This model allows us to simulate conditions when the person is a slow-responding novice operator or is suprised by an unexpected motion of the machine. These equations are:

$$
\begin{aligned}
T_l + (I_b + m_b x_b^2)\ddot{\theta}_{bl} + 0.5 m_b x_b b \sin(\theta_{bl})\ddot{\beta} - m_b x_b g \cos(\theta_{bl}) \\
-(I_{bx} - I_{bz} - m_b x_b^2)\sin(\theta_{bl})\cos(\theta_{bl})\dot{\beta}^2 - m_b x_b \sin(\theta_{bl})\dot{v} = 0
\end{aligned}
\tag{9}
$$

$$
\begin{aligned}
T_r + (I_b + m_b x_b^2)\ddot{\theta}_{br} - m_b x_b g \cos(\theta_{br}) - (I_{bx} - I_{bz} - m_b x_b^2)\sin(\theta_{br})\cos(\theta_{br})\dot{\beta}^2 \\
-m_b x_b \sin(\theta_{br})\dot{v} - 0.5 m_b x_b b \sin(\theta_{br})\ddot{\beta} = 0
\end{aligned}
\tag{10}
$$

$$
\begin{aligned}
&m_p z_p \cos(\theta_p)\ddot{\theta}_p + (m_p + 2m_b + 2m_w + 2I_{wy}/r^2)\dot{v} - (T_l + T_r)/r \\
&-m_b x_b \cos(\theta_{bl})(\dot{\beta}^2 + \dot{\theta}_{bl}^2) - m_b x_b \cos(\theta_{br})(\dot{\beta}^2 + \dot{\theta}_{br}^2) - m_p z_p \sin(\theta_p)(\dot{\beta}^2 + \dot{\theta}_p^2) \\
&-m_b x_b \sin(\theta_{bl})\ddot{\theta}_{bl} - m_b x_b \sin(\theta_{br})\ddot{\theta}_{br} = 0
\end{aligned} \tag{11}
$$

$$
\begin{aligned}
&m_p z_p \cos(\theta_p)\ddot{\theta}_p + (m_p + 2m_b + 2m_w + 2I_{wy}/r^2)\dot{v} - (T_l + T_r)/r \\
&-m_b x_b \cos(\theta_{bl})(\dot{\beta}^2 + \dot{\theta}_{bl}^2) - m_b x_b \cos(\theta_{br})(\dot{\beta}^2 + \dot{\theta}_{br}^2) - m_p z_p \sin(\theta_p)(\dot{\beta}^2 + \dot{\theta}_p^2) \\
&-m_b x_b \sin(\theta_{bl})\ddot{\theta}_{bl} - m_b x_b \sin(\theta_{br})\ddot{\theta}_{br} = 0
\end{aligned} \tag{12}
$$

$$
\begin{aligned}
&b(T_l - T_r)/r + 2(I_{bx} - I_{bz})\sin(\theta_{bl})\cos(\theta_{bl})\dot{\beta}\dot{\theta}_{bl} \\
&+2(I_{bx} - I_{bz})\sin(\theta_{br})\cos(\theta_{br})\dot{\beta}\dot{\theta}_{br} + 2(I_{px} - I_{pz})\sin(\theta_p)\cos(\theta_p)\dot{\beta}\dot{\theta}_p \\
&+m_p z_p \sin(\theta_p)\dot{\beta}(v + 2z_p\cos(\theta_p)\dot{\theta}_p) + 0.5m_b x_b \cos(\theta_{bl})(b\dot{\theta}_{bl}^2 \\
&+2\dot{\beta}(v - 2x_b\sin(\theta_{bl})\dot{\theta}_{bl})) + 0.5m_b x_b b\sin(\theta_{bl})\ddot{\theta}_{bl} \\
&+0.5(2I_{pz} + 4I_{bz} + 4I_{wx} + 2m_b x_b^2 + 4m_w b^2 + 4I_{wy}b^2/r^2 \\
&+2(I_{bx} - I_{bz})\sin(\theta_{bl})^2 + m_b(b^2 + 2x_b^2\cos(\theta_{bl})^2) \\
&+2(I_{bx} - I_{bz} - m_b x_b^2)\sin(\theta_{br})^2 - 2(I_{pz} - I_{px} - m_p z_p^2)\sin(\theta_p)^2)\ddot{\beta} \\
&-0.5m_b x_b \cos(\theta_{br})(b\dot{\theta}_{br}^2 - 2\dot{\beta}(v \\
&-2x_b\sin(\theta_{br})\dot{\theta}_{br})) - 0.5m_b x_b b\sin(\theta_{br})\ddot{\theta}_{br} = 0
\end{aligned} \tag{13}
$$

$$
\begin{aligned}
&m_p z_p \cos(\theta_p)\dot{v} + (I_{py} + m_p z_p^2)\ddot{\theta}_p - \sin(\theta_p)(m_p g z_p - \\
&(I_{pz} - I_{px} - m_p z_p^2)\cos(\theta_p)\dot{\beta}^2) = 0
\end{aligned} \tag{14}
$$

2.3.1 Experimental testing of hoverboard dynamics

2.3.1.1 Experimental setup

In order to test and inform the preceding models, three types of tests were performed on a commercial hoverboard. A first set of tests consisted of a person operating the

hoverboard. The motion of each side of the hoverboard and the legs of the person were measured during turning and accelerating motions. The second set of tests was conducted without a human rider operating the hoverboard. One subset of these tests consisted of loading the hoverboard with an unbalanced mass and letting it tilt forward while the device is turned off. Another subset of these tests was performed with a heavy structure placed on an active hoverboard in order to mimic the inertial properties of a person. The third type of test consisted of measuring the wheel angular speed response to the tilt angle of the hoverboard base.

During many of these tests, a Vicon MX motion capture system was used to measure the position and orientation of the vehicle in real-time. The motion capture system consists of 12 MX-3+ cameras that record the position of reflective markers attached to the vehicle, the dummy passenger, and the actual person. Each MX-3+ camera can record 659x493 grayscale pixels, and position measurements made using this system have a resolution of approximately 1 mm [10, 60, 61].

To measure the angular wheel speed, the vicon system was not required. Rather, the hoverboard was mounted on a platform to allow the wheels to rotate without resistance from the ground. A level was mounted on one side of the hoverboard. The level was used both to set the hoverboard on a horizontal angle with respect to the ground and to track the hoverboard angle using image processing techniques. A marker of a similar color as the level was mounted on the wheel. The experimental setup is shown in Figure 10. A video was recorded while the hoverbaord platform was rotated to various angles. The video had a resolution of 1080x1920 pixels and the frame rate was 30 fps.

2.3.1.2 Turning Dynamics

At the beginning of a turning experiment conducted in the Vicon lab, the vehicle was driven in a straight line. Then, at the 3 second mark it was commanded to turn

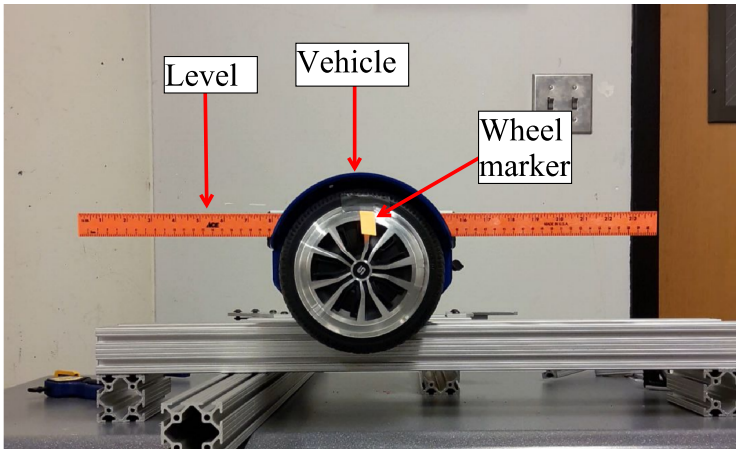

Figure 10: Hoverboard wheel pulse response experimental setup.

right. Figure 11 shows the pitch angles of both sides of the hoverboard and the right leg of the operator. Initially, both the left and right leg were kept at a similar angle, although the left side shows more variation. At the 3 second mark, the left pitch angle was kept approximately constant, while the right leg angle decreased. A reduced pitch angle decreases the speed at which the right side of the hoverboard travels. Note that the right leg angle initially decreases starting at the 3 second mark, but once the turning is initiated, it returns to its initial value at approximately the 4 second mark. This means that the leg is pulled backwards to reduce the pitch angle, but it returns to its initial position when the right side pitch angle is kept approximately constant. This speed variation is shown in Figure 12. This turning motion toward the right is indicated by the negative yaw angle shown in Figure 13 that occurs after the 3 second mark.

2.3.1.3 Acceleration

Figure 14 shows the vehicle initially at rest. At the 1 second mark, the operator accelerates the device forward. It is clear that it requires some effort from the operator to stay still, as evidenced by the pitch angle variation of both sides during this period, as shown in Figure 15. At approximately 1.25 seconds, the vehicle begins to accelerate. At this moment the pitch angle of both sides of the hoverboard began to increase. The

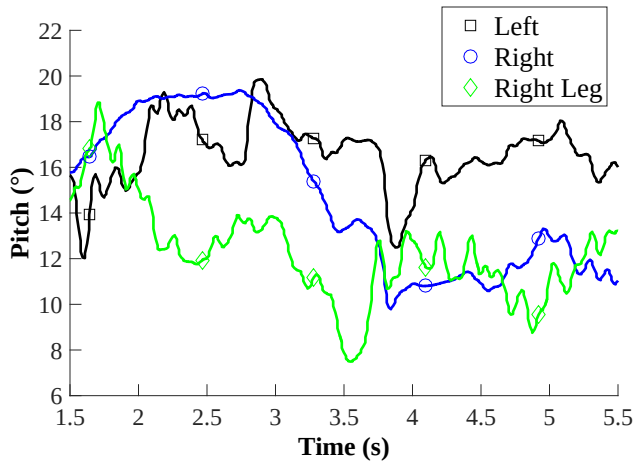

Figure 11: Pitch angles during turning motion

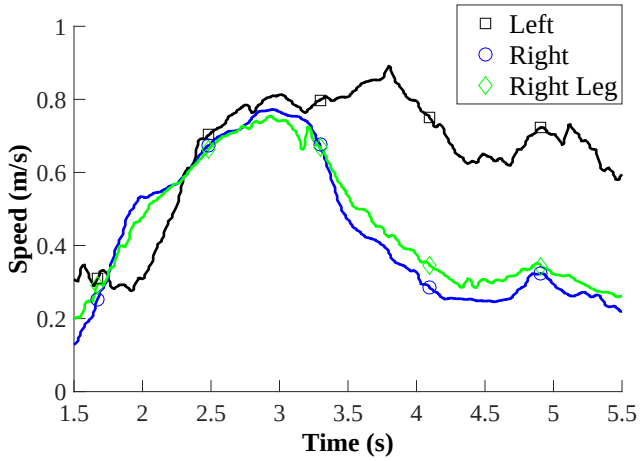

Figure 12: Speed during turning motion

pitch angle of the right leg however, initially increased and then decreases. In order to accelerate the vehicle, the operator used his own momentum to tilt the hoverboard forward. Afterwards he returned his leg to its initial pitch angle, effectively increasing the angle between his leg and the hoverboard. Figure 16 shows the yaw angle that resulted from this action. The orientation of the hoverboard remained approximately constant. However, the operator is unable to accelerate both sides at the same exact speed, so some turning motion was present. The results of these tests are used to set the turning parameters of the dynamic model.

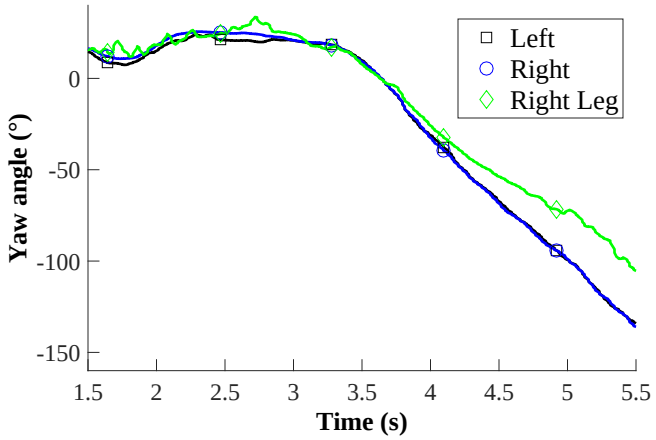

Figure 13: Heading angle during turning motion

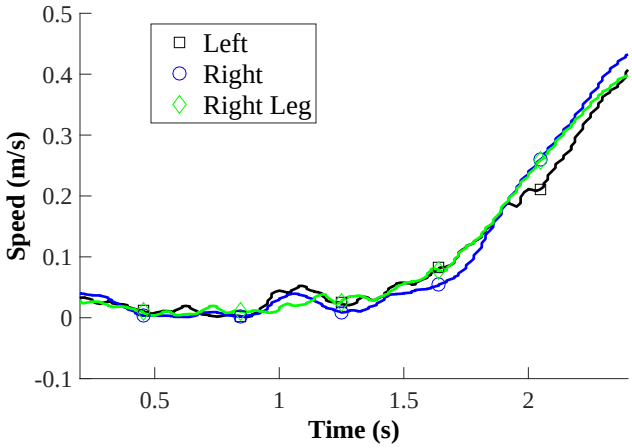

Figure 14: Speed during acceleration

2.3.1.4 Model calibration experiments - System inertias

In the second type of experiments, which are directed at measuring inertias,, an unbalanced mass was placed on top of the right side of the hoverboard, as shown in Figure 17. Figure 18, shows the pitch angle, speed, and yaw angle of both sides of the hoverboard as it falls forward during this test. As the pitch increased to over 40°, the speed of the vehicle only reached 0.2 m/s, as shown in Figure 19. Meanwhile, the yaw angle remained approximately constant for both sides, as shown in Figure 20. It is important to note that even though only one side of the hoverboard was unbalanced,

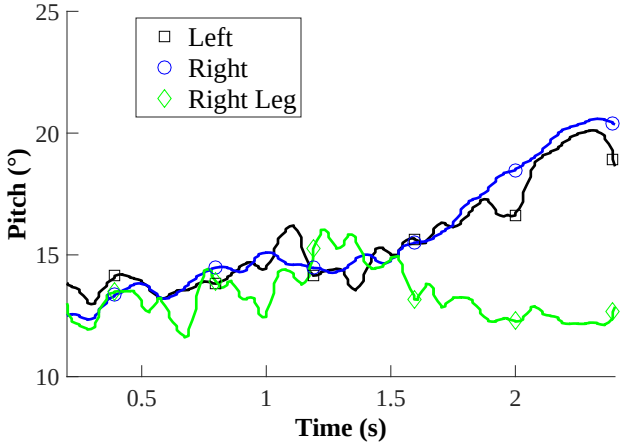

Figure 15: Pitch angles during acceleration

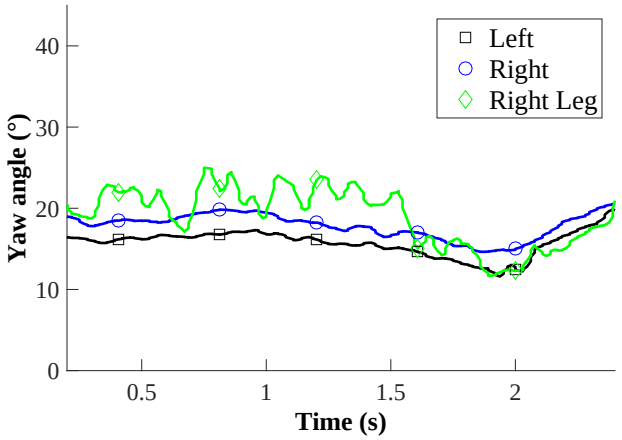

Figure 16: Heading angle during acceleration

the weight was not enough to cause a relative pitch rotation between both sides. This linking between the two sides arises from a torsional spring that connects the two base platforms. The spring is used to return the two sides to parallel after the user stops applying active control forces to the standing platforms. This information is used to calibrate a model on which further studies will be performed.

2.3.1.5 Model calibration experiments - Control system and person

The pitch and speed of the hoverboard were recorded while it balanced a dummy structure. The structure is not perfectly balanced with respect to the axis of the

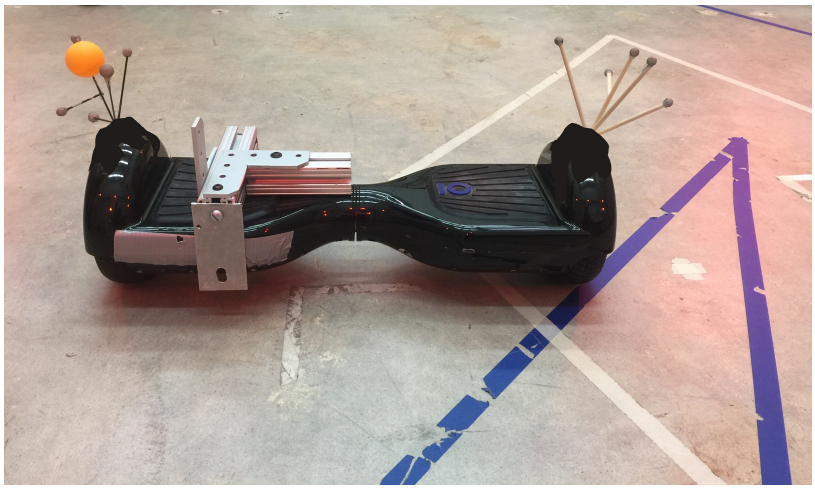

Figure 17: Calibration experiment to obtain system inertias.

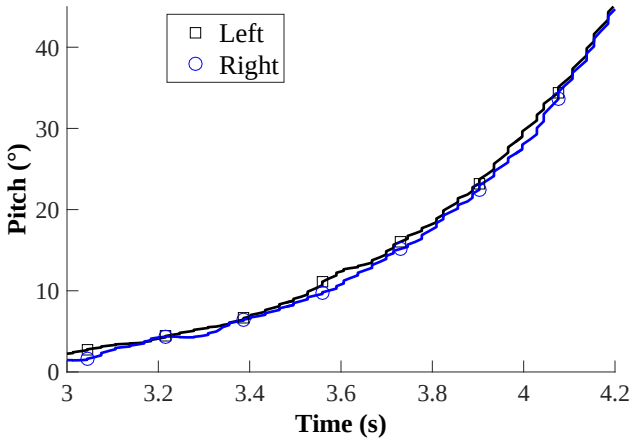

Figure 18: Pitch angles during fall

hoverboard. Therefore, when the hoverboard is released, it starts moving forward in an attempt to balance. This test structure is shown in Figure 21. Figure 22 shows the pitch angle resulting from such a test. Both left and right side angles are kept nearly constant. However, there is some asymmetry between the interval from 8-10 seconds. Part of this discrepancy is due to the resolution of the system being limited to 0.5°. More precise measurements may be required to capture more detailed dynamic behavior of the system. The speed initially increased to a maximum speed of approximately 0.15 m/s before decreasing back to zero, as shown in Figure 23. Because of space limitations the experiment was stopped at the 15 second mark.

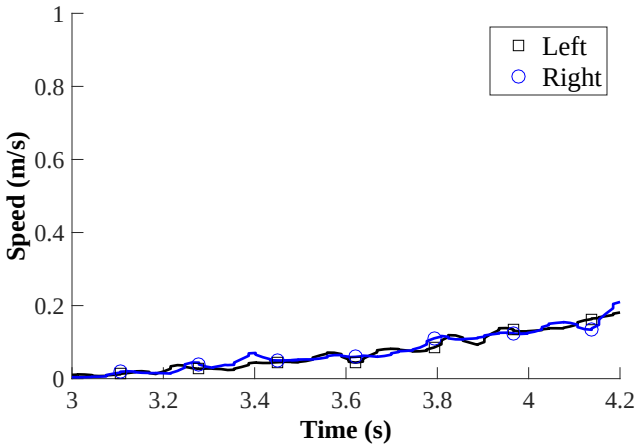

Figure 19: Speed during fall

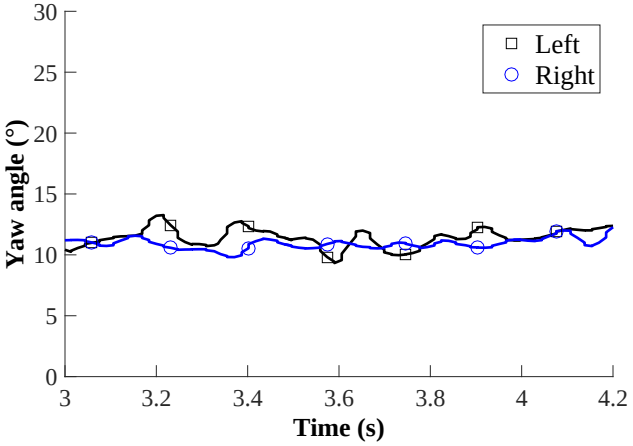

Figure 20: Heading angle during fall

Additionally, the wheel speed response to a change in the tilt angle of the base was measured. The response is shown in Figure 24. Note that the wheel takes approximately 0.5 seconds to reach its maximum speed. These experiments were conducted on one side of the hoverboard, while maintaining the other side horizontal and the corresponding wheel remained at rest.

2.3.2 Calibrated pitch dynamic model

The model parameters were optimized to match the dynamical behavior obtained in the experimental data by using a grey-box model identification routine in MATLAB.

Figure 21: Pitch angles with dummy

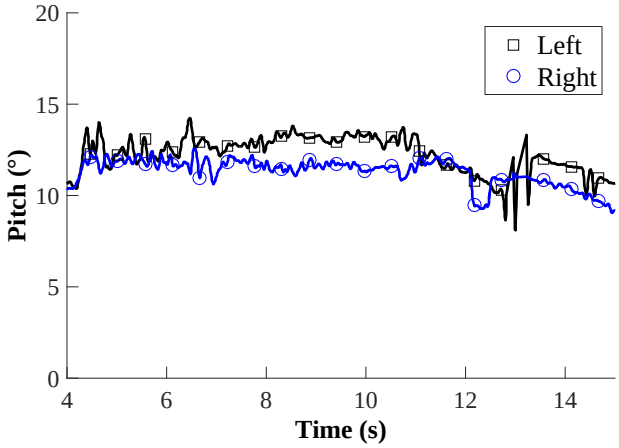

Figure 22: Pitch angles with dummy

In this type of optimization, the structure of the model is known, while the parameter values are optimized. To match the experimental pitch and speed dynamics of the vehicle, the controller gains, and the locations of the centers of mass of the vehicle and the dummy were optimized by the identification routine. The rest of the parameters

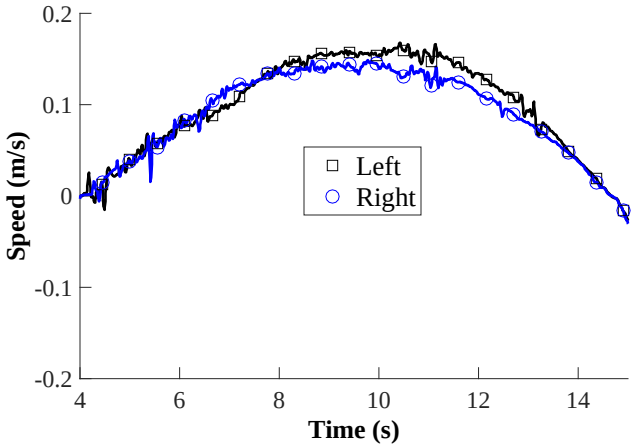

Figure 23: Speed with dummy

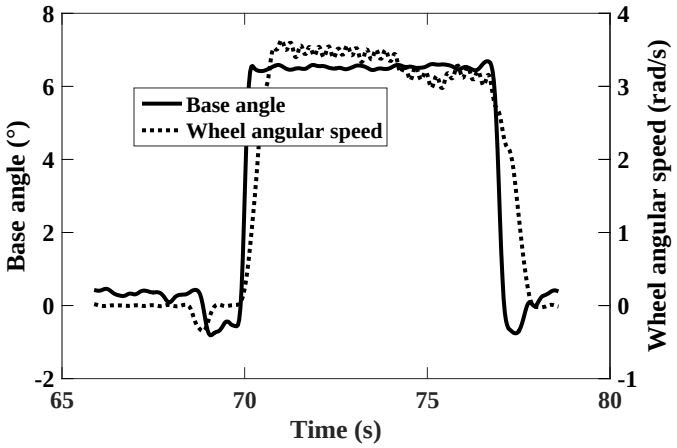

Figure 24: Speed with dummy

were estimated by using CAD models of the dummy and the hoverboard.

Based on other commercial products on the market, it was assumed that the feedback control consists of two PD controllers [41], one on each side of the hoverboard. These controllers measure the pitch angle and pitch rate of each side and output a torque to each of the wheels according to the following equations:

$$T_l = K_p\theta_{bl} + K_d\dot{\theta}_{bl} \tag{15}$$

$$T_r = K_p\theta_{bl} + K_d\dot{\theta}_{br} \tag{16}$$

Table 2: Hoverboard controller gains and system parameters

Parameter	Value
K_p	9.704 N·m/rad
K_d	998 N·m·s/rad
x_b	0.04599 m
z_b	0.0199 m
I_{by}	0.01356 kg· m^2
I_{wy}	0.00323 kg· m^2
m_b	5.88 kg
m_p	16.48 kg
m_w	1.73 kg
z_p	0.584 m
x_p	-0.1384 m
I_{py}	0.88436 kg· m^2
r	0.0775 m

where K_p, is the proportional gain, and K_d is the derivative gain of the balancing controller.

For the calibration process, it was assumed that both sides of the platform and the dummy had the same pitch angle. In addition, it was assumed that the yaw rate of rotation was zero so it traveled in a straight line. The experimental data from the left and right side were averaged in order to produce the same controller values for both sides of the vehicle. This allowed the calibration of the simulated pitch dynamics to follow the behavior captured in the collected data. The final parameter values are shown in Table 2.

2.3.3 Comparison of model and experiments

The initial conditions in the measured data were input to the optimized simulation. The experimental and simulated pitch responses are compared in Figure 25. The pitch angle was maintained approximately constant at 10°. The experimental response shows a small degree of noise that is not produced by the simulation.

Figure 26 shows the experimental and simulated speed of the hoverboard. It can be seen that the simulation follows the experimental response closely, and recreates

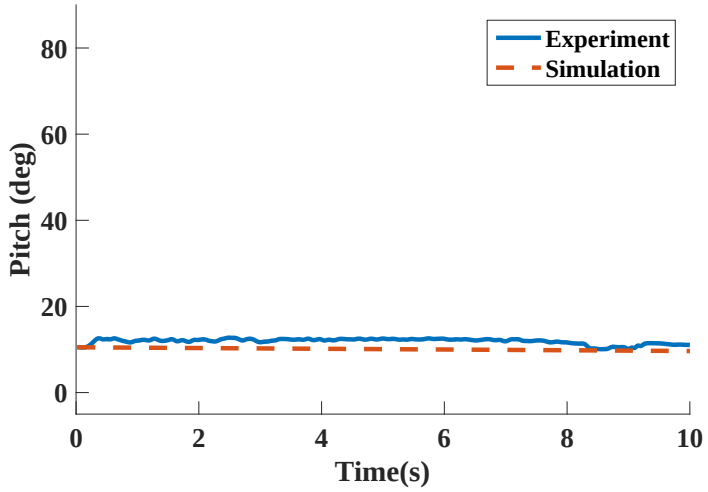

Figure 25: Experiment and simulation pitch responses

a similar response shape. The experimental speed response also shows some small variations that are due to measurement noise, which are not produced by the model.

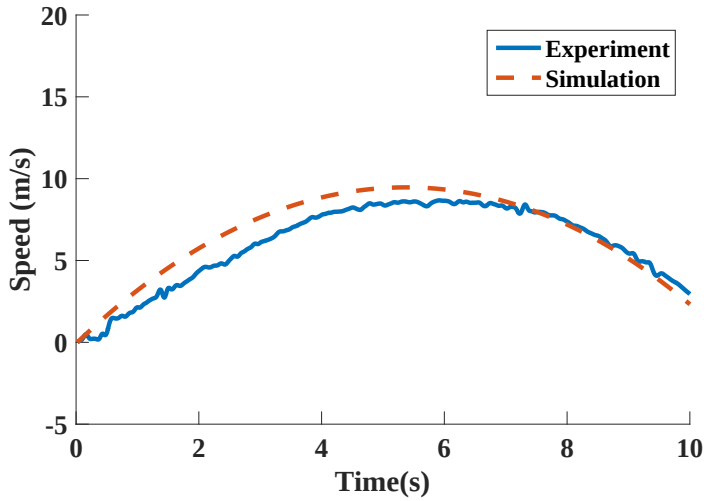

Figure 26: Experiment and simulation speed responses

2.4 Experimental observation of human body motions during the operation of a personal transporter

A Vicon motion capture system was used to measure human-body motion during basic maneuvers while riding a Segway i2 and a Swagway hoverboard. Figure 27(a)

shows a person riding a Segway i2 with optical markers placed on his waist and upper back. Figure 27(b) show additional markers were placed on the Segway chasis and handlebar. Figure 28 shows the markers placed on the hoverboard. Each side of the hoverboard was tracked independently.

(a) Person Markers (b) Segway Markers

Figure 27: Markers placed on a Segway i2 and its passenger

Both the vehicle and the person where tracked during the following maneuvers:

- Turning while leaning into the turn.
- Turning while leaning away from the turn.
- Turning with no leaning.

Figure 28: Markers placed on a Swagway hoverboard

2.4.1 Human motion during Segway turning maneuvers

Figure 29 shows the trajectories followed by the Segway's base, handlebar, and the persons' waist and back during three different turning maneuvers, as well as the person leaning angle for each case. Figure 29(a) corresponds to a case where the person leans away from the center of the curved trajectory, 29(b) is the case when the person does not attempt to lean in either direction, and 29(c) when the person leans into the turn.

When leaning away from the turn, the person's back was outside of the curved path followed by the Segway's base, but his waist was almost directly above it. His leaning angle reached a maximum of almost 3.8°. The negative sign indicates that the lean was away from the center of curvature of the trajectory followed by the vehicle. When the person tried not to lean in any direction, initially he leaned into the turn and then tried to reduce his leaning angle as the turn progressed. In this case, the maximum leaning angle was close to 5°. When leaning into the turn, the person leaned as far as 9°, and then reduced his leaning angle gradually.

Figure 30 shows the yaw rate and the speed of the vehicle as it made the turn.

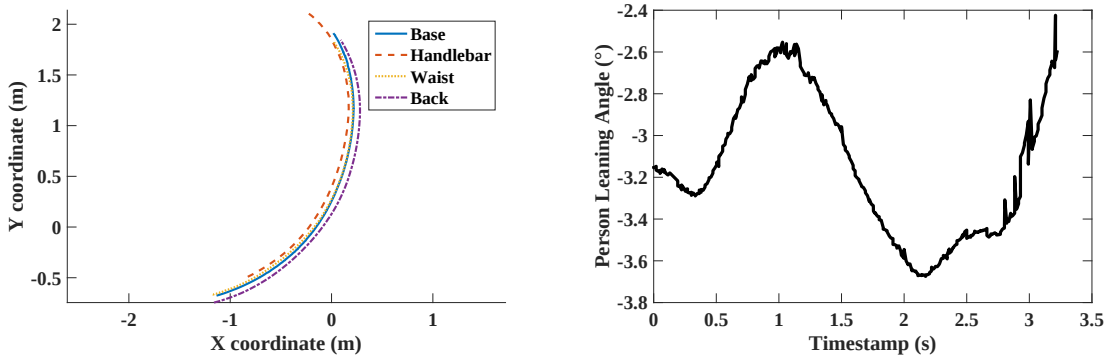

(a) Leaning away from the turn

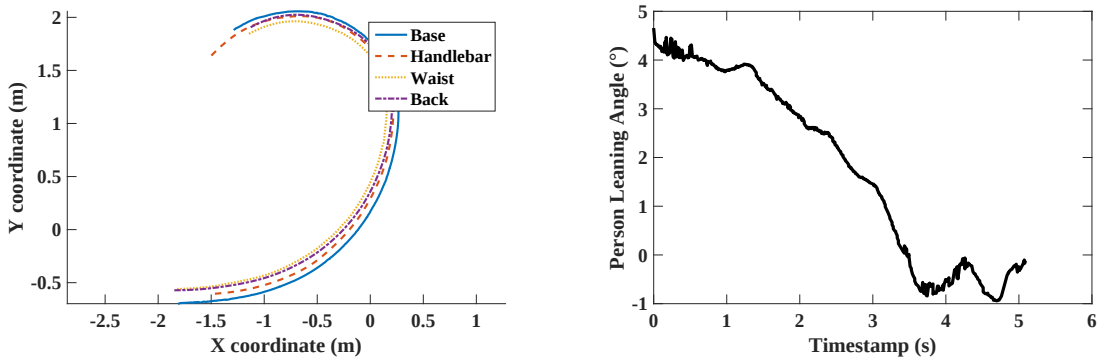

(b) No Leaning

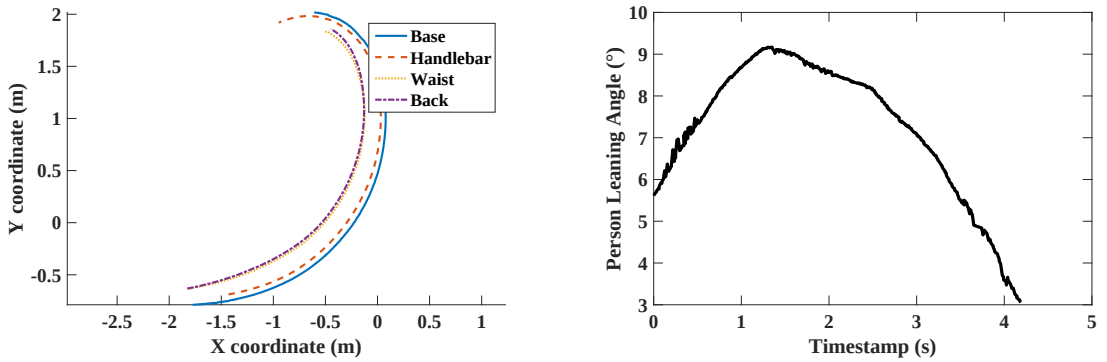

(c) Leaning into the turn

Figure 29: Tracked trajectories and passenger leaning angle during a turning maneuver on a Segway i2

The right column of Figure 30 shows a plot of the leaning angle of the person vs the centripetal acceleration of the vehicle. The speed plots show that in all three cases the vehicle was driven at close to 0.1 m/s, except for the leaning into the turn case where the speed was closer to 0.15 m/s. The yaw rate was kept almost constant for

all three cases at around 0.1 rad/s. However, the maximum yaw rates differed for all three cases. The highest yaw rate occurred when the person leaned into the turn.

The rider leans when turning in order to counteract the effect of the centrifugal force that tries to push him away from the turn. The centripetal acceleration on the right hand side of Figure 30 shows no significant differences in maximum magnitude between all three cases. Because the turns where relatively slow, the person did not feel any tendency to roll over. Therefore, there was no relation between his leaning angle and the centripetal acceleration. If the centripetal acceleration required to stay in the turn had been larger, then the person would necessarily lean more into the turn to avoid falling off.

2.4.2 Human motion during hoverboard turning maneuvers

The left column of Figure 31 shows the trajectories of both sides, of the hoverboard base, the person's waist, and his back. The right column shows the leaning angle of the person. This leaning angle was calculated from the average positions of the vehicle bases and the position of the back of the person. The leaning away case shows negative values. Initially the person leaned away from the turn, but then reduced his leaning angle perhaps sensing he was leaning too far out of the turn. Then, he leaned away further and then reduced his leaning angle by the end of the turn. The behavior was similar to the leaning away case for the Segway shown in Figure 29(a).

When attempting to maintain a neutral position, the person kept his leaning angle between -3° and 2°. When attempting to lean into the turn, he increased his lean angle up to 6° and then reduced it gradually. This behavior was similar to the one found in the Segway leaning into the turn case, except that the maximum leaning angle was lower for the Hoverboard.

Figure 32 shows the yaw rate and speed of the vehicle in the left column, and the leaning angle plotted vs the centripetal acceleration in the right column. No relation

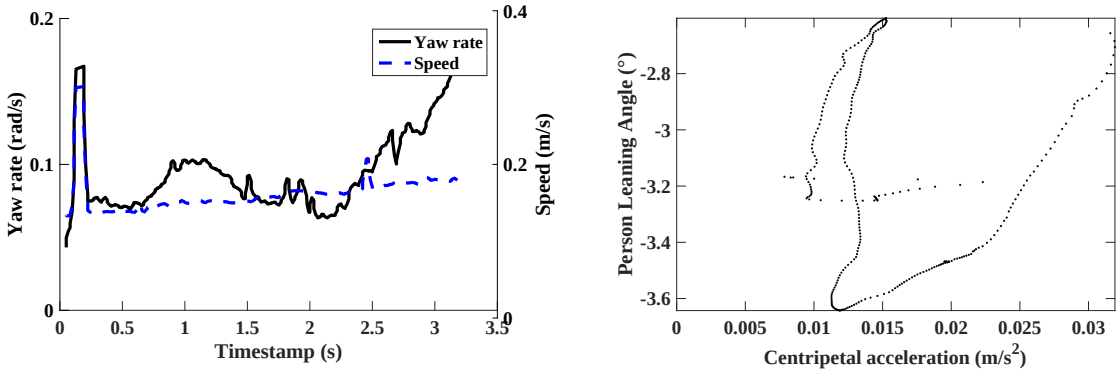

(a) Leaning away from the turn

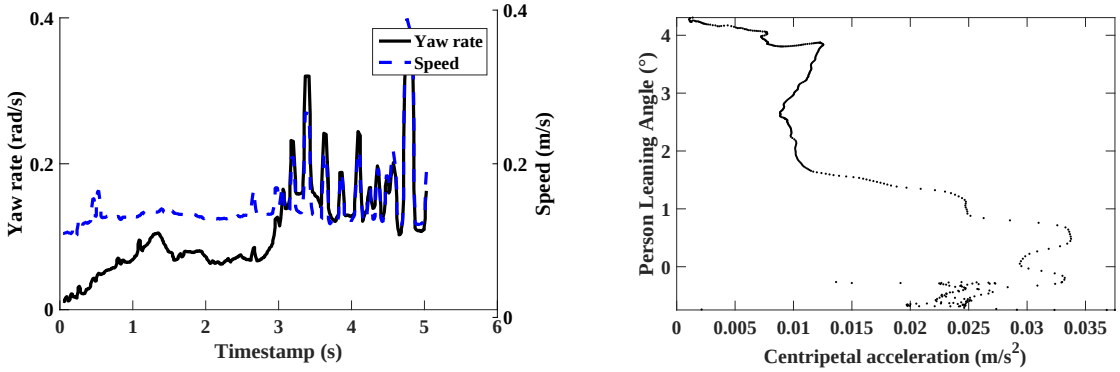

(b) No Leaning

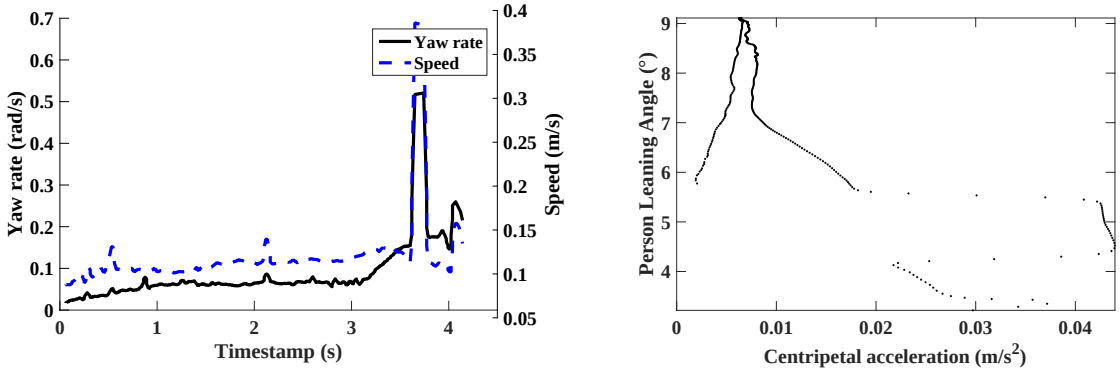

(c) Leaning into the turn

Figure 30: Yaw rate, speed, centripetal acceleration during a turning maneuver on a Segway i2

is apparent between the leaning angle and the centripetal acceleration. The possible explanation for this is the same as for the Segway case: the centripetal acceleration was so low that the person did not need to lean much to avoid rolling over. However,

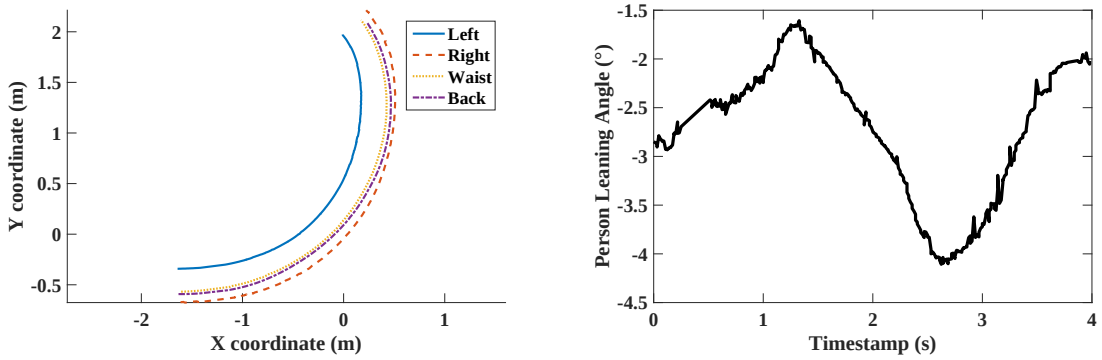

(a) Leaning away from the turn

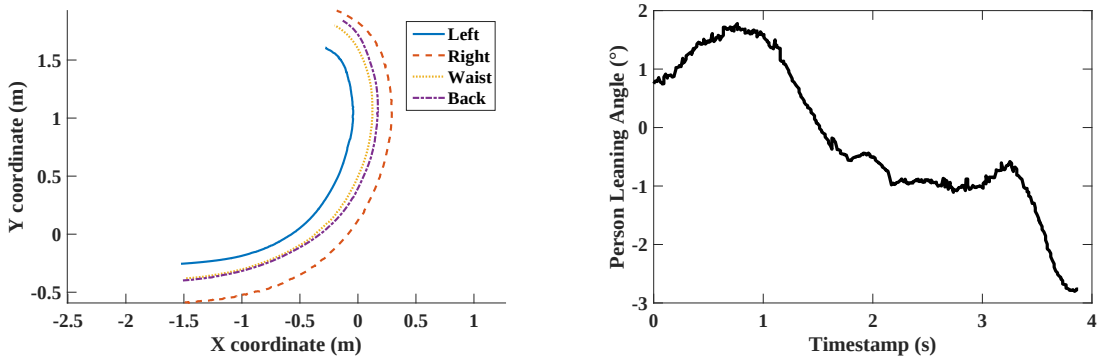

(b) No Leaning

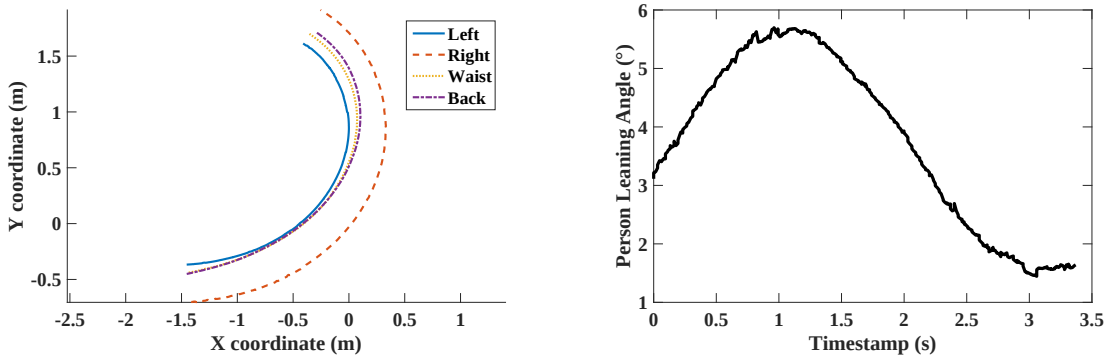

(c) Leaning into the turn

Figure 31: Tracked trajectories and passenger leaning angle during a turning maneuver on a Segway i2

Figure 32(a) shows significantly smaller centripetal acceleration values than the other two cases, meaning that leaning away from the turn did prevent the person from performing a more aggressive maneuver. It is important to take into account that

in order to command a turn, the person must tilt each side of the hoverboard base at different angles, and leaning away from the turn might make it more difficult to command the desired turning command. In the case of the Segway, leaning to the side does not affect the capability of the user to roll the handlebar and command a turn. In fact, leaning into the turn coincides with the required tilting of the handlebars to produce the turn.

2.5 Summary

This chapter presented the foundational dynamic equations of two types of self-balancing transporters: a Segway and a Hoverboard. Realistic parameters for a Segway-type vehicle were previously presented in [8]. For this thesis, parameter tuning experiments were performed on a Hoverboard to understand it's dynamic response characteristics. Turning maneuvers were recorded by using a motion capture system and the data was used to calibrate the model parameters. The calibrated model showed a response that closely approximates the response of the actual vehicle. Finally, operator movements were recorded during turning motions in order to understand how riders compensate for the lateral instability of the vehicle by leaning into the curve.

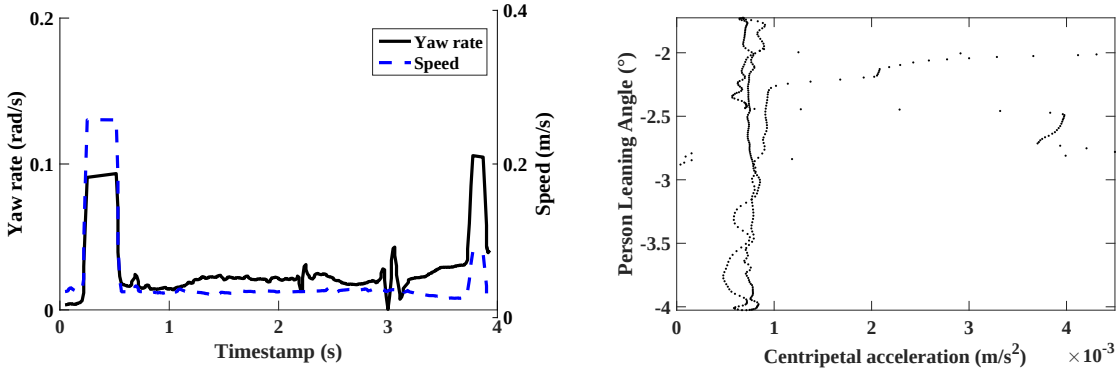

(a) Leaning away from the turn

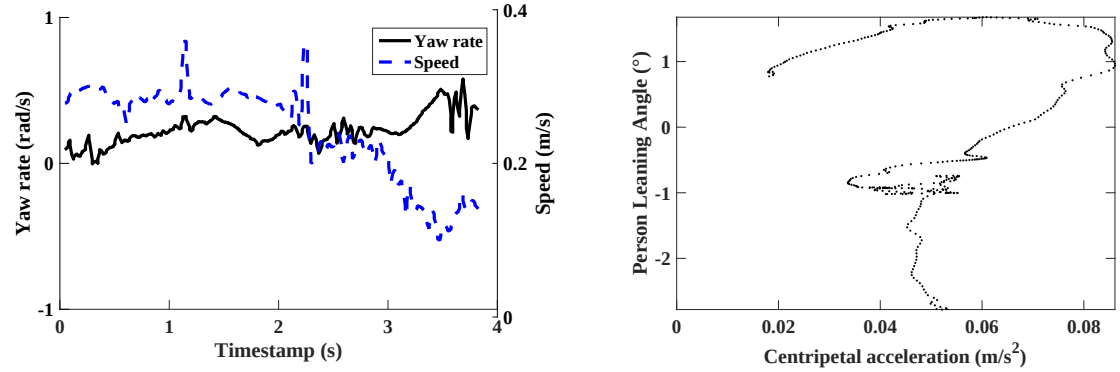

(b) No Leaning

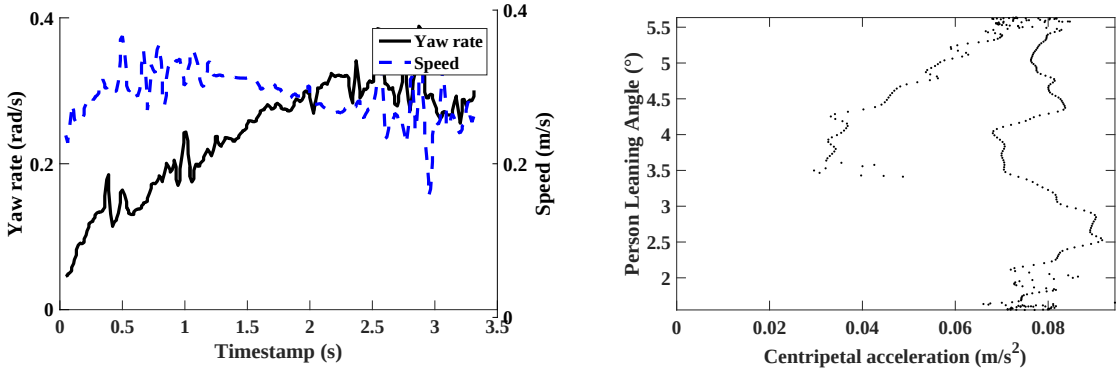

(c) Leaning into the turn

Figure 32: Yaw rate, speed, centripetal acceleration during a turning maneuver on a Segway i2

CHAPTER III

WHEEL SLIPPING

In order to consider scenarios where the wheels of inverted-pendulum transporters can slip, the no-slip constraint on the wheels in the dynamics models from the previous chapter must be relaxed. This means that, in general,

$$\dot{\theta}_w r \neq v_w \dot{\theta}_s \tag{17}$$

where $\dot{\theta}_w$ is the angular speed of the wheel, r is the wheel radius and v_w is the speed of the wheel center, also referred to as the wheel hub.

Additionally, the vehicle can slip laterally at a speed v_y in the y-direction, as shown in Figure 33. In Figure 33 the midpoint between the wheel hubs moves at a speed of v_x and yaws around the z-axis at an angular rate of $\dot{\beta}$. The left and right wheels turn at rates $\dot{\theta}_l$ and $\dot{\theta}_r$, respectively. The speed of of the lowermost point of each wheel with respect to the ground is represented by $v_{s,l}$ and $v_{s,r}$. These are the points at which wheel slip occurs. The traction/braking forces on the left and right wheels are given by $F_{x,l}$ and $F_{x,r}$ while the cornering forces are $F_{y,l}$ and $F_{y,r}$.

The equations of motion for this system are:

$$\begin{aligned}(I_{py} + m_p(x_{wp}^2 + z_{wp}^2))\ddot{\theta}_p - m_p(x_{wp}\sin\theta_p - z_{wp}\cos\theta_p)\dot{v}_x = \\ -[(I_{px} - I_{pz})\sin\theta_p\cos\theta_p + m_p(x_{wp}\sin\theta_p - z_{wp}\cos\theta_p)(x_{wp}\cos\theta_p \\ + z_{wp}\sin\theta_p)]\dot{\beta}^2 + m_p(x_{wp}\sin\theta_p - z_{wp}\cos\theta_p)v_y\dot{\beta} + T_l + T_r \\ -m_p g(x_{wp}\cos\theta_p + z_{wp}\sin\theta_p)\end{aligned} \tag{18}$$

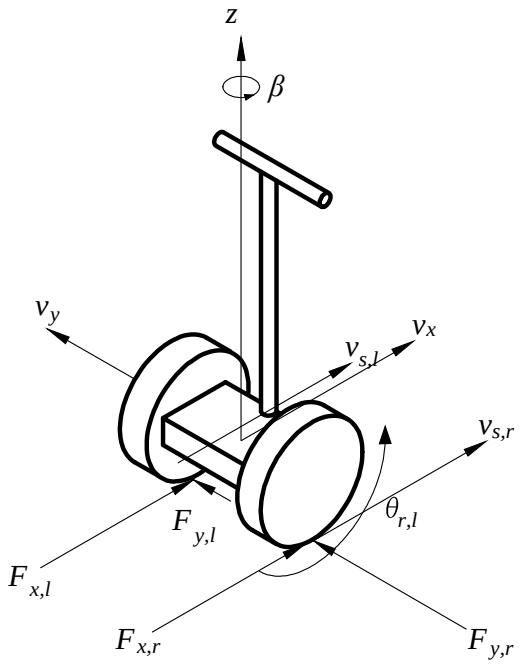

Figure 33: Traction and Cornering Forces and Velocities.

$$\begin{aligned} -m_p(x_{wp}\sin\theta_p - z_{wp}\cos\theta_p)\ddot{\theta}_p + (m_p + 2m_w + 2I_y/r^2)\dot{v}_x \\ +I_y/r^2\dot{v}_{s,l} + I_y/r^2\dot{v}_{s,r} = -(2m_w + m_p)\dot{\beta}v_y - m_p(x_{wp}\cos\theta_p \\ +z_{wp}\sin\theta_p)\dot{\theta}_p^2 - m_p(x_{wp}\cos\theta_p + z_{wp}\sin\theta_p)\dot{\beta}^2 - (T_l + T_r)/r \end{aligned} \tag{19}$$

$$\begin{aligned} +m_p(x_{wp}\cos\theta_p + z_{wp}\sin\theta_p)\ddot{\beta} + (m_p + 2m_w)\dot{v}_y = (-m_p(2x_{wp}\sin\theta_p \\ -2z_{wp}\cos\theta_p))\dot{\theta}_p\dot{\beta} + (2m_w v_x - v_x)\dot{\beta} - F_{y,l} - F_{y,r} \end{aligned} \tag{20}$$

$$-I_y w/r^2\ddot{\beta} - I_y/r^2\dot{v}_x - I_y/r^2\dot{v}_{s,l} = -F_{x,l} - rT_l/r^2 \tag{21}$$

$$-I_y w/r^2\ddot{\beta} - I_y/r^2\dot{v}_x + I_y/r^2\dot{v}_{s,r} = rT_r/r^2 - F_{x,r} \tag{22}$$

$$
\begin{aligned}
&(I_{pz} + 2I_{xz} + 2m_w w^2 + 2I_y w^2/r^2 + (I_{px} - I_{pz})\sin\theta_p^2 \\
&+m_p(x_{wp}\cos\theta_p + z_{wp}\sin\theta_p)^2)\ddot{\beta} + m_p(x_{wp}\cos\theta_p + z_{wp}\sin\theta_p)\dot{v}_y \\
&+wI_y/r^2\dot{v}_{s,l} - wI_y/r^2\dot{v}_{s,r} = 2[(I_{px} - I_{pz})\sin\theta_p\cos\theta_p \\
&-m_p(x_{wp}\cos\theta_p + z_{wp}\sin\theta_p) + (2x_{wp}\sin\theta_p - 2z_{wp}\cos\theta_p)]\dot{\theta}_p\dot{\beta} \\
&+m_p(x_{wp}\cos\theta_p + z_{wp}\sin\theta_p)v_x\dot{\beta} + w(T_l - T_r)/r
\end{aligned} \tag{23}
$$

Traction forces can be represented as functions of the normal forces between the wheels and the ground $F_{z,l}$ and $F_{z,r}$ as follows:

$$
\begin{aligned}
F_{x,i} &= \mu_x(\kappa_i)F_{z,i} \\
F_{y,i} &= \mu_y(\alpha_i)F_{z,i}
\end{aligned} \tag{24}
$$

where $i = r, l$, the longitudinal slip ratio is κ, and the slip angle is α. The longitudinal slip ratio is the ratio between the longitudinal speed of the point of the wheel in contact with the ground and the longitudinal speed of the wheel hub. Here, longitudinal refers to the x-direction. The longitudinal slip is given by:

$$
\begin{aligned}
\kappa_l &= \frac{\dot{\theta}_l r - (v_x - w\dot{\beta})}{v_x - w\dot{\beta}} \\
\kappa_r &= \frac{\dot{\theta}_r r - (v_x + w\dot{\beta})}{v_x + w\dot{\beta}}
\end{aligned} \tag{25}
$$

The slip angle is the angle between the net velocity vector of the wheel hub and its longitudinal speed. It is given by:

$$
\alpha_i = \operatorname{atan}\frac{v_y}{v_{x,i}} \tag{26}
$$

PacejkaLabeled

In this work, surfaces of various friction coefficients were simulated by developing μ_x and μ_y curves inspired by the Magic Formula model [44]. Figure 34 shows a sample curve. The longitudinal and lateral traction coefficients are:

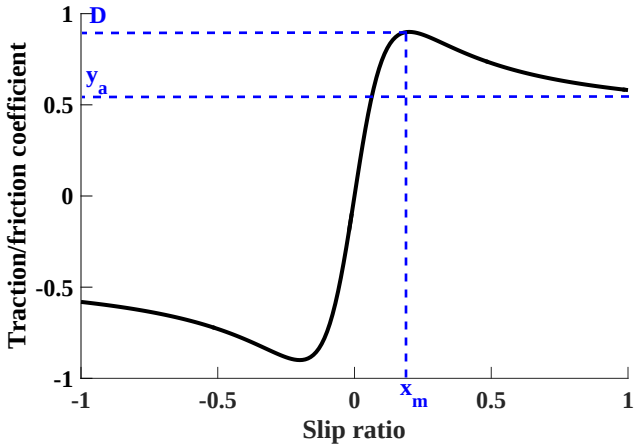

Figure 34: Pacejka tracion model.

$$\mu_x = D_x \sin(C_x \arctan(B_x\kappa - E_x(B_x\kappa - \arctan(B_x\kappa)))) \tag{27}$$

$$\mu_y = D_x \sin(C_y \arctan(B_y\alpha - E_y(B_y\alpha - \arctan(B_y\alpha)))) \tag{28}$$

where B is the slope of the curve at the $\kappa = 0$ or $\alpha = 0$, and D is the maximum traction coefficient. The constans C and E are given by:

$$C = 1 + \left(1 - \frac{2}{\pi}\right) \arcsin\left(\frac{y_a}{D}\right) \tag{29}$$

$$E = \frac{Bx_m - \tan\frac{\pi}{2C}}{Bx_m - \arctan(Bx_m)} \tag{30}$$

where y_a is the coefficient value when $\mu \to \infty$, and x_m is the value of κ for the maximum coefficient.

Figure 35 shows the traction/braking coefficient, as a function of the longitudinal slip, and Figure 36 shows the lateral force as a function of the slip angle.

3.1 One wheel slip

Two-wheeled inverted-pendulum transporters have no redundancy in terms of wheel slip. If one wheel slips, then the system immediately transforms into a very different

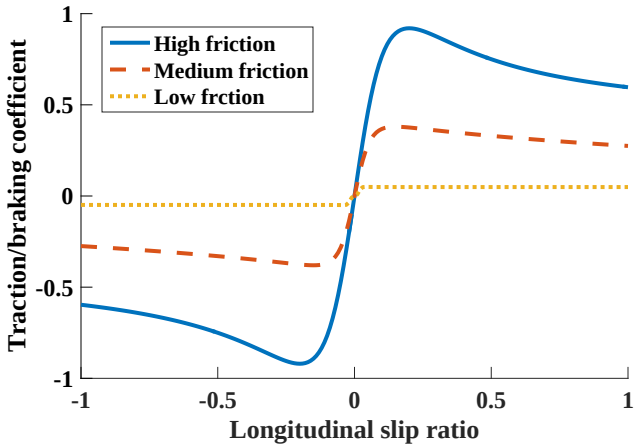

Figure 35: Traction/Braking coefficient

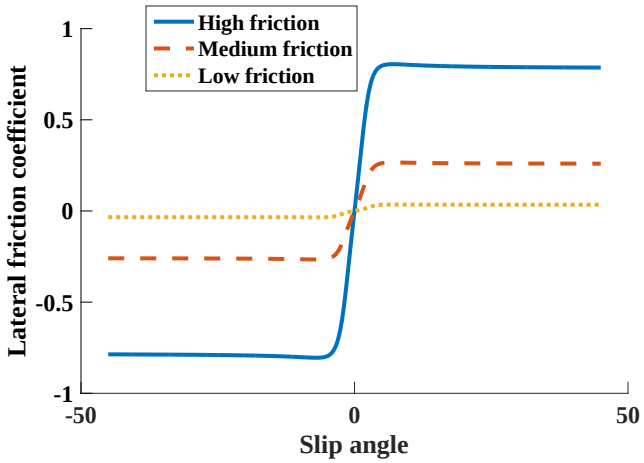

Figure 36: Lateral force coefficient

dynamic state that is challenging to control and stabilize. Simulations are used to show that a reduction in the friction coefficient between one wheel and ground can lead to a loss of stability for typical transporter motions.

To investigate a realistic case that yields interesting wheel-slip results, the vehicle was simulated as initially going 1 m/s and the rider leaned forward for 1 second, as he would when trying to accelerate the vehicle. A range of leaning angles was simulated while the right wheel passed over an area of reduced friction. Different reductions in the right wheel available traction forces by using traction curves scaled down to different maximum friction coefficient values. Examples of these curves are shown in

Figure 35 and Figure 36. Several surfaces were simulated for each leaning angle to find the maximum traction coefficient value that results in right wheel slip.

Figure 37 shows the leaning angle at which slip occurs for each coefficient of friction. A range of angles between 0.5° to 35° were simulated and the range of coefficient of friction extended between 0.12 and 1.0. Leaning angles below 4.5° did not cause slipping to occur even with the lowest coefficient of friction.

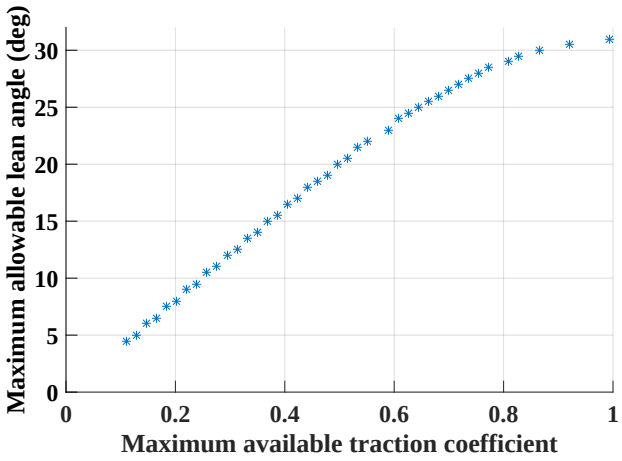

Figure 37: Maximum lean angle for different coefficients of friction

An example case is useful for understanding the vehicle behavior when slipping of one wheel occurs. The simulation was stopped when the normal force on one of the wheels became zero or when the pitch angle reached 60°. Figure 38 shows the slip ratios of both wheels. Note that the right wheel slips more than the left wheel and its slip ratio increases at a higher rate at near the 0.3 second mark. At the same time, the slip ratio of the left wheel stays significantly smaller. The left wheel slip starts increasing at around 0.8 seconds, shortly before the simulation is stopped because the pitch angle limit is reached.

As the right wheel slips with respect to the ground, it falls behind the left wheel. This causes the vehicle to make a right turn. The yaw rate of the vehicle is shown in Figure 39 for both the high-traction and reduced-traction cases. In the high-traction case, where both wheels roll across the same surface with $\mu = 0.92$, the

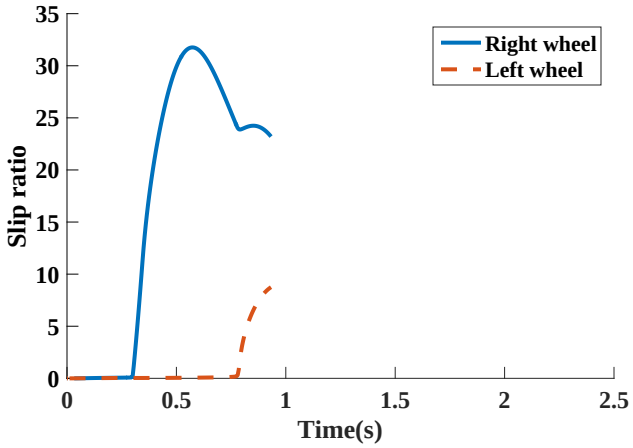

Figure 38: Wheel slip ratios while leaning forward 18.5° and experiencing reduced traction on the right wheel.

yaw rate remains at zero and the vehicle keeps going forward on a straight path. When the right-wheel traction is reduced, the yaw rate increased significantly after the 0.3 second mark and the vehicle is not able to stabilize itself in the yaw direction. The wheel slip and resulting increase in yaw rate occur quickly, and such a sudden, unexpected turning motion would give a rider little time to react. The yaw rate starts decreasing again when the left wheel starts slipping at about 0.8 seconds.

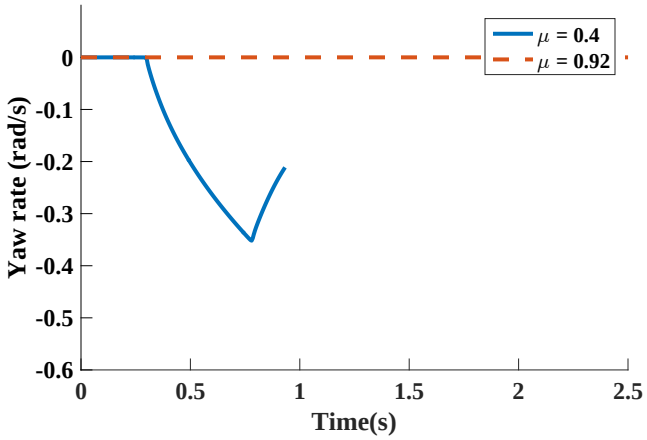

Figure 39: Yaw rate while leaning forward 18.5°.

Figure 40 show the pitch angle of both cases followed a similar trajectory before the right wheel started slipping. However, after the right wheel loses traction and

the yaw rate starts to increase, the vehicle is not able to balance itself and the pitch angle increases in an unstable manner.

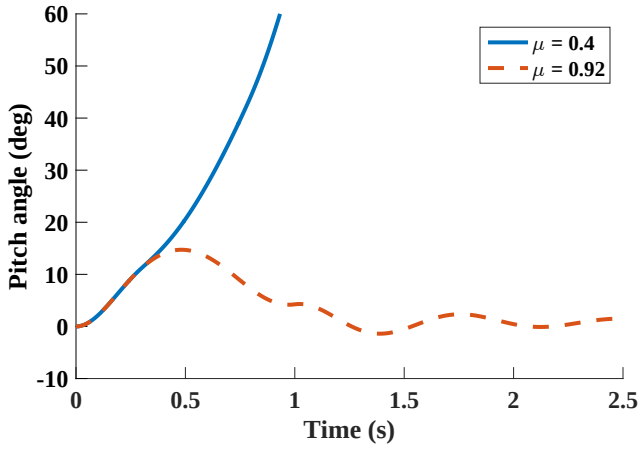

Figure 40: Pitch angle response while leaning forward 18.5°.

Figure 41 shows the speed response of the vehicle for both surfaces. In both cases, the vehicle accelerates forward as a result of the rider leaning forward. However, in the reduced traction case, the vehicle cannot accelerate as much because the right wheel is left behind as it spins out and the vehicle turns to the right.

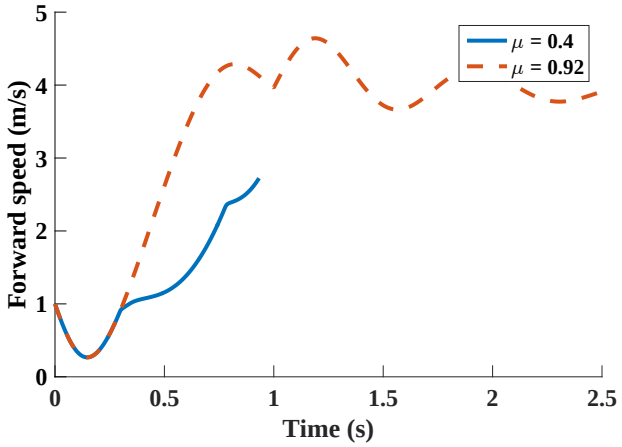

Figure 41: Speed while leaning forward 18.5°.

Figure 42 shows the normal forces between both wheels and the ground. As the vehicle starts turning right the normal force between the right wheel and the ground

decreases significantly. The forward speed and the yaw rate are not so large as to cause the vehicle to fall sideways at this point. As the pitch angle further increases, a larger torque is applied to the left wheel in order to regain balance. However, once the torque becomes too large, the left wheel starts slipping and the vehicle yaw rate decreases. The normal force on the left wheel is reduced as a result. The sum total of both forces decreases as the wheel slip even progresses because the system continues to pitch forward more and more, as was shown in Figure 40.

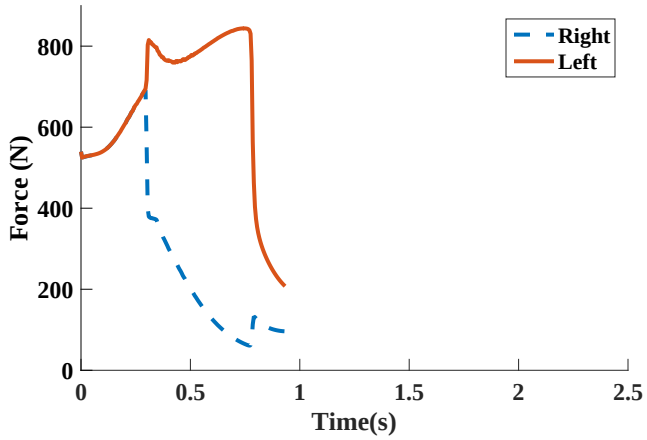

Figure 42: Normal forces while leaning forward 18.5° and experiencing reduced traction on the right wheel.

3.2 Two wheel slip - leaning backward

Slip can also occur in both wheels almost at the same time. In this section the dynamic behavior of a transporter in such situation is explored. An initial speed 5 m/s was set and the initial pitch angle was set to 0°. The person was simulated leaning back for 1 second to different angles and the maximum coefficient of friction between the wheel and the ground was varied to find the maximum leaning angle before slip occurs. Such backward leaning motions by the rider are required to stop the vehicle.

Figure 43 shows the minimum coefficient of friction required to prevent slipping

when the person leans back at different angles. As the leaning angle increases, slip takes place at larger coefficients of friction. This means that if a stopping maneuver is too aggressive, then the vehicle is more prone to slipping even on higher friction surfaces.

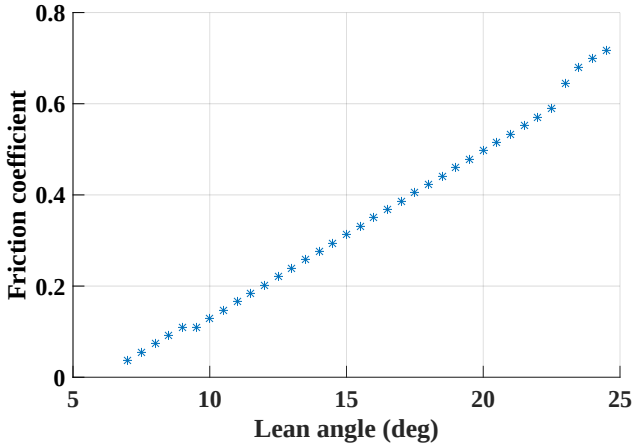

Figure 43: Coefficient of friction required to prevent the onset of slip at different leaning angles

Figure 44 shows the pitch response of the vehicle for the case when the person leaned back to 20°. In this case, slipping occurred when the ground-wheel friction coefficient was 0.54. The simulation was stopped when the vehicle reached an angle of 40° because it is unlikely that would be able to recover back to its vertical position after it has reached such a large angle. As seen, the vehicle is unable to remain stable in the pitch direction because the slipping wheels cannot provide the deceleration required for stability.

Figure 45 shows the speed of the vehicle. Initially, the vehicle accelerates forward as is the expected response from a non-minimum phase system. Around the 0.2 s mark, the speed starts decreasing until about 0.45 s. Then the speed increases again, contrary to what would be the expected behavior of the transporter when the person leans back. At the same time, the pitch angle becomes more negative. Because the motors are unable to decelerate the vehicle effectively, the transporter falls backwards

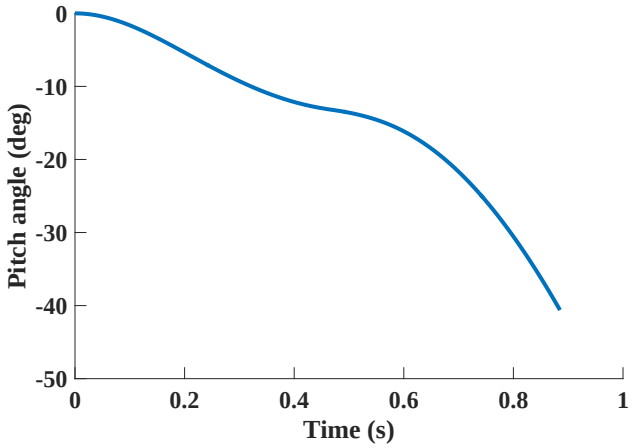

Figure 44: Pitch angle response while leaning back 20° with a ground-wheel friction coefficient of 0.54.

and the wheels translate forward simultaneously. Basically, the machine shoots out from underneath the rider.

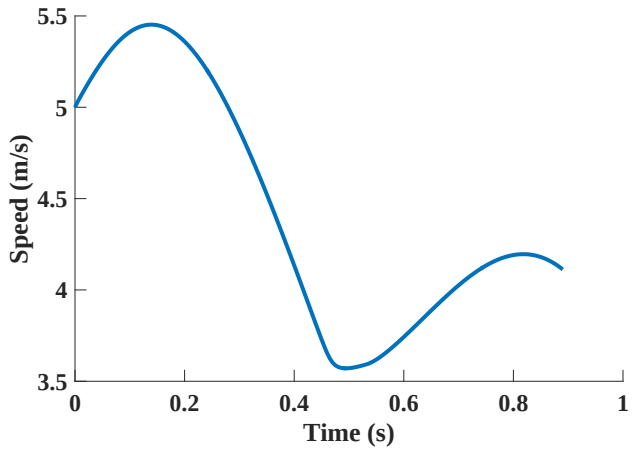

Figure 45: Speed response while leaning back

Figure 46 shows the slip ratio of the wheels. Note that the time when the vehicle stops decelerating is the same instance at which the slip ratio becomes suddenly more negative. This is the point where the slip ratio becomes greater than the slip ratio for maximum friction and where the wheel angular speed becomes unstable.

The traction coefficient, defined as the ratio between the wheel-ground normal force and the wheel-ground force in the forward/backward directin, is shown in Figure

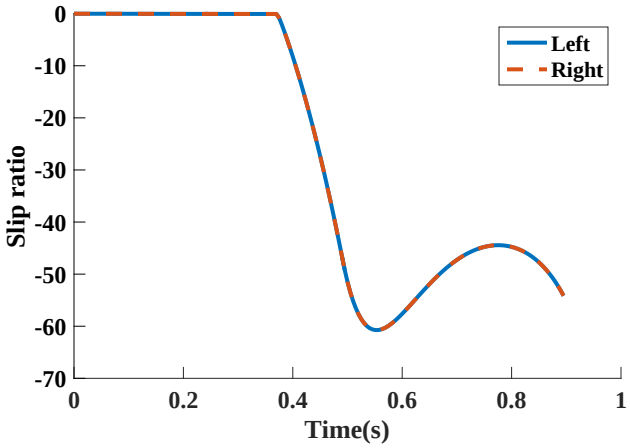

Figure 46: Wheel slip ratio while leaning back

47 for each slip ratio. Even though the maximum absolute value of the slip ratio was only 12, it was enough to make the vehicle unstable in just under 0.5 seconds. For the same leaning angle, a surface with lower traction would make the vehicle unstable in even a shorter amount of time.

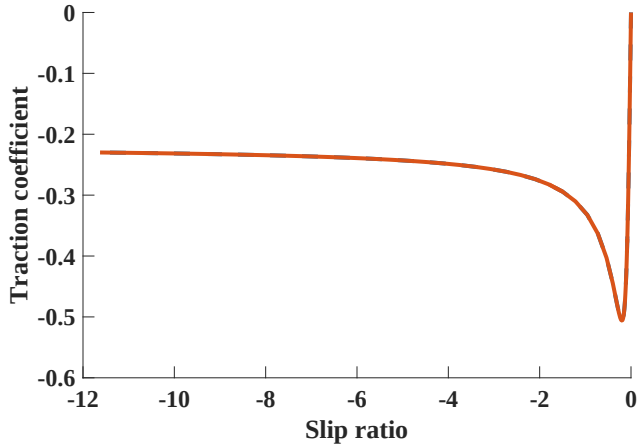

Figure 47: Traction coefficient vs slip ratio while leaning back

3.3 Effect of length of low friction region and speed

The previous section used unending low-friction ground regions. In many practical scenarios, a vehicle will encounter only a small section of low-friction terrain. This

section investigates the length of low-friction regions. The dynamic effects were simulated for different initial speeds, friction coefficients, and leaning angles.

Figure 48 shows the maximum leaning angle at different coefficient of friction. The low friction patch had a length of 0.15 m for one set of cases and 0.35 m for another set. An initial speed of 2.4 m/s was used for the transporter. For a given lean angle, the friction coefficient was reduced until slip was detected. Because the friction coefficient was reduced in steps of 0.02, several lean angles show the same friction coefficient at slip onset. Varying the friction coefficient at smaller steps would show a more smooth curve. Note that for the shorter region, the person can lean to a larger angle before slipping takes place. For coefficients of friction larger than 0.1, the person can lean forward without much risk of making the vehicle slip as it accelerates through the small region of low-friction ground. While going over the short distance of low friction the slipping wheels have less time to reach high angular speeds. Therefore, the slip ratio remains low enough that the friction coefficient remains within the linear region of the friction curve.

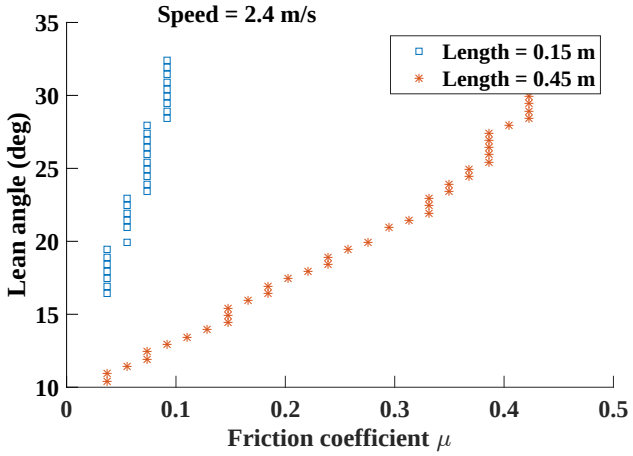

Figure 48: Maximum lean angle for each friction coefficient at different lengths of low friction surface

Figure 49 shows the maximum leaning angle at different speeds for a region of low friction that is 0.35 m long. When going at higher speeds, the person is able to lean

to larger angles without the vehicle slipping. This means that the faster the vehicle is traveling, the less likely it is to slip because it quickly passes over the slick spot. The wheel remains under low friction conditions for less time when it is going faster and does not allow the wheel angular speed to increase to a slip ratio beyond the linear region of the friction curve.

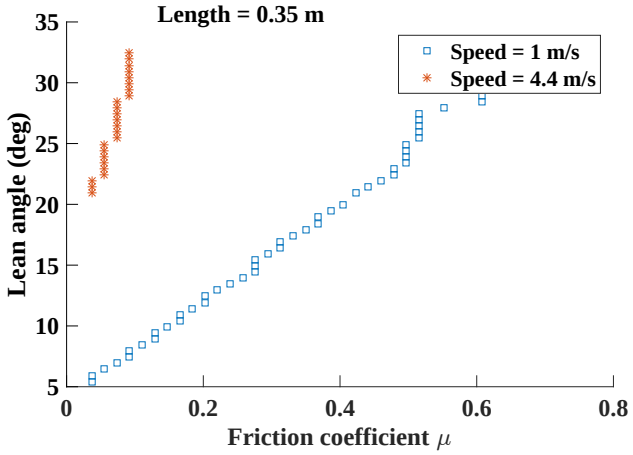

Figure 49: Maximum lean angle for each friction coefficient at different speeds

Figure 50 shows the maximum length of the low friction region given a vehicle speed, a specified leaning angle, and a friction coefficient. As expected from the previous results, the faster the vehicle goes, the larger low friction area it can travel over without it slipping. In addition, a higher wheel-ground traction coefficient makes it possible to travel over larger distances without wheel slip. The person can lean safely to an angle of 18.5°, as long as there is a friction coefficient larger than 0.4 and the speed is larger than 1 m/s.

A sample case where the vehicle is going at 1 m/s over a 0.35 long region of low friction and the person leans to an angle of 23 ° is analyzed in detail to reveal the dynamic effects that arise. In this simulation the person leaned forward for a period of 0.42 s.

Figure 51 shows the pitch angle of the vehicle under both a high and a lower friction surface. For the lower friction surface, the pitch angle increases for a longer

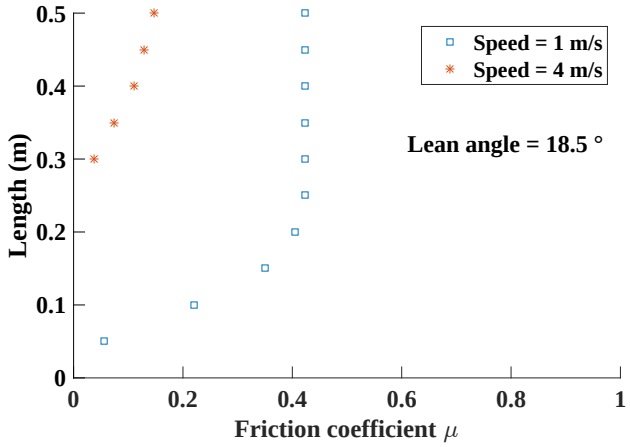

Figure 50: Maximum low friction distance for each friction coefficient at different speeds

time before reaching a maximum. For the high friction surface. the pitch angle reaches a maximum almost at the same time that the person stops leaning forward. The maximum pitch angle is also larger for the lower friction case, meaning that the lower friction increases the risk of the vehicle losing its balance. Additionally, the lower friction case takes longer to stabilize.

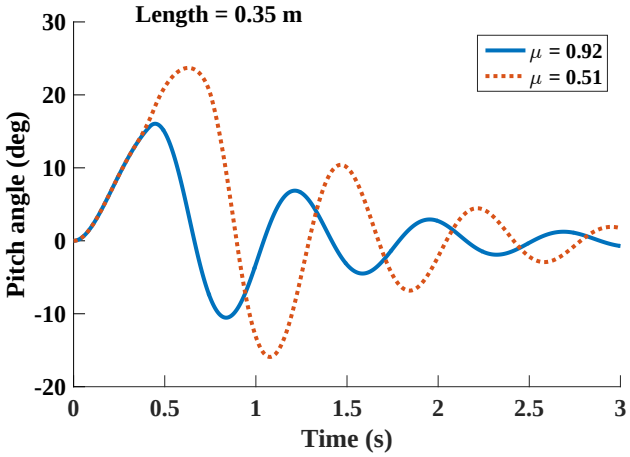

Figure 51: Pitch response at different friction coefficients going over 0.35 m long region of low friction..

Figure 52 shows the speed response for the low and high friction cases. Under lower friction the speed initially decreases because of the non minimum phase nature

of the system and then increases until the leaning command stops. At this point, there is an abrupt change in acceleration, but then the speed continues increasing even though the person is not leaning forward anymore. The speed reaches a greater maximum value when the friction is smaller, but the initial acceleration after the command stops is smaller.

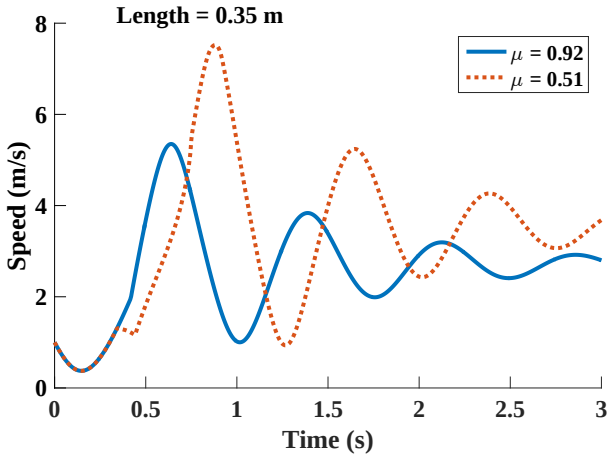

Figure 52: Speed response at different friction coefficients going over 0.35 m long region of low friction..

Figure 53 shows the slip ratio of the wheels for both cases. As expected, the lower friction surface exhibited a far larger slip ratio well above the linear region of the friction curve. In spite of this, the vehicle was able to maintain stability. The point of maximum slip ratio coincides with the time when the speed showed a discontinuous acceleration on the speed plot. The slip ratio increased dramatically after the person leaning motion stopped. However, the person leaning forward did not immediately produce slipping. It was the rider leaning back to a neutral position with respect to the vehicle that was the final catalyst for instability.

Although at first glance it seems that both the high-traction and low-traction surfaces have no effect before the slip ratio becomes unstable, looking more closely at the first few seconds of the simulation shows that the slip ratio of the right wheel increases at a faster rate than the slip ratio of the left wheel. This is shown in Figure

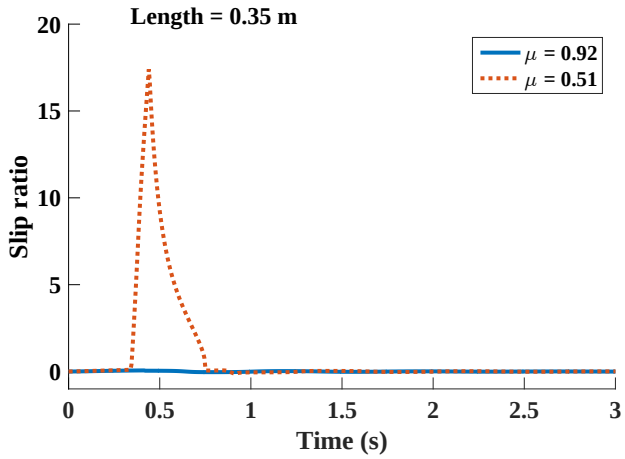

Figure 53: Slip ratio at different friction coefficients going over 0.35 m long region of low friction.

54. However, the difference in the slip ratios is too small to cause any significant difference in the speed and pitch responses during the first few seconds.

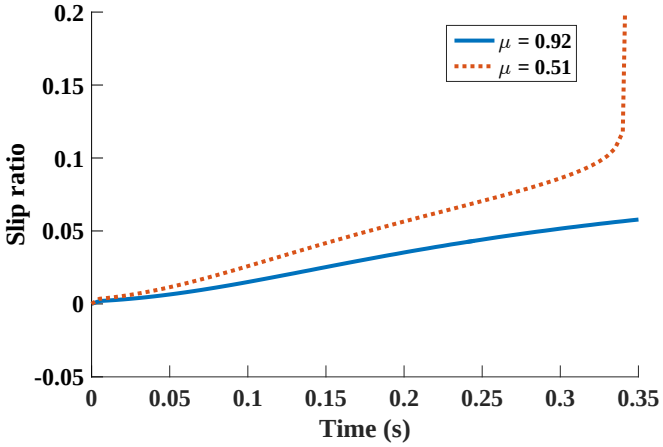

Figure 54: Slip ratio at different friction coefficients going over 0.35 m long region of low friction before slips occurs.

3.4 Effect of Wheel ground model parameters on dynamic behavior and stability

In this section the effect of the shape of the traction coefficient vs slip ratio curve is explored. The friction curve is defined by four parameters:

- d: Maximum friction coefficient.
- x_m: Slip ratio at which the maximum coefficient occurs.
- b: Slope at origin.
- y_a: Friction coefficient at infinity.

The following sections explore the effects of these parameters on the pitch, speed and the slip ratio responses of the vehicle when the person leans forward to a specified lean angle.

3.4.1 Slope at origin

Three cases were simulated where the person lean angle was 18° using curve slopes of: b = 2, b = 7, and b = 12. Figure 55 shows the pitch angle response for the three cases. In all three cases the vehicle lost balance. When the slope is larger, it takes a longer time for the pitch angle to increase. This indicates that it is more difficult for the slip ratio to depart from the linear region of the friction curve. These results demonstrate that the slope of the curve at the origin does affect the pitch angle response in a significant way.

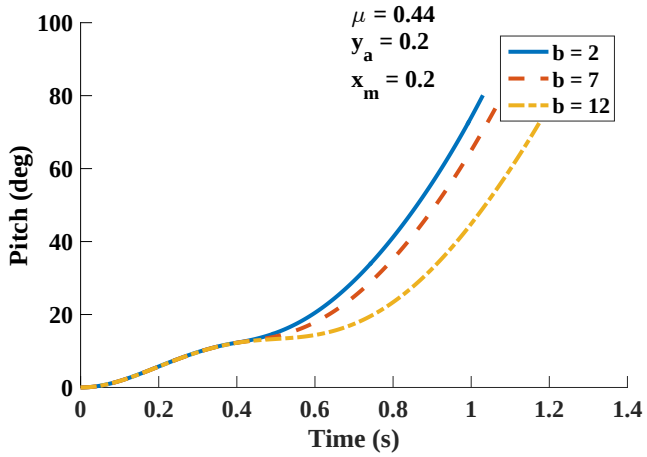

Figure 55: Effect of slope at origin on pitch response

Figure 56 shows the speed response of the vehicle. In the higher slope case, the vehicle was able to reach a higher speed, which explains why it was able to maintain balance for a slightly longer time than the other cases. The case with the smallest slope at the origin had a lower peak velocity, until it entered the final phase of bucking instability.

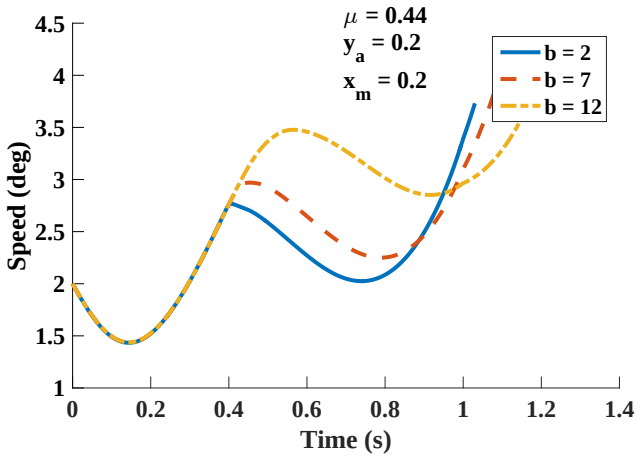

Figure 56: Effect of slope at origin on speed response

Figure 57 shows the slip ratio. Note that for the lower slope case, the slip ratio initially increased more rapidly and the maximum slip ratio for each curve was reached sooner. For the higher slope, the slip ratio increased more slowly. This means that at higher slopes it is more difficult for the vehicle to go beyond the linear region. The maximum value reached was higher when the slope was larger. Even though the slope of the curve might not control whether slip occurs, it significantly affects the dynamics of the vehicle during slipping as seen in the pitch and speed responses.

3.4.2 Slip for maximum value

In this section, the effect of the slip ratio at which the maximum traction coefficient (x_m) occurs is examined. In all cases, the person lean angle was 18° for 1 second.

Figure 58 shows the pitch response at three different values of x_m: 0.05, 0.2, and 0.35. The vehicle was able to remain stable when x_m was 0.35, but failed to do so

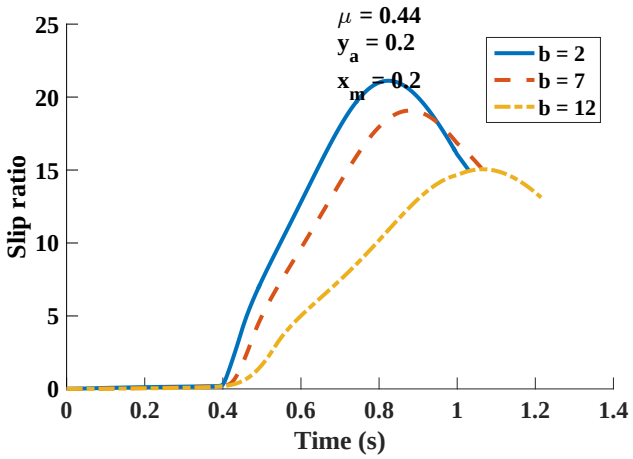

Figure 57: Effect of slope at origin on slip ratio response

at smaller values, even when the maximum friction coefficient was the same. For the smallest x_m value, the vehicle pitch went unstable sooner. Therefore, reducing x_m makes the vehicle more prone to instability.

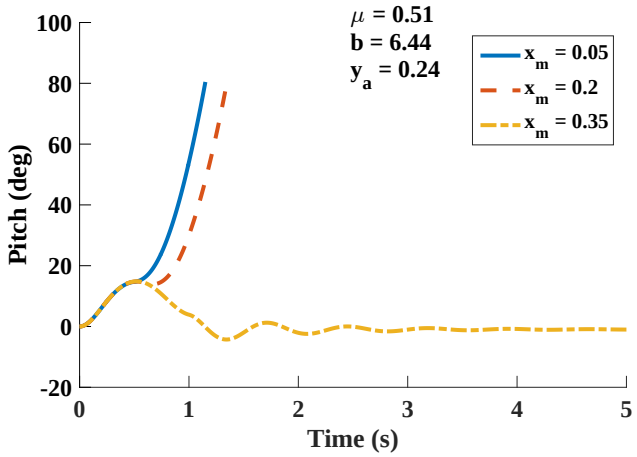

Figure 58: Effect of maximum friction slip on pitch response

Figure 59 shows the speed for each case. Larger values of x_m allow the system to achieve higher speeds. This indicates that the vehicle was better able to accelerate when x_m was larger and, therefore, more capable of limiting the pitch angle.

These results can be explained by examining the wheel slip ratio for all three cases, as shown in Figure 60. The results indicate that as the x_m value becomes smaller, the

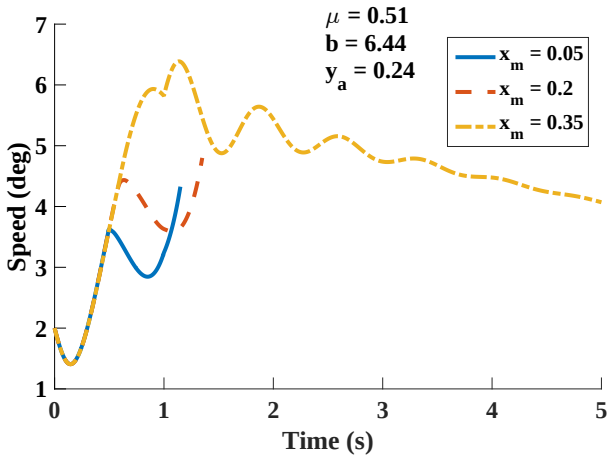

Figure 59: Effect of maximum friction slip on speed response

slip onset occurs sooner. This means that the wheel goes beyond the linear region of the friction curve with more ease as the maximum value increases. The slip onset for $x_m = 0.2$ takes place later and slip does not occur when $x_m = 0.35$. This indicates that other surface characteristics, besides the maximum coefficient of friction, can influence not only the behavior after slip occurs, but also whether or not it occurs.

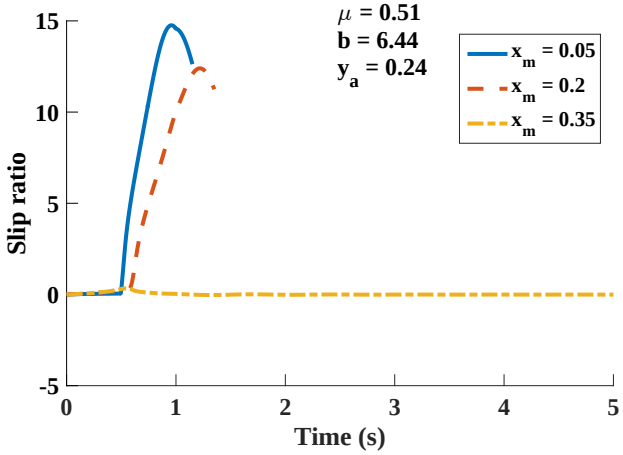

Figure 60: Effect of maximum friction slip on slip ratio response

3.4.3 Value at large slip ratios

Three cases using different values of the asymptotic friction coefficient, y_a, were simulated. For these cases a rider lean angle of 20° for 1 s was used.

Figure 61 shows the pitch responses. In all three cases the vehicle went unstable. However, when y_a was larger, the vehicle struggled to maintain balance for about 3 seconds. For the smaller y_a cases, the vehicle went unstable very rapidly. The pitch angle increased more aggressively with the smallest y_a case.

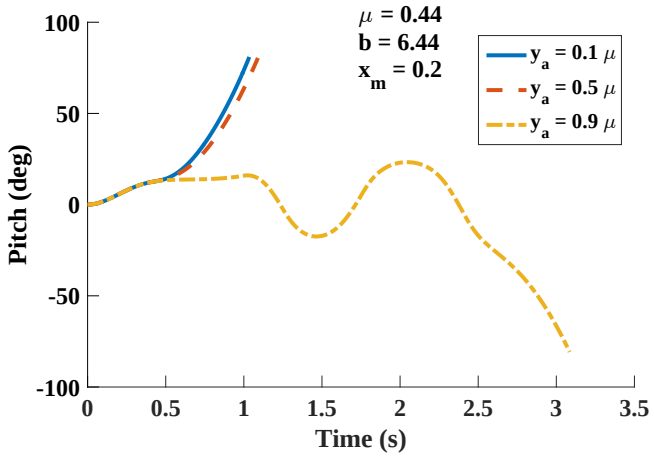

Figure 61: Effect of asymptotic friction coefficient on pitch response

Figure 62 shows the speed responses. During the initial response, before the 0.5 second mark, the three responses look similar. Afterwards, the $y_a = 0.9$ speed keeps increasing, while the other two decrease. The larger y_a allows the vehicle to accelerate more and enables it to balance itself slightly better. A lower y_a significantly reduces the available friction after the onset of slip.

Figure 63 shows how the slip ratio increased more for the smaller y_a cases. The smaller the y_a value, the higher the slip ratio. The onset of slip occurred at the same time for all three cases, but the available friction after slip was larger for $y_a = 0.9$. This prevented the wheel from spinning so dramatically and allowed the vehicle to accelerate and balance itself for a few more seconds. This is also evidence that the curve parameters affect the behavior of the vehicle after the onset of slip has occurred.

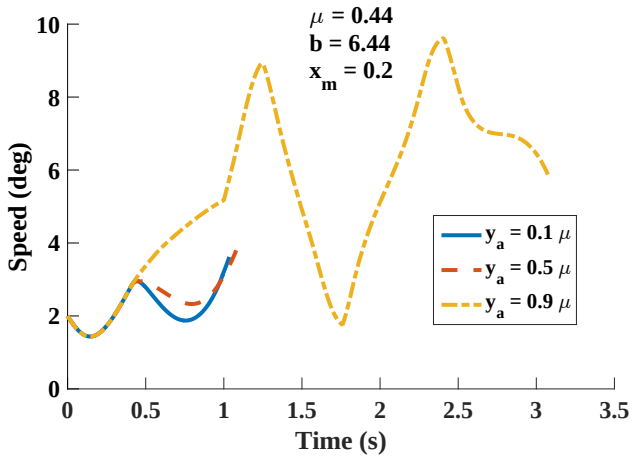

Figure 62: Effect of asymptotic friction coefficient on speed response

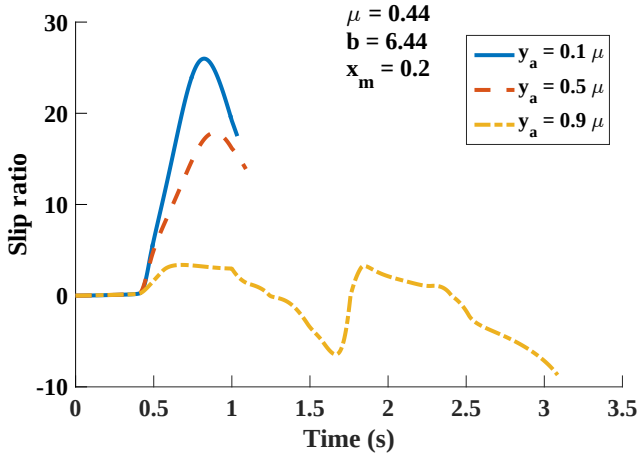

Figure 63: Effect of asymptotic friction coefficient on slip ratio response

3.5 Summary

This chapter presented a model of a self-balancing transporter that includes a wheel-ground traction model based on the empirical Pacejka equations. This model was used to simulate acceleration maneuvers under two-wheel and one-wheel slip conditions. In both cases, the reduced wheel-ground traction limits the vehicle acceleration and the angle that the person can lean before slipping occurs. For example, if the coefficient of friction is reduced to 0.5, the maximum leaning angle is limited to 20°. If slipping takes place, then the vehicle can lose pitch stability in less than 1 second. When

slipping occurs in one wheel, an unexpected turning motion occurs that can cause the vehicle to tip-over in the roll direction in a very short amount of time as low as 1 second. As the vehicle goes faster, it is capable of remaining stable over longer patches of low friction surfaces. Finally, other wheel-ground traction characteristics beside the peak traction coefficient can have a significant influence on the dynamic response of the vehicle. Increasing the slope of the friction coefficient curve, the slip ratio for its maximum value, and the asymptotic friction coefficient makes the vehicle more stable.

CHAPTER IV

LATERAL STABILITY

The most obvious failure mode of a two-wheeled inverted-pendulum transporter is the loss of pitch stability. However, loss of lateral stability, which leads to bucking or complete tip-over in the roll direction can occur very rapidly and unexpectedly.While inverted-pendulum transporters actively control their pitch stability, there is no such control on their lateral stability. The machines rely on lateral wheel separation to provide sideways tip-over stability. Of course, there are limits on what such an approach can provide.

One practical limitation on wheel width is the need for such transporters to fit through doorways. Lateral instability can occur as a result of different causes. For example, the machine can tip over during turns at certain combinations of speed and turning radii. The rider can also fall over sideways because their feet cannot be moved laterally to regain balance. Lateral instability can also occur as a result of a wheel losing traction. When this happens, and the wheel spins excessively, the machine may turn off. Losing traction can occur as a result of dropping off of a curb, or passing over slick surfaces as was thoroughly examined in the previous chapter. Lateral instability can also occur from of an unexpected turn when a wheel contacts an obstacle. The vehicle would turn in the direction of the obstacle and pitch forward. The machine can also make an unexpected turn when the operator accidentally commands a turning motion. This can happen by accidentally twisting the steering grip or when the person pushes the handlebar sideways in a way that could lift one of the wheels of the ground. Doing this would also cause the machine to turn [4, 52].

This chapter investigates such lateral stability dynamics. The next section examines lateral stability while moving at a constant speed. Section 4.2 examines the effect of rider motion. Finally, Section 4.3 examines the effect of wheel slip with an emphasis on lateral stability effects.

4.1 Roll stability turning at a constant speed v along a curved path with radius r_g

A vehicle moving along a curved path has a tendency to tip over in the direction away from the center of curvature. A simple way to quantify this tendency is to estimate the normal forces between the vehicle and the ground at the contact points. Figure 64 shows a free body diagram of a two-wheeled vehicle, and a lumped-mass model of a passenger when the system is turning right while traveling into the page.

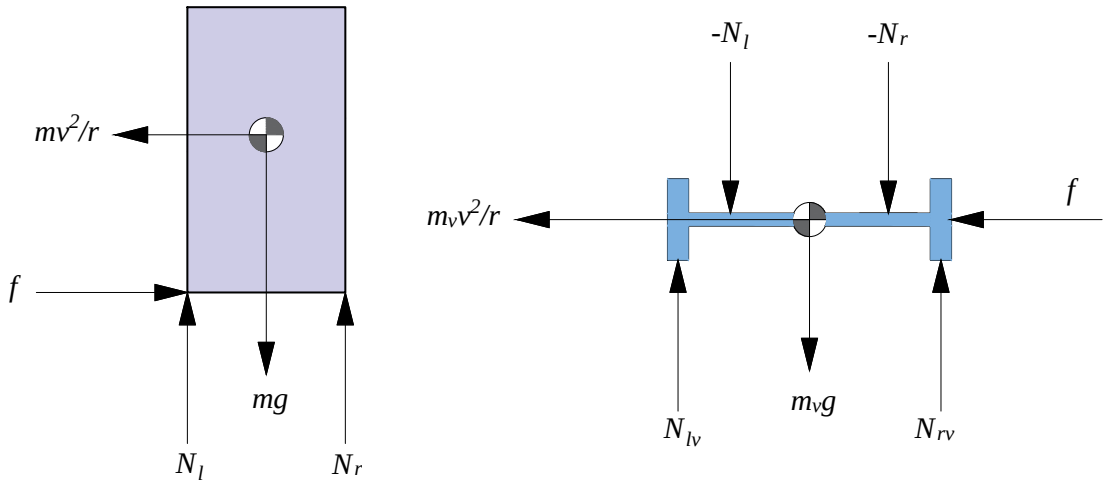

(a) Passenger (b) Vehicle

Figure 64: Free body diagram during a right turning motion (assuming no lateral wheel slip)

N_l and N_r are the left and right normal forces at the contact points between the person and the vehicle. N_{lv} and N_{rv} are the left and right normal forces between

the vehicle wheels and the ground, and g is the gravitational acceleration. The centrifugal force in the rotating reference frame is mv^2/r where r is the radius of the turn. Balancing moments at each contact point between the person, the vehicle, and the ground, results in the following system of equations that allows us to find the friction force f, the normal forces between the vehicle and the ground (N_{lv} and N_{rv}), and the normal forces between the ground and the passenger (N_l and N_r):

$$\begin{cases} f - \frac{mv^2}{r_g} = 0 \\ \frac{mv^2}{r_g} H_{cm} + mg\frac{b}{2} - N_l b = 0 \\ \frac{mv^2}{r_g} H_{cm} - mg\frac{b}{2} + N_r b = 0 \\ \frac{m_v v^2}{r_g} r + fr - m_v g\frac{d}{2} - N_l\frac{d-b}{2} - N_r\frac{d+b}{2} + N_{rv} d = 0 \\ \frac{m_v v^2}{r_g} r + fr + m_v g\frac{d}{2} + N_l\frac{b+d}{2} + N_r\frac{d-b}{2} - N_{lv} d = 0 \end{cases} \tag{31}$$

By solving this system of equations, the contact forces were found. The normal forces between the vehicle and the ground are:

$$N_{lv} = \frac{mg + m_v g}{2} + \frac{(m + m_v)v^2 r}{dr_g} + \frac{mv^2 H_{cm}}{dr_g} \tag{32}$$

$$N_{rv} = \frac{mg + m_v g}{2} - \frac{(m + m_v)v^2 r}{dr_g} - \frac{mv^2 H_{cm}}{dr_g} \tag{33}$$

The normal forces between the passenger and the vehicle are:

$$N_l = \frac{mg}{2} + \frac{mv^2 H_{cm}}{br_g} \tag{34}$$

$$N_r = \frac{mg}{2} - \frac{mv^2 H_{cm}}{br_g} \tag{35}$$

The maximum turning speed and the minimum turning radius at which the vehicle or rider becomes unstable are those for which the right normal forces become zero:

$$N_r = 0 \tag{36}$$

$$N_{rv} = 0 \tag{37}$$

Solving for $N_{rv} = 0$ gives the minimum radius for a given speed at which the vehicle begins to roll sideways relative to the ground.

The combined center of mass of the vehicle-body system is:

$$H_{cm,global} = \frac{H_{cm}m + r(m + m_v)}{m + m_v} \tag{38}$$

A basic Newtonian analysis assuming constant speed and constant turning radius shows that the minimum turning radius $r_{g_{vehicle}}$ and the maximum turning speed $v_{vehicle}$ before the vehicle tips over can be expressed as:

$$\begin{aligned} r_{g_{vehicle}} &= \frac{2H_{cm,global}v^2}{dg} \\ v_{vehicle} &= \sqrt{\frac{dr_g g}{2H_{cm,global}}} \end{aligned} \tag{39}$$

This result is based on the assumption that the rider does not fall off before the vehicle starts to tip over.

Similarly, solving for $N_r = 0$ gives the minimum radius for a given speed at which the person falls off the vehicle. The minimum turning radius $r_{g_{person}}$ and the maximum turning speed v_{person} before the person falls off the vehicle are given by:

$$\begin{aligned} r_{g_{person}} &= \frac{2H_{cm}v^2}{bg} \\ v_{person} &= \sqrt{\frac{br_g g}{2H_{cm}}} \end{aligned} \tag{40}$$

4.1.1 Relative stability between the vehicle and the passenger

There can be cases when the passenger will fall off before the vehicle tips. The conditions at which both $r_{g_{vehicle}}$ and $r_{g_{person}}$ are equal can be found by subtracting $r_{g_{person}}$ from $r_{g_{vehicle}}$ and equating the result to zero. By doing so and noting that v^2 and g can be cancelled out from both sides of the equation, the following relationship is found:

$$\frac{2[H_{cm}bm - H_{cm}d(m+m_v) + Rb(m+m_v)]}{bdg(m+m_v)} = 0 \tag{41}$$

Multiplying this expression by bg, dividing by R, and letting $\lambda = \frac{H_{cm}}{R}$, $\delta = \frac{b}{d}$, and $\rho = \frac{m}{m+m_v}$, we obtain:

$$f = \lambda\delta\rho - \lambda + \delta = 0 \tag{42}$$

This defines a surface in the $(\lambda\delta\rho)$ coordinate system. If the above relationship is greater than zero, then the minimum turning radius of the vehicle before it tips over is greater than the tip-over radius of the passenger. This means that the vehicle is more prone than the rider to become unstable, or becomes unstable at lower-curvature turns.

4.1.2 Limits on speed and turning radius imposed by available lateral friction forces

A vehicle can only turn as long as there is a lateral force applied on the wheels and directed towards the center of the curved path. This lateral force depends on the coefficient of friction between the wheels and the ground. This lateral sliding coefficient of friction can be different from the braking coefficient of friction in the forward direction [51]. By balancing forces in the direction parallel to the radius of the curved path, a relationship can be found between the speed, the path radius, and the coefficient of friction that leads to such sideways wheel slip.

Figure 64 can expanded to account for these forces, as shown in Figure 65. These forces must be greater than or equal to the centripetal acceleration multiplied by the mass of the vehicle. If they are not, then the vehicle will slide sideways before it tips over. The radial forces between the person and the vehicle are balanced against the

centripetal acceleration as follows:

$$f_{lat,r} + f_{lat,r} \geq \frac{mv^2}{r} \tag{43}$$

$$\mu_{base}\left(N_l + N_r\right) \geq \frac{mv^2}{r} \tag{44}$$

$$\mu_{base} mg \geq \frac{mv^2}{r} \tag{45}$$

$$v^2 \leq \mu_{base} rg \tag{46}$$

By a similar procedure, the following relationship that relates the maximum turning speed, the turning radius, and the coefficient of friction between the wheels and the ground is:

$$v^2 \leq \mu_{lat} rg \tag{47}$$

where μ_{lat} is the lateral coefficient of friction, r is the radius of the curve, and g is the acceleration of gravity.

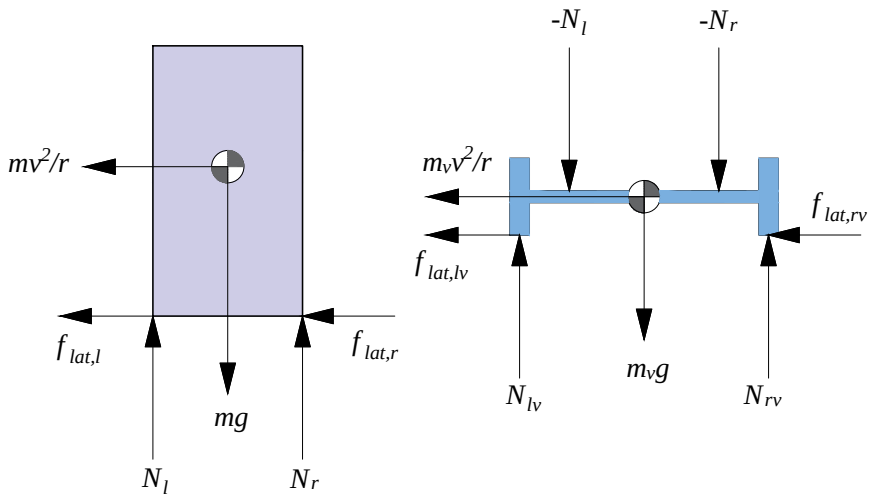

Figure 65: Free body diagram during a turning motion to the right

4.1.3 Roll stability analysis of a Segway i2

In this section the relations developed above are examined when the system has the parameters and conditions found in Table 3. These values correspond to those of a Segway i2 with an average operator [9].

Table 3: System parameters of a Segway i2 and initial conditions [8]

Parameter	Value
m	85
m_v	46
g	9.81 m/s^2
H_{cm}	1.2 m
R	0.2415 m
d	0.53 m
b	0.283 m
v	4.47 m/s
θ	0°

The turning radius at which the normal force on the right wheel is zero during a right turn at 10 mph is listed in Table 4. The first row shows the results obtain from the analysis of this section, while the second row shows the results from a dynamic simulation. The results of the analysis of this section are close to the more complete description of the system provided by a dynamic simulation. However, these results show that a simplified analysis can provide a useful estimate of the tip-over radius of the vehicle.

Table 4: Tip over radius at 10 m/h

Model	Vehicle tip over radius	Payload tip over radius
Static	7.84 m	17.27 m
Dynamic	8.11 m	15.76 m

The maximum speed and the minimum turning radius for the vehicle and the person according to (39) and (40) are shown in Figure 66. For this system, the maximum speed for stability of the person is less than the maximum speed for stability of the vehicle. The opposite can be said about the turning radius. Therefore, for this particular system and conditions, the rider will tip-over sideways before the vehicle goes into a roll instability.

Equation (42) can be used to determine how the maximum speed for stability of the vehicle compares to the maximum speed for stability of the rider. The parameters

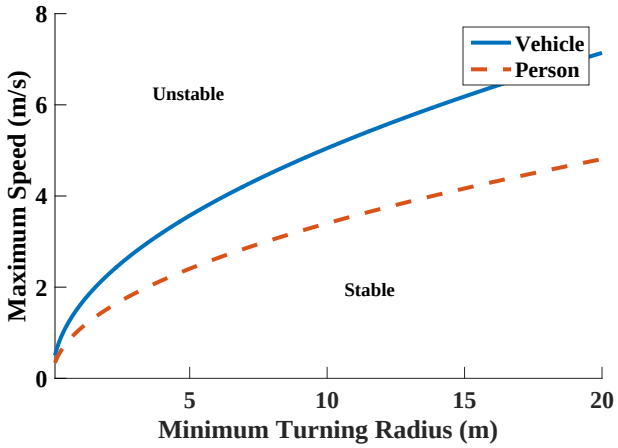

Figure 66: Maximum Speed vs Minimum Turning Radius.

λ, δ and μ for this system are:

$$\begin{aligned} \lambda &= \frac{H_{cm}}{r} = 4.97 \\ \delta &= \frac{b}{d} = 0.534 \\ \rho &= \frac{m}{m + m_v} = 0.649 \end{aligned} \tag{48}$$

Using these parameters in (42) gives a value of $f = -2.713$. A negative value means that the minimum turning radius for vehicle stability is less than for passenger stability. This means that even though the vehicle can remain stable at certain turning radii, the person would fall off. Equivalently, this means that the person becomes unstable with respect to the vehicle at lower speeds than the ones at which the vehicle becomes unstable with respect to the ground. However, these results assume the person is standing straight up and down. If the rider "leans into" the turn, then the machine instability can become the limiting factor.

Figure 67 shows a plot of (42). The surface represents the combination of parameters for which the maximum permissible speeds of the vehicle and the person are equal. The system considered above is located with a marker to the right of the surface. The surface shows how the height of the center of mass has almost no effect in moving the system towards the surface. The easier way to move the marker towards

the surface in this case would be to increase δ, which is the ratio of the rider feet separatin and the machine wheel separation.

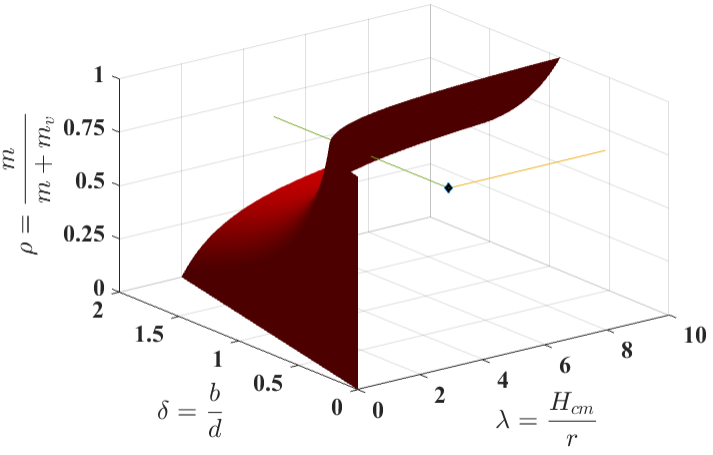

Figure 67: Surface at which the maximum speed of the vehicle at lateral instability is equal to the maximum speed of the person at lateral instability.

4.2 Effect of rider motion on lateral stability

4.2.1 Roll stability with rolling rider

In this section, the system is similar to the one studied in Section 4.1 except that the rider is allowed to lean into the turn with an angle θ. This allows a rider to redistribute the normal forces across the left and right sides. A diagram of this system is shown in Figure 68.

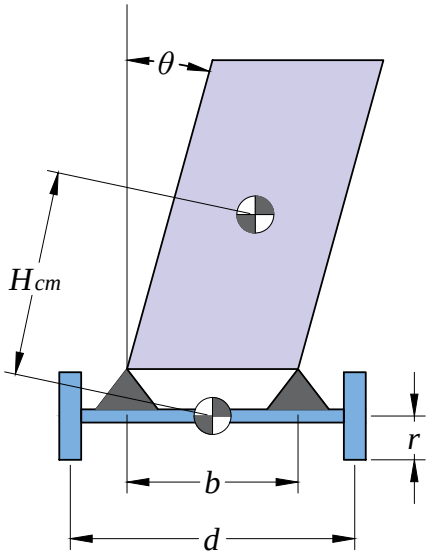

Figure 68: System with a leaning rider.

4.2.1.1 Roll stability turning at a constant speed v along an arc path with radius r_g

A similar procedure to the one used in the previous section was used to obtain the normal forces between the vehicle, the person, and the ground. The normal forces between the vehicle and the ground are:

$$N_{lv} = \frac{mg + m_v g}{2} + \frac{(m + m_v)v^2 r}{dr_g} - \frac{mgH_{cm}\sin\gamma}{d} - \frac{mv^2 H_{cm} r\sin\gamma}{dr_g^2} - \frac{mv^2 H_{cm}^2 \sin\theta\cos\gamma}{dr_g^2} + \frac{mv^2 H_{cm}\cos\gamma}{dr_g} \tag{49}$$

$$N_{rv} = \frac{mg + m_v g}{2} - \frac{(m + m_v)v^2 r}{dr_g} + \frac{mgH_{cm}\sin\theta}{d} + \frac{mv^2 H_{cm} r \sin\theta}{dr_g^2} + \frac{mv^2 H_{cm}^2 \sin\theta\cos\theta}{dr_g^2} - \frac{mv^2 H_{cm}\cos\theta}{dr_g} \tag{50}$$

The normal forces between the load and the vehicle on each side are:

$$N_r = \frac{mg}{2} + \frac{mgH_{cm}\sin\theta}{b} - \frac{mv^2 H_{cm}\cos\theta}{br_g} + \frac{mv^2 H_{cm}^2 \sin\theta\cos\theta}{br_g^2} \tag{51}$$

$$N_l = \frac{mg}{2} - \frac{mgH_{cm}\sin\theta}{b} + \frac{mv^2 H_{cm}\cos\theta}{br_g} - \frac{mv^2 H_{cm}^2 \sin\theta\cos\theta}{br_g^2} \tag{52}$$

Even though these equations look more complex, they have the same structure as in the non-leaning case. For example, N_r can be rewritten as:

$$N_r = \frac{mg}{b}\left(\frac{b}{2} + H_{cm}\sin\theta\right) - \frac{m}{r_g - H_{cm}\sin\theta}\left(\frac{r_g - H_{cm}\sin\theta}{r_g}v\right)^2\left(\frac{H_{cm}\cos\theta}{b}\right) \tag{53}$$

Here, the first term corresponds to the fraction of the weight that is transmitted through the right support which can be expressed relative to the vehicle mass as αm. In the non-leaning case this would be half of the mass of the person. The second term corresponds to the force generated by the turning motion. Because the person is leaning, the height of the center of mass lowers slightly to $H_{cm,\theta} = H_{cm}\cos\theta$, and the radius of its turn also decreases to $r_{g,\theta} = r_g - H_{cm}\sin\theta$. The speed of the center of mass of the person becomes:

$$v_\theta = \frac{r_g - H_{cm}\sin\theta}{r_g}v \tag{54}$$

Therefore, (53) can be rewritten as:

$$N_r = mg\alpha - \frac{mv_\theta^2 H_{cm,\theta}}{r_{g,\theta} b} \tag{55}$$

where:

$$\alpha = \frac{1}{2} + \frac{H_{cm}}{b} \sin\theta \tag{56}$$

The forces between the wheels and the ground also follow the same structure and a similar procedure can be followed to find the coefficients that would allow us to express them in a manner similar to (55).

Because lateral instability can result from either underleaning or overleaning, the left normal force can become zero if the lean angle to the right exceeds a critical value. The conditions at which either the left or right normal forces become zero are discussed next.

By solving for $N_r = 0$, the relationship between the lean angle, turning radius, and speed at which the normal force between the right wheel and the ground becomes zero is found to be:

$$v_{right}^2 = \frac{g r_g^2 [2mH_{cm} \sin\theta + (m + m_v)d]}{2[(m + m_v)Rr_g - mH_{cm}^2 \cos\theta \sin\theta - mH_{cm}R \sin\theta + mH_{cm}r_g \cos\theta]} \tag{57}$$

By solving for $N_l = 0$, the relationship between lean angle, turning radius, and speed for when normal force on the left wheel is becomes zero is:

$$v_{left}^2 = \frac{g r_g^2 [2mH_{cm} \sin\theta - (m + m_v)d]}{2[(m + m_v)Rr_g - mH_{cm}^2 \cos\theta sin\theta - mH_{cm}R \sin\theta + mH_{cm}r_g \cos\theta]} \tag{58}$$

An equivalent relationship can be found for the speed at which the normal force between the vehicle and the passenger's right support becomes zero:

$$v_{right_{person}}^2 = \frac{g r_g^2 (2H_{cm} \sin\theta + b)(r_g - H_{cm} \sin\theta) H_{cm} \cos\theta}{2(H_{cm}^2 \cos\theta \sin\theta - H_{cm} r_g \cos\theta)^2} \tag{59}$$

Similarly, the speed at which the normal force between the vehicle and the passenger's left support becomes zero is:

$$v_{left_{person}}^2 = \frac{g r_g^2 (2H_{cm} \sin\theta - b)(r_g - H_{cm} \sin\theta) H_{cm} \cos\theta}{2(H_{cm}^2 \cos\theta \sin\theta - H_{cm} r_g \cos\theta)^2} \tag{60}$$

In order to determine whether the person, or the vehicle, is more unstable, the speeds given by the previous equations can be compared. Given the complexity of the relations it is not practical to obtain a concise expression as the one found in (42). However, we can obtain an expression that defines the condition at which the person-vehicle and vehicle-ground forces become zero simultaneously. If the expression is less than zero, then the speed at which the person falls off the vehicle is less than the speed at which the vehicle tips over. If it is greater than zero, then the vehicle tips over before the person falls off. This tip-over bifurcation expression is:

$$\begin{aligned} f = {} & Rbr_g(m+m_v) - 2H_{cm}^2 Rm\sin^2\theta + H_{cm}^2\cos\theta\sin\theta[(m+m_v)d+mb] \\ & + H_{cm}R\sin\theta[2(m+m_v)r_g - mb)] - H_{cm}r_g\cos\theta[(m+m_v)d - mb] \end{aligned} \tag{61}$$

4.2.1.2 Analysis of a Segway i2

The equations from Section 4.2.1.1 are used with the parameters for the Segway i2 in Table 3 to find the leaning angle limit. By setting (49) and(50) equal to zero, the range of passenger lean angles θ for which the vehicle remains stable can be found as a function of speed. This range is shown in Figure 69. The normal force on the left wheel is greater than zero if the speed, radius, and tilting angle are below the upper surface. Similarly, the normal force on the right wheel is greater the zero if the operating conditions are above the lower surface. The vehicle and passenger remain stable if it operates within the volume between both surfaces.

Figure 70 shows the maximum speed at which the vehicle can travel at different leaning angles. The data shows that as the person leans further to the right (positive leaning angle), the maximum turning speed is increased. This effect is why riders are encouraged to "lean into the turn."

A 1 m radius turn was simulated for a wide range of speeds. As shown in Figure 71, at each speed there is a range of leaning angles at which the vehicle can turn safely.

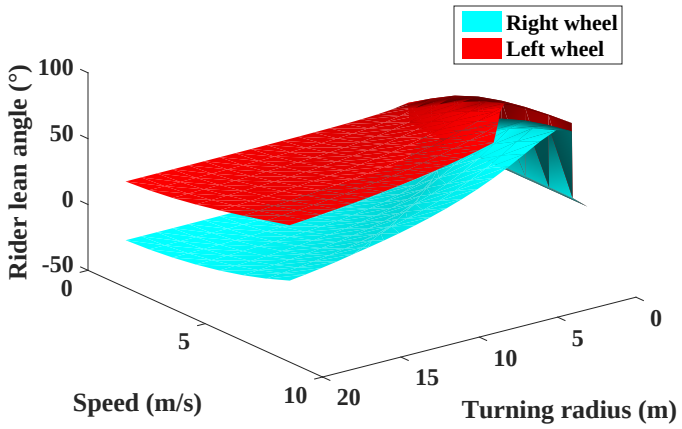

Figure 69: Rider lean limits.

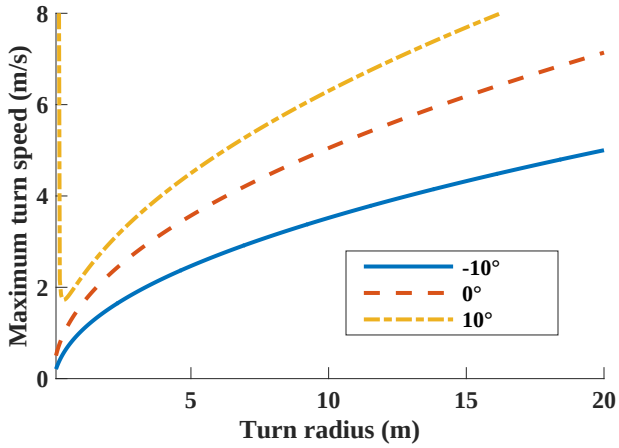

Figure 70: Speed limit for a specified lean angle and radius.

This range is largest at low speed and decreases as the speed is increased. Both the maximum and minimum allowable leaning angles increase as the speed increases. Therefore, a rider intending to "lean into the turn" needs to have some knowledge of the speed of the vehicle.

Note that the curves in Figure 71 represent the points where the normal forces between the right (minimum lean angle) or left wheel (maximum lean angle) become zero. For certain speeds, there are two passenger lean angles that can make each force zero. This can be explained by examining (50) and (49) and noting that the $\sin\gamma\cos\gamma$ term increases initially when the person starts leaning. However, it reaches

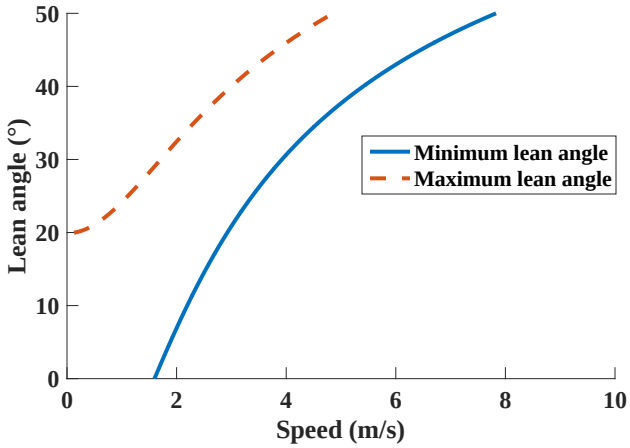

Figure 71: Lean angle limits for a 1 m radius turn.

a maximum the begins to decrease. This means that if the person leans too far into the turn, for certain combinations of speeds and turning radius, the force at the right wheel (inside of the turn) can become zero again. Conversely, the person could lean to an angle larger than the maximum allowable lean angle for the force on the left side to remain above zero and find a stable position. However, the transition to this configuration might involve having a wheel lose contact with the ground. Furthermore, these secondary lean angles are unrealistically large, generally above 60°.

4.2.1.3 Dynamic equations of motion including rider lean

The previous section examined the static stability limits of riders "leaning into the turn." While that analysis provided useful bounds, it is also important to consider dynamic effects. The model from Section 2.1 was modified to account for the operator leaning sideways at a non constant speed. This system is shown in Figure 72.

Because the operator is often required to lean sideways when commanding a turn to most self balancing transporters, the dynamic equations of motion were developed for the case when this motion takes place. The location of the center of mass of the passenger is at point (x_b, z_b). His body has a mass m_b and moments of inertia of I_{bx},

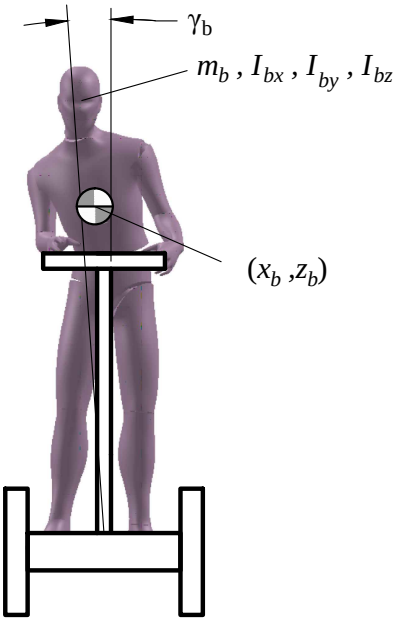

Figure 72: Rider leaning while operating a two-wheeled inverted pendulum

I_{by}, and I_{bz}. The body leans sideways at an angle γ_b with respect to the transporter. These mass and geometric relations were entered into a commercial multibody dynamic modeling software MotionGenesis to produce the dynamic equations of motion:

$$
\begin{aligned}
&(-(I_{bx}-I_{by})\sin^2\gamma_b\sin\theta_p\cos\theta_p+m_p(x_{wp}\sin\theta_p(x_{wp}\cos\theta_p+z_{wp}\sin\theta_p)\\
&-z_{wp}\cos\theta_p(x_{wp}\cos\theta_p+z_{wp}\sin\theta_p))-(I_{px}-I_{pz})\sin\theta_p\cos\theta_p-(I_{bx}\\
&-I_{bz})\cos^2\gamma_b\sin\theta_p\cos\theta_p-m_bz_b^2\cos^2\gamma_b\sin\theta_p\cos\theta_p)\dot\beta^2+(I_{bz}\sin^2\gamma_b\cos\theta_p\\
&+I_{by}\cos^2\gamma_b\cos\theta_p+(I_{bx}-I_{by})\sin^2\gamma_b\cos\theta_p+(I_{bx}-I_{bz})\cos^2\gamma_b\cos\theta_p\\
&+2m_bz_b^2\cos^2\gamma_b\cos\theta_p)\dot\gamma_b\dot\beta+(I_{bz}\sin\gamma_b\cos\gamma_b\sin\theta_p-I_{by}\cos\gamma_b\sin\gamma_b\sin\theta_p\\
&-(I_{bx}-I_{by})\sin\gamma_b\sin\theta_p\cos\gamma_b+(I_{bx}-I_{bz})\cos\gamma_b\sin\theta_p\sin\gamma_b)\dot\theta_p\dot\beta\\
&+m_p(-z_{wp}\cos\theta_pv_y+x_{wp}\sin\theta_pv_y\dot\beta)-m_bz_b\cos\gamma_b\cos\theta_pv_y\dot\beta-(-z_b^2m_b-I_{by}\\
&+I_{bz})\sin\gamma_b\cos\gamma_b\cos\theta_p\ddot\beta+(I_{py}+m_p(x_{wp}^2+z_{wp}^2)+I_{by}\cos^2\gamma_b+I_{bz}\sin^2\gamma_b\\
&+m_bz_b^2\cos^2\gamma_b)\ddot\theta_p+(m_bz_b\cos\gamma_b\cos\theta_p-m_p(x_{wp}\sin\theta_p-z_{wp}\cos\theta_p))\dot v_x\\
&+(I_{bz}\sin\gamma_b\cos\gamma_b-I_{by}\cos\gamma_b\sin\gamma_b+(I_{bx}-I_{by})\sin\gamma_b\cos\gamma_b\\
&-(I_{bx}-I_{bz})\cos\gamma_b\sin\gamma_b-2m_bz_b^2\cos\gamma_b\sin\gamma_b)\dot\theta_p\dot\gamma_b+T_l+T_r\\
&-m_bgz_b\sin\theta_p\cos\gamma_b-m_pg(x_{wp}\cos\theta_p+z_{wp}\sin\theta_p)=0
\end{aligned}
\tag{62}
$$

$$
\begin{aligned}
&m_bz_b\sin\gamma_b\ddot\beta+(m_b+m_p+2m_w+2I_y/r^2)\dot v_x+(m_bz_b\cos\gamma_b\cos\theta_p\\
&-m_p(x_{wp}\sin\theta_p-z_{wp}\cos\theta_p))\ddot\theta_p-2m_w\dot\beta v_y-m_p(\dot\beta v_y+x_{wp}\cos\theta_p\dot\theta_p^2\\
&+z_{wp}\sin\theta_p\dot\theta_p^2+(x_{wp}\cos\theta_p+z_{wp}\sin\theta_p)\dot\beta^2)-m_b(\dot\beta v_y+z_b\sin\theta_p\cos\gamma_b((\dot\gamma_b\\
&-\sin\theta_p\dot\beta)^2+(\cos\gamma_b\dot\theta_p+\sin\gamma_b\cos\theta_p\dot\beta)^2)+z_b\sin\gamma_b\sin\theta_p(\cos\gamma_b\dot\theta_p\\
&+\sin\gamma_b\cos\theta_p\dot\beta)(\sin\gamma_b\dot\theta_p-\cos\gamma_b\cos\theta_p\dot\beta)-z_b\cos\theta_p(\cos\gamma_b\cos\theta_p\dot\beta\dot\gamma_b\\
&-\sin\gamma_b\dot\gamma_b\dot\theta_p-(\dot\gamma_b-\sin\theta_p\dot\beta)(\sin\gamma_b\dot\theta_p-\cos\gamma_b\cos\theta_p\dot\beta)))-m_bz_b\sin\gamma_b\sin\theta_p\ddot\gamma_b\\
&-(r(T_l+T_r)+I_y\dot v_{s,l})+I_y\dot v_{s,r})/r^2=0
\end{aligned}
\tag{63}
$$

$$
\begin{aligned}
& m_b(z_b \sin\gamma_b(\sin^2\gamma_b \cos^2\theta_p + \sin^2\theta_p) + z_b \cos^2\gamma_b \sin\gamma_b \cos^2\theta_p)\dot{\beta}^2 \\
& +(-2m_b z_b \sin\gamma_b \sin\theta_p \dot{\gamma}_b + (m_b(2z_b \sin^2\gamma_b \cos\gamma_b \cos\theta_p + z_b \cos\gamma_b(-\sin^2\gamma_b \cos\theta_p \\
& + \cos^2\gamma_b \cos\theta_p + \cos\theta_p)) - m_p(-2z_{wp} \cos\theta_p + 2x_{wp} \sin\theta_p))\dot{\theta}_p + m_b v_x + m_p v_x \\
& +2m_w v_x)\dot{\beta} + (m_b z_b \sin\theta_p \cos\gamma_b + m_p(x_{wp} \cos\theta_p + z_{wp} \sin\theta_p))\ddot{\beta} - m_b z_b \cos\gamma_b \ddot{\gamma}_b \\
& +(m_b + m_p + 2m_w)\dot{v}_y
\end{aligned} \tag{64}
$$

$$
+m_b z_b \sin\gamma_b \dot{\gamma}_b^2 - F_{y,l} - F_{y,r} = 0 \tag{65}
$$

$$
-F_{x,l} - (I_{wy}\dot{v}_x - rT_l - I_{wy}v_{s,l} - I_{wy}w\ddot{\beta})/r^2 = 0 \tag{66}
$$

$$
(rT_r + I_{wy}v_{s,r} - I_{wy}\dot{v}_x - I_{wy}w\ddot{\beta})/r^2 - F_{x,r} = 0 \tag{67}
$$

$$
\begin{aligned}
&((I_{bx}-I_{by})\cos\gamma_b\cos^2\theta_p\sin\theta_p\sin\gamma_b-(I_{bx}-I_{bz})\sin\gamma_b\cos^2\theta_p\sin\theta_p\cos\gamma_b\\
&+(I_{by}-I_{bz})\sin\theta_p\sin\gamma_b\cos^2\theta_p\cos\gamma_b)\dot\beta^2+((I_{by}\sin\gamma_b\cos^2\theta_p\cos\gamma_b\\
&-I_{bz}\cos\gamma_b\cos^2\theta_p\sin\gamma_b-(I_{bx}-I_{by})\cos\gamma_b\cos^2\theta_p\sin\gamma_b+(I_{bx}\\
&-I_{bz})\sin\gamma_b\cos^2\theta_p\cos\gamma_b+2m_bz_b^2\sin\gamma_b\cos^2\theta_p\cos\gamma_b)\dot\gamma_b+(I_{bx}\sin\theta_p\cos\theta_p\\
&+(2(I_{px}-I_{pz}))\sin\theta_p\cos\theta_p-I_{by}\sin^2\gamma_b\cos\theta_p\sin\theta_p-I_{bz}\cos^2\gamma_b\cos\theta_p\sin\theta_p\\
&-m_p(x_{wp}\cos\theta_p+z_{wp}\sin\theta_p)(-2z_{wp}\cos\theta_p+2x_{wp}\sin\theta_p)+(I_{bx}\\
&-I_{by})\cos^2\gamma_b\cos\theta_p\sin\theta_p+(I_{bx}-I_{bz})\sin^2\gamma_b\cos\theta_p\sin\theta_p+(I_{by}\\
&-I_{bz})\sin\theta_p\cos^2\gamma_b\cos\theta_p-(I_{by}-I_{bz})\sin\theta_p\sin^2\gamma_b\cos\theta_p\\
&-m_bz_b(z_b\sin^2\gamma_b\cos\theta_p\sin\theta_p-\sin\theta_pz_b(\cos^2\gamma_b\cos\theta_p+\cos\theta_p)))\dot\theta_p\\
&+m_p(x_{wp}\cos\theta_p+z_{wp}\sin\theta_p)v_x-m_bz_b(-\sin\theta_p\cos\gamma_bv_x+\sin\gamma_bv_y))\dot\beta+(I_{bz}\\
&+I_{pz}+2ixz+2m_ww^2+2I_yw^2/r^2+(I_{by}-I_{bz})\sin^2\gamma_b+m_p(x_{wp}\cos\theta_p\\
&+z_{wp}\sin\theta_p)^2+m_bz_b^2(\sin^2\gamma_b\cos^2\theta_p+\sin^2\theta_p)+\sin^2\theta_p(I_{bx}+I_{px}-I_{bz}-I_{pz}\\
&-(I_{by}-I_{bz})\sin^2\gamma_b))\ddot\beta-(z_b^2m_b+I_{bx})\sin\theta_p\ddot\gamma_b-(-z_b^2m_b-I_{by}
\end{aligned}
\tag{68}
$$

$$
\begin{aligned}
&+I_{bz})\sin\gamma_b\cos\gamma_b\cos\theta_p\ddot\theta_p+wI_y(\dot v_{s,l})/r^2-wI_y(\dot v_{s,r})/r^2+m_bz_b\sin\gamma_b\dot v_x\\
&+(m_bz_b\sin\theta_p\cos\gamma_b+m_p(x_{wp}\cos\theta_p+z_{wp}\sin\theta_p))\dot v_y+(-I_{by}\sin^2\gamma_b\cos\theta_p\\
&-I_{bz}\cos^2\gamma_b\cos\theta_p-(I_{bx}-I_{by})\cos^2\gamma_b\cos\theta_p-(I_{bx}-I_{bz})\sin^2\gamma_b\cos\theta_p\\
&-2m_bz_b^2\sin^2\gamma_b\cos\theta_p)\dot\theta_p\dot\gamma_b+(-(I_{by}-I_{bz})\sin\theta_p\cos\gamma_b\sin\gamma_b\\
&-m_bz_b^2\sin\theta_p\cos\gamma_b\sin\gamma_b)\dot\theta_p^2+w(T_l-T_r)/r=0
\end{aligned}
\tag{69}
$$

$$
\begin{aligned}
&(-(I_{by}-I_{bz})\sin\gamma_b\cos^2\theta_p\cos\gamma_b-m_bz_b^2\sin\gamma_b\cos^2\theta_p\cos\gamma_b)\dot\beta^2\\
&+((-(I_{by}-I_{bz})\cos^2\gamma_b\cos\theta_p+(I_{by}-I_{bz})\sin^2\gamma_b\cos\theta_p-m_bz_b^2(\cos^2\gamma_b\cos\theta_p\\
&-\sin^2\gamma_b\cos\theta_p+\cos\theta_p)-I_{bx}\cos\theta_p)(\dot\theta_p)+m_bz_b(\sin\gamma_b\sin\theta_pv_y-\cos\gamma_bv_x))\dot\beta\\
&-(z_b^2m_b+I_{bx})\sin\theta_p\ddot\beta+(z_b^2m_b+I_{bx})\ddot\gamma_b-m_bz_b\sin\gamma_b\sin\theta_p\dot v_x-m_bz_b\cos\gamma_b(\dot v_y)\\
&+((I_{by}-I_{bz})\cos\gamma_b\sin\gamma_b+m_bz_b^2\cos\gamma_b\sin\gamma_b)\dot\theta_p^2-m_bgz_b\sin\gamma_b\cos\theta_p=0
\end{aligned}
\tag{70}
$$

4.2.2 Roll stability with a pitching rider

When the passenger leans forward, the height of the center of mass decreases slightly and moves forward. This effects the normal forces. Figure 73 illustrates such a leaning passenger.

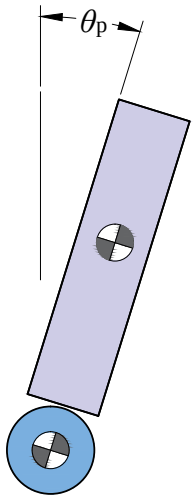

Figure 73: System with a rider leaning forward.

A forward lean also increases the acceleration of the center of mass. As the rider leans forward during a turn, the location of the center of mass moves away from the circular path that the midpoint between the wheels follow. Therefore, the acceleration of this point is no longer directed in the same direction as the midpoint between the wheels. Instead, it has two components, one in the direction of the wheel axle and another one perpendicular to it. Only the acceleration component in the axle direction can generate a torque that makes the vehicle unstable in the roll direction and that can be compensated for by the normal forces N_l and N_r. This situation is shown in Figure 74.

By performing a balance of forces, as in the previous sections, the normal forces

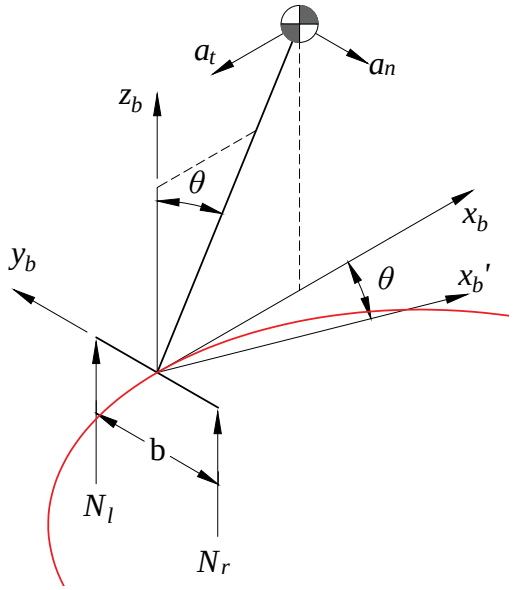

Figure 74: System with a rider leaning forward.

were found. The forces between the wheels and the ground are:

$$N_{lv} = \frac{mg + m_v g}{2} + \frac{(m + m_v)v^2 r}{dr_g} + \frac{mv^2 H_{cm} \cos\theta_p}{dr_g} \tag{71}$$

$$N_{rv} = \frac{mg + m_v g}{2} - \frac{(m + m_v)v^2 r}{dr_g} - \frac{mv^2 H_{cm} \cos\theta_p}{dr_g} \tag{72}$$

The normal forces between the load and the vehicle on each side are:

$$N_l = \frac{mg}{2} + \frac{mv^2 H_{cm} \cos\theta_p}{br_g} \tag{73}$$

$$N_r = \frac{mg}{2} - \frac{mv^2 H_{cm} \cos\theta_p}{br_g} \tag{74}$$

Note that in all cases, the last term of these expressions is multiplied by a $\cos\theta_p$ factor. As θ_p increases, the magnitude of this value becomes smaller. This means that, during a turn, the normal forces on the right side decrease less with a forward-leaning rider when compared with the upright position. Essentially, leaning forward increases the roll stability by reducing the height of the center of mass.

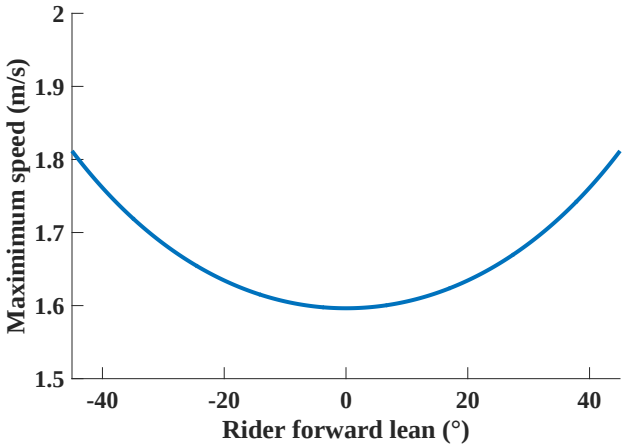

Figure 75: Lean angle limits for a 1 m radius turn on a Segway i2.

4.2.2.1 Rider pitching on a Segway i2

Figure 75 shows the maximum speed of the vehicle while traveling along a 1m radius turn for different rider forward-lean (pitch) angles. Note that as the pitch angle increases, the vehicle is able to travel the curve at higher speeds without rolling over. However, for a real rider operating such a transporter, the pitching angle is limited to perhaps 15°. Within this range the maximum turning speed remains approximately constant. However, if for some reason the vehicle loses pitch stability and falls forward during a turn, this turn can occur at higher speeds than expected.

4.2.3 Roll stability during simultaneous pitching and rolling of the passenger

A passenger can obviously lean forward and sideways simultaneously. The pitch angle θ and the roll angle γ are shown in the free body diagram of the passenger in Figure 76. The pitch angle is measured around the y_b axis which points toward the center of the curved path that the vehicle is following. The roll angle is measured around the x'_b axis which is fixed to the person and rotates as the person pitches forward.

When the passenger leans forward, the center of mass translates towards the inside of the curved path followed by the vehicle, and its height decreases. As a result, the

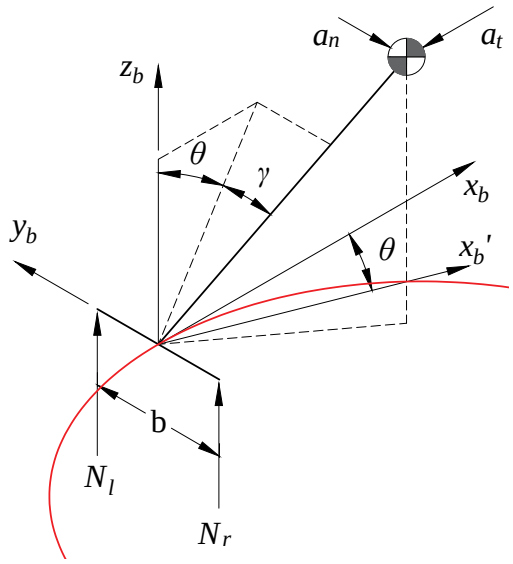

Figure 76: Free body diagram of a passenger leaning forward and sideways.

acceleration of the center of mass has two components in the reference frame of the vehicle. As in the previous section, only the acceleration component in the y_b direction, a_n, generates a torque that affects the normal forces N_l and N_r.

The forces between the vehicle and the ground are:

$$N_{lv} = \frac{mg + m_v g}{2} + \frac{(m + m_v)v^2 r}{dr_g} - \frac{mgH_{cm}\sin\gamma}{d} - \frac{mv^2 H_{cm} r \sin\gamma}{dr_g^2} - \frac{mv^2 H_{cm}^2 \sin\gamma\cos\gamma}{dr_g^2}\cos\theta + \frac{mv^2 H_{cm}\cos\gamma}{dr_g}\cos\theta \tag{75}$$

$$N_{rv} = \frac{mg + m_v g}{2} - \frac{(m + m_v)v^2 r}{dr_g} + \frac{mgH_{cm}\sin\gamma}{d} + \frac{mv^2 H_{cm} r \sin\gamma}{dr_g^2} + \frac{mv^2 H_{cm}^2 \sin\gamma\cos\gamma}{dr_g^2}\cos\theta - \frac{mv^2 H_{cm}\cos\gamma}{dr_g}\cos\theta \tag{76}$$

The normal forces between the passenger and the vehicle on each side are:

$$N_r = \frac{mg}{2} + \frac{mgH_{cm}\sin\gamma}{b} - \frac{mv^2 H_{cm}\cos\gamma}{br_g}\cos\theta + \frac{mv^2 H_{cm}^2 \sin\gamma\cos\gamma}{br_g^2}\cos\theta \tag{77}$$

$$N_l = \frac{mg}{2} - \frac{mgH_{cm}\sin\gamma}{b} + \frac{mv^2 H_{cm}\cos\gamma}{br_g}\cos\theta - \frac{mv^2 H_{cm}^2 \sin\gamma\cos\gamma}{br_g^2}\cos\theta \qquad (78)$$

These expressions for the normal forces between the wheels and the ground are very similar to the ones found for the case when the person leans only sideways. The primary difference in this case is that the terms that contain v^2 are multiplied by $\cos\theta$. This means that the effect of the turn is diminished in comparison with only sideways leaning.

Dynamic and inertial effects will be further analyzed to understand the effect that each particular motion and system parameter has on the lateral stability of the vehicle.

4.2.4 Non-inertial Dynamic effects

In this section, the normal forces between the rider and vehicle are analyzed. The normal force between the vehicle and the ground is:

$$N_{rv} = \frac{m_v g}{2} - \frac{(m+m_v)v^2 r}{dr_g} + \frac{N_l + N_r}{2d} + \frac{N_r - N_l}{2d} \qquad (79)$$

When the person leans to accelerate/decelerate and turn the vehicle at the same time, simultaneous rotations occur around two axes. These rotations are linked to tangential and centripetal accelerations that can have an effect on the normal forces and the roll stability of both the person and the vehicle. Figure 77 shows the tangential and radial accelerations of the center of mass of the passenger with respect to the midpoint of the vehicle base. In the figure, neither the centripetal acceleration caused by the rotation of the vehicle as it follows a curved path, nor the Coriolis acceleration caused by the relative motion of the body are shown.

The relative speed of the center of mass with respect to the vehicle is:

$$\vec{v}_{b/v} = \vec{\omega}_{b/v} \times \vec{r}_{b/v} \qquad (80)$$

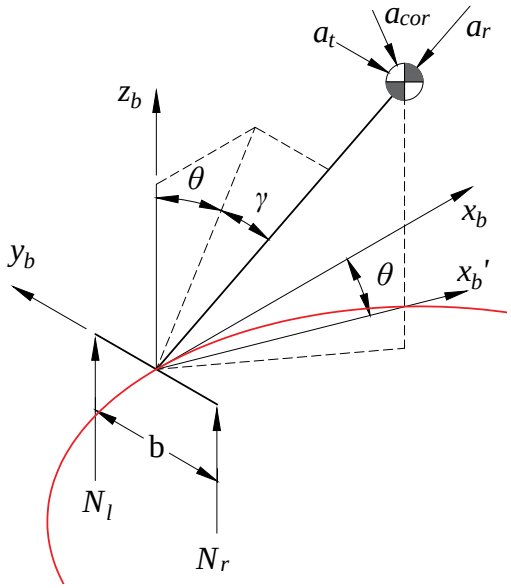

Figure 77: Free body diagram of a rider leaning forward and sideways - dynamic effects.

The tangential and centripetal accelerations of the center of mass of the rider with respect to the vehicle are given by:

$$\vec{a}_t = \vec{\alpha}_{b/v} \times \vec{r}_{b/v} \tag{81}$$

and

$$\vec{a}_r = \vec{\omega}_{b/v} \times (\vec{\omega}_{b/v} \times \vec{r}_{b/v}) \tag{82}$$

where the angular speed and acceleration of the rider with respect to the vehicle are:

$$\vec{\omega}_{b/v} = \dot{\gamma}\cos\theta\vec{x}_b + \dot{\theta}\vec{y}_b - \dot{\gamma}\sin\theta\vec{z}_b \tag{83}$$

$$\vec{\alpha}_{b/v} = (-\dot{\theta}\dot{\gamma}\sin\theta + \ddot{\gamma}\cos\theta)\vec{x}_b + \ddot{\theta}\vec{y}_b + (-\dot{\theta}\dot{\gamma}\cos\theta - \ddot{\gamma}\sin\theta)\vec{z}_b \tag{84}$$

The relative position of the center of mass with respect to the vehicle is:

$$\vec{r}_{b/v} = H_{cm}\sin\theta\cos\gamma\vec{x}_b - H_{cm}\sin\gamma\vec{y}_b + H_{cm}\cos\gamma\cos\theta\vec{z}_b \tag{85}$$

It is evident that because the angular speed and acceleration are such complex expressions, the full expressions of (81) and (82) will also be very complex.

The position of the center of mass with respect to the Newtonian reference frame is:

$$\vec{r}_b = H_{cm}\sin\theta\cos\gamma\vec{x}_b + (r_g - H_{cm}\sin\gamma)\vec{y}_b + H_{cm}\cos\gamma\cos\theta\vec{z}_b \tag{86}$$

The speed of the center of mass is:

$$\vec{v}_b = \vec{v}_{b/v} + \frac{v}{r_g}(-\vec{z}) \times \vec{r}_b \tag{87}$$

where v/r_g is the angular speed of the reference frame attached to the vehicle.

The acceleration of the center of mass is:

$$\vec{a}_b = \vec{a}_t + \vec{a}_r + \frac{v}{r_g}(-\vec{z}) \times \left[\frac{v}{r_g}(-\vec{z}) \times \vec{r}_b\right] + 2\frac{v}{r_g}(-\vec{z}) \times \vec{v}_{b/v} \tag{88}$$

Note that the third term in (88) does not depend on the relative motion between the body and the vehicle. This term represents the total acceleration of the center of mass for the static rider cases considered in the previous sections.

The above expression can be rewritten as:

$$\vec{a}_b = \vec{a}_t + \vec{a}_r + \vec{a}_c + \vec{a}_{cor} \tag{89}$$

where the acceleration due to the vehicle turning is:

$$\vec{a}_c = \frac{v}{r_g}(-\vec{z}) \times \left[\frac{v}{r_g}(-\vec{z}) \times \vec{r}_b\right] \tag{90}$$

and the Coriolis acceleration is:

$$\vec{a}_{cor} = 2\frac{v}{r_g}(-\vec{z}) \times \vec{v}_{b/v} \tag{91}$$

The other three terms will generate new terms in the expression for the normal force. This force can be found by using D'Alembert principle to balance the moments

around the contact point between the vehicle and the rider on the left side of the platform.

The position vector of the center of mass with respect to the left side of the platform is:

$$\vec{r}_{b/lf} = H_{cm}\sin\theta\cos\gamma\vec{x}_b - (0.5b - H_{cm}\sin\gamma)\vec{y}_b + H_{cm}\cos\gamma\cos\theta\vec{z}_b \tag{92}$$

The sum of moments about the left platform support point is:

$$-b\vec{y}_b \times N_r + r_{b/lf} \times (-mg)\vec{z}_b + r_{b/lf} \times (-\vec{a}_b) = 0 \tag{93}$$

The roll stability is determined by the sum of moments around the x axis. Taking this into account, (93) can be solved for N_r as follows:

$$N_r = \frac{1}{b}\left[r_{b/lf} \times (-mg)\vec{z}_b + r_{b/lf} \times (-m\vec{a}_b)\right]_x = 0 \tag{94}$$

By expanding a_b and using the distributive property of the cross product operator:

$$\begin{aligned} N_r = \frac{1}{b}[r_{b/lf} \times (-mg)\vec{z}_b + r_{b/lf} \times (-m\vec{a}_t) + r_{b/lf} \times (-m\vec{a}_n) + \\ r_{b/lf} \times (-m\vec{a}_c) + r_{b/lf} \times (-m\vec{a}_{cor})]_x = 0 \end{aligned} \tag{95}$$

This equation can be rewritten as:

$$N_r = N_{r,g} + N_{r,c} + N_{r,t} + N_{r,r} + N_{r,cor} \tag{96}$$

where,

$$N_{r,g} = \frac{mg}{2} + \frac{mH_{cm}g\sin\gamma}{b} \tag{97}$$

$$N_{r,c} = \frac{mH_{cm}^2\cos\gamma\sin\gamma\cos\theta v^2}{br_g^2} - \frac{mH_{cm}\cos\theta\cos\gamma v^2}{br_g} \tag{98}$$

$$N_{r,t} + N_{r,r} = \left(\frac{2mH_{cm}^2 \sin\theta}{b} - \frac{2mH_{cm}^2 \cos^2\gamma \sin\theta}{b} + mH_{cm} \sin\theta \sin\gamma\right)\dot{\gamma}\dot{\theta} - \frac{mH_{cm} \cos\theta \cos\gamma \dot{\gamma}^2}{2} - \left(\frac{mH_{cm} \cos\theta \sin\gamma}{2} + \frac{mH_{cm}^2 \cos\theta}{b}\right)\ddot{\gamma} - \left(\frac{mH_{cm}^2 \sin\gamma \sin\theta \cos\gamma}{b} + \frac{mH_{cm} \sin\theta \cos\gamma}{2}\right)\ddot{\theta} - \left(\frac{mH_{cm}^2 \cos\theta \sin\gamma \cos\gamma}{b} + \frac{mH_{cm} \cos\theta \cos\gamma}{2}\right)\dot{\theta}^2 \tag{99}$$

$$N_{r,cor} = -\frac{2mH_{cm}^2 \cos^2\gamma \cos^2\theta \dot{\theta} v}{br_g} + \frac{2mH_{cm}^2 \sin\gamma \sin\theta \cos\gamma \cos\theta \dot{\gamma} v}{br_g} \tag{100}$$

Each term above is associated with the corresponding acceleration in (89). Note that the first two terms in the above expression are those present when the body is static, while the last three terms are the ones that occur when the passenger moves with respect to the vehicle. For the left side support of the passenger, the forces are:

$$N_{l,g} = \frac{mg}{2} - \frac{mH_{cm} g \sin\gamma}{b} \tag{101}$$

$$N_{l,c} = -\frac{mH_{cm}^2 \cos\gamma \sin\gamma \cos\theta v^2}{br_g^2} + \frac{mH_{cm} \cos\theta \cos\gamma v^2}{br_g} \tag{102}$$

$$N_{l,t} + N_{l,r} = \left(-\frac{2mH_{cm}^2 \sin\theta}{b} + \frac{2mH_{cm}^2 \cos^2\gamma \sin\theta}{b} + mH_{cm} \sin\theta \sin\gamma\right)\dot{\gamma}\dot{\theta} - \frac{mH_{cm} \cos\theta \cos\gamma \dot{\gamma}^2}{2} + \left(\frac{mH_{cm} \cos\theta \sin\gamma}{2} + \frac{mH_{cm}^2 \cos\theta}{b}\right)\ddot{\gamma} - \left(-\frac{mH_{cm}^2 \sin\gamma \sin\theta \cos\gamma}{b} + \frac{mH_{cm} \sin\theta \cos\gamma}{2}\right)\ddot{\theta} + \left(\frac{mH_{cm}^2 \cos\theta \sin\gamma \cos\gamma}{b} + \frac{mH_{cm} \cos\theta \cos\gamma}{2}\right)\dot{\theta}^2 \tag{103}$$

$$N_{l,cor} = \frac{2mH_{cm}^2 \cos^2\gamma \cos^2\theta \dot{\theta} v}{br_g} - \frac{2mH_{cm}^2 \sin\gamma \sin\theta \cos\gamma \cos\theta \dot{\gamma} v}{br_g} \tag{104}$$

In this section, the analysis is limited to the last three terms because the first two terms were covered in the previous sections. Furthermore, $N_{r,t}$ and $N_{r,n}$ produce a very complex expression. Therefore, to understand their effect on the normal forces

between the vehicle and the person, the analysis will be limited to studying each rotation motion of the rider independently from one another.

4.2.4.1 Sideways leaning

Figure 78 shows a free body diagram of the rider leaning sideways and the acceleration components relative to the vehicle. As the angle γ increases, there is a centripetal acceleration directed from the center of mass to the midpoint between the left and right support. This generates a fictitious force that acts in the opposite direction. When taking the sum of moments about the left support, this fictitious centripetal force causes a negative moment in the direction of the negative x_b axis and reduces the normal force on the right support as a result. Note that while leaning towards the turn makes the vehicle more stable, a sudden lean (at a very high angular speed) might negate this advantage.

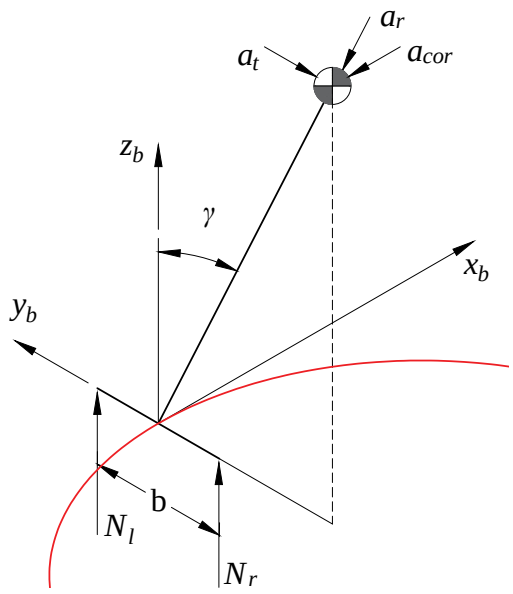

Figure 78: Free body diagram of a person leaning sideways - dynamic effects.

The force produced by the tangential acceleration as γ increases acts in a direction perpendicular to the fictitious centripetal force on the $y_b z_b$ plane opposite the arrow

that represents a_t in Figure 78. When taking moments about the left platform support, this force also generates a torque in the direction of the negative x_b axis. This means that a very high angular acceleration for γ can also decrease the roll stability of the system by reducing the normal force on the right support.

Finally, the Coriolis acceleration acts in the direction of the negative x_b axis which generates a fictitious force in the opposite direction. Because this force is parallel to the x_b direction, it does not generate a moment that affects the roll stability of the rider. Note that this is only true when the rider is not leaning forward. When forward leaning starts moving the center of mass forward, it is no longer on the $y_b z_b$ plane. Then, the fictitious Coriolis force generates a moment associated with the increased rate of γ that increases the stability of the rider by generating a moment in the direction of the x_b axis.

4.2.4.2 Forward leaning

Figure 79 shows a free body diagram of the rider leaning forward and the acceleration components relative to the vehicle.

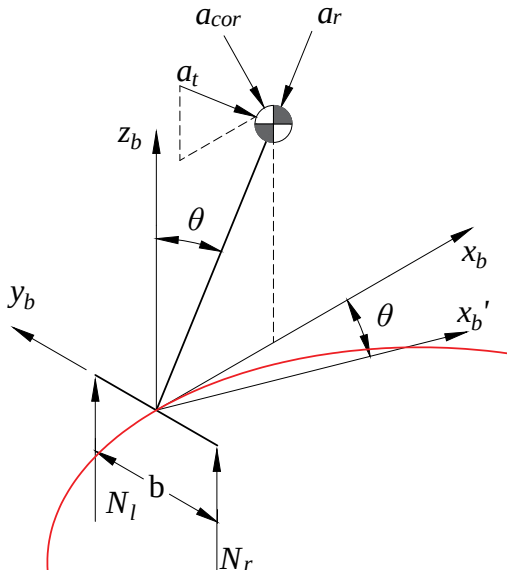

Figure 79: Free body diagram of a rider leaning forward - dynamic effects.

As the rider lean angle, θ, increases, the rotation of the center of mass of the body experiences a centripetal acceleration a_r directed toward the origin. This can be treated as a fictitious centrifugal force acting toward the positive $x_b z_b$ quadrant. When taking the sum of moments about the left platform support, this centrifugal force acts in the negative x_b direction, which reduces the normal force on the right support.

A tangential acceleration a_t, perpendicular to a_r, is associated with the angular acceleration of θ. When the angular acceleration is positive, a fictitious tangential force is generated on the vehicle that acts in the opposite direction as the one shown in Figure 79. When taking moments about the left platform support point, this force generates a torque in the negative x_b direction, as does N_r.

Note that because these forces are contained on the $x_b z_b$ plane they have the effect of reducing the normal force on both sides of the vehicle. Due to this, the vehicle is more prone to tipping over because the available normal force on the inside of the turn is reduced.

Finally, the relative rotation of the rider with respect to the vehicle generates a Coriolis acceleration. When $\dot{\theta}$ is positive, the Coriolis acceleration is directed towards the negative y_b axis. The associated inertial force acts along the y_b direction. When taking moments about the left support, this force generates a torque in the negative x_b direction and makes the vehicle more prone to tipping over. Therefore, leaning forward suddenly can also make the vehicle more unstable while making a turn.

4.2.4.3 Simultaneous forward and sideways leaning

When the passenger leans in both directions, three terms containing $\dot{\gamma}\dot{\theta}$ appear in the expression for the normal force. The sign of these terms together will depend on both lean angles and their rates. These terms are given by:

$$\left[\frac{2mH_{cm}^2 \sin\theta}{b} - \frac{2mH_{cm}^2 \cos^2\gamma \sin\theta}{b} + mH_{cm} \sin\theta \sin\gamma\right] \dot{\gamma}\dot{\theta} \tag{105}$$

It is not immediately evident which of these terms has the greatest effect on the normal force.

4.2.5 Inertial effects

When a rigid body model of the rider is considered, the effect of the new terms in the angular momentum appear in the expressions for the normal forces. The resulting expressions in this case contain additional components related to the angular speed and acceleration of the rider. In addition, when taking moments about the x-axis of the vehicle frame, the moments of inertia of the rider need to be transformed to the vehicle coordinate system and complex functions of the angle and angular rates arise. In this section, the inertial effects of the forward leaning and sideways leaning motions are analyzed separately.

The resulting normal force on the right wheel is

$$N_{r,total} = N_r + N_{r,inertia} \tag{106}$$

N_r is given by (96) and $N_{inertia}$ is:

$$\begin{aligned} N_{r,inertia} = \frac{1}{b}[&-I_{b,xx}\alpha_x + I_{b,xy}\alpha_y + I_{b,xz}\alpha_z + I_{b,yz}\omega_y^2 - I_{b,yz}\omega_z^2 \\ &+I_{b,xz}\omega_x\omega_y - I_{b,zz}\omega_y\omega_z - I_{b,xy}\omega_x\omega_z + I_{b,yy}\omega_y\omega_z] \end{aligned} \tag{107}$$

where the subindices refer to the vehicle coordinate system, α is the angular acceleration, and ω is the angular speed of the rider.

For the left side support,

$$N_{l,inertia} = -N_{r,inertia} \tag{108}$$

The passenger inertias in the vehicle frame are expressed in terms of the principal inertias in the body frame as follows:

$$
\begin{aligned}
I_{b,xx} &= I_{b,x} - \sin^2\theta[I_{b,x} - I_{b,z} - (I_{b,y} - I_{b,z})\sin^2\gamma] \\
I_{b,xy} &= \sin\theta\sin\gamma\cos\gamma(I_{b,y} - I_{b,z}) \\
I_{b,xz} &= -\sin\theta\cos\theta[I_{b,x} - I_{b,z} - (I_{b,y} - I_{b,z})\sin^2\gamma] \\
I_{b,yy} &= \cos^2\gamma I_{b,y} + \sin^2\gamma I_{b,z} \\
I_{b,yz} &= \sin\gamma\cos\theta\cos\gamma(I_{b,y} - I_{b,z}) \\
I_{b,zz} &= \sin^2\theta I_{b,x} + \sin^2\gamma\cos^2\theta I_{b,y} + \cos^2\gamma\cos^2\theta I_{b,z}
\end{aligned} \tag{109}
$$

The angular speed expressed in terms of the forward and sideways leaning angles as:

$$
\vec{\omega} = \begin{bmatrix} \cos\theta\dot{\gamma} \\ \dot{\theta} \\ \dfrac{v}{r_g} - \sin\theta\dot{\gamma} \end{bmatrix} \tag{110}
$$

Similary, the angular acceleration is given by:

$$
\vec{\alpha} = \begin{bmatrix} \cos\theta\ddot{\gamma} - \sin\theta\dot{\gamma}\dot{\theta} \\ \ddot{\theta} - \cos\theta\dot{\gamma}\dfrac{v}{r_g} \\ -\cos\theta\dot{\gamma}\dot{\theta} - \dfrac{\dot{v}}{r_g} - \sin\theta\ddot{\gamma} \end{bmatrix} \tag{111}
$$

4.2.5.1 Sideways leaning

When the rider leans sideways and the vehicle is traveling at a constant speed along an arc path, the angular speed becomes:

$$
\vec{\omega} = \begin{bmatrix} \dot{\gamma} \\ 0 \\ \dfrac{v}{r_g} \end{bmatrix} \tag{112}
$$

and the angular acceleration is:

$$\vec{\alpha} = \begin{bmatrix} \ddot{\gamma} \\ -\dot{\gamma}\dfrac{v}{r_g} \\ 0 \end{bmatrix} \tag{113}$$

The body inertias in the vehicle frame then become:

$$\begin{aligned} I_{b,xx} &= I_{b,x} \\ I_{b,xy} &= 0 \\ I_{b,xz} &= 0 \\ I_{b,yy} &= \cos^2\gamma I_{b,y} + \sin^2\gamma I_{b,z} \\ I_{b,yz} &= \sin\gamma\cos\gamma(I_{b,y} - I_{b,z}) \\ I_{b,zz} &= \sin^2\gamma I_{b,y} + \cos^2\gamma I_{b,z} \end{aligned} \tag{114}$$

The resulting normal force associated with the angular rotation of the rider results in the following expression:

$$N_{inertia} = \frac{1}{b}[-I_{b,xx}\alpha_x - I_{b,yz}\omega_z^2] \tag{115}$$

Substituting (112), (113) and (114) into the above expression results in:

$$N_{inertia} = \frac{1}{b}[-I_{b,x}\ddot{\gamma} - \sin\gamma\cos\gamma(I_{b,y} - I_{b,z})(\frac{v}{r_g})^2] \tag{116}$$

The first term of this expression indicates that leaning sideways very suddenly can reduce the normal force on the right side of the rider making him more prone to fall. This situation can occur when a rider tries to avoid an obstacle in an abrupt manner. The second term becomes larger as the leaning angle approaches $\gamma = \frac{\pi}{4}$ and decreases for larger angles. Its effect depends on how fast the vehicle is going and how large the inertia about the y-axis is when compared to the inertia about the z-axis. For a

typical human, the y-axis inertia is large, so the second term would also reduce the normal force.

4.2.5.2 Forward leaning

When the rider leans forward instead of sideways, and the vehicle travels at a constant speed along an arc, the angular speed is given by:

$$\vec{\omega} = \begin{bmatrix} 0 \\ \dot{\theta} \\ \dfrac{v}{r_g} \end{bmatrix} \tag{117}$$

and the angular acceleration is:

$$\vec{\alpha} = \begin{bmatrix} 0 \\ \ddot{\theta} \\ 0 \end{bmatrix} \tag{118}$$

The inertias of the rider in the vehicle frame then become:

$$\begin{aligned} I_{b,xx} &= I_{b,x} - \sin^2\theta[I_{b,x} - I_{b,z}] \\ I_{b,xy} &= 0 \\ I_{b,xz} &= -\sin\theta\cos\theta[I_{b,x} - I_{b,z}] \\ I_{b,yy} &= I_{b,y} \\ I_{b,yz} &= 0 \\ I_{b,zz} &= \sin^2\theta I_{b,x} + \cos^2\theta I_{b,z} \end{aligned} \tag{119}$$

The resulting normal force associated to the angular rotation is:

$$N_{inertia} = \frac{1}{b}[-I_{b,zz}\omega_y\omega_z + I_{b,yy}\omega_y\omega_z] \tag{120}$$

Substituting (117), (118) and (119) into the above expression results in:

$$N_{inertia} = \frac{1}{b}\left[-(\sin^2\theta I_{b,x} + \cos^2\theta I_{b,z})\dot{\theta}\frac{v}{r_g} + I_{b,y}\dot{\theta}\frac{v}{r_g}\right] \tag{121}$$

which can be rewritten as:

$$N_{inertia} = \frac{1}{b}\left[-(\sin^2\theta(I_{b,x} - I_{b,y}) + \cos^2\theta(I_{b,z} - I_{b,y}))\dot{\theta}\frac{v}{r_g}\right] \tag{122}$$

From this expression it is evident that the sign depends on the relation between the body moments of inertia. It can be assumed that, for a person, the inertias around the x and y axes are similar, so the first term should be relatively small. However, the inertia around the z axis is smaller, so the second term is less significant. Considering this, if the the rider leans forward, the normal force is reduced as long as he is tilting at a non zero angular rate. Faster tilting rates cause a larger reduction of the force. However, this depends on the tilting angle. As the pitch is increased the cosine term becomes smaller.

4.2.5.3 Effects of the wheel inertias

In this section, the effect of the rotation of the wheels around the y axis is studied. Figure 80 shows the angular momentum of the wheel H_w and the direction of its derivative as the vehicle follows a circular path. As seen in the figure, the rate of change of the angular momentum generates a torque around the x_b axis that has a direct effect on the normal forces of the wheels.

Each wheel speed has a different value because, while the vehicle travels along an arc, each wheel has to travel a different distance. The speed of each wheel, v_l and v_r is given by:

$$\begin{aligned} v_l &= v + \frac{b}{2}\frac{v}{r_g} \\ v_r &= v - \frac{b}{2}\frac{v}{r_g} \end{aligned} \tag{123}$$

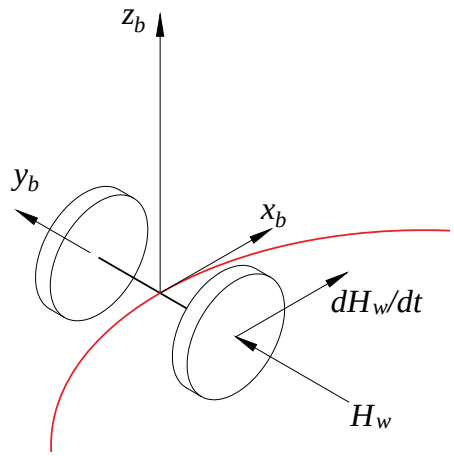

Figure 80: Moment generated by the inertia of the wheels.

The angular velocity of each wheel is given by:

$$\begin{aligned} \vec{\omega}_l &= \frac{v_l}{r_w}\vec{y}_b \\ \vec{\omega}_r &= \frac{v_r}{r_w}\vec{y}_b \end{aligned} \tag{124}$$

The angular velocity of the vehicle frame is:

$$\vec{\Omega} = \frac{v}{r_g}\vec{z}_b \tag{125}$$

The angular momentum of each of the wheels H_w is given by:

$$\begin{aligned} \vec{H}_l &= I_{wy} \cdot \vec{\omega}_l \\ \vec{H}_r &= I_{wy} \cdot \vec{\omega}_r \end{aligned} \tag{126}$$

The rate of change of the angular momentum of each of the wheels is:

$$\begin{aligned} \frac{d\vec{H}_l}{dt} &= \vec{\Omega} \times I_{wy} \cdot \vec{\omega}_l \\ \frac{d\vec{H}_r}{dt} &= \vec{\Omega} \times I_{wy} \cdot \vec{\omega}_r \end{aligned} \tag{127}$$

The following system of equations provides the normal forces on each side:

$$\begin{aligned} \frac{d\vec{H}_l}{dt} + \frac{d\vec{H}_r}{dt} &= \frac{b}{2}(N_{l,wheel} - N_{r,wheel}) \\ m_v g + mg &= N_{l,wheel} + N_{r,wheel} \end{aligned} \tag{128}$$

The normal force on the right side of the vehicle associated with the wheel inertias is given by:

$$N_{r,wheel} = -\frac{I_{wy} v^2}{r_g^2 r_w} \left(\frac{b + 2r_g}{b r_g} \right) \tag{129}$$

This component of the normal force becomes more negative at higher speeds, smaller wheel radius, and smaller curve radius.

4.3 Dynamic simulation of turning motions

Although the preceding results can predict some limits on the operating parameters of the person-vehicle system, do not take fully take into account the influence of the feedback controller or the forces between the wheel and the ground. In this section, the dynamic equations from Chapter 3 are used to simulate turning motions on a self balancing transporter that can experience wheel slip both in the longitudinal and transversal direction of the wheel plane.

4.3.1 Simulation Results

A series of left turns (positive yaw rate) were simulated to investigate which combinations of turning rates and forward speeds result in roll instability. These simulations best describe the turning motion of a Segway by an inexperienced or surprised operator because the passenger is modeled as a lumped mass on top of the Segway platform. The turning rate in these simulations was specified as a ramp input in the desired yaw rate parameter via the yaw angle control law (3). The relation between the handlebar roll angle and the yaw rate was found in previous studies and is reproduced here in Figure 81 [8]. Recall that on the Segway i2, the desired yaw rate is specified by the rider through use of the handlebar roll angle. The slope of the input ramp was set to 64.45°/s, which was the maximum slope measured during those previous experiments [8].

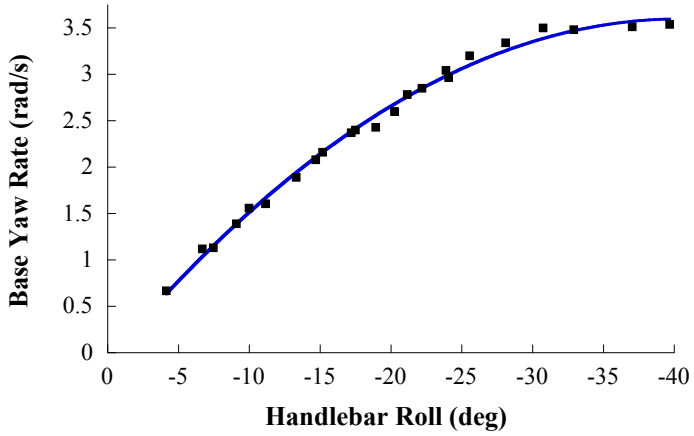

Figure 81: Handlebar roll and yaw rate responses during the spinning test [8].

In order to predict whether or not a roll instability will occur during a left turn, it is necessary to know the magnitude of the normal force between the left wheel and the ground. This force is given by the following expression:

$$
\begin{aligned}
F_{nl} = {} & g m_w + 0.5 g m_p - 0.5 \Big\{ I_{py} \dot{\beta} \dot{\theta}_p + I_{wy} \dot{\beta} \dot{\theta}_l + I_{wy} \dot{\beta} \dot{\theta}_r + \\
& 2 m_w r v \dot{\beta} - m_p r \Big[2 x_{wp} \sin\theta_p \dot{\beta} \dot{\theta}_p - v \dot{\beta} - x_{wp} \cos\theta_p \ddot{\beta} - z_{wp} \\
& \left(2 \cos\theta_p \dot{\beta} \dot{\theta}_p + \sin\theta_p \ddot{\beta} \right) \Big] - \cos\theta_p \Big[I_{pz} \cos\theta_p \dot{\beta} \dot{\theta}_p - m_p w \\
& \left(z_{wp} \dot{\theta}_p^2 + x_{wp} \ddot{\theta}_p \right) - I_{px} \left(\cos\theta_p \dot{\beta} \dot{\theta}_p + \sin\theta_p \ddot{\beta} \right) - m_p z_{wp} \\
& \left(v \dot{\beta} + x_{wp} \cos\theta_p \ddot{\beta} + z_{wp} \left(2 \cos\theta_p \dot{\beta} \dot{\theta}_p + \sin\theta_p \ddot{\beta} \right) \right) \Big] - \\
& \sin\theta_p \Big[I_{px} \sin\theta_p \dot{\beta} \dot{\theta}_p + m_p w \left(x_{wp} \dot{\theta}_p^2 - z_{wp} \ddot{\theta}_p \right) - I_{pz} (\sin\theta_p \\
& \dot{\beta} \dot{\theta}_p - \cos\theta_p \ddot{\beta} \Big) - m_p x_{wp} \left(2 x_{wp} \sin\theta_p \dot{\beta} \dot{\theta}_p - v \dot{\beta} - x_{wp} \right. \\
& \left. \cos\theta_p \ddot{\beta} - z_{wp} \left(4 \cos\theta_p \dot{\beta} \dot{\theta}_p + \sin\theta_p \ddot{\beta} \right) \right) \Big] \Big\} / w
\end{aligned}
\tag{130}
$$

Contact between the left wheel and the ground is lost when this normal force decreases to zero.

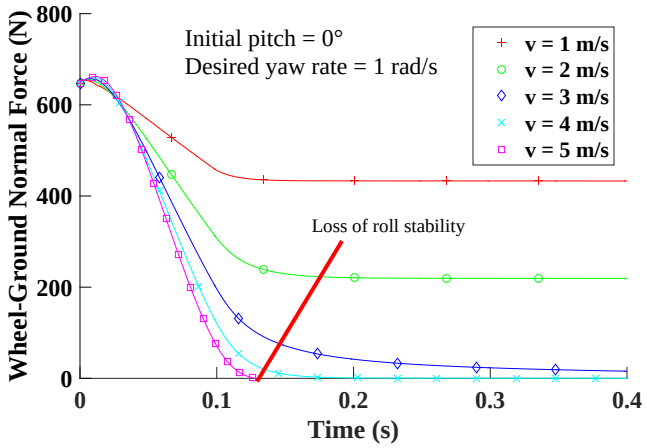

Figure 82: Left wheel-ground normal force at different initial speeds with yaw rate = 1 rad/s.

Figure 82 shows the normal force on the left wheel for different forward speeds during turns with a desired yaw rate of 1 rad/s. At time zero, the normal force is the same for all initial speeds. However, as the vehicle turned, the wheel-ground force decreased. When the initial speed was 3 m/s or higher, the force decreased to zero in less than 0.13 seconds. The simulation was terminated when this condition occurred because the contact between the wheel and the ground was lost. When the transporter experienced a roll instability.

The preceding results are combined in Figure 83. It shows that as the speed increases, the maximum yaw rate at which the vehicle can turn before rolling is reduced.

Figure 84 shows the normal force between the left wheel and the ground for left turns with different desired yaw rates with an initial forward speed of 1 m/s. Roll instability is not triggered at this speed by turns with desired yaw rates up to 3 rad/s. However, once the rider tries to turn with a yaw rate of 3.5 rad/s, the roll instability will occur within about 0.4 seconds.

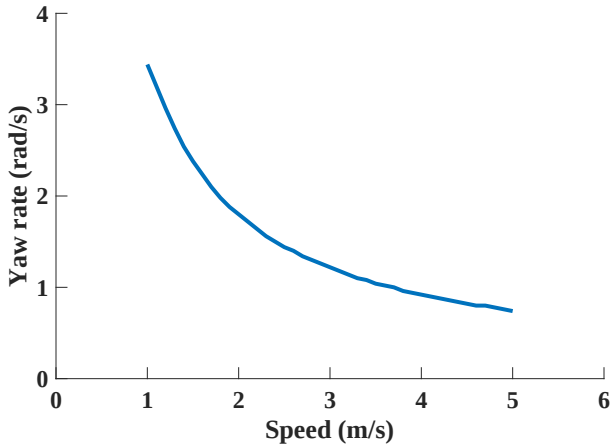

Figure 83: Maximum yaw rate before the transporter tips over.

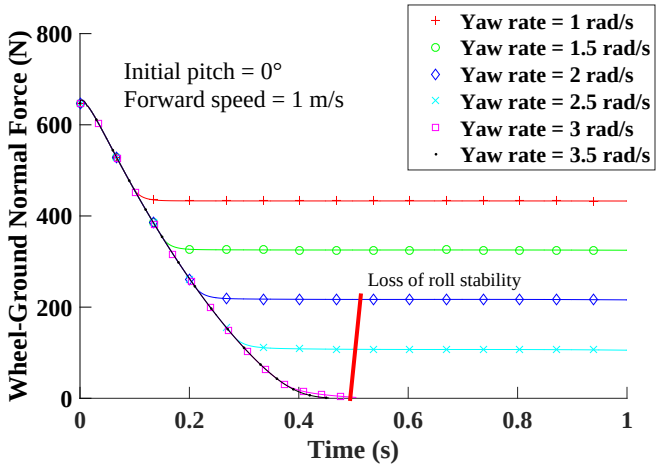

Figure 84: Left wheel-ground normal force for different yaw rates with forward speed = 1 m/s.

4.3.2 Experimental Results

High-speed turn testing was conducted using a Segway i2. However, because the rider knew that a turn was going to occur, they leaned into the turn. The Segway experienced roll instability during some turning test trials due to the rider *overleaning into the turn*. Leaning into the turn was necessary during the experiments to avoid a serious crash. However, in some cases the rider overcompensated and leaned too far. Such overleaning to induce roll stability was considered previously in Section 4.2.1. This resulted in the Segway rolling to the left (into the turn), and the right (outer)

wheel leaving the ground.

Figure 85 shows the Segway forward speed, yaw rate, and base roll angle during one such turning experiment. Figure 85(a) shows the Segway traveling 2 m/s when the turn was initiated at 0.3 seconds. Figure 85(b) shows the yaw rate increasing as the turn was executed. When the yaw rate reached approximately 3.25 rad/s at 0.7 seconds, the Segway base suddenly rolled to the left. Figure 85(b), also shows the roll angle of the Segway base during the trial. The sudden increase in roll angle at 0.7 seconds corresponds to the right (outer) wheel leaving the ground.

The yaw rate oscillated as the rider attempted to recover from the instability while turning on one wheel. In this case, the expert rider was able to recover from the instability and begin slowing the Segway to a stop. The pair of smaller increases in roll angle around 1 second correspond to the right wheel bouncing once the Segway base fell back to the ground.

The results indicate that rider lean has a significant impact on roll instability, and that the roll instability may occur into or away from the turn, depending on forward speed, turning rate, and the amount of rider lean. Simulation results show that roll instability may occur at certain combinations of turning rate and forward speed when the rider does not lean. On the other hand, experimental results showed cases of the rider overleaning into the turn, resulting in the Segway rolling into the turn.

When riding a Segway, the rider does not know the vehicle's forward speed or turning rate. While it is clear that there is an envelope of roll-stable rider lean and an appropriate amount of lean could be determined from the vehicle's forward speed and desired turning rate, it is up to the rider to estimate an appropriate amount of lean in real time with no accurate information about the vehicle speed. This can make it difficult for riders to know how much to lean into a turn without triggering roll instability to either side.

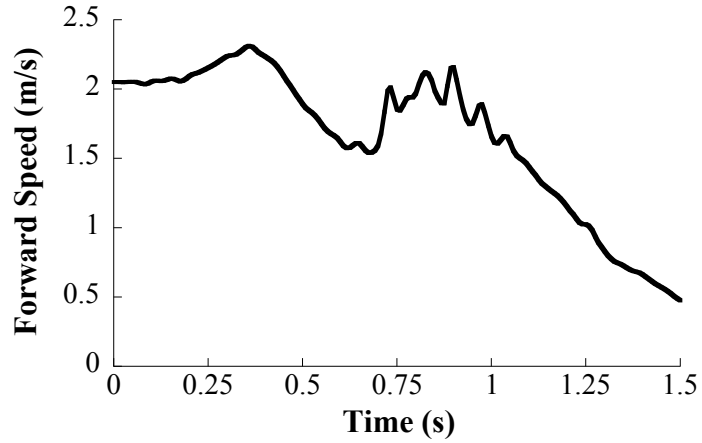

(a) Forward Speed.

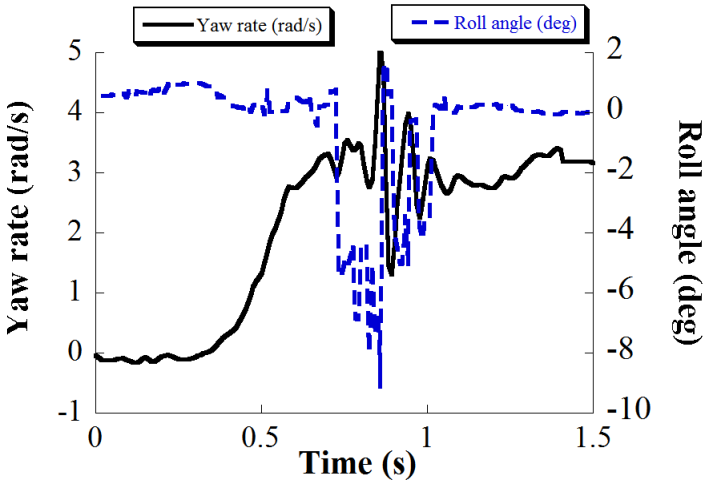

(b) Yaw Rate and Roll Angle.

Figure 85: (a) Segway Forward Speed, and (b) Yaw Rate and Base Roll Angle during one turning test trial.

4.3.3 Real roll-instability accident analysis

Recall that Figures 82 and 84 showed stability failure can occur very quickly once the vehicle starts to turn. In this section a real accident case is analyzed to determine the plausibility of these types of accidents occurring so abruptly.

Numerous accidents have been recorded and uploaded to the Internet. The sequence of events in one of these accidents [1] is shown in Figure 86. Figure 86(a) shows the person riding a Segway away from the camera and initiating a turn to the

left. However, the turning command was too aggressive and the person's lean into the turn was insufficient. As a result, the Segway rolls to the right. The moment it starts tipping is shown in the Figure 86(b). The time interval from the beginning of the turn and the tipping over is only 0.4s. Figure 86(c) shows that the person has lost control of the transporter. Finally, Figure 86(d) shows that the person falls completely off the Segway.

(a) Timestamp = 1.24 s.

(b) Timestamp = 1.64 s.

(c) Timestamp = 1.91 s.

(d) Timestamp = 2.37 s.

Figure 86: Segway Rolling Instability Incident [1]

4.4 Summary

This chapter examined the conditions that lead to vehicle lateral roll instability during turning. The maximum speed of the vehicle during a turning maneuver is limited by the available cornering forces. The tip-over conditions also depend on the geometrical characteristics of the vehicle. A wider footprint and a lower center of mass make the vehicle more stable. These conditions also depend on the posture and the motions of the rider. If he leans too far or too little into the turn, he might risk falling sideways. Equations were presented to predict the tip over speed and radius when the person is either leaning forward or sideways, or both, at the same time. It was also shown that tip over can be induced more easily when these motions are fast or abrupt. The wheel inertias also increase the risk of tip-over as the vehicle speed is greater. Finally, a dynamic model that includes a feedback pitch and yaw control was used to simulate the tip-over dynamics of a vehicle with mass properties similar to those of a Segway i2. Both the dynamic model and an accident analysis demonstrated that lateral instability can be triggered in as little as 0.12 seconds.

CHAPTER V

IRREGULAR SURFACES

The vast majority of research on inverted-pendulum transporters has focused on motion occurring on flat surfaces. A few previous investigations examined smooth inclined planes. This chapter investigates the effects of irregular surfaces by more thoroughly investigating inclined planes and examining dynamic effects of surface irregularities such as holes and bumps.

5.1 Traction loss on inclined surfaces

When a vehicle travels uphill on an inclined surface, traction will be reduced. On an inclined surface the traction force between the wheels and the surface is reduced because the normal force between them is reduced by a $\cos\theta$ factor, and the traction forces depend largely on this normal force. Additionally, there is a component of the weight force that pushes the system down the inclined plane. This increases the power demand on the motors to accelerate the machine forward, and up, the incline. Figure 87 shows a simplified diagram of an inverted-pendulum transporter carrying a load while traveling on an inclined surface with a slope angle of θ_s.

Note that this diagram is representative of a photograph shown in one of the first papers published on wheeled inverted pendulum transporters in 1990 [39]. That photograph has been reproduced here in Figure 88. Even though the concern for operation on inclined planes was expressed in this very early paper, there are still important questions about performance limitations on sloped surfaces. The remainder of this section seeks to fill in knowledge gaps in this area.

A simple analysis can show the effect of the inclination of the surface on the traction and the acceleration that the vehicle can achieve. The vehicle load can be

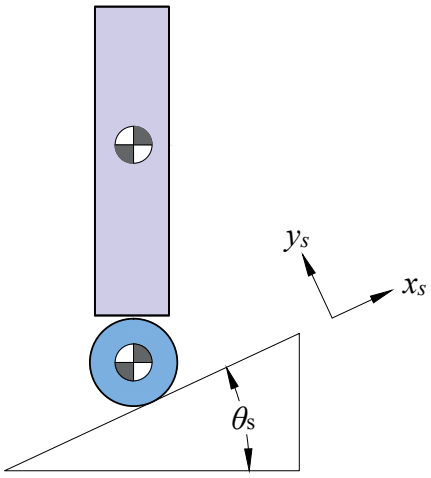

Figure 87: Diagram of transporter traveling uphill.

modeled as a vertical force acting on the wheel hubs with a magnitude equal to the sum of the weight of the vehicle and the weight of the rider. A free body diagram of the wheel is shown in Figure 89.

The x-axis is defined parallel to the inclined surface, while the the y-axis is perpendicular to it. Balancing the forces in both directions yields:

$$\Sigma F_x = (m + m_v)a_x \tag{131}$$

$$f - (m + m_v)g \sin\theta_s = (m + m_v)a_x$$

$$\Sigma F_y = 0 \tag{132}$$

$$N - (m + m_v)g \cos\theta_s = 0$$

If the acceleration along the inclined plane is set to zero, then the relations above can be solved for the minimum friction coefficient required for the vehicle to maintain traction:

$$f > (m + m_v)g \sin\theta_s \tag{133}$$

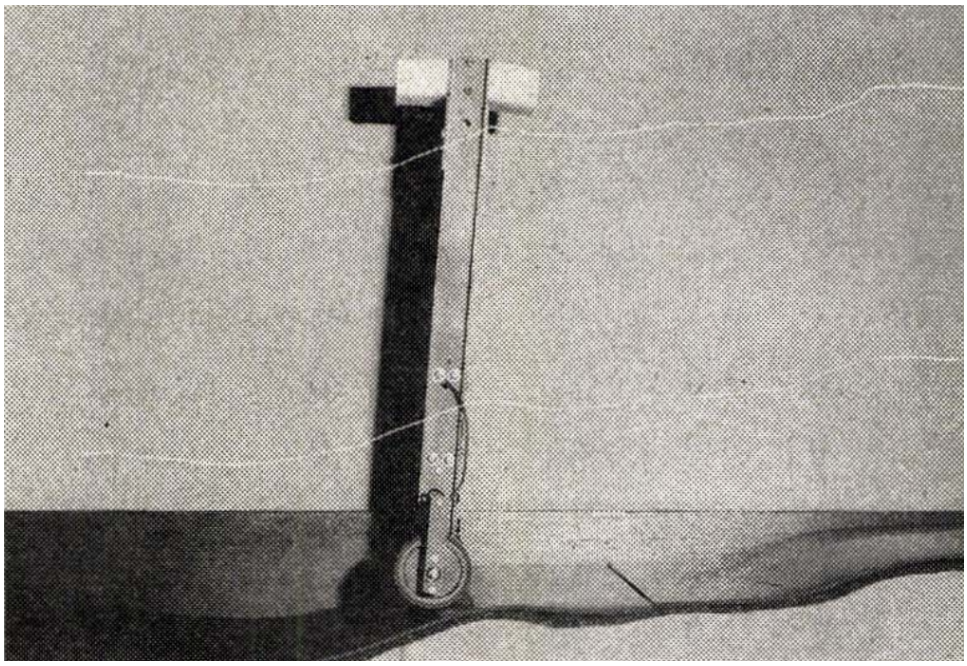

Figure 88: Experimental setup by Matsumoto [39].

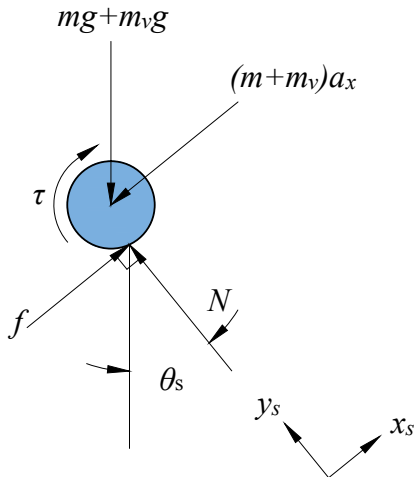

Figure 89: Simplified analysis

If it is assumed that the traction force is represented by:

$$f = \mu N \tag{134}$$

Substituting (134) into (133) yields:

$$\mu N > (m + m_v) g \sin \theta_s \tag{135}$$

Solving (132) for N and substituting into (135) gives the relation between the minimum required friction coefficient as a function of the incline angle θ_s:

$$\mu(m + m_v)g\cos\theta_s \geq (m + m_v)g\sin\theta_s \tag{136}$$

$$\mu \geq \tan\theta_s \tag{137}$$

Equation (137) is plotted in Figure 90.

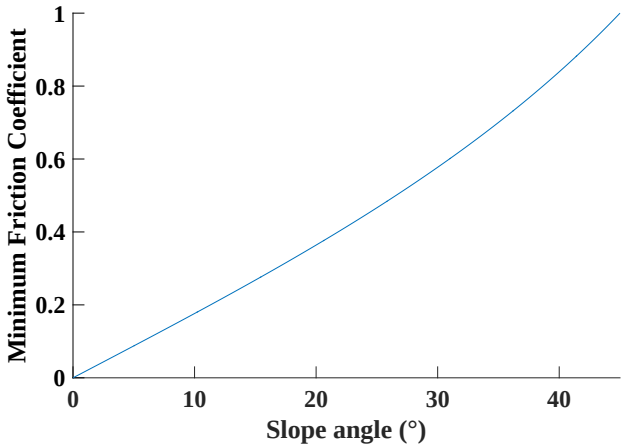

Figure 90: Minimum friction coefficient as a function of the slope angle.

Equation (131) can be solved for the acceleration along the inclined surface a_x:

$$a_x = \frac{f}{m + m_v} - g\sin\theta_s \tag{138}$$

Substituting (134) into (138) yields:

$$a_x = \frac{\mu N}{m + m_v} - g\sin\theta_s \tag{139}$$

Substituting the normal force found in (132) produces an expression for the maximum achievable acceleration of the vehicle, for a given slope angle θ_s, and friction coefficient μ:

$$a_{x,max} = \mu g\cos\theta_s - g\sin\theta_s \tag{140}$$

Equation (140) indicates that the capacity of the vehicle to accelerate is reduced in two different ways. The first term shows that the friction force is reduced as a result of a smaller normal force as the angle of the slope increases. The second term shows a reduction in the possible acceleration resulting from the presence of the weight component in the direction of the inclined plane that pushes the vehicle down the plane. In order to compare these two effects over a wide range a relatively high coefficient of friction of 0.8 is assumed. Figure 91 shows the gravity component along the plane, the traction force, and the total possible acceleration as a function of the inclination angle of the plane. A negative total acceleration means that despite the traction force attempting to drive the vehicle up, it will slide down due to its own weight. This situation is inevitable above angles of 40°.

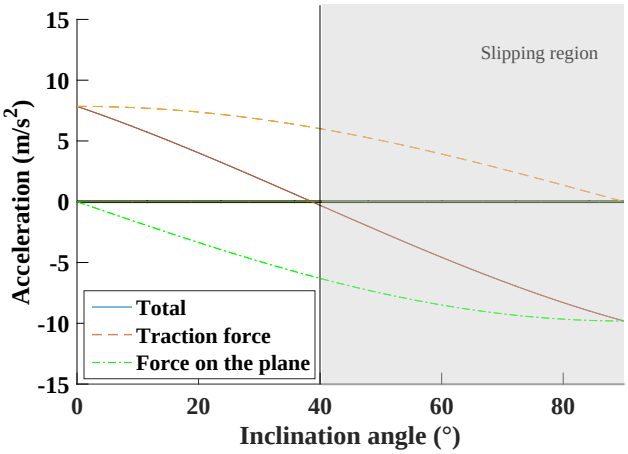

Figure 91: Total available vehicle acceleration at different slopes.

This analysis shows that there is a fundamental limit to the steepness of the surface that a vehicle can climb. This limit is obviously dependent on the traction characterstics between the wheel and the ground. Furthermore, even on surfaces with a relatively high coefficient of friction, such as values near 1, a vehicle cannot climb slopes with angles significantly greater than 40°.

5.1.1 Inclined surface with tilting body

In order to operate inverted-pendulum transporters, the rider must lean forward and backward. Therefore, let us consider a vehicle climbing up a slope where the body can lean forward or backwards with a lean angle of θ_p. Matsumoto et. al. developed equations of motion for this system assuming that the wheels do not slip [58]. These are:

$$(mH_{cm}^2 + I)\ddot{\theta}_p + [mrH_{cm}\cos(\theta_p + \theta_s)]\,\frac{a_x}{r} - mH_{cm}g\sin\theta_p = -\tau \tag{141a}$$

$$[mrH_{cm}\cos(\theta_p + \theta_s)]\ddot{\theta}_p + [(m + m_v)r^2 + I_v]\frac{v}{r} \tag{141b}$$

$$-mrH_{cm}\sin(\theta_p + \theta_s)\ddot{\theta}_p^2 + (m + m_v)rg\sin\theta_s = \tau$$

where θ_s is the slope angle, I is the inertia of the body, I_v is the moment of inertia of the wheels, and τ is the torque of the motors.

If the derivatives with respect to time are set to zero, then the following relations are obtained:

$$\tau_{eq} = mH_{cm}g\sin\theta_p \tag{142}$$

$$\tau_{eq} = (m + m_v)rg\sin\theta_s \tag{143}$$

These equations show that for a given slope angle, the vehicle can only be in static equilibrium when the body is leaned forward to a specific angle. Similarly, the motor torque required to stabilize the position is determined by the slope angle. Therefore, for a given slope θ_s the minimum torque required to climb the surface is that given above in (143) and the corresponding body lean angle is:

$$\theta_p = \arcsin\left[\frac{(m + m_v)r\sin\theta_s}{mH_{cm}}\right] \tag{144}$$

By replacing the mass ratio by λ_m and the height-to-radius ratio by λ_h as in Section 4.1.1, the required lean angle is:

$$\theta_p = \arcsin\left(\frac{\sin\theta_s}{\mu_m \lambda}\right) \tag{145}$$

where $\lambda_m = \frac{m}{m+m_v}$ and $\lambda_h = \frac{H_{cm}}{r}$.

Using the parameters from Table 3, which lists the mass and inertia parameters of a Segway i2 with an average operator, the minimum torque required to climb a slope can be calculated using (143). The variation of the required torque with respect to the slope angle is shown in Figure 92. Note that large values of slope incline require unrealistically large values for the wheel-slope coefficient of friction. Therefore, the range of slope angles has been limited to a realistic range.

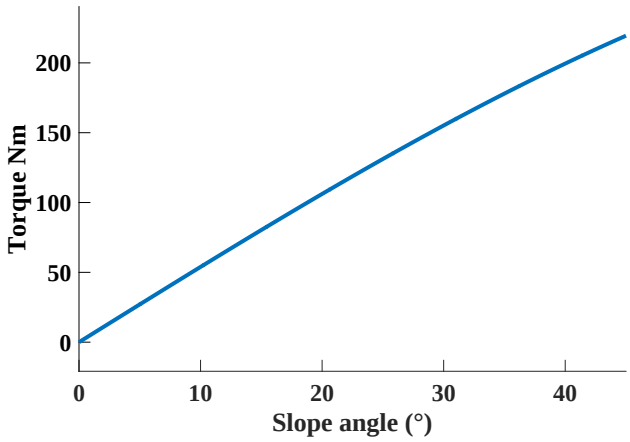

Figure 92: Minimum torque vs slope angle.

Equation (144) gives the corresponding body lean angle as a function of the slope. This is plotted in Figure 93. Once again, the range shown has been limited to realistic values of the coefficient of friction.

5.1.2 Conditions for maintaining balance

When the required traction force is greater than what the surface can provide, wheel slipping can occur. Two ways in which the available traction can be reduced is by

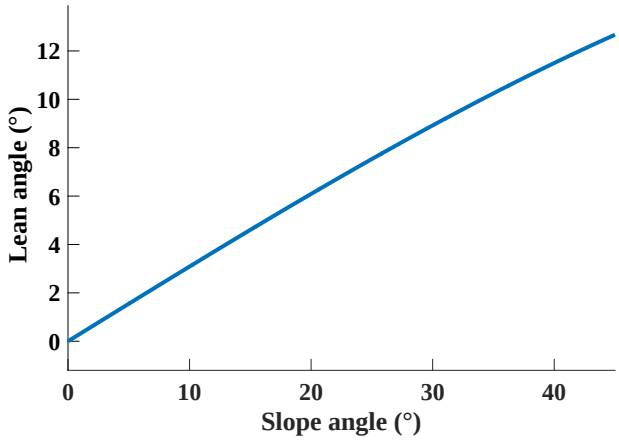

Figure 93: Body lean angle required for static equilibrium.

reducing the normal force or by reducing the coefficient of friction. Consider the system from the previous section where the traction force between the wheel and the ground is directed upwards along the inclined surface.

By performing a balance of moments on the wheel, as was shown in Figure 89, and assuming that the traction force is limited by the available coefficient of friction μ, we obtain:

$$\tau = f \cdot r \tag{146}$$

$$\tau = \mu N r \tag{147}$$

$$\tau = \mu(m + m_v) r g \cos\theta_s \tag{148}$$

At the same time, the torque required to maintain the body from falling is:

$$\tau = m g H_{cm} \sin\theta_p \tag{149}$$

As evidenced by the sine term in this relation, as the center of mass of the body moves forward from the wheel, the torque increases.

Combining the relations above yields the following expression for the minimum

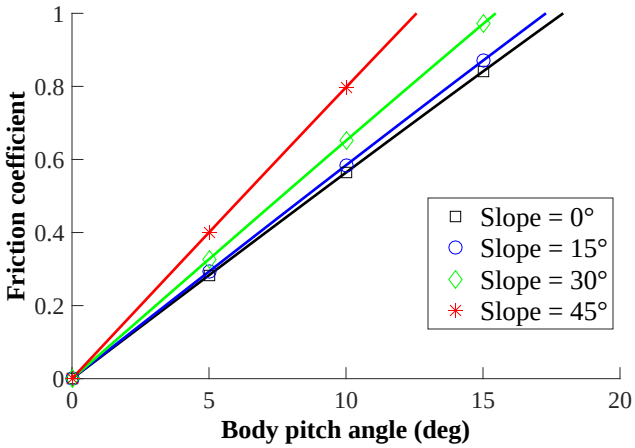

Figure 94: Requiered traction coefficient to maintain body balance

coefficient of friction required to maintain the stability of the wheeled inverted pendulum:

$$\mu_{min} = \frac{mH_{cm}\sin\theta_p}{r(m+m_v)\cos\theta_s} \qquad \text{(incline)} \tag{150}$$

For a horizontal surface this expression is reduced to:

$$\mu_{min} = \frac{mH_{cm}\sin\theta_p}{r(m+m_v)} \qquad \text{(horizontal)} \tag{151}$$

For a Segway i2, this relation is approximately:

$$\mu = 3.2305\sin\theta_p \qquad \text{(Segway i2 horizontal)} \tag{152}$$

Figure 94 shows the required friction coefficient to keep the pendulum body in static equilibrium while the vehicle is at rest or the wheel is rotating at constant speed. Note that as the body leans forward, the required traction between the wheel and ground increases. If sufficient traction is unavailable, then the wheel slips and accelerates. If the wheel cannot spin any faster and the torque is not enough to keep the body upright, then it will fall forward.

Given that real surfaces can provide a limited amount of traction, the available

torque can be reduced considerably. This effect is shown in Figure 95 for three values of μ. Similarly, the equilibrium angle for the pendulum is reduced, as shown in Figure 96.

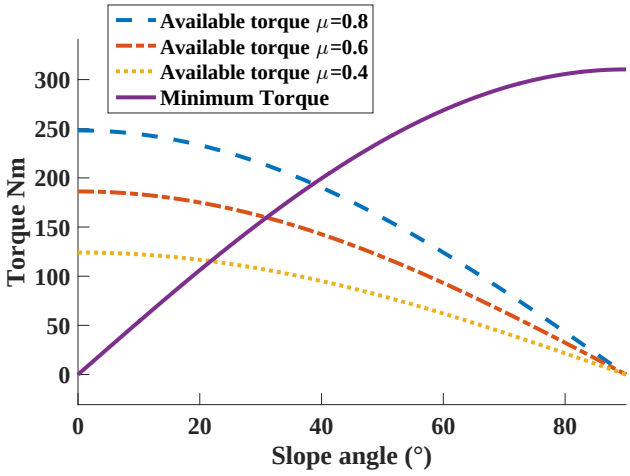

Figure 95: Minimum torque vs slope angle and available torque at different friction coefficients.

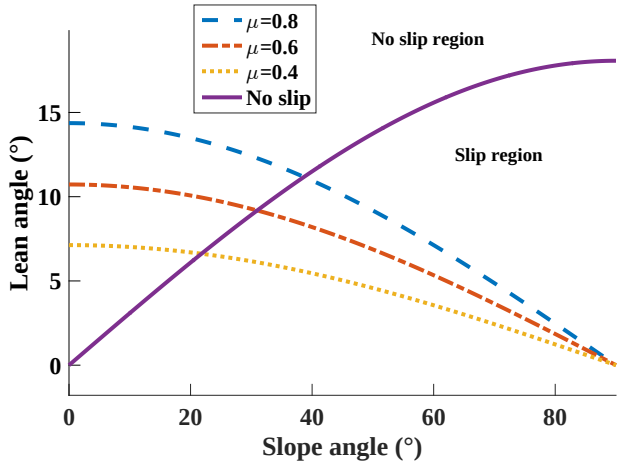

Figure 96: Body lean angle required for static equilibrium of the pendulum.

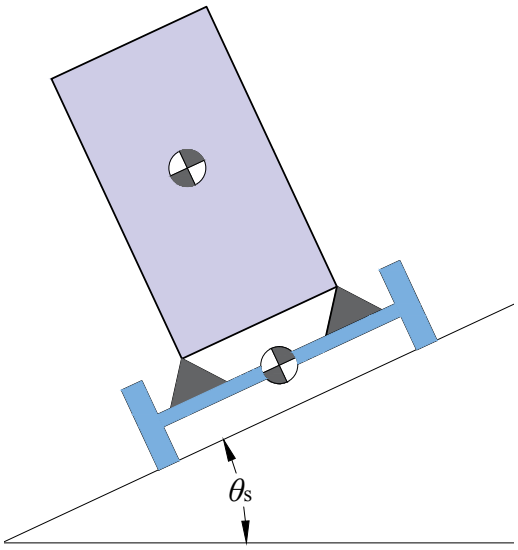

Figure 97: Vehicle traveling perpendicular to an inclined surface

5.2 Lateral static stability on an inclined surface

An inclined surface can also generate a roll instability condition when the vehicle travels in a direction transverse to the incline of the plane. The most critical case is when the direction of travel is perpendicular to the slope. Such scenario when a rider is turning in a circle is illustrated in Figure 97. A perspective view is shown in Figure 98. The scenario considered in this section is when the vehicle is in position I, at the bottom of the turning circle.

5.2.1 Constant uniform speed

First, the case where the vehicle travels in a straight line is considered. This scenario is shown in Figure 99. Following a similar procedure to Section 4.1, the normal forces between the vehicle's two wheels and the ground are:

$$N_{lv} = \frac{mg + m_v g}{2}\cos\theta_s + m_v g \sin\theta_s \frac{r}{d} + mg\sin\theta_s \frac{H_{cm} + r}{d} \tag{153}$$

$$N_{rv} = \frac{mg + m_v g}{2}\cos\theta_s - m_v g \sin\theta_s \frac{r}{d} - mg\sin\theta_s \frac{H_{cm} + r}{d} \tag{154}$$

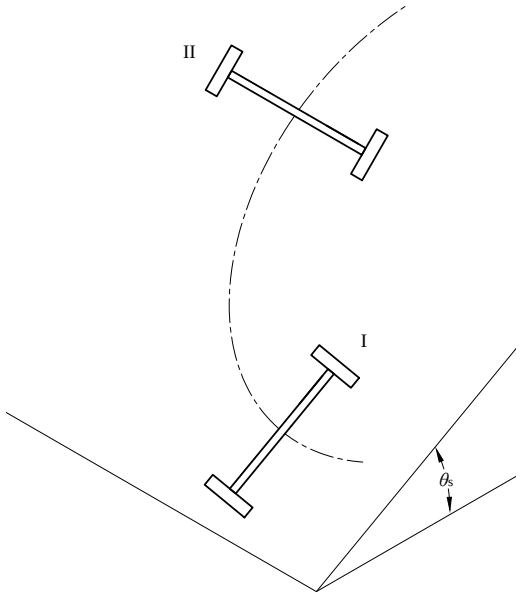

Figure 98: Vehicle traveling perpendicular to an inclined surface - top view

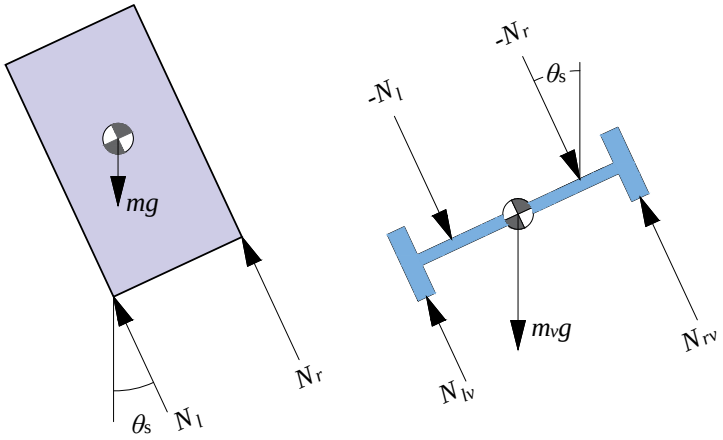

Figure 99: Free body diagrams during a straight line motion on an inclined plane.

where N_{lv} and N_{rv} are the forces between the wheels and the ground.

The normal forces between the person and the vehicle on each side are:

$$N_l = \frac{mg}{2}\cos\theta_s + mg\sin\theta_s\frac{H_{cm}}{b} \tag{155}$$

$$N_r = \frac{mg}{2}\cos\theta_s - mg\sin\theta_s\frac{H_{cm}}{b} \tag{156}$$

Note that as the slope angle θ_s increases, both N_{rv} and N_r decrease. By setting $N_r = 0$ the following relationship for the critical slope angle at which the person is no longer supported on both feet is obtained:

$$\tan\theta_s = \frac{b}{2H_{cm}} \tag{157}$$

This equation shows that the person will remain stable on the vehicle at higher slope angles when the distance between the rider's feet is larger or when the rider's center of mass is lower. This equation is plotted in Figure 100.

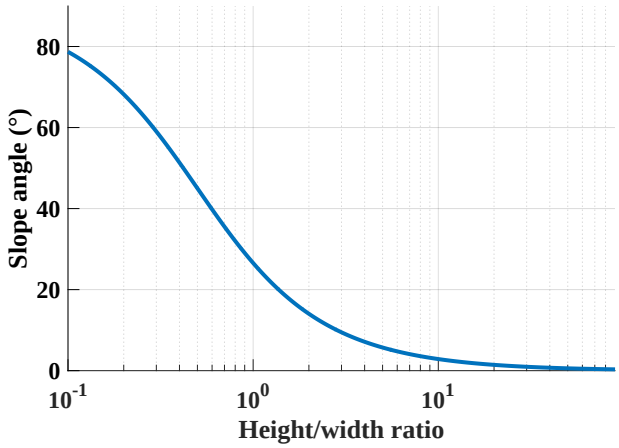

Figure 100: Maximum slope angle vs center of mass width to height ratio.

In a similar manner, setting $N_{rv} = 0$ produces the following relationship:

$$\tan\theta_s = \frac{d(m+m_v)}{2[m(H_{cm}+r)+m_v r]} \tag{158}$$

This expression can be rearranged by dividing both the numerator and denominator by the total mass $m + m_v$:

$$\tan\theta_s = \frac{1}{2}\frac{d}{\lambda_m H_{cm} + r} \tag{159}$$

where $\lambda_m = \frac{m}{m+m_v}$. In this expression, the denominator is the height measured from the wheel axis at which the center of mass of the person-vehicle system is located. The stability is increased when the distance between the wheels increases. However, it is reduced as the height of the center of mass of the system is increased. The center of mass can be lowered by making the vehicle heavier in relation to the person or by reducing the height of the wheels. Of course, decreasing wheel size has the drawback of making the machine more sensitive to bumps.

If the parameters from Table 3 are substituted into (157) and (158), then they predict that the maximum slope before the person loses balance is 6.73°, while the maximum slope before the vehicle loses balance (assuming its payload is firmly attached) is 14.56°. This means that a vehicle with these parameters is very limited in its maneuverability while traveling along a line perpendicular to the direction of greatest ascent. To improve the stability margin, the rider needs to lean into the slope. However, such inward leaning has the drawback of increasing the chances of wheel slip down the plane, as a result of a reduction in the normal force in the outside wheel, and hence, a reduction in the traction force.

5.2.2 Roll stability turning at constant speed on an inclined plane

Now consider the case when the vehicle is turning while on an inclined plane. Assume the vehicle is following a circular path at speed v with its center of curvature located at a distance r_g up the inclined surface, as was illustrated in Figure 98. Figure 101 shows free body diagrams indicating the forces acting on both the person and the vehicle.

The normal forces were found by following a similar procedure to the one followed in previous sections. The normal forces between the left and right wheels and the ground are:

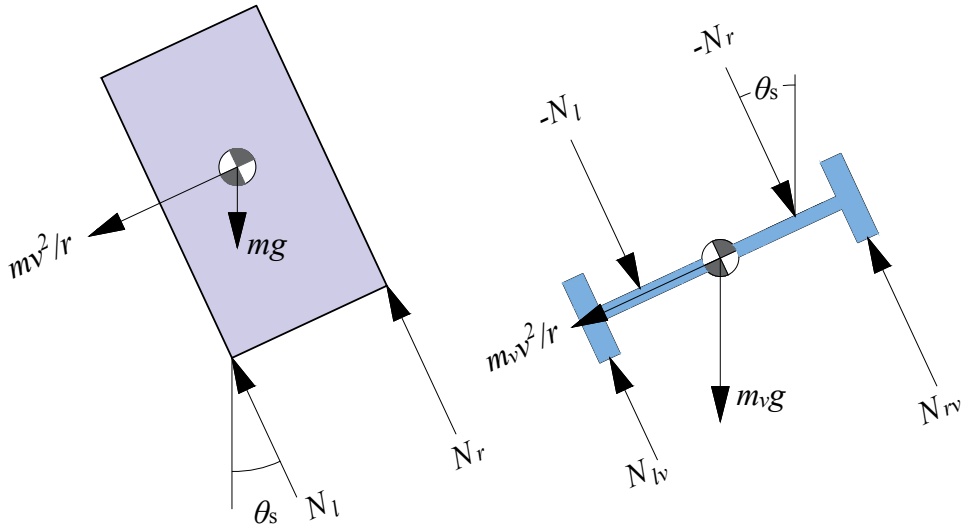

Figure 101: Free body diagrams during a turning motion on an inclined plane.

$$N_{lv} = \frac{mg + m_v g}{2}\cos\theta_s + \left(\frac{m_v v^2}{r_g} + m_v g \sin\theta_s\right)\frac{r}{d} + \left(\frac{mv^2}{r_g} + mg\sin\theta_s\right)\frac{H_{cm} + r}{d} \tag{160}$$

$$N_{rv} = \frac{mg + m_v g}{2}\cos\theta_s - \left(\frac{m_v v^2}{r_g} + m_v g \sin\theta_s\right)\frac{r}{d} - \left(\frac{mv^2}{r_g} + mg\sin\theta_s\right)\frac{H_{cm} + r}{d} \tag{161}$$

The normal forces between the load and the vehicle on each side are:

$$N_l = \frac{mg}{2}\cos\theta_s + \left(\frac{mv^2}{r_g} + mg\sin\theta_s\right)\frac{H_{cm}}{b} \tag{162}$$

$$N_r = \frac{mg}{2}\cos\theta_s - \left(\frac{mv^2}{r_g} + mg\sin\theta_s\right)\frac{H_{cm}}{b} \tag{163}$$

Note that the forces on the right foot and right wheel are reduced as the turning speed is increased or as the turning radius is decreased. A more convenient way to express these equations is by grouping the gravity terms together. For instance, the force between the right support and the vehicle can be rewritten as:

$$N_r = \frac{mg}{b}\left(\frac{b}{2}\cos\theta_s - H_{cm}\sin\theta_s\right) - \frac{mv^2}{r_g}\frac{H_{cm}}{b} \tag{164}$$

The inclined plane effectively redistributes part of the weight from the support higher on the plane to the the support on the downhill side. The second term is the effect that the turning motion has on reducing the normal force on the right foot (the foot higher up the incline). The maximum turning speed before the operator looses right-foot support is obtained by setting (164) equal to zero:

$$v_{person} = \sqrt{\frac{\left(b\cos\theta_s - 2H_{cm}\sin\theta_s\right) r_g g}{2H_{cm}}} \tag{165}$$

This expression has a similar form to that of (39), which gives the maximum vehicle turning speed during a turn before tipping over. Note that the numerator becomes zero when the slope angle is equal to the angle found in (157). By defining:

$$b(\theta_s) = b\cos\theta_s - 2H_{cm}\sin\theta_s \tag{166}$$

(165) can be rewritten as:

$$v_{person} = \sqrt{\frac{b(\theta_s) r_g g}{2H_{cm}}} \tag{167}$$

Both of the terms in $b(\theta_s)$ decrease with increasing slope angle. Therefore, the maximum turning speed is reduced by an increasing slope.

Another way of expressing the maximum speed can be obtained by recognizing that the term multiplying $\cos\theta_s$ is the same one found in (157). If we define θ_{cr} as the maximum admissible slope at static conditions, then (165) becomes:

$$v_{person} = \sqrt{\left(\tan\theta_{cr}\cos\theta_s - \sin\theta_s\right) r_g g} \tag{168}$$

The normal force on the right wheel (inside the turn on the uphill side) becomes zero when:

$$v_{vehicle} = \sqrt{\frac{d(\theta_s) r_g g}{2H_{cm,global}}} \tag{169}$$

where,

$$d(\theta_s) = d\cos\theta_s - 2H_{cm,global}\sin\theta_s \tag{170}$$

Note that $d(\theta_s)$ becomes zero at the angle found in (158).

Performing this type of turning motion transverse to an incline is only possible when there is enough traction available. By balancing forces along the radial direction, a relation between the slope angle, the coefficient of friction, turning speed, and turning radius was found to be:

$$\frac{v^2}{r} = \mu g\cos\theta_s - g\sin\theta_s \tag{171}$$

In order for the turning motion to be possible without wheel slip, the coefficient of friction must meet the following constraint:

$$\mu \geq \tan\theta_s \tag{172}$$

Using real parameter estimates in (157) and (158), it was found that the maximum slope before the person loses balance is 6.73° while the maximum slope before the vehicle loses balance (assuming its payload is firmly attached) is 14.6°. This means that a vehicle with these parameters is very limited in its maneuverability while traveling along a line perpendicular to the direction of greatest ascent. Therefore, the rider needs to lean into the slope in order to improve stability.

An example case of a 1 meter radius turn is examined. Compared to the static case without a turning motion, the admissible slope angle is limited even for speeds below 2 m/s. As in previous cases, the maximum speed at which the person remains stable with respect to the vehicle is smaller than the speed at which the vehicle can remain stable.

At a slope angle of above 6.73° the maximum speed is zero for the person to remain stable. Meanwhile, the maximum speed for the vehicle to remain stable is zero at slope angles above 14.6°. This matches what was found in the previous section. Figure 102 shows the maximum turning speed before the vehicle and the rider loses balance.

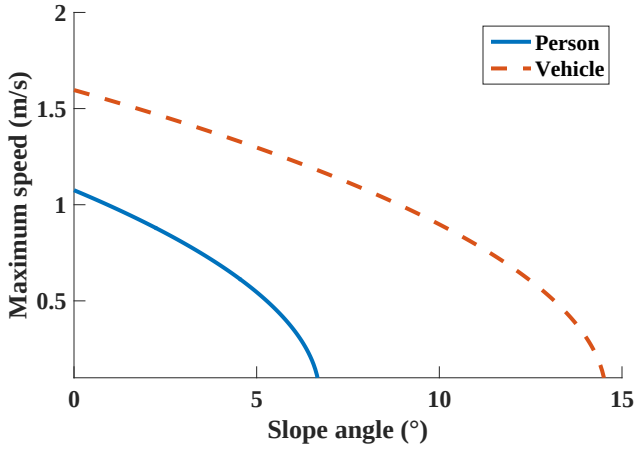

Figure 102: Slope angle limits for a 1 m radius turn.

5.2.3 Leaning while turning at a constant speed

In this section, the case where the rider leans into the slope with an angle θ_b with respect to the vehicle is studied. This situation is illustrated in Figure 103.

In this case, the normal forces between the vehicle and the person are:

$$N_l = \frac{mg}{b}\left[\left(\frac{b}{2} - H_{cm}\sin\theta_b\right)\cos\theta_s + H_{cm}\cos\theta_b\sin\theta_s\right] + \frac{mv^2(r_g - H_{cm}\sin\theta_b)}{r_g^2}\frac{H_{cm}\cos\theta_b}{b} \tag{173}$$

$$N_r = \frac{mg}{b}\left[\left(\frac{b}{2} + \frac{H_{cm}\sin\theta_b}{b}\right)\cos\theta_s - H_{cm}\cos\theta_b\sin\theta_s\right] - \frac{mv^2(r_g - H_{cm}\sin\theta_b)}{r_g^2}\frac{H_{cm}\cos\theta_b}{b} \tag{174}$$

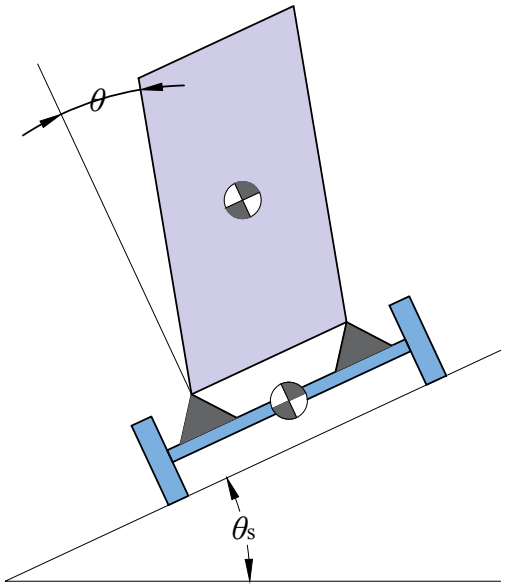

Figure 103: Vehicle traveling perpendicular to an inclined surface with payload tilting.

The forces between the vehicle and the ground are:

$$\begin{aligned} N_{rv} = {} & \frac{m_v g}{d}\left(\frac{d}{2}\cos\theta_s - r\sin\theta_s\right) \\ & + \frac{mg}{d}\left[\left(\frac{d}{2} + H_{cm}\sin\theta_b\right)\cos\theta_s - (r + H_{cm}\cos\theta_b)\sin\theta_s\right] \\ & - \frac{m_v v^2}{r_g}\frac{r}{d} - \frac{mv^2(r_g - H_{cm}\sin\theta_b)}{r_g^2}\frac{H_{cm}\cos\theta_b + r}{d} \end{aligned} \tag{175}$$

$$\begin{aligned} N_{lv} = {} & \frac{m_v g}{d}\left(\frac{d}{2}\cos\theta_s + r\sin\theta_s\right) \\ & + \frac{mg}{d}\left[\left(\frac{d}{2} - H_{cm}\sin\theta_b\right)\cos\theta_s + (r + H_{cm}\cos\theta_b)\sin\theta_s\right] \\ & + \frac{m_v v^2}{r_g}\frac{r}{d} + \frac{mv^2(r_g - H_{cm}\sin\theta_b)}{r_g^2}\frac{H_{cm}\cos\theta_b + r}{d} \end{aligned} \tag{176}$$

The parameters in Table 3 for the Segway i2 were substituted into (175) and (176) to estimate the maximum leaning angle for each slope angle at which these forces become zero and to estimate a permissible leaning angle range. Figure 104 shows the maximum and minimum leaning angle while doing turns flat ground (0°) and a 15° slope. In the figure, the lighter colors refer to the case where the slope is 15°. Note that increasing the slope angle from 0° to 15° has the effect of moving

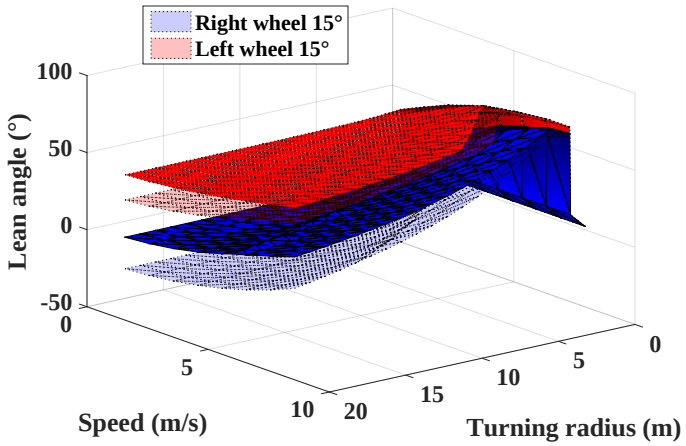

Figure 104: Lean limits at which normal forces become zero at different slopes.

the zero normal force surfaces towards larger angles of lean into the incline slope. In other words, both the minimum and maximum leaning angle required for stability increase with slope angle.

Figure 105 shows the leaning angle required when the turn has a 1m radius. Note that as the slope angle is increased, both the minimum and maximum leaning angle required for lateral stability increase, as explained above. In addition, the difference between the maximum and minimum leaning angle is reduced as the speed is increased.

Figure 106 shows a plot of the margin between the maximum and minimun angle at different slope angles. In both the 0° and 15° slope cases, the margin is reduced as the speed increases. In addition, the margin is reduced as the slope increases. This means that the user loses some permissible leaning range in order to keep the vehicle laterally stable when the surface is more inclined. At the higher range of achievable operating speeds, the rider lean angle margin is approximately 12°. Therefore, the rider must stay within a very small leaning envelope in order to avoid tipping over.

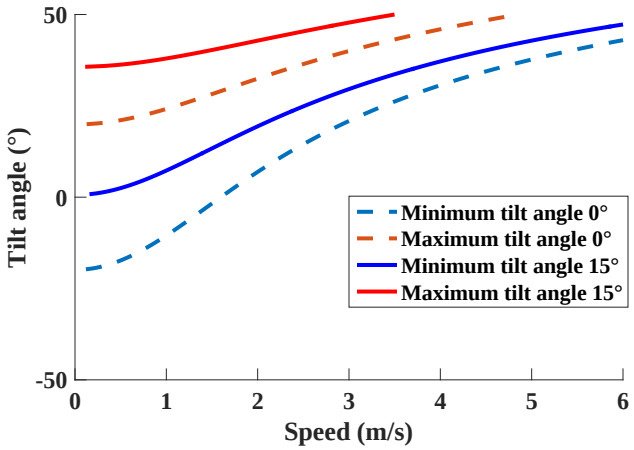

Figure 105: Tilting limits at which normal forces become zero at different slopes for a 1 m turn.

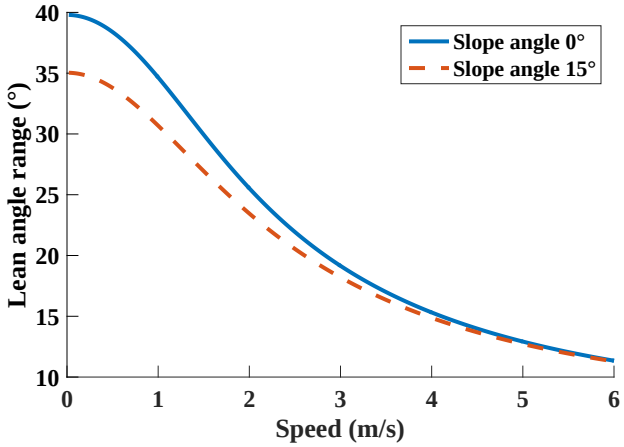

Figure 106: Lean angle range at which normal forces become zero for a 1 m turn.

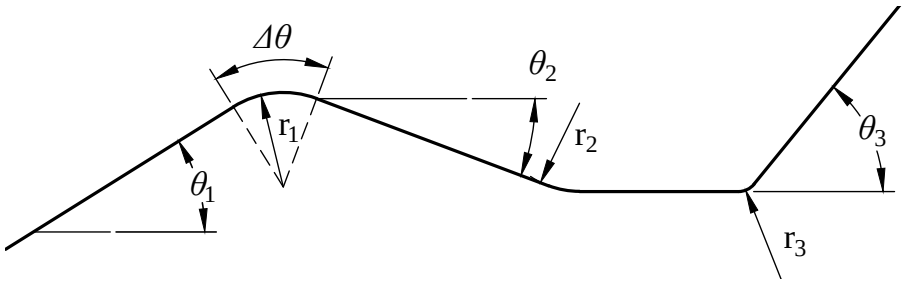

Figure 107: Geometric description of an irrregular surface

5.3 Geometrical description of general irregular surfaces

In order to extend the analysis to more complex surfaces beyond those with a constant slope angle, a general surface description can be defined by joining constant slope surface profiles of different slope angles with surface arcs of a prescribed radius and arc length. Such a generic surface profile is illustrated in Figure 107.

The arc surface irregularity has a radius r_s that encompasses an angle $\Delta\theta$. The surface slope at one end is θ_{s1} and θ_{s2} at the other end. A surface irregularity can be classified as convex or concave. In a convex surface irregularity the surface center of curvature is below the "ground." This type of irregularity is also referred to as a "bump." Meanwhile, in a concave surface irregularity, the surface center of curvature is above the surface. This type of irregularity constitutes a "hole."

Figure 108 shows a wheel of radius r_w traveling over a bump. The wheel axis follows the dashed path, which has a radius $r_s + r_w$. The distance traveled by the wheel center, assuming it is going from left to right, is given by $d = (r_s + r_w)\Delta\theta$. Note that in this type of surface, according to the convention implicit in Figure 108, the angle θ_s increases as the wheel moves to the right once the wheel is on the bump.

Figure 109 shows a wheel of radius r_w traveling through a hole. The wheel axis follows the dashed path, which has a radius $r_s - r_w$. The distance traveled by the wheel center, assuming it is going from left to right, is given by $d = (r_s - r_w)\Delta\theta$. In this type of surface, according to the convention implicit in Figure 109, the slope angle decreases as the wheel moves to the right.

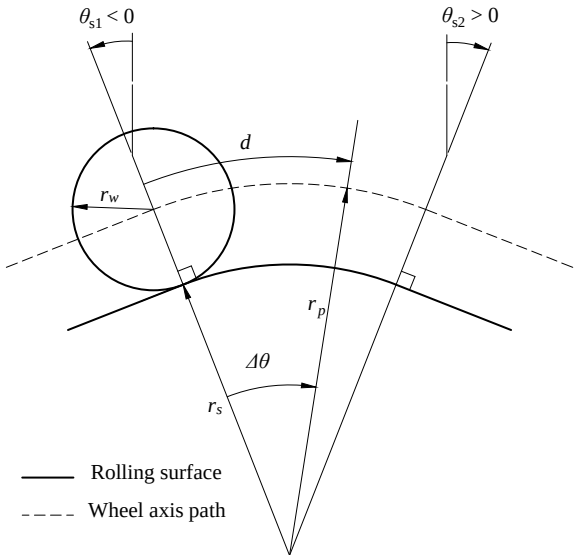

Figure 108: Geometric description of convex "bump" surface irregularity

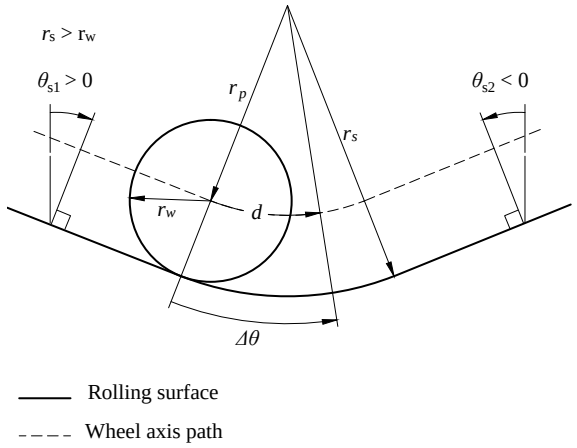

Figure 109: Geometric description of concave "hole" surface irregularity

5.4 Non dynamic analysis of a transporter going over a surface irregularity

5.4.1 Convex surfaces (bumps)

In this section the effect of traveling over a bump at a constant speed is studied. Figure 110 shows a transporter traveling over a bump with a constant curvature. It is assumed that the body of the person is static and vertical and that the vehicle travels at a constant speed. The origin of the system of coordinates is at point O, at

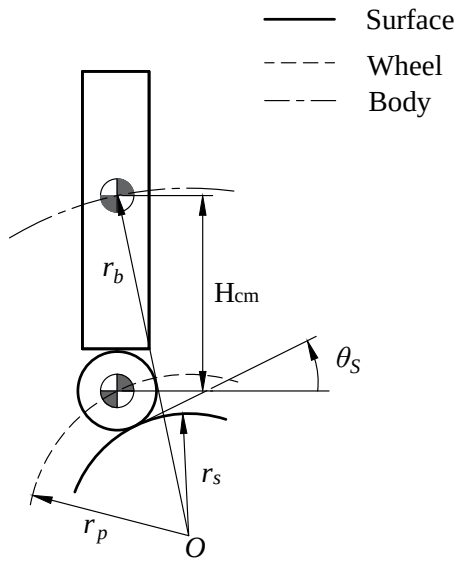

Figure 110: Vehicle going over bump.

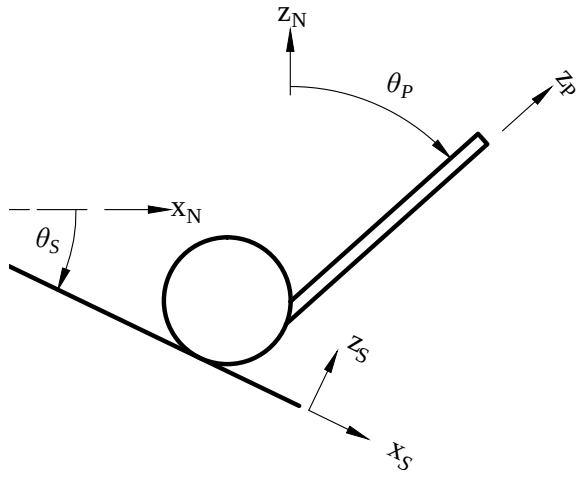

Figure 111: Coordinate system for a transporter on an inclined surface.

the center of curvature of the surface. The distance between the origin and the body center of mass is r_b, the surface radius is r_s, and the wheel axis path has a radius of r_p. The distance between the wheel axis and the center of mass of the person is H_{cm}. Figure 111 shows the coordinate axes x_s, which is tangent to the surface at the contact point between the wheel at the ground. Axis z_s is perpendicular to x_s.

The location of the wheel axis, $r_{w/o}$, the relative position of the body with respect to the wheel axis $r_{b/w}$, and the position of the body with respect to the origin $r_{b/o}$ are:

$$\vec{r}_{w/o} = (r_s + r_w)\vec{z}_s \tag{177}$$

$$\vec{r}_{b/w} = r_b\vec{z}_N = H_{cm}(\sin\theta_s\vec{x}_s + \cos\theta_s\vec{z}_s) \tag{178}$$

$$\vec{r}_{b/o} = r_{w/o} + r_{b/w} \tag{179}$$

The angular speed of the slope frame, $\vec{\omega_s}$ is:

$$\vec{\omega_s} = \dot{\theta}_s\vec{y}_s \tag{180}$$

If the wheel axis travels at a constant speed v, then the angular speed of the slope frame and the speed of the vehicle are related by:

$$\vec{\omega_s} = \frac{v}{r_s + r_w}\vec{y}_s \tag{181}$$

The acceleration of the axis of the wheel, $\vec{a}_v$ is:

$$\vec{a}_v = \vec{\omega_s} \times (\vec{\omega_s} \times \vec{r}_{w/o}) \tag{182}$$

$$= -(r_s + r_w)\dot{\theta_s}^2\vec{z}_s \tag{183}$$

At the same time, the acceleration of the center of mass of the rider, $\vec{a}_b$ is

$$\vec{a}_b = \vec{\omega_s} \times (\vec{\omega_s} \times \vec{r}_{b/o}) \tag{184}$$

$$= -H_{cm}\sin\theta_s\dot{\theta_s}^2\vec{x}_s - (r_s + r_w + H_{cm}\cos\theta_s)\dot{\theta_s}^2\vec{z}_s \tag{185}$$

By balancing forces between the body and the vehicle, the following relations are found:

$$\vec{F} - \vec{F}_{g,b} = m_b\vec{a}_b \tag{186}$$

$$-\vec{F} - \vec{F}_{g,v} + \vec{N} = m_v\vec{a}_v \tag{187}$$

where $\vec{F}$ is the force vector between the vehicle and the body, $\vec{F}_{g,b}$ and $\vec{F}_{g,v}$ are the weight of the person and the vehicle, and $\vec{N}$ is the force between the wheel and the ground.

By solving the above system of equations, the normal force between the vehicle and the ground, N_z, is:

$$N_z = (m_b + m_v)g\cos\theta_s - [m_b(H_{cm}\cos\theta_s + r_s + r_w) + m(r_s + r_w)]\dot{\theta_s}^2 \tag{188}$$

The expression $\dot{\theta}_s$ can be rewritten as $\frac{v}{r_s+r_w}$, which results in:

$$N_z = (m_b + m_v)g\cos\theta_s - [m_b(H_{cm}\cos\theta_s + r_s + r_w) + m(r_s + r_w)]\left(\frac{v}{r_s + r_w}\right)^2 \tag{189}$$

Equation 189 can be reordered as follows:

$$\begin{aligned} N_z = \left[(m_b + m_v)g + m_b H_{cm}\left(\frac{v}{r_s + r_w}\right)^2\right]\cos\theta_s - \\ [(m_b + m)(r_s + r_w)]\left(\frac{v}{r_s + r_w}\right)^2 \end{aligned} \tag{190}$$

Note that the sign of the coefficient of the cosine term depends on the rate of change of the slope. This will influence whether the normal force will reach a maximum or a minimum at $\theta_s = 0$.

The coefficient of the cosine term is positive when (given $v > 0$ and $r_s > 0$)

$$v < (r_s + r_w)\sqrt{\frac{(m_b + m_g)g}{m_b H_{cm}}} \tag{191}$$

The parameters from Table 3 where substituted into (189) to study the behavior of the normal force under different surface radii, slope angles, and vehicle speeds.

Figure 112 shows the normal force when traveling at 1 m/s at three different surface curvature radii r_i. As the machine travels over the surface, the slope angle changes along the horizontal axis of the graph. Note that for this speed and surface radii, the normal force is zero both at the beginning and the end of the bump. If

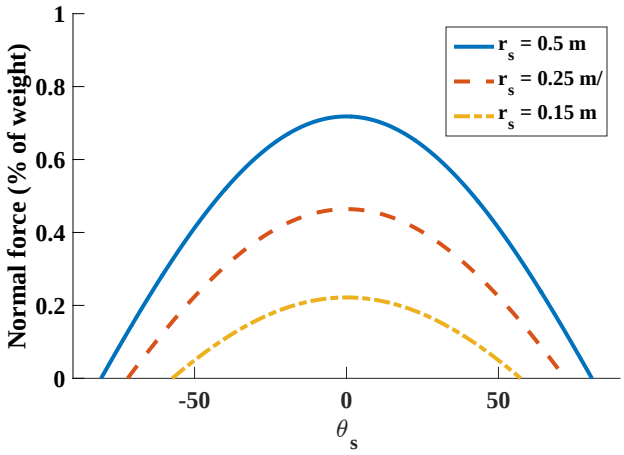

Figure 112: Effect of bump radius at 1 m/s.

the slope angle is too large at any point along the bump, then the vehicle can lose contact with the ground. For the vehicle to remain in contact with the ground, the slope angles should not go beyond the range where the normal force is greater than zero. As the surface radius is increased, the normal force increases as well, but in all cases, the normal force is reduced when compared to the weight of the vehicle. This increases the risk of the wheels slipping relative to the ground.

Figure 113 shows the effect of increasing the speed. Note that as the speed is increased, the range of slopes for which the normal force is greater than zero is reduced. This means that as the vehicle goes faster, the risk of jumping off the ground when encountering a bump is increased.

Figure 114 shows the combination of surface slope angles and surface radius at which the normal force becomes zero at different vehicle speeds. As the slope angle becomes more positive or negative, the minimum surface radius to keep the normal force above zero increases. An increase in the speed of the vehicle also has the effect of increasing the minimum required surface radius to maintain contact with the ground.

Figure 115 shows the maximum speed that the vehicle can travel at each slope angle for a given surface radius. Note that as the slope angle increases the speed is

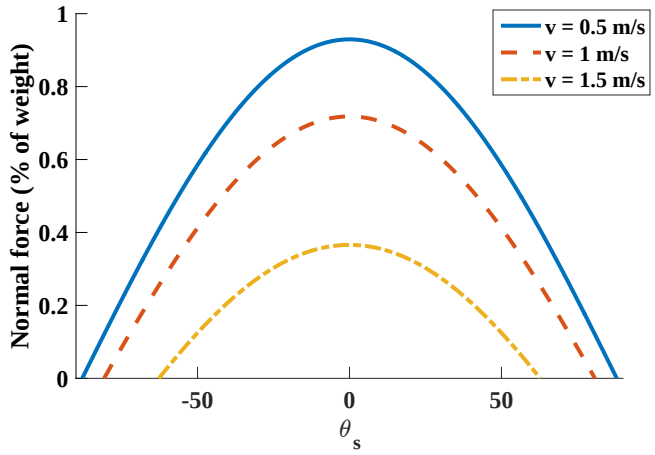

Figure 113: Effect of speed going over a bump with a surface radius of 1 m.

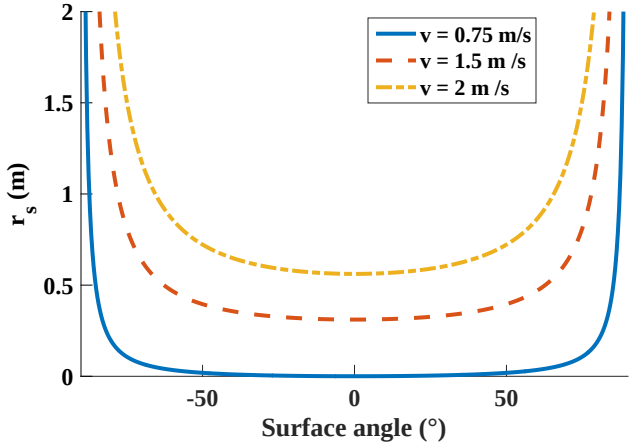

Figure 114: Minimum surface radius for each slope angle to maintain contact with the ground at different speeds.

reduced. At the same time, an increase in the surface radius allows the vehicle to go over a bump at greater speeds without losing contact with the ground.

The behavior of the normal force with respect to the slope angle will show a maximum or a minimum depending on the sign of the cosine term in (190). The cosine term is positive if the condition in (191) is met and negative if not. A positive cosine term means the normal force will have a maximum with respect to the slope angle. Figure 116 shows the combinations of speeds and surface radii at which the cosine term is positive or negative.

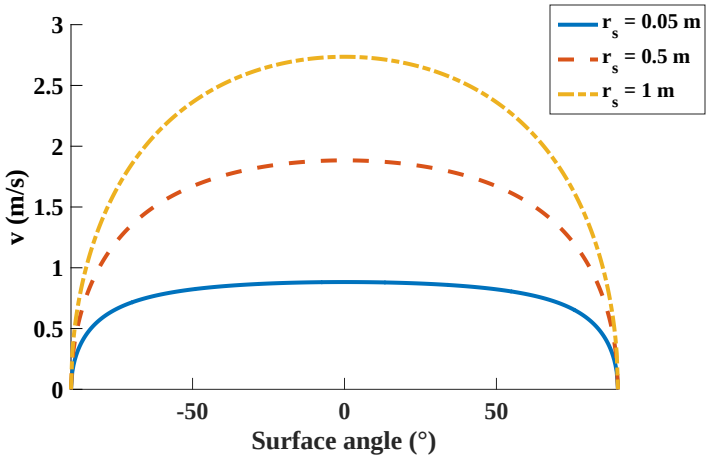

Figure 115: Maximum speed for each slope angle to maintain contact with the ground at different surface radii.

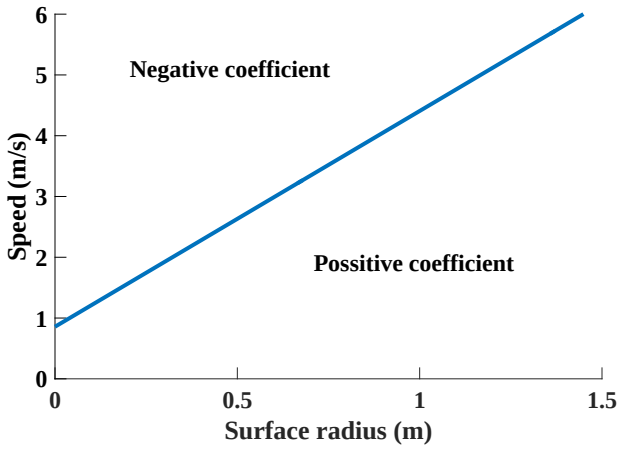

Figure 116: Sign of the coefficient of the cosine term in the normal force.

A special case of a convex surface is when the initial slope angle is $\theta_s = 0$. This is the case where the vehicle initially travels on a flat ground and suddenly finds itself on a downhill slope surface. In such surfaces there is a risk that the sudden drop in the ground will cause the vehicle wheel to lose ground. Figure 117 shows the maximum speed at which the vehicle can travel at each surface radius (or the minimum surface radius for each speed) without losing contact with the ground. For a surface radius of $r_s = 0$ the maximum speed is 0.7489. Even though a real vehicle might not actually lose contact with the ground at these conditions because of the wheel elasticity, the

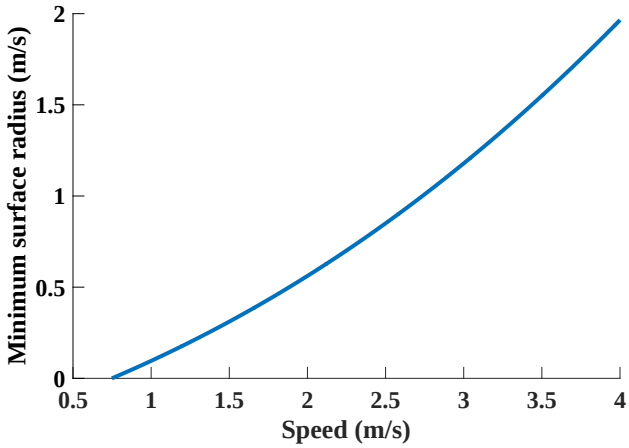

Figure 117: Minimum radius starting at slope zero that induces a "flying off" response

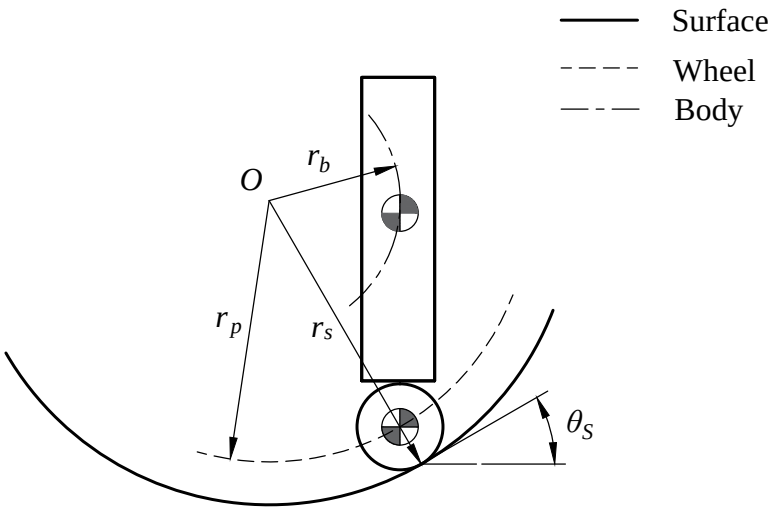

Figure 118: Vehicle going over a hole

normal force can be greatly reduced and make wheel slipping a significant risk.

5.4.2 Concave surfaces (holes)

Figure 118 shows a vehicle going through a hole. In this figure the parameters are virtually the same as specified in the previous section. However, note that in the distance between the wheel axis and the center of curvature of the surface is now $r_s - r_w$

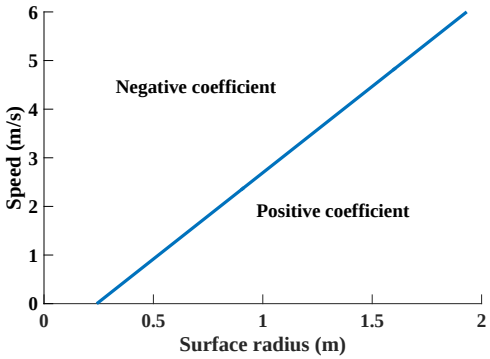

Figure 119: Sign of the coefficient of the cosine term in the normal force.

For this case, the normal force between the vehicle and the ground becomes:

$$N_z = (m_b + m_v)g\cos\theta_s - [m_b(H_{cm}\cos\theta_s + r_w - r_s) + m(r_w - r_s)]\dot{\theta_s}^2 \tag{192}$$

In a hole, the cosine term is positive when (given $v > 0$ and $r_s > 0$):

$$v < (r_s - r_w)\sqrt{\frac{(m_b + m_g)g}{m_b H_{cm}}} \tag{193}$$

Figure 119 shows the sign of the coefficient of the cosine term in (192)for given speeds and surface radii. This curve is translated downwards with respect to the corresponding one for a hole presented above in Figure 116.

Figure 120 shows the normal force between the vehicle and the ground as a function of the slope angle at different surface radius for a vehicle going through a hole at 1 m/s. As the surface radius becomes smaller, the maximum force is reduced, even becoming zero for a radius of 0.45 m for a significant range of slope angles because the vehicle "flys" over the hole.

Figure 121 shows the normal force going through a hole with a surface radius of 1 m at different speeds. As the speed is increased, the normal force is reduced, increasing the risk of the vehicle losing contact with the ground.

Figure 122 shows the minimum surface radius at each slope angle required to maintain the normal force above zero. As in the case of a bump, the required surface radius to maintain wheel/ground contact increases as the speed increases.

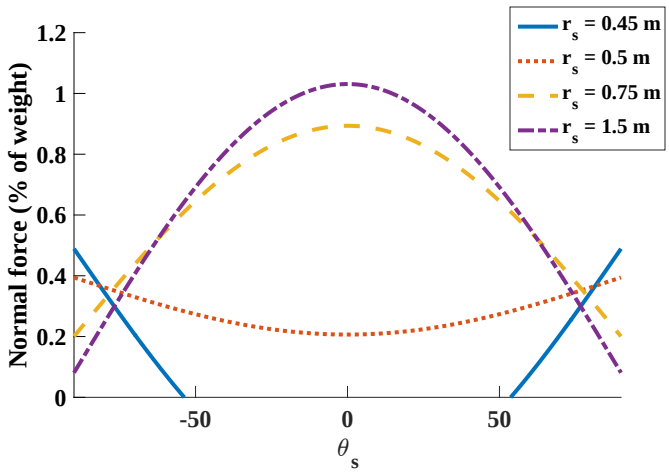

Figure 120: Effect of hole radius at 1 m/s.

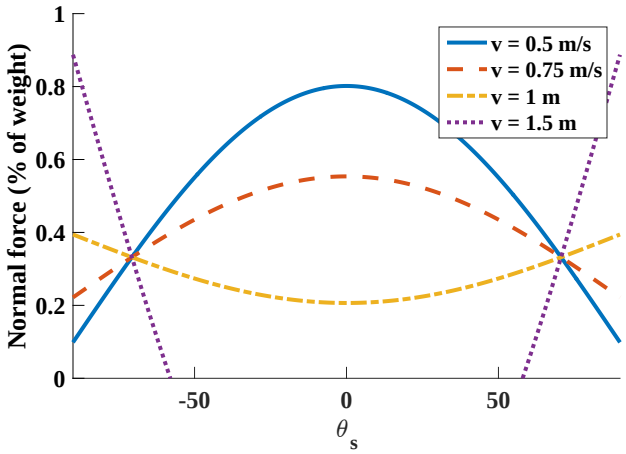

Figure 121: Effect of speed going through a hole with a surface radius of 1 m.

Figure 123 shows the maximum speed allowed at each surface radius in order to maintain contact with the ground. The maximum speed is significantly reduced as the radius of the hole is reduced.

5.4.3 Special case: when the hole surface radius is smaller than the wheel radius

When the radius of the hole is smaller than the radius of the wheel it is impossible for the wheel to maintain single-point contact with the ground. A wheel going through a hole with a radius smaller than the wheel radius is shown in Figure 124. Note that

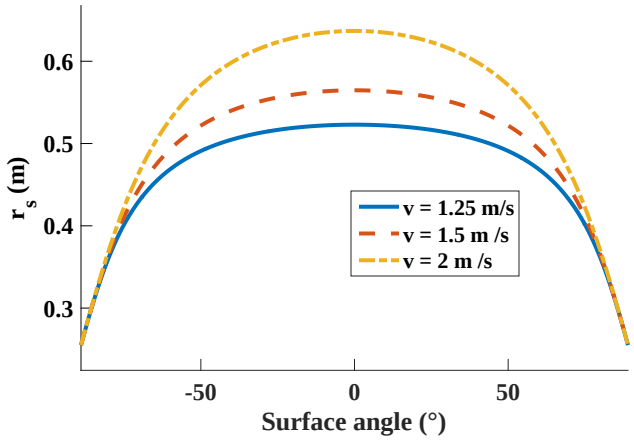

Figure 122: Minimum surface radius for each slope angle required to maintain contact with the ground at different speeds.

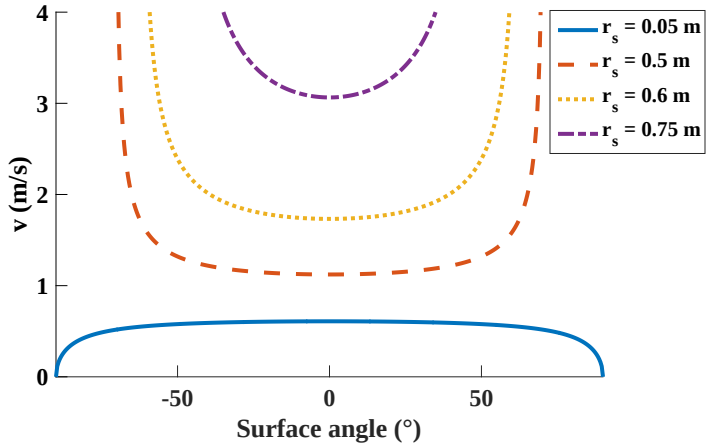

Figure 123: Maximum speed for each slope angle to maintain contact with the ground at different surface radii.

the path followed by the wheel axes experiences an instantaneous change in the slope angle upward as the wheel hits the bottom of the hole.

In this section, the special case where the initial slope is zero is examined. This is the equivalent to encountering a rectangular bump if the initial slope angle is zero and the final slope angle is -90°. The wheel axis initially follows a horizontal path until the wheel makes contact with the edge of the bump. Then, it follows the same path as if it was following a convex circular surface with an initial slope θ_{s0}. The

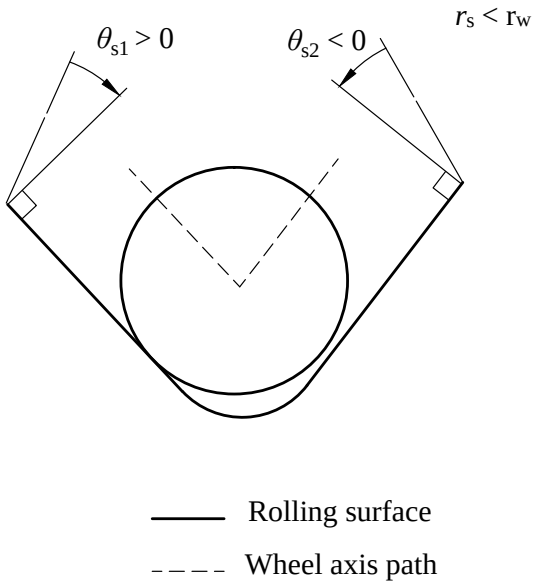

Figure 124: Geometric description of small radius hole

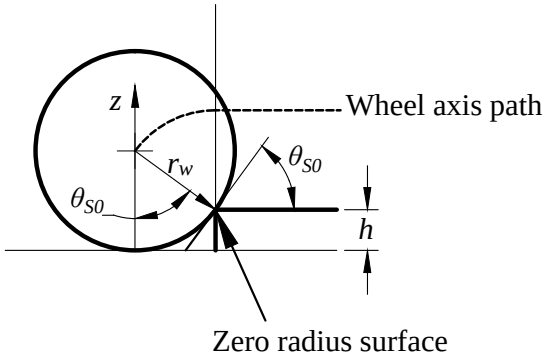

Figure 125: Geometric description of bump as a slope

step hight is called "equivalent step height." When it finishes climbing the bump, the slope becomes zero. This is shown in Figure 125.

The height of the bump can be related to the initial equivalent slope angle by the following relation:

$$\cos\theta_{s0} = \frac{r_s - h}{r_w} \tag{194}$$

If the vehicle is traveling at speed v_0 when it encounters a rectangular bump, then it will be assumed that this is the same speed at which it will begin to follow the

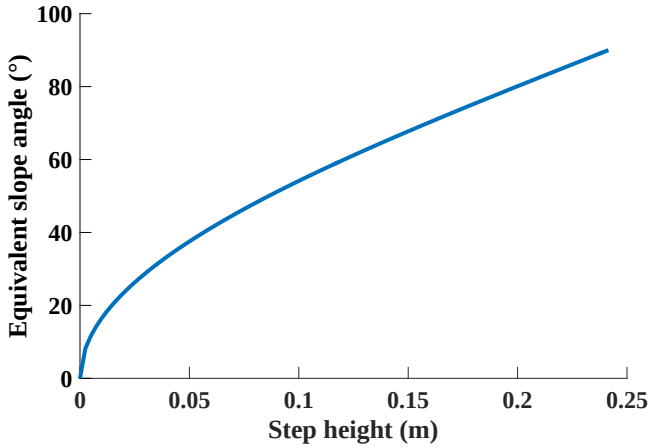

Figure 126: Equivalent inital slope angle for a rectangular bump.

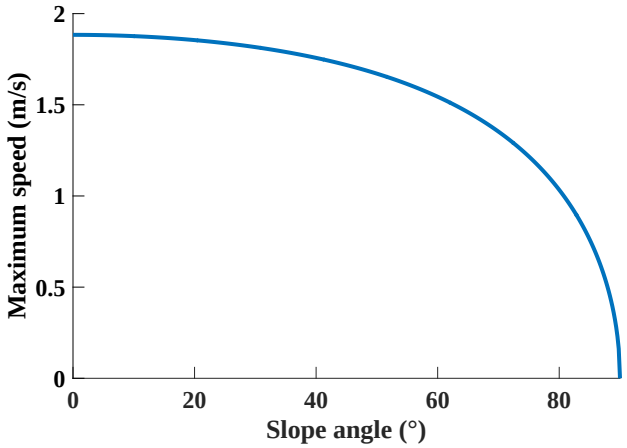

Figure 127: Maximum speed allowed at each equivalent initial slope angle.

circular path of radius r_w around the edge of the step. Equation (189) can be used to determine whether the vehicle can climb the step without losing contact with the ground or if it will jump into the air as indicated by a normal force equal to zero.

Figure 126 shows the equivalent slope angle for each step height for the wheel of a Segway i2.

Figure 127 shows the maximum speed allowed for the vehicle to climb a step with a specified initial slope angle. If the speed is above this maximum, then the vehicle will jump off the top of the step. It is important to note that this curve is undetermined at an initial slope of zero.

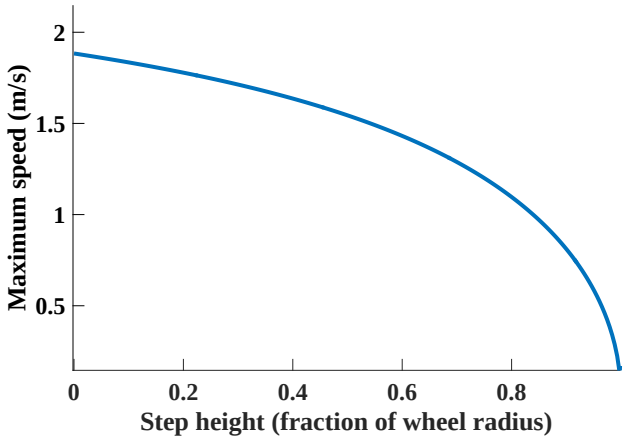

Figure 128: Maximum speed allowed at each step height.

Figure 127 can be plotted against the equivalent step height as defined in Figure 125. Figure 128 shows the maximum speed allowed for the vehicle to climb a step as a function of the height of the step. If the speed is above this maximum, the vehicle will jump off the step. This curve is also undetermined at a step height of zero.

5.5 Dynamic simulations of irregular surfaces

In order to examine the pitch stability of the vehicle, the slip behavior, and the speed response, it is necessary to perform dynamic simulations of holes and bumps. In this section, a dynamic model is presented and used to simulate the vehicle going over inclined surfaces, holes, and bumps.

The dynamic equations of motion, considering travel in the x-direction parallel to the surface, were developed. These equations are:

$$\begin{aligned}
&(I_{py} + m_p(x_{wp}^2 + z_w p^2))(\ddot{\theta}_p) + (I_{py} + m_p(x_{wp}^2 + z_w p^2))(\ddot{\theta}_s) \\
&-m_p(x_{wp}\sin(\theta_p) - z_w p\cos(\theta_p))(\dot{v}_x) + m_p(x_{wp}\cos(\theta_p)v_x + z_w p\sin(\theta_p)v_x)(\dot{\theta}_s) \\
&+T_l + T_r - m_p g(x_{wp}\cos(\theta_p + \theta_s) + z_w p\sin(\theta_p + \theta_s))
\end{aligned} \tag{195}$$

$$
\begin{aligned}
&-2I_y \sin(\theta_s)(\dot{\theta}_s)(\dot{\theta}_w)/(r\cos(\theta_s)^2) + 2I_y(\dot{v}_s)/(r^2\cos(\theta_s)^2) \\
&+(T_l + T_r)/(r\cos(\theta_s)) - 2I_y(\dot{v}_x)/(r^2\cos(\theta_s)^2) \\
&-F_{x,l} - F_{x,r} - 2I_y \sin(\theta_s)(\dot{\theta}_s)^2/(r\cos(\theta_s)^2)
\end{aligned} \tag{196}
$$

$$
\begin{aligned}
&m_p(z_w p\cos(\theta_p) - x_{wp}\sin(\theta_p) - \tan(\theta_s)(x_{wp}\cos(\theta_p) + z_w p\sin(\theta_p)))(\ddot{\theta}_p) \\
&+(-m_p(x_{wp}\sin(\theta_p) - z_w p\cos(\theta_p)) - \tan(\theta_s)(m_p\cos(\theta_p)x_{wp} \\
&+m_p\sin(\theta_p)z_w p))(\ddot{\theta}_s) + 2I_y\sin(\theta_s)(\dot{\theta}_s)(\dot{\theta}_w)/(r\cos(\theta_s)^2) \\
&-2I_y(\dot{v}_s)/(r^2\cos(\theta_s)^2) + (m_p + 2m_w + 2I_y/(r^2\cos(\theta_s)^2))(\dot{v}_x) \\
&+(-m_p(x_{wp}\cos(\theta_p) + z_w p\sin(\theta_p)) - \tan(\theta_s)(m_p\cos(\theta_p)z_w p \\
&-m_p\sin(\theta_p)x_{wp}))(\dot{\theta}_p)^2 + (-m_p(2x_{wp}\cos(\theta_p) + 2z_w p\sin(\theta_p)) \\
&-\tan(\theta_s)(2m_p\cos(\theta_p)z_w p - 2m_p\sin(\theta_p)x_{wp}))(\dot{\theta}_s)(\dot{\theta}_p) \\
&+(2I_y\sin(\theta_s)/(r\cos(\theta_s)^2) - m_p(x_{wp}\cos(\theta_p) + z_w p\sin(\theta_p)) \\
&-\tan(\theta_s)(m_p\cos(\theta_p)z_w p - m_p\sin(\theta_p)x_{wp}))(\dot{\theta}_s)^2 \\
&-\tan(\theta_s)(m_p + 2m_w)v_x(\dot{\theta}_s) - (T_l + T_r)/(r\cos(\theta_s))
\end{aligned} \tag{197}
$$

5.5.1 Constant slope

5.5.1.1 Effect of initial pitch angle

Figure 129 shows the effect of different initial pitch angles when encountering a sloped surface with a constant slope angle. Figure 129(a) shows the cases for downhill slopes and Figure 129(b) shows the cases for uphill surfaces. The simulations were stopped when the pitch angle reached 60° because transporters cannot recover from these conditions.

For positive slope angles (downhill) a positive pitch angle (forward leaning) makes the vehicle more prone to instability. This is evidenced by the $\theta_p = 10°$ and $\theta_p = 20°$ curves on Figure 129(a). Similarly, Figure 129(b) shows that leaning backwards reduces the stability of the vehicle when going uphill.

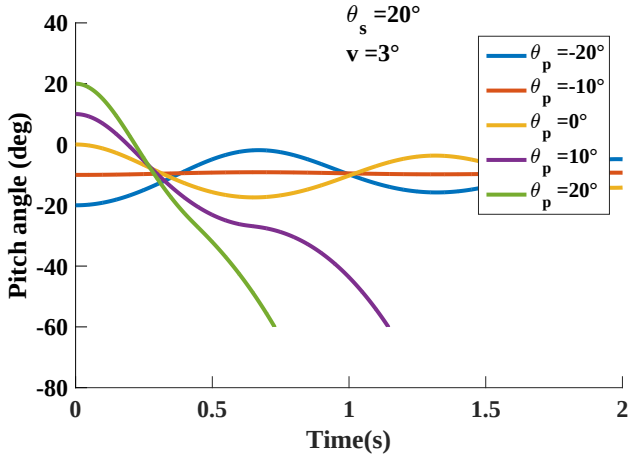

(a) Positive slope angle.

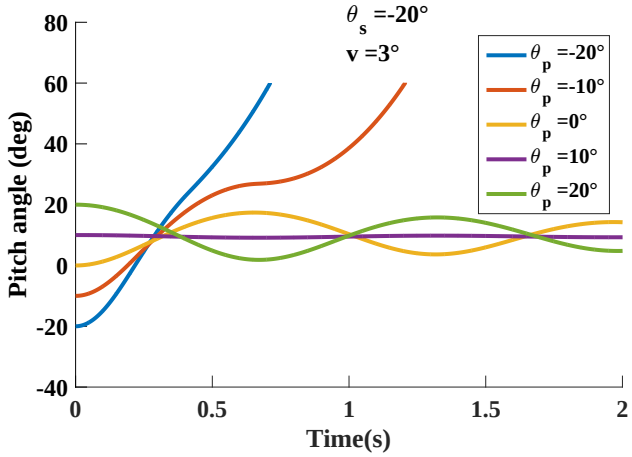

(b) Negative slope angle.

Figure 129: Effect of initial pitch angle when going over constant slope surfaces - Pitch response.

Figure 130 shows the speed response after the vehicle is given an initial pitch angle. Figure 130(a) shows the speed when going up an inclined surface. Going downhill, a forward leaning angle causes the speed to increase dramatically. Such an aggressive acceleration is what cases the pitch angle in Figure 129(a) to decrease very rapidly and eventually causes the vehicle to fall backward before the controller is able to slow down the base. On the other hand, when going uphill, if the vehicle pitch angle is too negative, then the speed is significantly reduced, as shown in Figure 130(b). This causes the vehicle to fall forward too quickly before the controller is able to speed up the vehicle. Note that in both cases, after the initial increase or decrease in speed, the vehicle attempts to slow down/speed up but fails to do so until the simulation is stopped by reaching an extreme pitch angle.

Figure 131 shows the normal force between the vehicle and the ground. In Figure 131(a) the downhill case is shown. Note that when the pitch angle reaches a value around -20° the normal force decreases significantly. In the uphill case, shown in Figure 131(b), the same occurs when the pitch angle goes past approximately 20°.

Figure 132 shows the slip ratio for both the uphill and downhill cases. Note that for the cases where the pitch angle became unstable, the slip ratio was also greater. As the normal force is reduced when the pitch angle goes beyond a certain limit, the traction force is reduced. This effect makes the vehicle unable to accelerate or deccelerate effectively. The moment when the slip ratio becomes unstable in Figure 132(a) is the same moment at which the speed stops decreasing in Figure 130(a). Similarly, the vehicle stops accelerating as shown in Figure 130(b) when the slip ratio becomes unstable in Figure 132(b).

5.5.1.2 Effect of initial speed

Figure 133(a) shows the speed response of the vehicle after releasing it on an inclined surface at an initial pitch angle of 5°, but with different initial speeds. Figure 133(a)

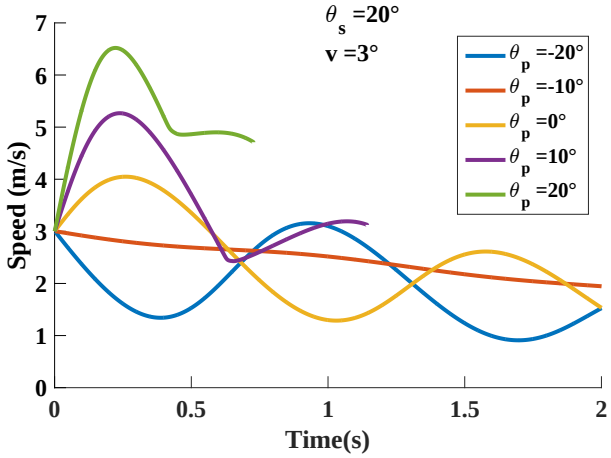

(a) Positive slope angle.

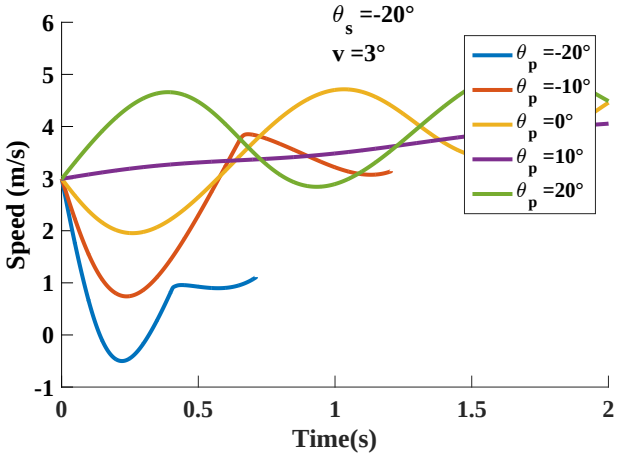

(b) Negative slope angle.

Figure 130: Effect of initial pitch angle when going over constant slope surfaces - Speed response.

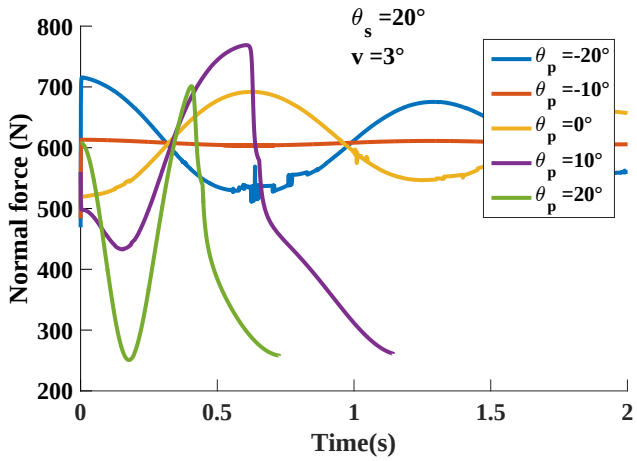

(a) Positive slope angle.

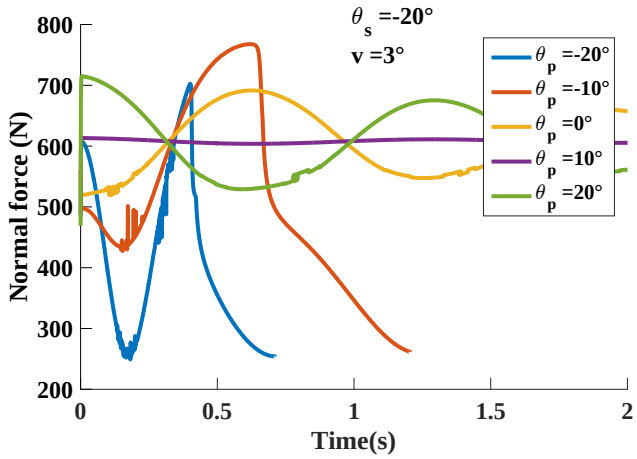

(b) Negative slope angle.

Figure 131: Effect of initial pitch angle when going over constant slope surfaces - Normal force.

shows the case where the slope angle is positive or downhill, while Figure 133(b) shows the negative slope angle case. In all cases, the only effect of changing the speed was to translate the response without changing its shape. There was no visible effect on either the pitch angle response, the normal force, or the slip ratio. Because of this, these data are omitted.

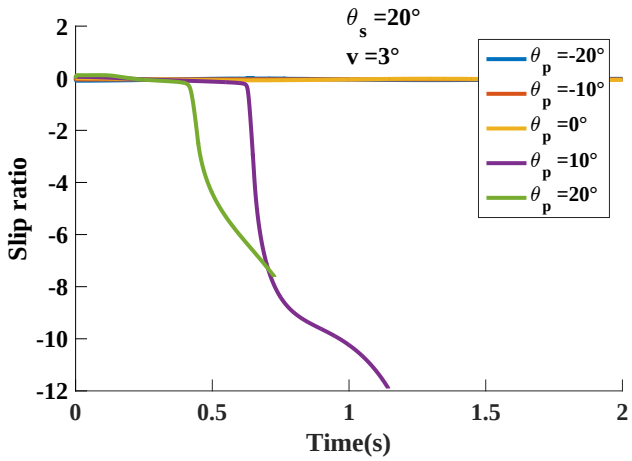

(a) Positive slope angle.

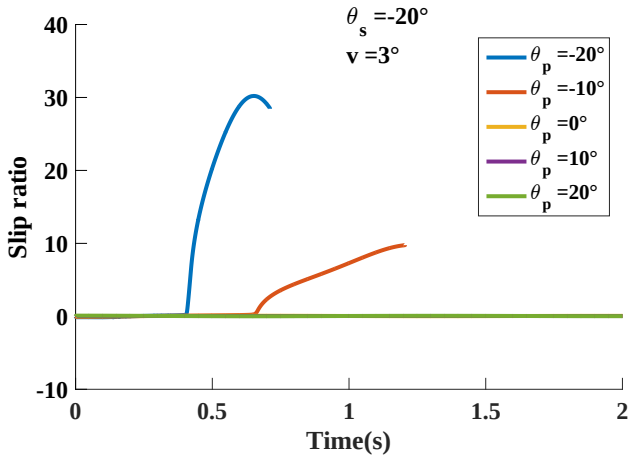

(b) Negative slope angle.

Figure 132: Effect of initial pitch angle when going over constant slope surfaces - Slip ratio.

5.5.1.3 Effect of slope angle

The vehicle was simulated going uphill and downhill at both positive and negative pitch angles and different surface angles. Figure 134 shows the pitch response of the vehicle. Figure 134(a) shows the case where the vehicle is leaning forward and Figure 134(b) when it is initially leaning backwards.

When the vehicle leans forward it remains stable for slope angles less than 10°. The pitch angle shows less variation at more negative slope angles. This means that

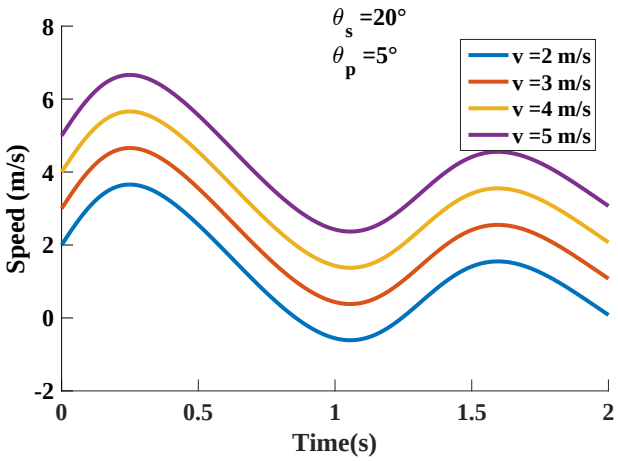

(a) Positive slope angle

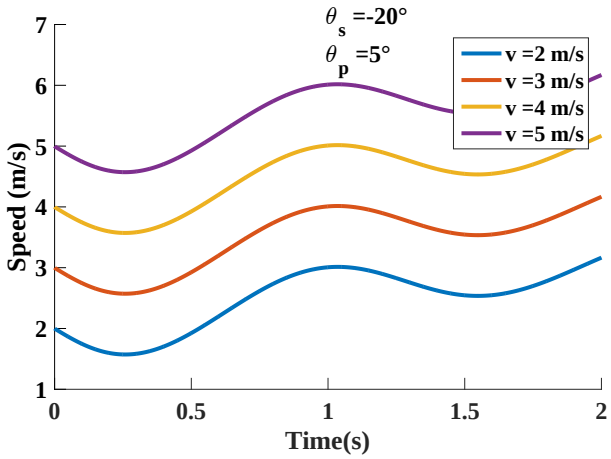

(b) Negative slope angle

Figure 133: Effect of initial speed when going over constant slope surfaces -Speed response.

pitching forward makes the vehicle more stable when climbing up a slope.

On the other hand, when the vehicle leans backwards at an angle of -10° the vehicle becomes unstable when the slope angle is more negative. This means that leaning backwards is beneficial when going down a slope (positive slope angle), but detrimental when going uphill.

Figure 135 shows the speed response of the vehicle for different slope angles and constant initial pitch angle of 10° and -10° and speed of 3 m/s. The behavior shown

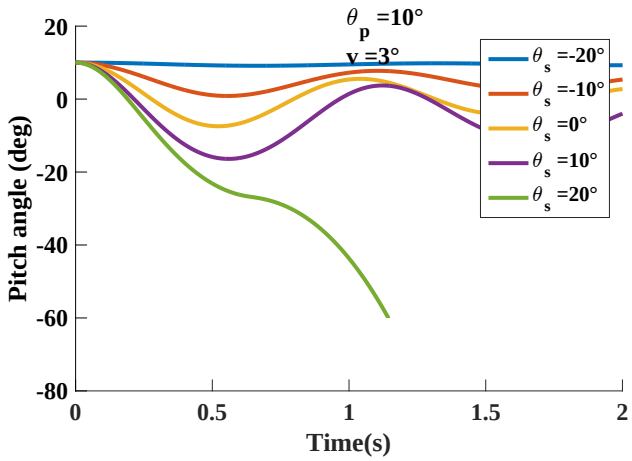

(a) Positive pitch angle.

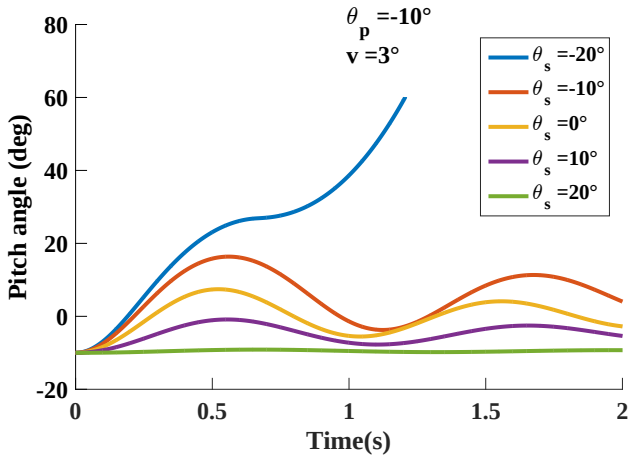

(b) Negative pitch angle.

Figure 134: Effect of slope angle when going over constant slope surfaces - Pitch response.

here is similar to the one exhibited in the previous section. When the vehicle pitch angle goes past an angle of approximately -20° for a downhill slope of 20° it was unable to continue reducing the speed as needed to maintain balance. This is shown in Figure 135(a). A similar behavior is shown for the case of an uphill slope of -20° when the pitch angle goes past 20°, but the vehicle is unable to accelerate, as shown in Figure 135(b).

Figure 136 shows the normal force between the vehicle and the ground. Similar to

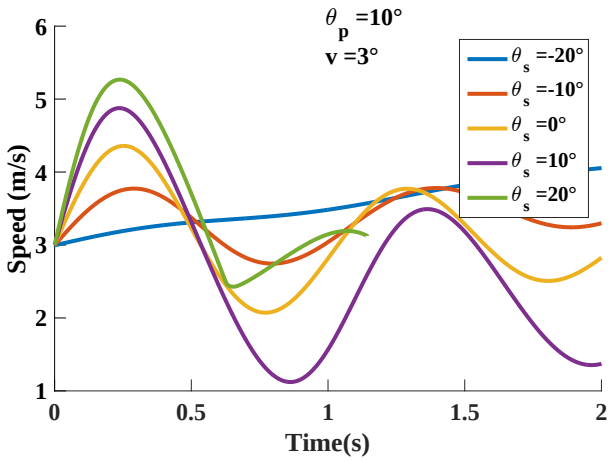

(a) Positive pitch angle.

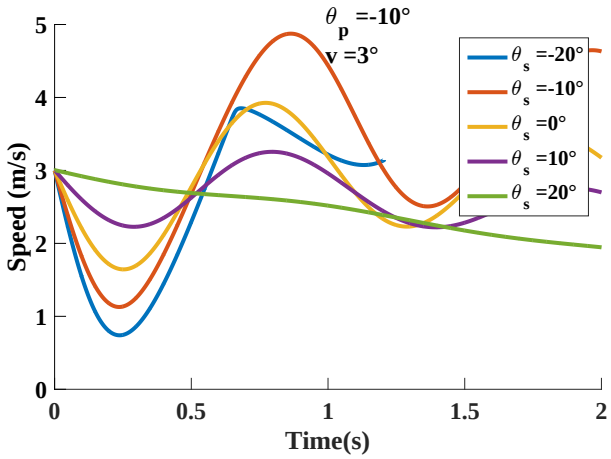

(b) Negative pitch angle.

Figure 135: Effect of slope angle when going over constant slope surfaces - Speed response.

what was observed in the previous section, when the pitch angle goes past a certain limit there is an abrupt reduction in the normal force between the vehicle and the ground for the cases when the vehicle went unstable.

Figure 137 shows again that this reduction in the normal force produces a marked increase in the wheel slip ratio, as shown in both Figure 137(a) and Figure 137(b). This is the reason why the vehicle was unable to accelerate as needed in order to preserve the pitch stability.

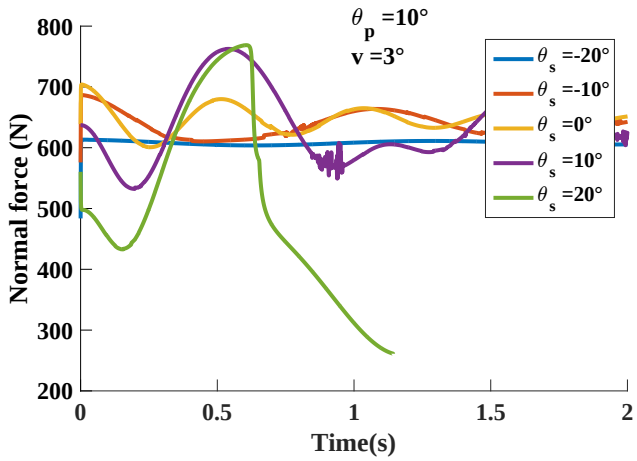

(a) Positive pitch angle.

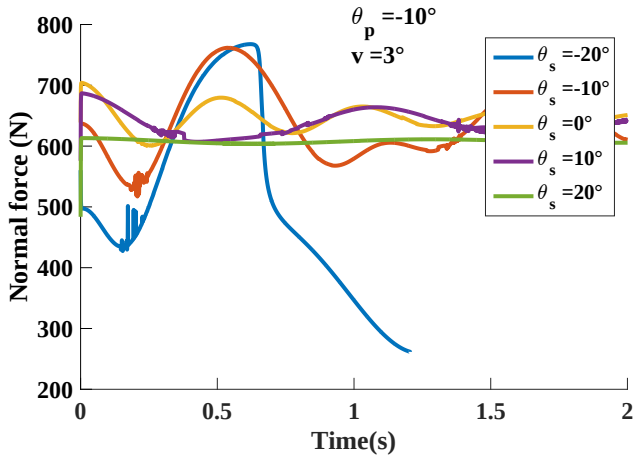

(b) Negative pitch angle.

Figure 136: Effect of slope angle when going over constant slope surfaces - Normal force.

5.5.2 Non constant slope

The vehicle was simulated while going over bump and holes. These surfaces have a specified initial slope angle, and surface radius. First, the results for when the vehicle goes over a hole are presented. Then, the results when the vehicle goes through a bump-like surface are presented.

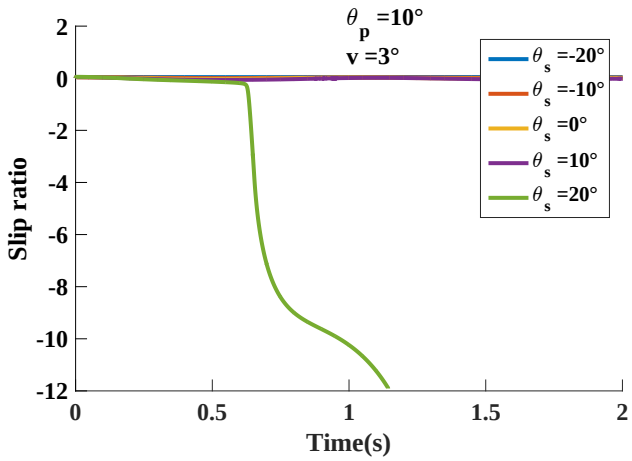

(a) Positive pitch angle.

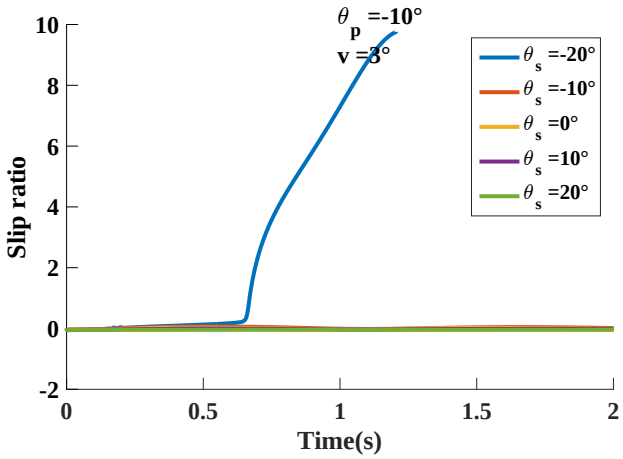

(b) Negative pitch angle.

Figure 137: Effect of slope angle when going of over constant slope surfaces - Slip ratio.

5.5.2.1 Holes

The vehicle was simulated going through a 0.5 m radius hole with initial and final slope angles of 45° and -45° at different initial speeds starting from level ground with a slope of 0°. The vehicle was initially in a balanced position with a pitch angle of 0°.

Figure 138 shows the pitch response of the vehicle. At low speeds, the pitch initially decreases, but the vehicle is able to regain balance. At 3 m/s and 5 m/s the

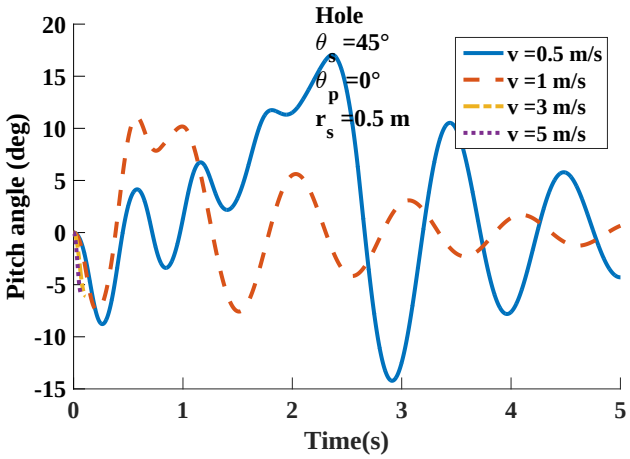

Figure 138: Pitch response while going through a hole at different speeds.

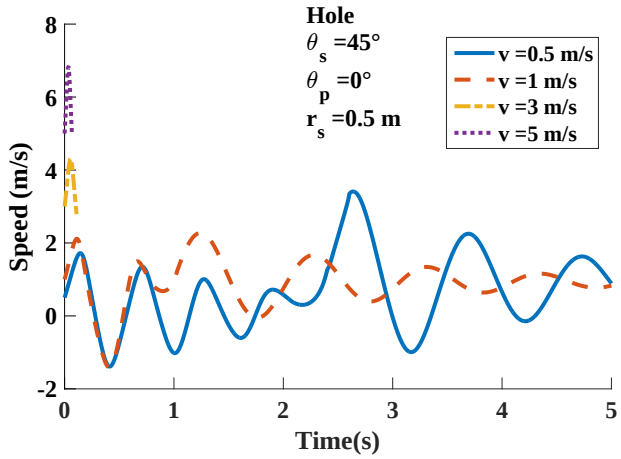

Figure 139: Speed response while going through a hole at different speeds.

simulation was stopped because the vehicle lost contact with the ground very rapidly. Interestingly, the amplitude of the pitch oscillation is larger at smaller speeds for the cases where contact with the ground was not lost. The simulation stopped sooner for the 5 m/s case than for the 3 m/s case.

Figure 139 shows the speed response at different initial speeds. Initially all the responses look quite similar except that they are translated in the vertical direction. The 0.5 m/s case shows a larger variation in speed as time progresses than the 1 m/s.

Figure 140 shows the normal force for all four cases. The 3 m/s and 5 m/s cases

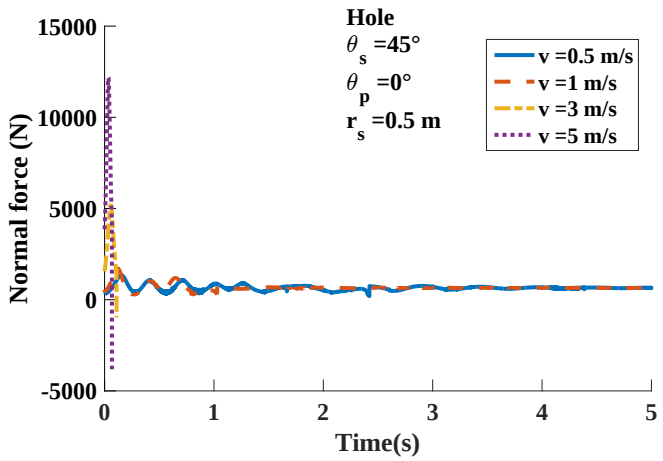

Figure 140: Normal force while going through a hole at different speeds.

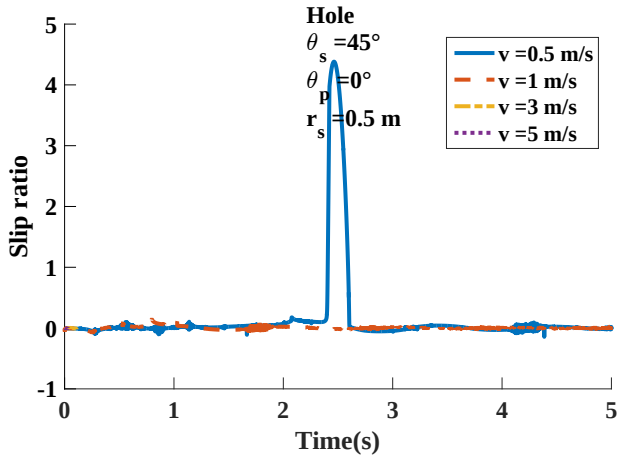

Figure 141: Slip ratio while going through a hole at different speeds.

show that the normal force very quickly drops below zero. This means that the vehicle is unable to travel on the ground following the surface of the hole, but instead, it flies off the edge shortly after entering it.

Figure 141 shows the slip ratio. The large variation in the pitch and speed of the 0.5 m/s case causes the vehicle to slip at around the 2.5 s mark. However, it was able to recover from the wheel-slip condition.

The vehicle was also simulated going at 1 m/s through a 0.5 m radius hole with slope angles of 45° and -45° at different initial pitch angles. Figure 142 shows the pitch response when the initial pitch angle is -10°, 0° and 10°. It shows that leaning

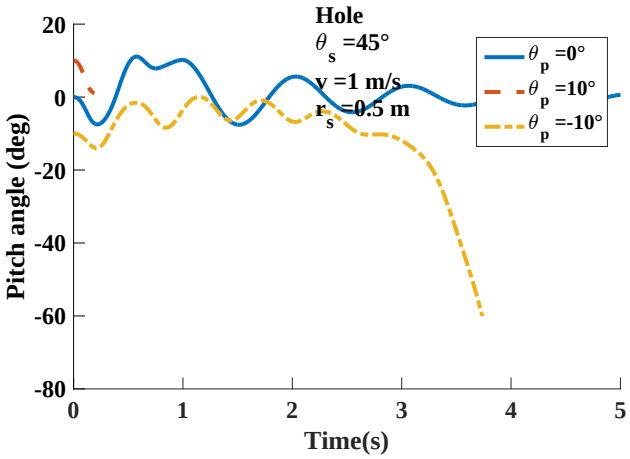

Figure 142: Pitch response while going through a hole at different pitch angles.

forward (10°) reduces the ability of the vehicle to go through the hole. In fact, in this case the simulation was stopped because the vehicle lost contact with the ground. For the initial pitch angle of 0°, the vehicle was able to remained balance for the whole duration of the simulation. However, for the leaning back case (-10°) the vehicle was able to stabilize itself only until the 3 second mark, where the pitch angle became unstable.

Figure 143 shows the speed response for each case. The further forward the vehicle leaned, the more it accelerated towards the hole and reached it at a higher speed. The combination of high speed and pitch angle cause the vehicle to lose contact with the ground in the 10° case. For the -10°, the vehicle took longer to go through the hole and it lost stability when it climbed out of it at around the 3.2 second mark.

Figure 144 shows that at the 3.2 second mark the normal force reaches one of its minimum values and it is at this time where the slip ratio also increased dramatically, as seen in Figure 145.

5.5.2.2 Bumps

The vehicle was also simulated going over bump surfaces with a radius of 0.5 m and 45° angles at the edges at different speeds. Figure 146 shows the pitch response of

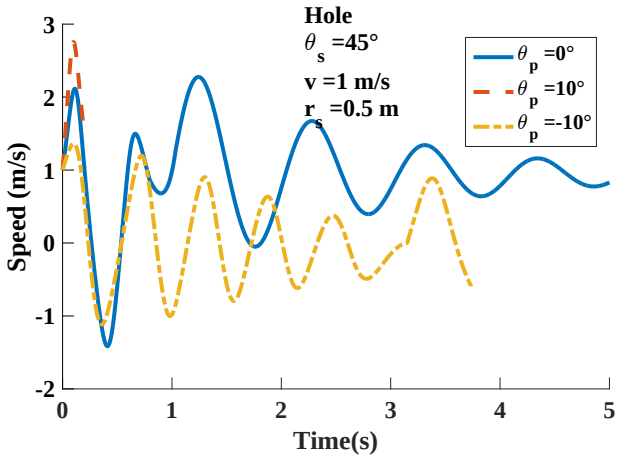

Figure 143: Speed response while going through a hole at different pitch angles.

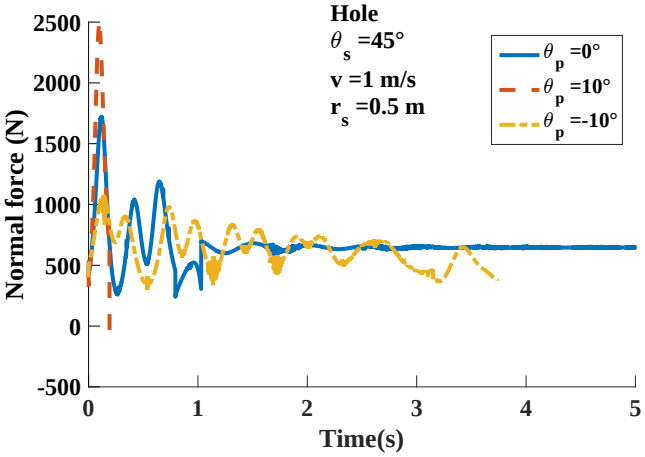

Figure 144: Normal force while going through a hole at different pitch angles.

the vehicle. The vehicle was only able to go over the bump without losing contact with the ground, incurring high wheel slip or losing balance, when the speed was 0.5 m/s. Higher speeds caused the vehicle to pitch over or jump off the bump.

The speed response is shown in Figure 147. Figure 148 shows the normal force between the vehicle and the ground. The force dropped below zero immediately at the beginning for the 3 m/s and 5 m/s cases. This means that the vehicle jumped off the surface immediately after hitting the bump and this is why it is not shown in the plots.

Figure 149 shows the slip ratio. The data show that the 1 m/s case experienced a

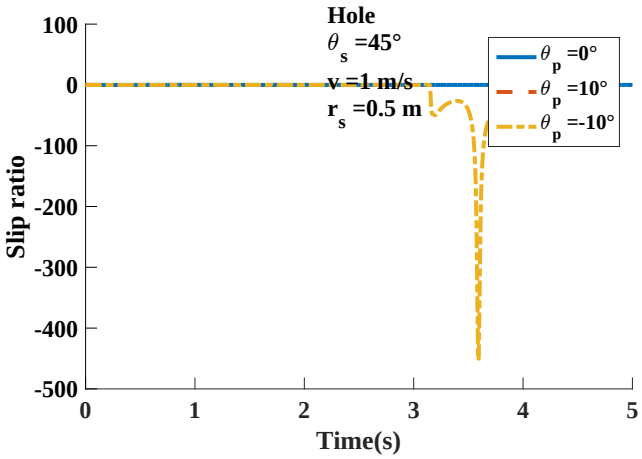

Figure 145: Slip ratio while going through a hole at different pitch angles.

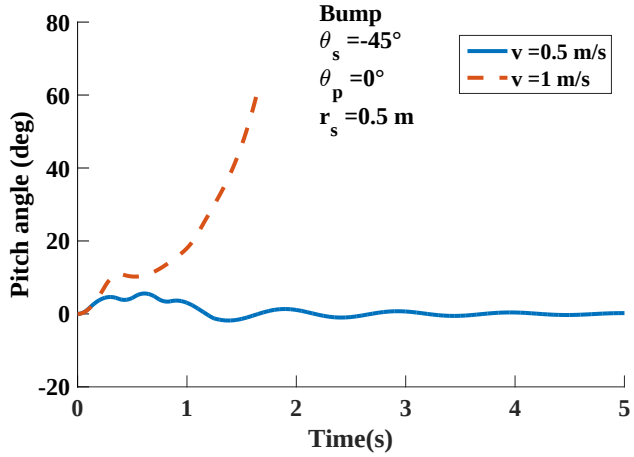

Figure 146: Pitch response while going over a bump at different speeds.

very large wheel slip that caused the vehicle to lose balance, as was shown in Figure 146.

The effect of different initial pitch angles was also studied. Figure 150 shows the responses going at 1 m/s and with initial pitch angles of 0, 10° and -10°. The 0° pitch case lost balance after 1 second by falling forward after hitting the bump. Meanwhile the 10° lost contact with the ground before the 1 second mark. The -10° case was able to balance itself throughout the motion over the bump. These results clearly demonstrate the value of leaning backward just before hitting a bump.

The speed behavior of the vehicle is shown in Figure 151. It shows that the

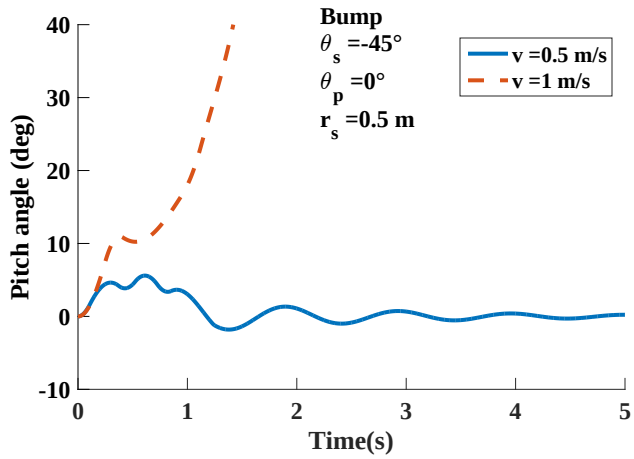

Figure 147: Speed response while going over a bump at different speeds.

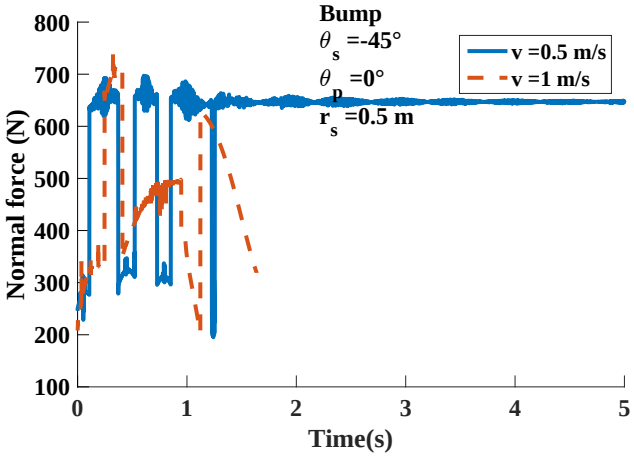

Figure 148: Normal force while going over a bump at different speeds.

more negative the initial pitch angle, the more the vehicle reduces its speed when encountering the bump. This helps the vehicle maintain its stability

The normal force is shown in Figure 152. When the initial pitch angle was 10°, the vehicle lost contact with the ground, as a result of hitting the bump at a higher speed than the other two cases.

Figure 153 shows the slip ratio. The responses that for the 0° case, after the vehicle starts leaning forward around the 0.4 second mark, the machine starts accelerating in order to regain balance. However, it is unable to do so, and at the 1 second mark, the slip ratio increases dramatically. As a result, the wheel slip significantly reduces

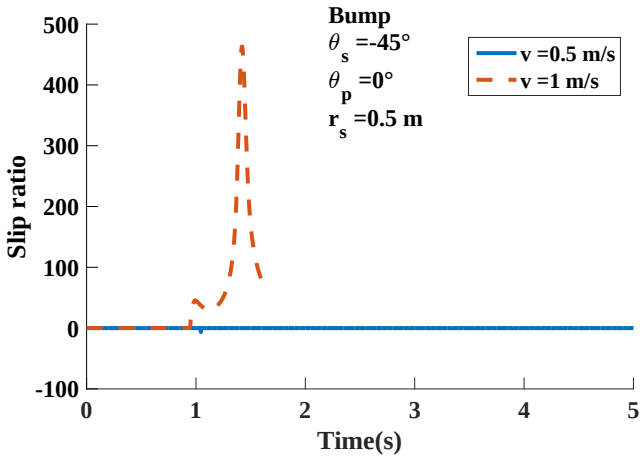

Figure 149: Slip ratio while going over a bump at different speeds.

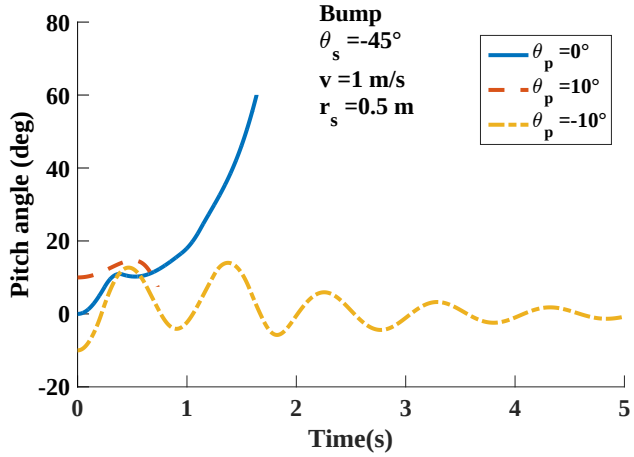

Figure 150: Pitch response while going over a bump at different initial pitch angles.

the ability of the vehicle to accelerate.

5.6 Summary

This chapter presented the effect of several types of non-flat surfaces on the stability of wheeled inverted pendulum vehicles. It was shown that an increasing slope angle requires a larger coefficient of friction for the vehicle to be able to climb and a larger pitch angle for the vehicle to achieve, at least, static equilibrium. It becomes physically impossible for a vehicle to climb a slope above 40°. The vehicle stability is also reduced laterally when traveling transverse on an inclined plane and is further

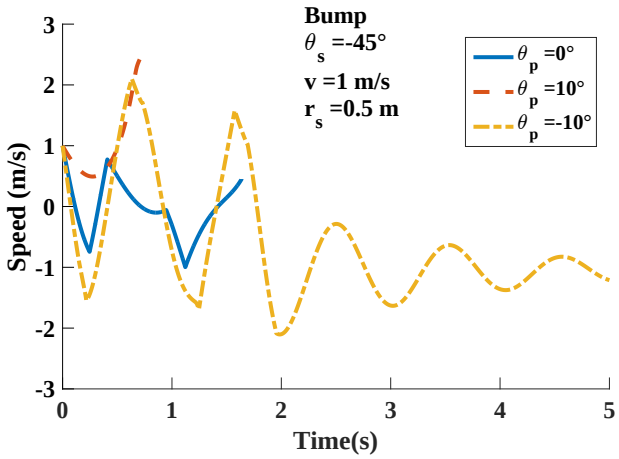

Figure 151: Speed response while going over a bump at different initial pitch angles.

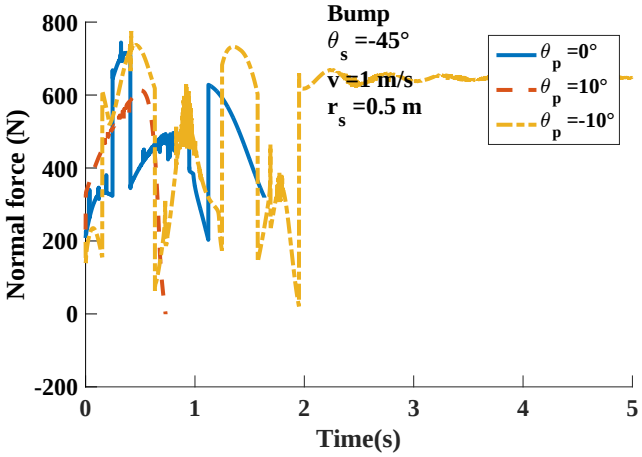

Figure 152: Normal force while going over a bump at different initial pitch angles.

reduced as the ratio between the height of the center of mass of the wheels and the separation between the wheels increases. A geometrical description of a generic irregular surface was introduced and used to build dynamic simulations of the vehicle going over bumps and through holes. The effects of the bump and hole surfaces were shown to reduce the wheel-ground forces and limit the speed at which the vehicle can safely travel without losing contact with the ground. Dynamic simulations showed that the slope angle can affect the pitch stability of the vehicle. In addition, when traveling through holes or bumps, pitch instability, wheel slipping, and loss of ground contact were observed.

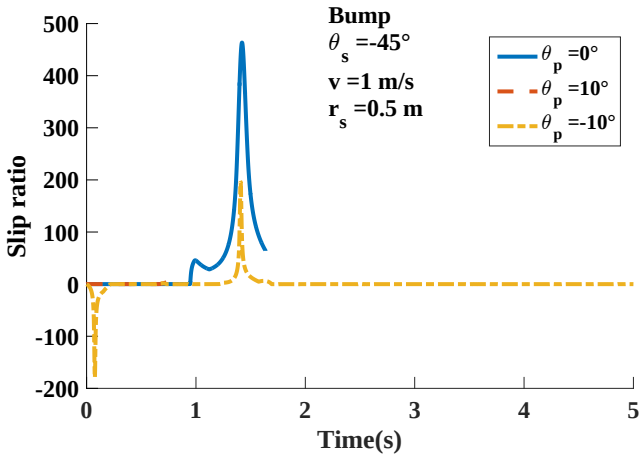

Figure 153: Slip ratio while going over a bump at different initial pitch angles.

CHAPTER VI

TRACTION CONTROL

As the previous chapters have demonstrated, wheeled inverted-pendulum transporters exhibit dangerous dynamic responses when one of their wheels slip. In order to lessen such dangers, traction-control algorithms have been developed.

The traction control used by the Segway is described in US Patent 6,408,240 [42]. Figure 154 shows a reproduction of Figure 11 from that patent, which is a flow chart of how the traction control works. The basic strategy employed is similar to anti-lock breaking on automobiles. If wheel slip is detected, then power to that wheel is reduced until the slipping stops. The patent considers two types of traction loss. The first type is when the rider tries to accelerate or decelerate faster than the wheel and the ground allow. The second type is when the transporter encounters a slick spot or loses contact with the ground.

The indicator used to initiate the traction control is the acceleration of the wheels. Given that the motors have known torque limits, the wheel acceleration is limited. When the measured acceleration exceeds a specified limit, the machine assumes the wheel is slipping and initiates the traction control. The computer estimates the inverse moment of inertia of the wheel by dividing the wheel acceleration by the commanded torque. If the angular acceleration is greater than the specified limit, then the slip condition flag is set. At this point, the wheel torque is reduced to zero and then gradually incremented back to the value required for balancing the machine if the slip condition is cleared. The inverse moment of inertia is compared to a minimum value and if it is less than that the slip condition is cleared.

According to the patent, the inverse inertia is very large when there is loss of

contact with the ground because it will include only the wheel inertia, rather than the wheel combined with the machine and rider. Note that the strategy employed by the Segway traction control is a risky one. The machine turns off the balancing controller in hopes that the wheels regain traction before the machine, and rider, fall too far over.

In the next sections of this chapter the effectiveness of two traction control systems similar to the one in the patent are presented and evaluated. Following that material, a traction control for one-wheel slip situations based on yaw rate feedback is presented. A one-wheel slip case with a forward leaning operator is used to simulate the traction controllers. In all cases, the simulations were stopped either when a pitch angle of 90° was reached, or when the normal force between one of the wheels and the ground became zero thereby indicating a roll instability.

6.1 Fixed limited wheel acceleration controller

The traction control presented in this section uses the wheel angular acceleration to limit the torque output to the wheels and control the wheel slip. This approach is similar to the method in the Segway patent. When the wheel angular acceleration exceeds a threshold, α_u, the torque output from the motor is rapidly ramped down to zero. Once the wheel angular acceleration is below a lower threshold α_l, the output torque is ramped back up to the torque desired by the balancing controller.

The feedback control is:

$$T_i = \begin{cases} T_{b,i}, & \text{if } Slip_i = false \\ 0, & \text{if } Slip_i = true \end{cases} \tag{198}$$

where $i = l, r$ for the left and right wheel respectively, $T_{b,i}$ is the torque commanded by the balancing controller, and $Slip_i$ is the slip condition flag.

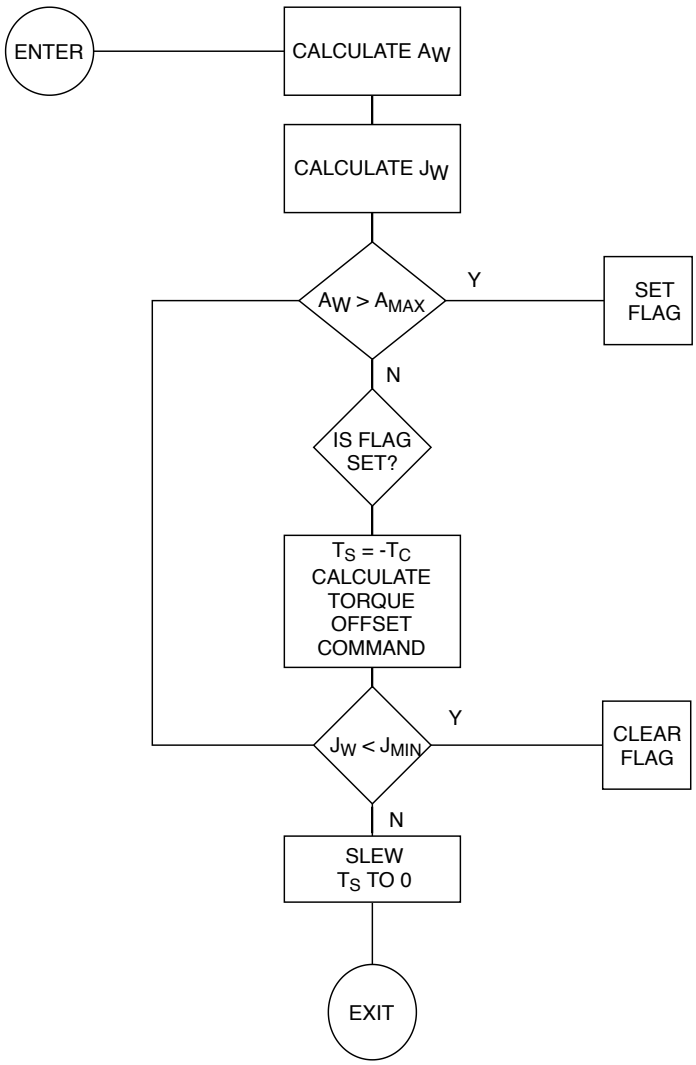

Figure 154: Segway traction control as described in US Patent 6,408,240, Fig. 11.

The slip condition is given by:

$$Slip_i = \begin{cases} true, & \text{if } \alpha_i > \alpha_u \\ true, & \text{if } \alpha_i > \alpha_l \text{ and } Slip_i = true \\ false, & \text{if } \alpha_i \leq \alpha_l \end{cases} \tag{199}$$

The torque commanded by the balancing controller is given by:

$$T_{b,l} = K_p\left(\theta_p - \theta_{des}\right) + K_d\dot{\theta}_p - T_\beta \tag{200}$$

$$T_{b,r} = K_p\left(\theta_p - \theta_{des}\right) + K_d\dot{\theta}_p + T_\beta \tag{201}$$

$$T_\beta = K_{ff}\dot{\beta}_{des} + K_{\beta p}\left(\dot{\beta} - \dot{\beta}_{des}\right) + K_{\beta i}\int_0^t \left(\dot{\beta} - \dot{\beta}_{des}\right) dt \tag{202}$$

The threshold values can be derived from the results in Section 5.1, where (140) indicates that on a flat surface, the maximum available acceleration is given by:

$$a_x = \mu g \tag{203}$$

If a maximum friction coefficient of 0.92 is assumed, along with a wheel radius of 0.2415 m, the maximum angular acceleration that should occur under no slip conditions is:

$$\alpha_u = 37.37 \text{ rad/s}^2 \tag{204}$$

This value was rounded up to $\alpha_u = 40$ rad/s^2 for simulation purposes. The lower angular acceleration limit which is used to clear the slip flag, was set to $\alpha_l = 1$ rad/s^2 for one version of the traction controller (Accurate-Limit traction controller). A second controller (Excess-Value traction control) with angular acceleration limits of $\alpha_l = 5$ rad/s^2 and $\alpha_u = 400$ rad/s^2 was also simulated for comparison purposes.

A simulation of an operator accelerating a two-wheeled inverted pendulum transporter by leaning forward to an angle if 18.5° from an initial speed of 1 m/s, while the right wheel travels over a reduced-friction surface, was used to evaluate the performance of the traction controller. The high-friction side has a coefficient of friction of 0.92, while the low-friction side has a coefficient of friction of 0.4.

Figure 155 shows the slip ratio on the right wheel without traction control, with the Accurate-Limit controller (angular acceleration limits between 1 rad/s^2 and 40

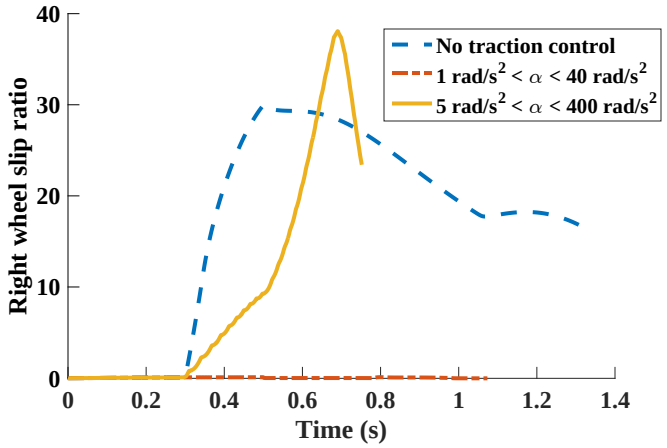

Figure 155: Slip ratio with and without traction control - Fixed wheel acceleration limits.

rad/s^2) and the Excess-Value controller (angular acceleration limits of 5 rad/s^2 and 400 rad/s^2). The dashed line shows the slip ratio without traction control. The dash-dotted line shows the slip ratio was significantly reduced when the controller has accurate and narrow acceleration limits. The Excess-Value controller was able to reduce the wheel slip at the beginning of the wheel slip event; however, it ended up reaching a greater wheel slip than the case without any traction control.

Figure 156 shows the pitch response without traction control and with the two fixed acceleration limited traction controllers. Note that the controller with accurate and narrower wheel acceleration limits actually caused the transporter to fall over faster than with no traction control. Without any traction control it took the transporter about 1.3 seconds to fall completely to the ground. Using controller 1, the pitch angle increased more slowly between 0.4 and 0.5 seconds, but after that, it increased more rapidly than in the case without any traction control because the balancing controller is effectively disabled by the traction control. When the upper acceleration limit was set to 400 rad/s^2, the pitch angle increased more rapidly than in the other two cases. Both the no traction control and the Accurate-Limit controller simulations stopped when an angle of 90° was reached. The Excess-Value controller

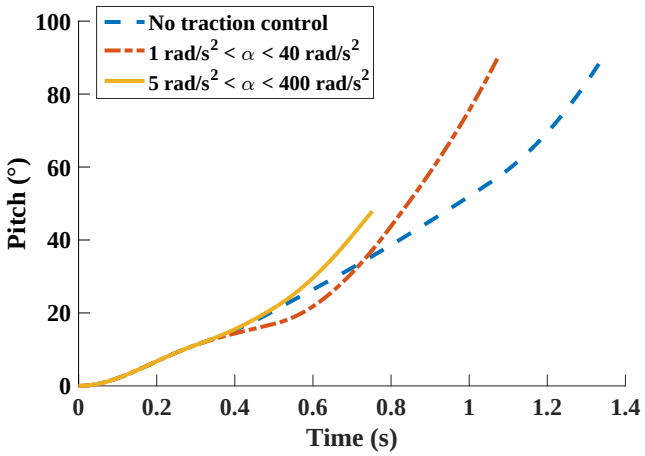

Figure 156: Pitch with and without traction control - Fixed wheel acceleration limits.

simulation was stopped at vehicle tip over, at around 0.7 s.

Figure 157 shows the normal force between the right wheel and the ground. Note that the Accurate-Limit controller prevented the vehicle from getting as close to a roll tip-over condition compared with the case without traction control. The Excess-Value controller, however, made the situation worse and caused the vehicle to tip over in a roll instability before 0.8 s. This occurs because the traction controller allowed the slipping wheel to reach higher accelerations and higher slip ratios before cutting power. Therefore, the wheel did not move forward as fast and caused the vehicle to perform a more aggressive turn towards the right.

Figure 158 shows the vehicle yaw angle. Note that both traction controllers where able to significantly limit the angle that the vehicle deviated from a straight path. The Accurate-Limit traction control was more effective in this task than the Excess-Value traction control. However, this positive effect is countered by the faster pitch failure they induce.

6.1.1 Fixed limit controller on a low friction surface of a specified length

A leaning motion by the operator of 0.5 seconds over a surface with low friction over the entire distance that is traveled by the wheel proved to be too challenging for

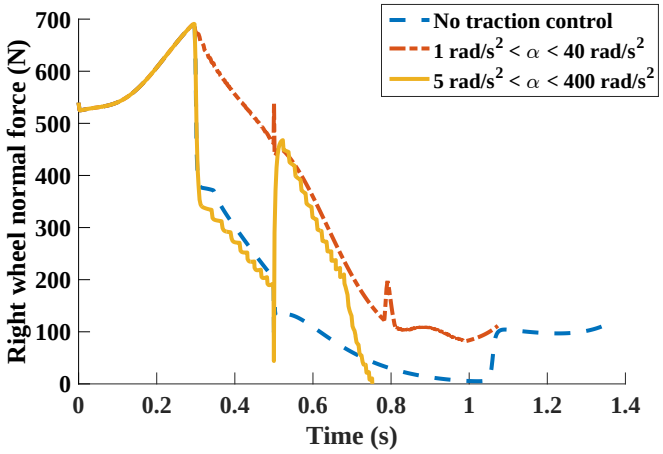

Figure 157: Right wheel normal force with and without traction control - Fixed wheel acceleration limits.

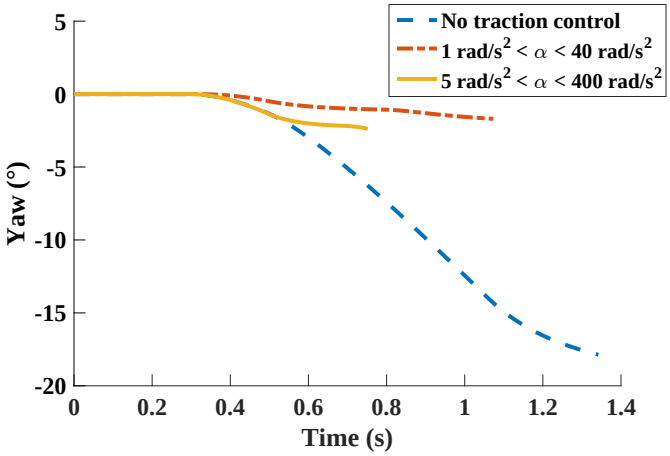

Figure 158: Yaw rate with and without traction control - Fixed wheel acceleration limits.

the traction controller. In this section, the performance of the traction controllers is measured on a low friction surface that is 0.15 m in length.

Figure 159 shows the pitch angle response of the transporter for the three cases considered in the previous section. Note that both the case without traction control and the case whith the Excess-Value traction controller were unable to balance the vehicle. However, the Accurate-Limits controller did provide the desired effect and allowed the vehicle to balance itself after hitting the slick spot.

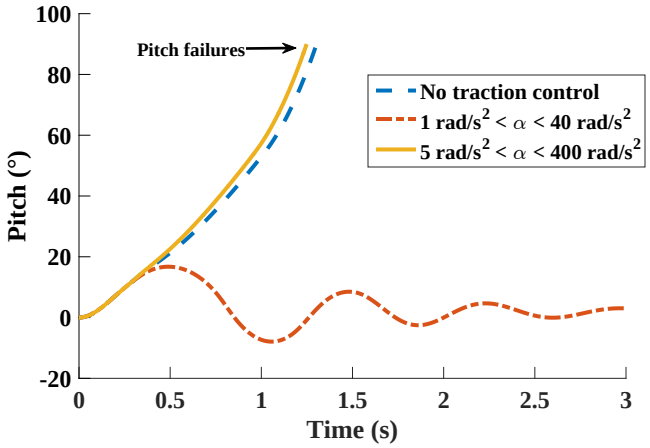

Figure 159: Pitch angle when traveling over a 0.15 m low friction patch - Fixed wheel acceleration limits.

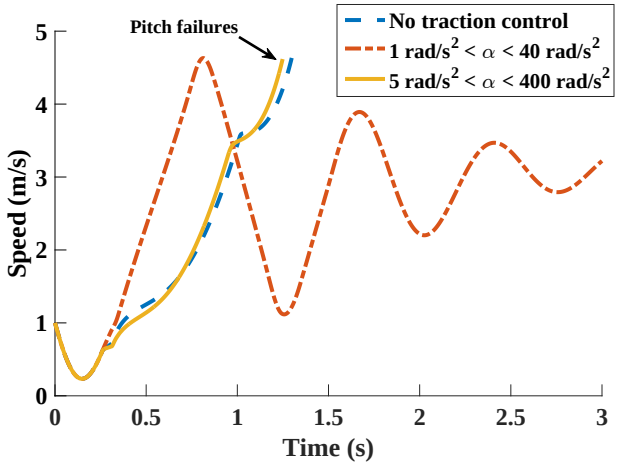

Figure 160: Speed when traveling over a 0.15 m low friction patch - Fixed wheel acceleration limits.

Figure 160 shows the speed response of the vehicle. This figure shows that the Excess-Value controller allowed the wheel to spin so much that the vehicle was unable to accelerate as needed in order to regain balance. On the other hand, the Accurate-Limits controller allowed the vehicle to move fast enough to prevent it from falling over. Note, however, that the resulting dynamic response is composed of "bucking" motions that could destabilize the rider.

Figure 161 shows that the normal force on the right whee dropped to almost zero

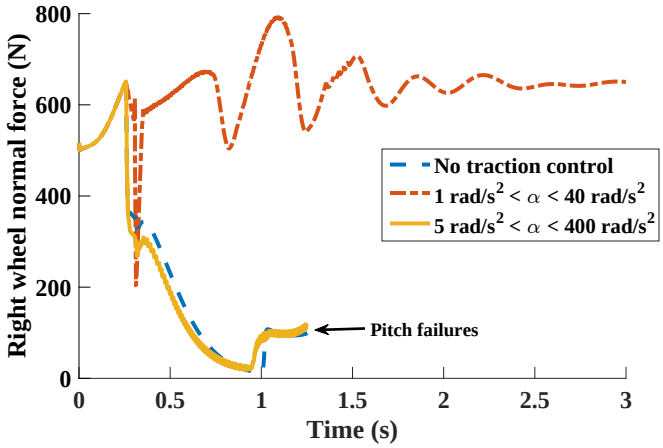

Figure 161: Right wheel normal force when traveling over a 0.15 m low friction patch - Fixed wheel acceleration limits.

for the no traction control case and the Excess-Value case. However, in the Accurate-Limits case the normal force did not decrease as much and the turning motion was not so aggressive.

Note that when the traction controller has excessive and inaccurate limits, it provides essentially no benefit over the case without traction control. In fact, the responses shown in Figures 159 - 161 indicate the machine reacts nearly the same in the no-traction control case and the Excess-Value case.

6.1.2 Optimized wheel angular acceleration limit

The simulations from the previous section was repeated for different angular acceleration limits and the maximum pitch angle, the maximum slip ratio, and the maximum yaw rate were compared to find an angular acceleration limit that would reduce these parameters.

Figure 162 shows the maximum pitch for each angular acceleration limit tested. Angular acceleration limits outside of the range shown were not able to maintain the vehicle balanced. The lowest maximum pitch angle occurred for a maximum angular acceleration of 90 rad/s^2.

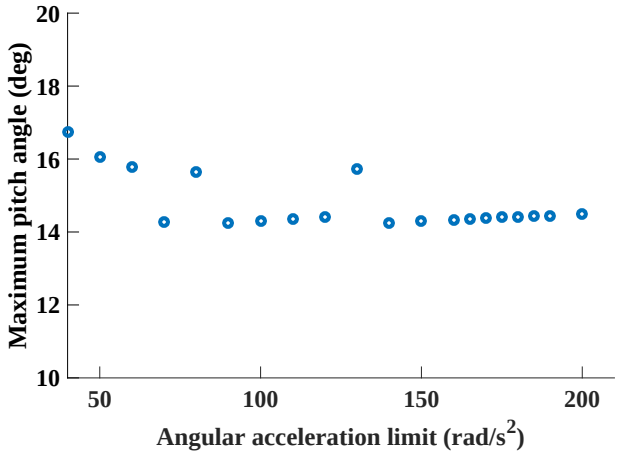

Figure 162: Maximum pitch angle vs. Wheel angular acceleration limit.

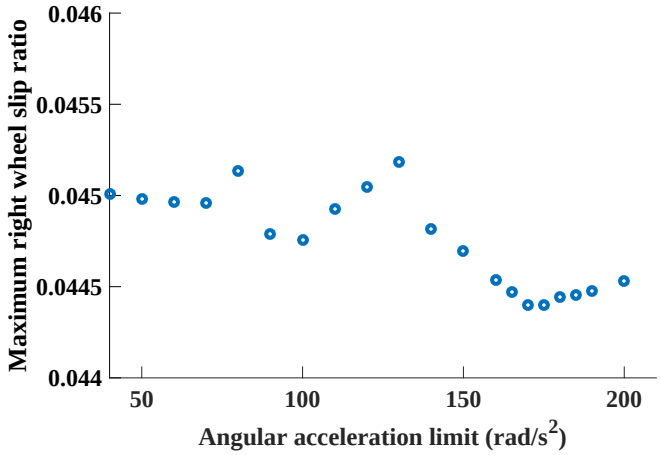

Figure 163: Maximum slip ratio vs. Wheel angular acceleration limit.

Figure 163 shows that the slip ratio was similar for all cases. However, the minimum slip ratio occurred when using an angular acceleration limit of 170 rad/s^2.

Figure 164 shows the maximum yaw angle. The maximum yaw angle is reduced as the wheel angular acceleration limit is increased. The minimum value occurs for a limit of 140 rad/s^2.

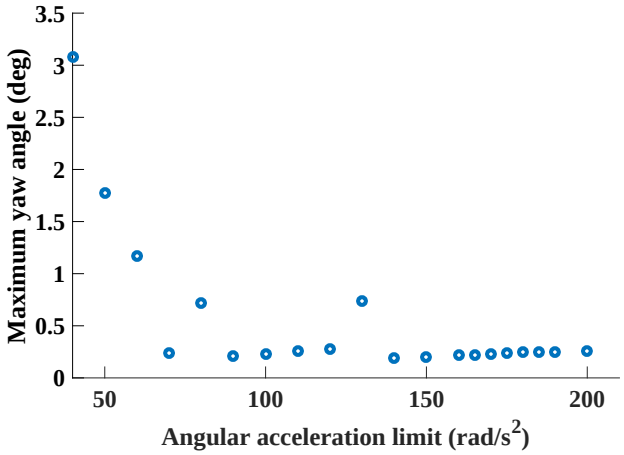

Figure 164: Maximum yaw angle vs. Wheel angular acceleration limit.

6.2 Acceleration-based wheel limiter

Even if the angular acceleration of the wheel is not above the threshold specified by (203) wheel slip might be occurring. When such limited wheel slip goes undetected and uncontrolled, a wheeled inverted-pendulum transporter can go into unstable behavior.

When there is no wheel slip, the angular acceleration of the wheels and and the acceleration of the vehicle are related by the following expressions:

$$\alpha_{exp,r} = \frac{a_x + w\ddot{\beta}}{r_w} \tag{205}$$

$$\alpha_{exp,l} = \frac{a_x - w\ddot{\beta}}{r_w} \tag{206}$$

where $\alpha_{r,l}$ are the angular accelerations of the right and left wheels, $2w$ is the width distance between both wheels, and $\ddot{\beta}$ is the angular acceleration of the vehicle in the yaw direction. Therefore, for a given vehicle acceleration and a given yaw acceleration, the no slip condition requires the angular acceleration of the wheels follow (205) and (206), even for low acceleration values. As noted above, with a fixed wheel angular acceleration limit, many slip situations would go unnoticed.

In this section two modified versions of the traction controller from Section 6.1 are introduced. The basic control algorithm is the same but the acceleration limits are actively adjusted. For controller 1 (Semi-adjustable traction control), the angular acceleration limits for each wheel are defined as:

$$\begin{aligned} \alpha_u &= \max(40\text{rad/s}^2, 1.5\alpha_{exp,i}) \\ \alpha_l &= 0.5\text{rad/s}^2 \end{aligned} \tag{207}$$

where $i = l, r$ for the left and right wheels respectively. For controller 2 (Adjustable traction control), the limits are set as:

$$\begin{aligned} \alpha_u &= 1.5\alpha_{exp,i} \\ \alpha_l &= 0.5\text{rad/s}^2 \end{aligned} \tag{208}$$

These controllers adjust the acceleration threshold to be proportional to the expected wheel angular acceleration given the current vehicle acceleration and yaw acceleration. The semi-adjustable controller only adjusts the acceleration limit while it is above 40rad/s^2.

The same simulation conditions using an unending low-friction surface under the right wheel were repeated using these modified controllers. Figure 165 shows the slip ratio of the right wheel. Both the semi-adjustable and the adjustable traction controller were able to keep the slip ratio near zero without any noticeable difference in performance between the two controllers. Both controllers were able to reduce the wheel slip significantly but were uncapable of preserving pitch stability.

The point of maximum traction occurs at a wheel slip ratio of 0.087, so it is important to examine the slip ratio behavior at smaller values to evaluate which controller performed better. Figure 166 shows the slip ratio of the transporter with both controllers. The adjustable controller was more effective in keeping the slip ratio below the slipping threshold.

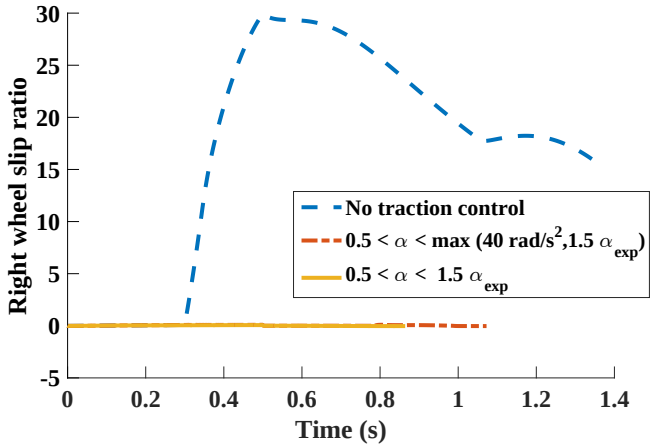

Figure 165: Slip ratio with and without traction control - Variable wheel acceleration limits.

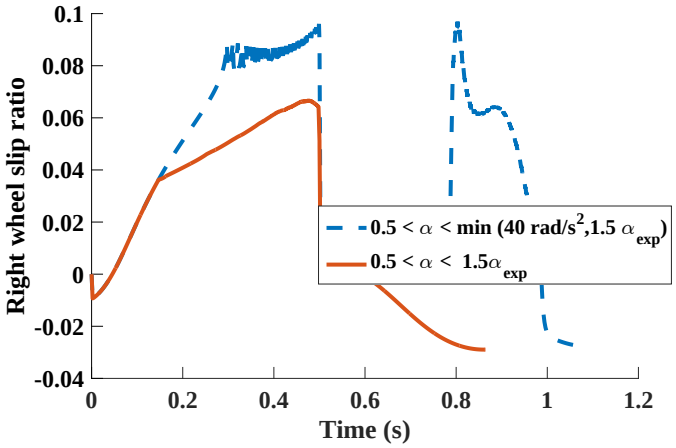

Figure 166: Slip ratio control - Variable wheel acceleration limits.

The pitch response of the vehicle, with and without traction control, is shown in Figure 167. Note that, similar to the controllers with the fixed acceleration limits, the more narrow the range of permissible wheel acceleration, the less effective the vehicle is at maintaining balance. This is evidenced by the fact that the case without traction control fell forward more slowly and the case with acceleration based limits lost its balanced and reached a pitch angle of 90° sooner than the others. So, even though limiting the wheel angular acceleration does greatly reduce wheel slipping, it does so at the expense of the vehicle losing its ability to balance itself.

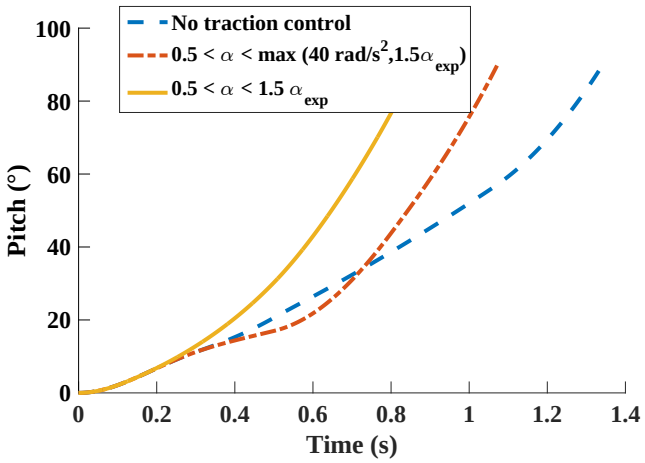

Figure 167: Pitch with and without traction control - Variable wheel acceleration limits.

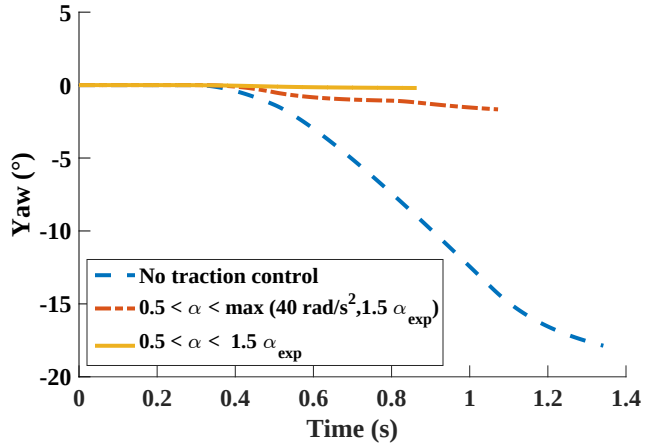

Figure 168: Yaw angle with and without traction control - Variable wheel acceleration limits.

Figure 168 shows the vehicle yaw angle. As in the cases shown in the previous section, limiting the wheel angular acceleration helped the vehicle maintain a straight path. The more narrow the range of permitted wheel acceleration, the less the vehicle turned to the right.

Limiting the wheel angular acceleration by decreasing the motor torque or setting it to zero is an effective way of reducing wheel slip and preventing the vehicle from making unexpected turns. However, it degrades the ability of the vehicle to

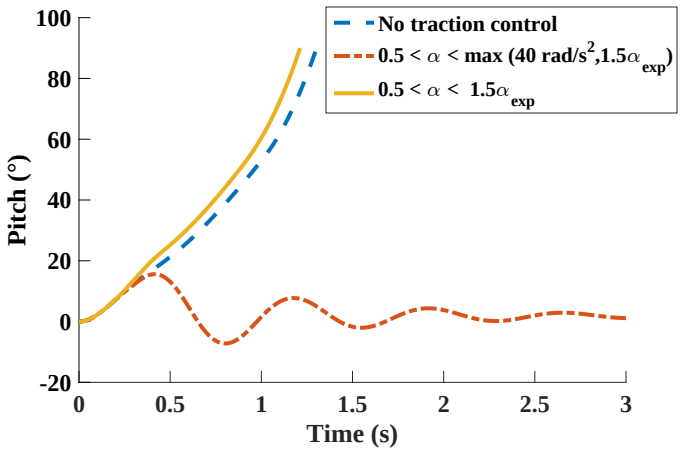

Figure 169: Pitch angle when traveling over a 0.15 m low friction patch - Variable wheel acceleration limits.

balance itself, making it a questionable traction control strategy for a self-balancing transporter.

6.2.1 Adjustable traction controller on a low friction surface of a specified length

The ajustable traction controllers were also tested on a 0.15 m low friction patch. The pitch angle response is shown in Figure 169. It shows that only the semi-adjustable controller was able to maintain the balance of the vehicle while the adjustable controller did not.

Figure 170 shows the speed response. It shows the adjustable controller allowed the vehicle to accelerate faster and stay balanced. This is because below the 40 rad/s^2 limit, the semi-adjustable controller allows the wheel to reach higher angular accelerations and does not limit the capability of the vehicle to accelerate in attempts to balance itself.

Figure 171 shows the right wheel slip for the adjustable and semi-adjustable controllers. Both controllers were similarly effective in reducing the magnitude of the wheel slip. However, the semi-adjustable controller provided a sudden reduction in slip before the 0.5 s mark that allowed the vehicle to accelerate and balance itself

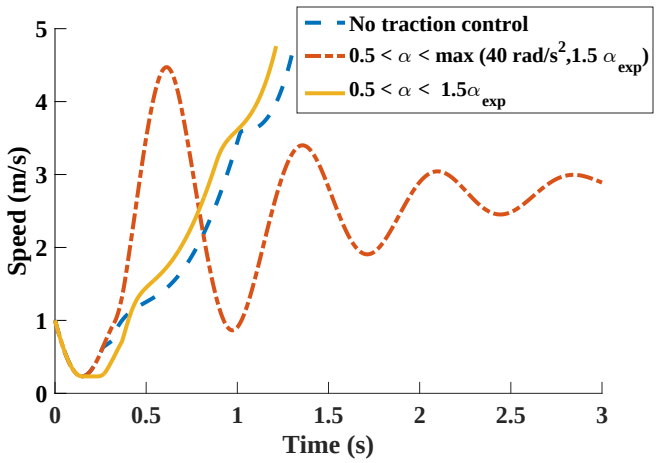

Figure 170: Speed when traveling over a 0.15 m low friction patch - Variable wheel acceleration limits.

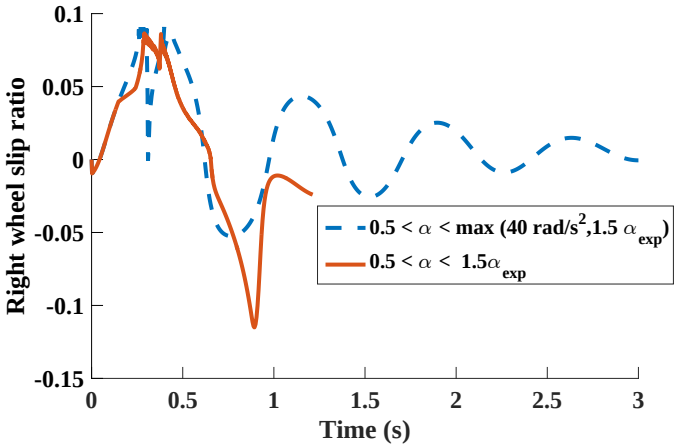

Figure 171: SR when traveling over a 0.15 m low friction patch - Variable wheel acceleration limits.

better. The adjustable controller, by being too aggressive in limiting the wheel acceleration, did not allow the vehicle to move as needed in order to remain stable.

Figure 172 shows the normal force on the right wheel. The semi-adjustable controller provided less reduction in the normal force. This means that while allowing the vehicle to remain stable, it also reduced the magnitude of the unexpected turning motions.

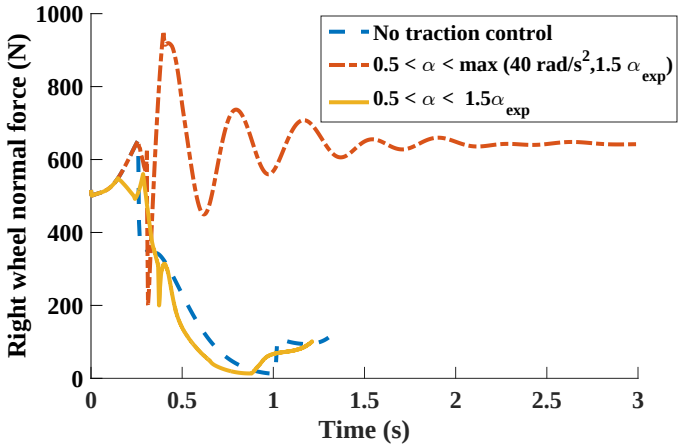

Figure 172: Right normal force when traveling over a 0.15 m low friction patch - Variable wheel acceleration limits.

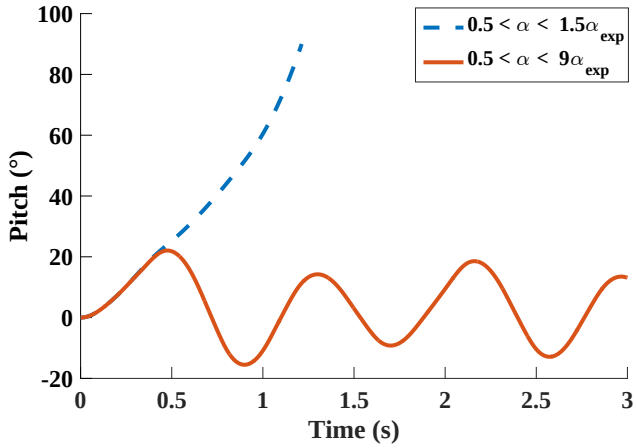

Figure 173: Right normal force when traveling over a 0.15 m low friction patch - Optimized variable wheel acceleration limits.

6.2.2 Optimized adjustable limits controller

The factor of 1.5 in (208) was gradually changed until a value of 9 was found to stabilize the transporter. Figure 173 shows the pitch response with the original controller and the optimized one. Even though the vehicle is able to avoid falling forward, the oscillations do not decay over time, even after the vehicle has gone over the low friction patch. This is a result of the controller not being able to detect that the slipping condition is no longer present and still limiting the angular acceleration of the wheel.

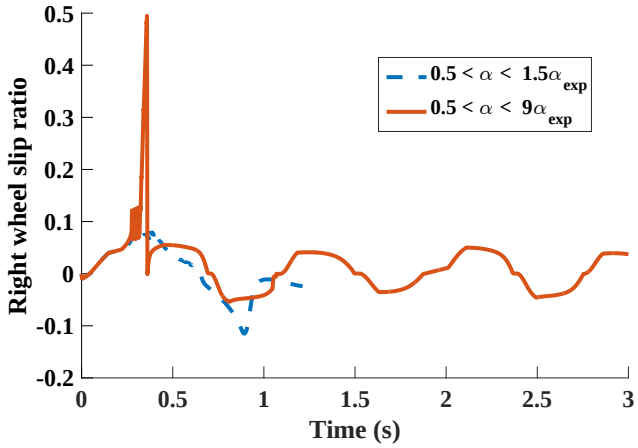

Figure 174: Right normal force when traveling over a 0.15 m low friction patch - Optimized variable wheel acceleration limits.

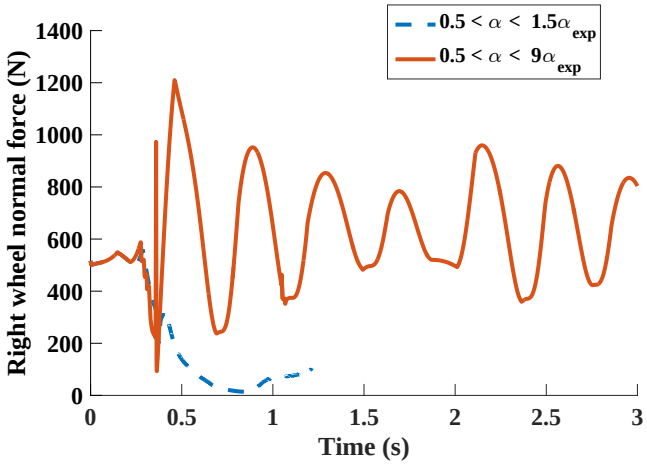

Figure 175: Right normal force when traveling over a 0.15 m low friction patch - Optimized variable wheel acceleration limits.

Figure 174 shows the slip ratio of the wheel. It shows that it initially lets the slip grow larger than in the non optimized controller, but then it stabilizes it at a value smaller than 0.1.

Figure **??** shows the normal force. It shows that the minimum normal force is larger in this case, reducing the tendency of the vehicle to tip over. However, the normal forces oscillate for the rest of the simulation as the vehicle enters an oscillatory state.

6.3 Yaw rate based wheel speed feedback traction controller

Estimating the slip ratio can be a difficult task. Many control algorithms on 4 wheeled vehicles depend on using reference wheel speed from a non driven wheel in order to estimate the slip ratio of a driven wheel and change the driving torque accordingly [22]. However, this is not possible with a two-wheeled inverted pendulum.

However, one can consider that in most cases, the wheel slip will occur in one of the two wheels. Even when there is slip in both wheels, it does not start ocurring in both wheels simultaneously. Therefore, it is possible to assume that when wheel slip starts, only one of the wheels is slipping and the speed of the other wheel can be used as a reference.

Using the concept above, the slipping condition can be detected by comparing two yaw rate measurements. One measurement is obtained from a gyroscope sensor that measures the angular velocity of the vehicle in the yaw direction. This measurement is $\dot{\beta}_g$. The second yaw rate estimate can be calculated using the angular speeds of both wheels and the following equation:

$$\hat{\dot{\beta}} = \frac{r_w(\omega_r - \omega_l)}{2w} \tag{209}$$

where $2w$ is the width of the vehicle, ω_l is the angular speed of the left wheel, ω_r is the angular speed of the right wheel and r_w is the wheel radius.

If the estimated yaw rate from the wheel speeds is greater than the measured yaw rate from the sensor ($\hat{\dot{\beta}} > \dot{\beta}_g$), then ω_r is greater than it should be or that ω_r is less than it should if there was no slipping taking place. The commanded torques to the wheels can provide additional information to distinguish from these two scenarios.

Let the torques applied to the wheels be T_r and T_l respectively. If $T_r > 0$, then the right wheel is finding little resistance from the ground and the input torque is accelerating it more than it would if it where not slipping. If $T_r < 0$ it would not make sense that the right wheel is going faster than expected, because if it was slipping while

being applied a negative torque, then it would decrease its angular speed more than it would if there was no slipping. If $T_l < 0$ then the left wheel is being deccelerated faster than expected and slipping is taking place.

Conversely, if $\hat{\dot{\beta}} > \dot{\beta}_g$ it can mean that ω_r is less than it should be or that ω_r is greater than it should if there was no slipping. Following a similar reasoning, $T_r < 0$ includes that the right wheel is slipping and $T_l > 0$ indicates that the left wheel is slipping.

One limitation of this traction controller is that it fails to distinguish which wheel is slipping when the torques applied to the wheels have opposite signs. However, this would only occur when both wheels are accelerated in opposite directions, which would happen at very sharp turns. This traction controller would need to be disabled when this condition takes place and perhaps an acceleration based traction controller would monitor those circumstances instead.

To summarize, the slip condition for the right wheel can be expressed as follows:

$$Slip_r = \begin{cases} true, & \text{if } \hat{\dot{\beta}} - \dot{\beta}_g > \Delta\dot{\beta}_u \text{ and } T_r > 0 \\ true, & \text{if } \hat{\dot{\beta}} - \dot{\beta}_g < -\Delta\dot{\beta}_u \text{ and } T_r < 0 \\ true, & \text{if } |\hat{\dot{\beta}} - \dot{\beta}_g| > \Delta\dot{\beta}_l \text{ and } Slip_r = true \\ false, & \text{otherwise} \end{cases} \tag{210}$$

where $\Delta\dot{\beta}_u$ is the yaw rate measurement error above which the slip condition is set to true, and $\Delta\dot{\beta}_l$ is the yaw rate measurement error below which the slip condition is cleared.

For the left wheel:

$$Slip_l = \begin{cases} true, & \text{if } \hat{\dot{\beta}} - \dot{\beta}_g > \Delta\dot{\beta}_u \text{ and } T_l < 0 \\ true, & \text{if } \hat{\dot{\beta}} - \dot{\beta}_g < -\Delta\dot{\beta}_u \text{ and } T_l > 0 \\ true, & \text{if } |\hat{\dot{\beta}} - \dot{\beta}_g| > \Delta\dot{\beta}_l \text{ and } Slip_l = true \\ false, & \text{otherwise} \end{cases} \tag{211}$$

When the slip condition is detected in one wheel, the angular speed of the other wheel can be used as a reference, along with the measured yaw rate, to calculate the no-slip angular speed of the wheel that is slipping. The no-slip angular speeds of the wheels are given by:

$$\begin{aligned} \omega_{r,NoSlip} &= \frac{\omega_l r_w + 2w\dot{\beta}_g}{r_w} \\ \omega_{l,NoSlip} &= \frac{\omega_r r_w - 2w\dot{\beta}_g}{r_w} \end{aligned} \tag{212}$$

When wheel slip is detected, a torque offset is subtracted from the commanded torque of the slipping wheel to slow it down and help it regain traction with the ground. This torque offset is defined to be proportional to the error between the measured angular speed and the no slip angular speed of the wheel. This allows the controller to slow down the wheels, while still taking into account the pitch angle of the transporter. This offset torque is given by the following expression:

$$T_{offset,i} = K_w(\omega_i - \omega_{i,NoSlip}) \tag{213}$$

where $i = l, r$ for the left and right wheels respectively.

The feedback control is:

$$T_i = \begin{cases} T_{b,i} & \text{if } Slip_i = false \\ T_{b,i} - T_{offset,i} & \text{if } Slip_i = true \end{cases} \tag{214}$$

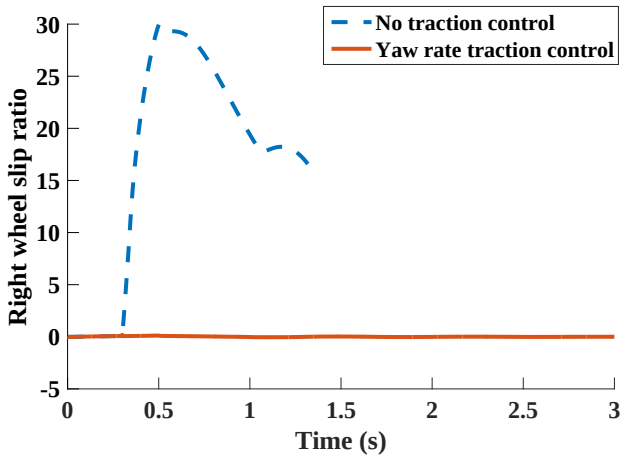

Figure 176: Slip ratio with and without traction control - Wheel speed fedback.

where $i = l, r$ for the left and right wheel respectively, $T_{b,i}$ is the torque commanded by the balancing controller, shown in (200), and (201), and $Slip_i$ is the slip condition flag.

The same conditions as in the previous sections where simulated using this traction control algorithm.

Figure 176 shows the slip ratio of the right wheel. Evidently, the controller was effective in limiting slip. Figure 177 shows a closer look to the slip ratio response of the traction controlled transporter. It shows that at one point the slip ratio went over the limit for peak traction of 0.087. However, the controller was able to rapidly stabilize the slip ratio and let the wheel regain traction for the rest of the simulation.

Figure 178 shows the pitch response of the vehicle. In this case, the controller was able to stabilize the vehicle, while simultaneously keeping the slip ratio under control. This is a significant difference with respect to the performance of the acceleration based controllers that turn off the torque input to the wheel and shows that allowing the commanded torque to always take into account the pitch angle lets the vehicle stay stable even if slipping occurs.

Figure 179 shows the yaw angle of the vehicle. The data shows that the controller also helped the vehicle stay in a relatively straight path. Although its effectiveness

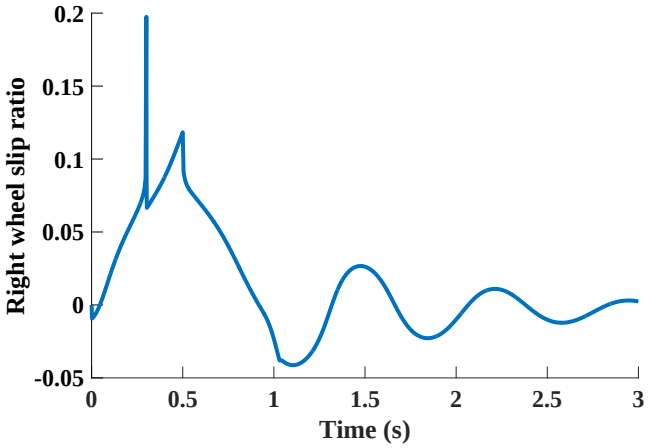

Figure 177: Close-up view of slip ratio with traction control - Wheel speed fedback.

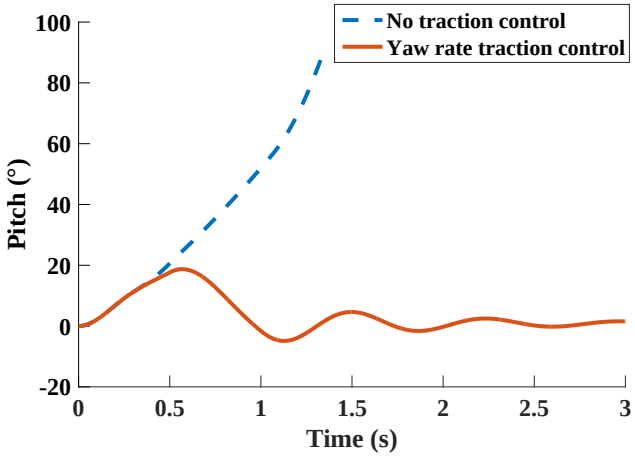

Figure 178: Pitch with and without traction control - Wheel speed fedback.

in doing so was slightly reduced when compared to the Semi-Adjustable controller of the previous section. However, it is not a significant disadvantage when taking into account that this controller prevents the vehicle from falling over.

6.3.1 Yaw rate based traction controller on a low friction surface of a specified length

The yaw rate based controllers were also tested on a low friction surface with a length of 0.15 m. As expected, the controller was able to balance itself and to limit its turning motion. Figure 180 shows the pitch angle response of the vehicle. The pitch angle

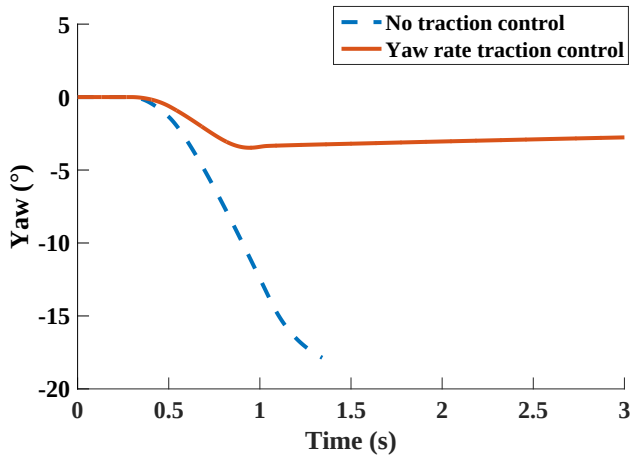

Figure 179: Yaw with and without traction control - Wheel speed fedback.

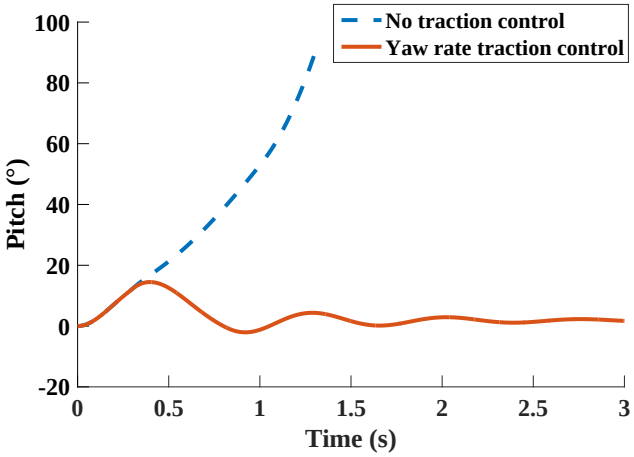

Figure 180: Pitch angle when traveling over a 0.15 m low friction patch - Wheel speed fedback.

did not surpass 20°.

Figure 181 shows the slip ratio of the right wheel. It shows a sudden increase at around the 0.3 s mark that reaches a value of 0.3, which is low in comparison with the no traction control cases studied above, although somewhat larger than the 0.2 value reached after a 0.5 second lean maneuver as seen in the previous section.

Figure 182 shows the yaw response of the vehicle. The maximum absolute yaw reached was only 2°, which shows that the vehicle barely turned off a straight path. This controller was successful in limiting the wheel slip, maintaining pitch stability,

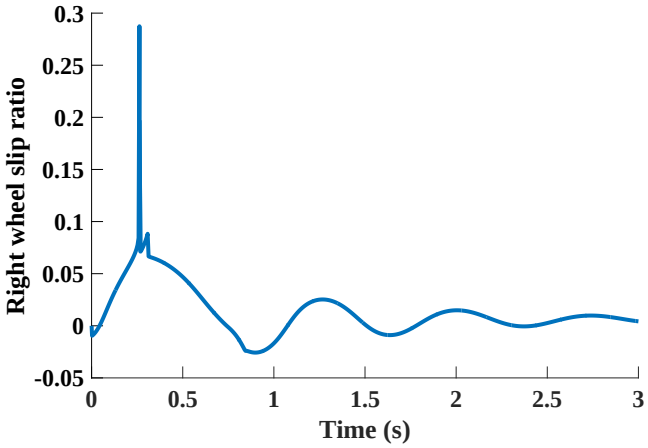

Figure 181: Slip ratio when traveling over a 0.15 m low friction patch - Wheel speed fedback.

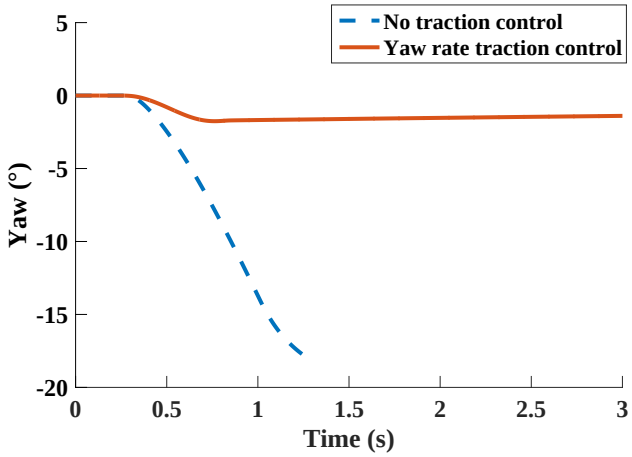

Figure 182: Yaw when traveling over a 0.15 m low friction patch - Wheel speed fedback.

and preventing the vehicle from making unexpected turns.

6.4 Performance evaluation of the traction controllers

The performance of the control methods presented in this chapter were evaluated and compared against each other.

The first comparison criteria is the maximum pitch angle reached by the vehicle after different rider forward leaning maneuvers while traveling over a low-friction patch of 0.1 m and a maximum friction coefficient of 0.4. Figure 183 shows that for

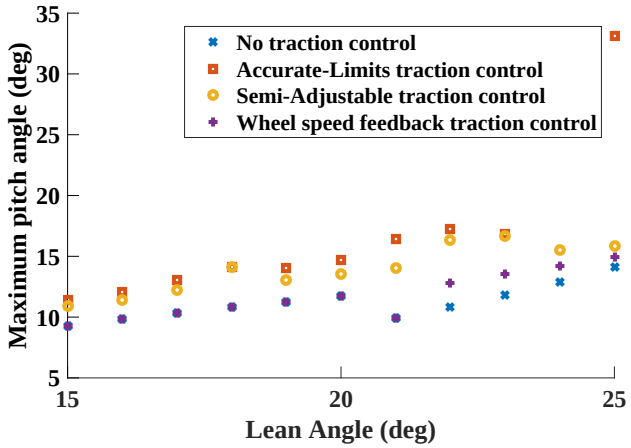

Figure 183: Maximum pitch angle reached at different rider lean angles under three different traction control methods.

all control methods there is a trend of increasing maximum pitch angle as the lean angle increases. For lean angles between 15° and 20° the maximum pitch angle was very similar for the case without any traction control and the Wheel Speed feedback traction controller. In that same range, the Semi-Adjustable traction controller exhibited larger pitch angles, while the Accurate-Limits traction control produced the largest pitch angles reached by the transporter. For angles between 20° and 25° the Wheel Speed feedback traction controller produced larger pitch angles than the case without any traction control, showing that any traction control can reduce the ability of the vehicle to balance itself.

The performance of the traction controller were also measured by examining the minimum right wheel normal force. For this evaluation a rider lean angle of 18.5° was used. The right wheel normal force provides a measure of how close the vehicle is to becoming unstable in the roll direction. For larger coefficients of friction, the Wheel speed feedback traction control and the no traction control cases showed the largest normal forces, indicating less risk to tip-over than the Accurate-Limits and the Semi-Adjustable traction control cases. However, as the coefficient of friction is reduced, the risk of tipping over increases for all cases. For lower coefficients of

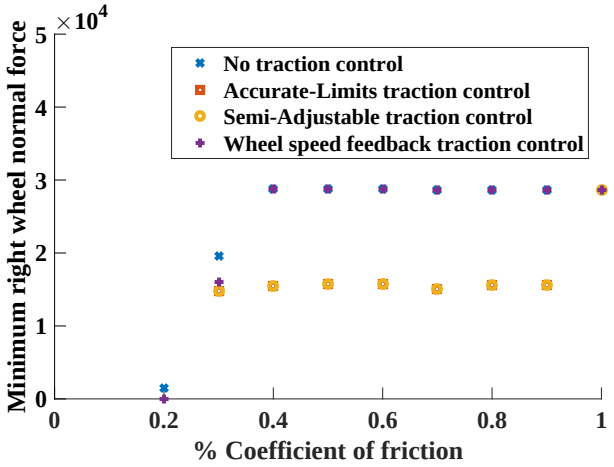

Figure 184: Minimum right normal force at different coefficients of friction under three different traction control methods.

friction, the wheel speed feedback traction control case showed a slightly higher risk of tipping over than the no traction control case.

6.5 Summary

This chapter presented and evaluated three traction control methods. The first method is based on the traction control used by the Segway that reduces the wheel torque to zero when the controller detects that the wheel angular acceleration is larger than a threshold value. A second traction control method continuously adjusted the wheel angular acceleration threshold according to the actual vehicle acceleration and yaw angular acceleration. Both methods were able to reduce wheel slip but were a detriment to the pitch stability. They only work when the acceleration or the slip patch is not too large. A third traction control based on the error between the yaw rate estimated from the angular speeds of the wheels and the yaw rate commanded by the user. This controller showed improved performance with respect to the first two methods. It was able to both reduce the wheel slip ratio and preserve the pitch stability of the vehicle.

CHAPTER VII

CONCLUSIONS

This chapter concludes the thesis by summarizing the results and contributions, and proposes topics for future study.

7.1 Conclusions

This thesis presented dynamic models for self-balancing transporters including a model of the wheel-ground traction forces. These models were used to find the operating conditions that can lead to instability in the pitch and roll directions. A model of an irregular ground surface was presented and simulations were performed to study the effect of a non-planar ground surfaces on the vehicle operation. Traction control methods that increase vehicle stability by reducing wheel slipping were presented and evaluated.

Foundational models of Segways and Hoverboards were developed. Experiments were performed to capture the dynamic behavior of these vehicles. This data was used to obtain model parameters that matched the dynamic behavior of the simulations to that of the actual vehicles. Experiments were also performed to observe the human body motions during turning maneuvers. These showed that the rider leans into the turn to varying degrees.

These models were extended with a comprehensive mathematical description of the wheel-ground traction forces. These were used to predict how aggressively a rider can accelerate the vehicle before slipping takes place. As the wheel-ground traction is reduced, the more likely it becomes for the wheels to slip and the vehicle acceleration capacity is greatly reduced. Slipping can occur even at relatively high coefficients of friction such as 0.8.

The wheel slipping was also found to affect the pitch stability of the vehicle. At lower coefficients of friction or larger lean angles, the vehicle can lose pitch stability in as little as 0.5 seconds.

When the slipping occurs in one wheel, the vehicle can become unstable in the yaw direction. As one wheel slips, one side of the vehicle advances more slowly and causes the vehicle to turn. This can also cause the vehicle to roll over if the turning motion is too fast.

Simulations also showed that the size of a low-friction area on the ground surface affects the capacity of the vehicle to remain stable. If the low-friction patch is short or the vehicle is traveling at a sufficiently fast speed, then the disturbance to the pitch and yaw stability of the vehicle will not be large enough to make the vehicle fall over.

In addition to the maximum traction coefficient, other characteristics of the wheel-ground force can affect the vehicle performance. For example, if the slip ratio at which the maximum slip occurs is larger, then the vehicle will remain within the stable regime of the wheel-ground traction force curve and the slip ratio has a higher chance of remaining bounded within this slip ratio value. Similarly, the larger the slope of the traction force curve is at the origin is, the less prone the vehicle is to going unstable. And finally, the friction coefficient value at large slip ratios also affects the stability of the vehicle. As this value becomes larger, it takes longer for the vehicle to fall over during an instability.

Dynamic simulations and mathematical analysis were used to find the conditions that lead to vehicle lateral roll instability during turning motions. The maximum speed of the vehicle and minimum turning radius are related to each other by the available cornering forces. When the speed is greater than what is imposed by this limit, the vehicle drifts away from a circular path and moves outside the turn.

The maximum speed and minimum turning radius are also related to the vehicle geometrical parameters. The separation distance between the wheels make the vehicle

more stable in the roll direction, but the height of its center of mass makes it more prone to pitch over. The way the rider moves while operating the vehicle can also affect lateral stability. Stability increases when the rider leans into a turn. Leaning away from the turn, or excessively into the turn, decreases stability so there is a narrow range of leaning angles for which the system is stable. A forward lean, however, increases the stability of the vehicle in the roll direction because as the rider leans forward or backward, the height of the center of mass decreases. The speed at which the rider moves can also have an effect on the roll stability. For example, a very aggressive sideways or forward lean can make the vehicle more unstable.

The wheel inertias also have an effect on the lateral stability. At higher speeds, smaller wheel radius or smaller curves, the gyroscopic effect of the wheel rotation generates a moment that has the effect of reducing the normal force on the inside wheel. Dynamic simulations of turning motions showed that the vehicle can lose contact with the ground in as little as 0.12 seconds. Experiments were performed that showed how hitting an obstacle on the ground can also cause the vehicle to become unstable.

The vehicle performance was shown to be degraded by traveling on irregular surfaces. Inclined planes limit the available traction force and it is almost impossible for a vehicle to climb a slope above 40°. Moving transversely to an incline plane is also more risky, and the risk increases with the ratio between the height of the center of mass of the system and the separation between the wheels. An analysis showed that turning while on an incline plane requires the rider to lean more into the turn to prevent tipping over.

A geometrical description of an irregular surface was introduced in order to model any type of surface as a continuous curve that can be integrated by numerical solvers. It was demonstrated that convex or bump surfaces cause a reduction in the normal force between the vehicle and the ground. This reduction in the normal force can

lead to loss of traction, wheel slipping, and pitch instability. The effect is magnified when the speed of the vehicle is larger.

In holes or concave surfaces a similar effect occurs. Dynamic simulations were performed to verify these results and confirm that these conditions can lead to pitch instability and loss of wheel traction. When the vehicle encounters a rectangular step, the maximum speed at which it can climb it without losing contact with the ground is very low and depends on the size of the wheel and the size of the step.

To reduce the danger associated with some of the conditions exposed in this thesis, three traction-control methods were proposed. The first method is based on the traction control used by the Segway, as described in US Patent 6,408,240. It works by reducing the torque applied to the wheel to zero when the controller detects that the wheel angular acceleration is larger than a threshold value. It does provide a reduction in the wheel slip ratio, but at the detriment to the pitch stability of the vehicle. Furthermore, it only works when the surface patch is of a limited length or the vehicle travels above a certain speed. A smaller wheel acceleration limit somewhat improved the performance of this controller.

A second traction control method consisted of continuously adjusting the wheel angular acceleration threshold according to the actual vehicle acceleration and yaw angular acceleration. Similar to the first method, it was able to reduce wheel slip, but to the detriment of the pitch stability, and only works when the acceleration or the slip patch is not too large. Two variations of this controller were proposed. One uses the angular acceleration threshold has a minimum limit and the other uses an acceleration threshold that can become very small at very low vehicle accelerations. Setting a minimum limit to the acceleration threshold improved the performance of the controller.

A third traction control based on the error between the yaw rate estimated from the angular speeds of the wheels and the yaw rate commanded by the rider. Working

under the assumption that when slip starts it only happens in one wheel, and using the torques outputs from the motors, it is possible to infer which wheel is slipping. If a wheel is slipping, then a torque offset is added to the control law. This offset is proportional to the error between the measured wheel angular speed and the estimated wheel angular speed if there was no slip. In this way, the control law still takes into account the pitch, and yaw error, while attempting to reduce the wheel slip. This controller showed improved performance with respect to the first two methods. It was able to both reduce the wheel slip ratio and preserve the pitch stability of the vehicle.

7.2 Thesis contributions

A succinct list of contributions is made by this thesis is:

- Foundational models that describe Segways and Hoverboards that are calibrated to match the dynamic behavior of real commercially-available vehicles.
- A description of the conditions that can lead to loss of traction.
- An explanation of the consequences that result from a loss of traction.
- An analysis of the conditions that reduce the lateral stability of such vehicle.
- Dynamic simulations that demonstrate the effects of lateral instability and loss of traction.
- Three traction-control methods that reduce wheel slip and preserve pitch stability to various degrees of effectiveness.

7.3 Future work

The research in this thesis can be expanded to account for more complexity in the dynamic models and to improve the traction-control methods proposed here.

The dynamic models can be modified to include more active rider models. These would require studying human-rider actions from a control systems perspective and modeling the control law that governs how the rider controls the speed and the yaw rate of the vehicle with his actions.

The wheel-ground traction force model can be expanded to account for effects like load dependence and non steady state conditions. This would include modeling the wheel slip as a dynamic variable governed by differential equations.

The dynamic effects of the rider leaning forward or sideways can be dynamically simulated to obtain a more precise evaluation of how they affect the lateral stability of the vehicle.

More complex surface geometries can be described and collision dynamics can be introduced to the models to better describe the dynamic effects of the vehicle going over irregular terrain.

The traction-control methods proposed can be optimized to find the parameters that improve their performance over a range of expected operating and environmental conditions.

Develop a traction-control method that uses the estimated surface angle to estimate the appropriate wheel angular acceleration limit.

REFERENCES

[1] "Accident case study." Available: https://www.youtube.com/watch?v=R_h98YLiRX0.

[2] "Segway mini pro," Accessed on June 26, 2018. Available: https://s7d1.scene7.com/is/image/BedBathandBeyond/149251663654462p?478.

[3] Abeygunawardhana, P. K. W. and Murakami, T., "Vibration suppression of two-wheel mobile manipulator using resonance-ratio-control-based null-space control," *IEEE Transactions on Industrial Electronics*, vol. 57, pp. 4137–4146, Dec 2010.

[4] Adams, C., Singhose, W., and Kim, D., "A system-dynamics-based hazard analysis of inverted-pendulum human transporters," in *ASME 2013 Dynamic Systems and Control Conference*, pp. V003T45A002–V003T45A002, American Society of Mechanical Engineers, 2013.

[5] Anderson, M. and Grantham, W., "Lyapunov optimal feedback control of a nonlinear inverted pendulum," *Journal of Dynamics, Systems, Measurement and Control*, vol. 111, pp. 554–558, Dec 1989.

[6] Bianchessi, A. G., Ongini, C., Boniolo, I., Alli, G., Spelta, C., Tanelli, M., and Savaresi, S. M., "A novel electric vehicle for smart indoor mobility," *IEEE Transactions on Intelligent Transportation Systems*, vol. 15, pp. 1429–1440, Aug 2014.

[7] Boniface, K., McKay, M. P., Lucas, R., Shaffer, A., and Sikka, N., "Serious injuries related to the Segway personal transporter: A case series," *Annals of Emergency Medicine*, vol. 57, no. 4, pp. 370–374, 2011.

[8] Castro, A., "Modeling and dynamic analysis of a two-wheeled inverted-pendulum," Master's thesis, Georgia Institute of Technology, 2012.

[9] Castro, A., Adams, C., and Singhose, W., "Dynamic response characteristics of a two-wheeled inverted-pendulum transporter," in *Decision and Control (CDC), 2013 IEEE 52nd Annual Conference on*, pp. 1532–1537, IEEE, 2013.

[10] Castro, A., Singhose, W., Liu, X., Sorensen, K., and Kwak, E. C., "Modeling and experimental testing of hoverboard dynamic behavior," in *ASME 2017 Dynamic Systems and Control Conference*, American Society of Mechanical Engineers Digital Collection, 2017.

[11] Chan, R. P. M., Stol, K. A., and Halkyard, C. R., "Effect of limiting wheel slip on two-wheeled robots in low traction environments," in *International Conference on Intelligent Robotics and Applications*, pp. 417–426, Springer, 2012.

[12] Chen, S., "Two-wheel, self-balancing vehicle with independently movable foot placement sections," May 27 2014. US Patent 8,738,278.

[13] Choi, D. and Oh, J.-H., "Human-friendly motion control of a wheeled inverted pendulum by reduced-order disturbance observer," in *IEEE International Conference on Robotics and Automation, Pasadena, CA.*, pp. 2521–2526, May 2008.

[14] Consumer Product Safety Commission, "CPSC, Segway LLC announce voluntary recall to upgrade software on Segway™ human transporters," 2003. Available: http://www.cpsc.gov/en/Recalls/2003/CPSC-Segway-LLC-Announce-Voluntary-Recall-to-Upgrade-Software-on-Segway-Human-Transporters/.

[15] Consumer Product Safety Commission, "Segway Inc. announces recall to repair Segway® personal transporters," 2006. Available: www.cpsc.gov/en/Recalls/2006/Segway-Inc-Announces-Recall-to-Repair-Segway-Personal-Transporters/.

[16] Dempster, W., "Space requirements of the seated operator, geometrical, kinematic, and mechanical aspects of the body with special reference to the limbs."

[17] Grasser, F., D'Arrigo, A., Colombi, S., and Rufer, A. C., "JOE: A mobile, inverted pendulum," *IEEE Transactions on Industrial Electronics*, vol. 49, pp. 107–114, 2002.

[18] Ha, Y. and Yuta, S., "Trajectory tracking control for navigation of the inverse pendulum type self-contained mobile robot," *Robotics and Autonomous Systems*, vol. 17, no. 1, pp. 65–80, 1996.

[19] Harber, J., Adams, C., Castro, A., and Singhose, W., "Dynamic effects of obstacles on two-wheeled inverted-pendulum transporters," in *ASME 2015 International Design Engineering Technical Conferences and Computers and Information in Engineering Conference*, pp. V006T10A080–V006T10A080, American Society of Mechanical Engineers, 2015.

[20] Hemami, H. and Katbab, A., "Constrained inverted pendulum model for evaluating upright postural stability," *Journal of Dynamic Systems Measurement and Control*, vol. 104, no. 4, pp. 343–349, 1982.

[21] Ho, M., Horn, B. D., Lin, I. C., Chang, B., Carrigan, R. B., and Shah, A. S., "Hoverboard safety: Lessons learned from the first year of injuries," 2018.

[22] Ise, K., Fujita, K., Inoue, Y., and Masutomi, S., "The" lexus" traction control (trac) system," *SAE transactions*, pp. 319–326, 1990.

[23] Jones, D. R. and Stol, K. A., "Modelling and stability control of two-wheeled robots in low-traction environments,"

[24] Kamen, D., Ambrogi, R., Dattolo, J., Duggan, R., Field, J., Heinzmann, R., McCambridge, M., Morrell, J., Piedmonte, M., Rosasco, R., and others, "Control of a personal transporter based on user position," *US Patent #7,275,607*, 2007.

[25] Kamen, D., Ambrogi, R., and Duggan, R., "Human transporter," *US Patent #5,701,965*, 1997.

[26] Kamen, D., Ambrogi, R., and Duggan, R., "Transportation vehicles and methods," *US Patent #5,971,091*, 1999.

[27] Kamen, D., Arling, R., Field, J., Morrell, J., and Pompa, J., "Steering control of a personal transporter," *US Patent #6,581,714*, 2003.

[28] Kane, T. R. and Mitiguy, P., "MotionGenesis – Kane 5.2." Available: `http://www.motiongenesis.com/`, 2011.

[29] Katariya, A. S., "Optimal State-Feedback and Output-Feedback Controllers for the Wheeled Inverted Pendulum System," Master's thesis, Georgia Institute of Technology, 2010.

[30] Kausar, Z., Stol, K., and Patel, N., "Performance enhancement of a statically unstable two wheeled mobile robot traversing on an uneven surface," in *Robotics Automation and Mechatronics (RAM), 2010 IEEE Conference on*, pp. 156–162, IEEE, 2010.

[31] Kausar, Z., Stol, K., and Patel, N., "The effect of terrain inclination on performance and the stability region of two-wheeled mobile robots," *International Journal of Advanced Robotic Systems*, vol. 9, no. 5, p. 218, 2012.

[32] Kemper, S., *Reinventing the Wheel: A Story of Genius, Innovation, and Grand Ambition*. New York, NY: HarperCollins Publishers Inc., 2005.

[33] Kim, M. and Sorensen, K., "Comparison of coulomb and brush tire models for characterizing tractive force in wip systems," in *IEEE International Conference on Control and Automation*, (Anchorage, Alaska, USA), IEEE, 2018.

[34] Kim, S., Seo, J., and Kwon, S., "Development of a two-wheeled mobile tilting & balancing MTB robot," in *2011 11th International Conference on Control, Automation and Systems (ICCAS)*, pp. 1–6, IEEE, 2011.

[35] Kim, Y., Kim, S. H., and Kwak, Y. K., "Improving driving ability for a two-wheeled inverted-pendulum-type autonomous vehicle," *Proceedings of the Institution of Mechanical Engineers, Part D: Journal of Automobile Engineering*, vol. 220, no. 2, pp. 165–175, 2006.

[36] Kim, Y., Kim, S. H., and Kwak, Y. K., "Dynamic analysis of a nonholonomic two-wheeled inverted pendulum robot," *Journal of Intelligent and Robotic Systems*, vol. 44, pp. 25–46, 2005.

[37] Ko, A., Lau, H., and Lau, T., "SOHO security with mini self-balancing robots," *The Industrial Robot*, vol. 32, no. 6, pp. 492–498, 2005.

[38] Li, J., Gao, X., Huang, Q., Du, Q., and Duan, X., "Mechanical design and dynamic modeling of a two-wheeled inverted pendulum mobile robot," in *2007 IEEE International Conference on Automation and Logistics, Jinan, China*, pp. 1614–1619, Aug. 2007.

[39] Matsumoto, O., Kajita, S., and Tani, K., "Estimation and control of the attitude of a dynamic mobile robot using internal sensors," *Journal of the Robotics Society of Japan*, vol. 8, no. 5, pp. 541–550, 1990.

[40] McIlvain, C., Hadiza, G., Tzavaras, T. J., and Weingart, G. S., "Injuries associated with hoverboard use: a review of the national electronic injury surveillance system," *The American journal of emergency medicine*, vol. 37, no. 3, pp. 472–477, 2019.

[41] Morrell, J. B. and Field, D., "Design of a closed loop controller for a two wheeled balancing transporter," in *Proceedings of the 2007 IEEE/RSJ International Conference on Intelligent Robots and Systems*, (San Diego, CA, USA), pp. 4059–4064, Oct. 29 - Nov. 2 2007.

[42] Morrell, J. B. and Pompa, J. B., "Traction control for a personal transporter," June 18 2002. US Patent 6,408,240.

[43] National Highway Traffic Safety Administration, "Investigation of the Inertial Properties of the Human Body, 1975," tech. rep., National Highway Traffic Safety Administration.

[44] Pacejka, H., Bakker, E., and Nyborg, L., "Tyre modelling for use in vehicle dynamics studies," *SAE paper*, vol. 870421, 1987.

[45] Pathak, K. and Agrawal, S. K., "Band-limited trajectory planning and tracking for certain dynamically stabilized mobile systems," *Journal of Dynamic Systems, Measurement, and Control*, vol. 128, no. 1, pp. 104–111, 2006.

[46] Ravichandran, M. T. and Mahindrakar, A. D., "Robust stabilization of a class of underactuated mechanical systems using time scaling and Lyapunov redesign," *IEEE Transactions on Industrial Electronics*, vol. 58, pp. 4299–4313, Sept 2011.

[47] Roider, D., Busch, C., Spitaler, R., and Hertz, H., "Segway® related injuries in vienna: report from the lorenz böhler trauma centre," *European Journal of Trauma and Emergency Surgery*, vol. 42, no. 2, pp. 203–205, 2016.

[48] Sasaki, M., Yanagihara, N., Matsumoto, O., and Komoriya, K., "Steering control of the personal riding-type wheeled mobile platform (pmp)," in *International Conference on Intelligent Robots and Systems, 2005*, pp. 1697–1702, IEEE.

[49] Segway Inc., "Reference Manual - Segway Personal Transporter PT i2, x2 [Online]," Accessed on March 26, 2012. Available: `http://www.segway.com/downloads/pdfs/ReferenceManual.pdf`.

[50] Shaheen, S. A. and Finson, R., "Bridging the last mile: a study of the behavioral, institutional, and economic potential of the segway human transporter," *Transportation Research Board*, no. 03-4470, 2003.

[51] Singh, K. B. and Taheri, S., "Estimation of tire–road friction coefficient and its application in chassis control systems," *Systems Science & Control Engineering*, vol. 3, no. 1, pp. 39–61, 2015.

[52] Singhose, W., Adams, C., and Kim, D., "A dynamics-based hazard analysis of inverted-pendulum human transporters using data-mined information," *ASCE-ASME Journal of Risk and Uncertainty in Engineering Systems, Part B: Mechanical Engineering*, vol. 2, no. 3, p. 031007, 2016.

[53] Sinha, S. C. and Joseph, P., "Control of general dynamic-systems with periodically varying parameters via Lyapunov-Floquet transformation," *Journal of Dynamic Systems Measurement and Control*, vol. 116, pp. 650–658, Dec 1994.

[54] Sorensen, K. and Singhose, W., "Wheeled inverted pendulum control and slip dynamics," in *IEEE International Conference on Control and Automation*, (Anchorage, Alaska, USA), IEEE, 2018.

[55] Stilman, M., Olson, J., and Gloss, W., "Golem Krang: Dynamically stable humanoid robot for mobile manipulation," in *2010 IEEE International Conference on Robotics and Automation*, (Anchorage, AK), 2010.

[56] Stilman, M., Wang, J., Teeyapan, K., and Marceau, R., "Optimized control strategies for wheeled humanoids and mobile manipulators," in *2009 IEEE/RAS International Conference on Humanoid Robotics*, (Paris, France), 2009.

[57] Takei, T., Imamura, R., and Yuta, S., "Baggage transportation and navigation by a wheeled inverted pendulum mobile robot," *IEEE Transactions on Industrial Electronics*, vol. 56, pp. 3985–3994, Oct. 2009.

[58] Takei, T., Matsumoto, O., and Komoriya, K., "Simultaneous estimation of slope angle and handling force when getting on and off a human-riding wheeled inverted pendulum vehicle," in *IEEE/RSJ International Conference on Intelligent Robots and Systems, 2009. IROS 2009. St. Louis, MO*, pp. 4553–4558, Oct. 2009.

[59] TODORUŢ, A., CORDOŞ, N., MARIAN, A., and BĂLCĂU, M., "Evaluation of the transversal stability parameters for the vehicles with two wheels locate in parallel, segway type," *ACTA TECHNICA NAPOCENSIS-Series: APPLIED MATHEMATICS, MECHANICS, and ENGINEERING*, vol. 60, no. 2, 2017.

[60] Vicon Motion Systems Limited, "Vicon — Products — Cameras — MX-3+ [Online]," Accessed on March 15, 2012. Available: `http://www.vicon.com/products/mx3.html`.

[61] Vicon Motion Systems Limited, "Vicon MX Hardware System Reference, Revision 1.6, Oxford, UK, 2007."

[62] Voth, D., "Segway to the future [autonomous mobile robot]," *IEEE Intelligent Systems*, vol. 20, no. 3, pp. 5–8, 2005.

[63] Weingart, G. S., Glueckert, L., Cachaper, G. A., Zimbro, K. S., Maduro, R. S., and Counselman, F., "Injuries associated with hoverboard use: a case series of emergency department patients," *Western journal of emergency medicine*, vol. 18, no. 6, p. 993, 2017.

[64] Yamafuji, K. and Kawamura, T., "Study on the postural and driving control of a coaxial bicycle," *Transactions of the JSME Series C*, vol. 54, no. 501, pp. 1114–1121, 1988.

[65] Zheng, N., Zhang, Y., Guo, Y., and Zhang, X., "Hierarchical fast terminal sliding mode control for a self-balancing two-wheeled robot on uneven terrains," in *Control Conference (CCC), 2017 36th Chinese*, pp. 4762–4767, IEEE, 2017.